

MANGANESE REDUCTIVE ALLOYING

THE KINETICS OF SILICOTHERMIC AND CARBOTHERMIC
MANGANESE REDUCTIVE ALLOYING FOR HIGH MANGANESE STEEL

By

BRIAN JAMIESON, B.ENG. & MGMT.

A Thesis

Submitted to the School of Graduate Studies

in Partial Fulfillment of the Requirements

for the Degree

Doctor of Philosophy

McMaster University

© Copyright by Brian Jamieson, April 2019

DOCTOR OF PHILOSOPHY (2019)
(Materials Engineering)

McMaster University
Hamilton, Ontario

Title: The Kinetics of Silicothermic and Carbothemic Manganese Reductive
Alloying for High Manganese Steel

Author: Brian Jamieson, B.Eng. & Mgmt. (McMaster University)

Supervisor: Professor Kenneth S. Coley & Professor Mansoor Barati (University
of Toronto)

Number of Pages: xviii, 238

Lay Abstract

3rd Generation Advanced High Strength steels (3G AHSS) are a promising opportunity to produce steels with improved mechanical properties. These steels are alloyed with up to 11wt% manganese; traditional alloy additions are added as ferroalloys which may not be the most economical solution to achieve the required concentrations of manganese. Reductive alloying is a potential method for achieving high concentrations of manganese in the metal. By adding manganese oxide to slag, and reductants like carbon or silicon to the molten metal, manganese can be reduced from slag to metal. This work has determined the kinetics (rate of reaction) during the silicothermic and carbothermic reduction of manganese oxide from slag. The silicothermic reduction of manganese oxide is fast and can achieve high levels of manganese in the metal. The carbothermic reduction is much slower with questionable viability.

Abstract

Fundamental research is required to support the commercialization of 3rd Generation Advanced High Strength steels (3G AHSS). Mid-manganese 3G AHSS steels can contain up to 11wt% manganese and are expensive if traditional ferroalloying practices are used; reductive alloying is a promising alternative.

This study has researched the fundamental science behind possible processing methods. Silicothermic reduction of MnO from slag was studied. The reaction is fast but can be blocked by a stagnant layer of SiO bubbles cutting the rate of reaction by one order of magnitude. A theoretical model for mixed mass transport control was tested against original experimental data. Across nine datasets, the mass transfer coefficient for metal species, k_{Metal} , was $2.3 \cdot 10^{-4}$ m/s and the slag mass transfer coefficient, k_{Slag} , was $6.7 \cdot 10^{-4}$ m/s. In real industrial systems, gas blockage should not have an effect because stirring will dislodge these bubbles.

Carbothermic reduction is dramatically different and has been qualitatively documented in this work. The reaction occurs in two stages: the first approximately three times faster than the second. The first stage is characterized by internal CO nucleation and growth and is rate-limited by the formation and growth of these CO bubbles. The second stage occurs along the metal interface and shows that the slag and metal are essentially separated by an intermediary gas phase. This reaction is controlled by decomposition of metal oxides at the gas-slag boundary, decomposition of CO₂ at the gas-metal boundary, and transport of CO₂ across the gas bubble; this mechanism is nearly identical to the carbothermic reduction of FeO.

Reductive alloying can be utilized with the silicothermic reduction process to obtain high levels of manganese in steel but the carbothermic reduction may be too slow to be a viable process.

Acknowledgements

For six years, across two degrees, I have had the privilege to study under the guidance of my supervisor Ken Coley. Through teaching style and direct supervision, I've become enthralled with steelmaking and pyrometallurgy, and it is all thanks to him. Without his encouragement, support, and confidence I would not and could not be writing this acknowledgement in completion of my Ph.D. For that, I extend my most sincere gratitude and hope to work together again in the future.

To my colleague's in the McMaster Process Metallurgy research group, thank you for everything. Never did I leave a meeting without learning something new or having laugh. Special thanks to Kezhuan Gu; as we both discovered, furnaces don't operate themselves, nor do they repair themselves. Thank you for all the help troubleshooting, without it a lot of the data within this thesis may not exist.

To the Department of Materials Science and Engineering, my home for 8 years, thank you for the tight knit family. From top to bottom, there is not a single faculty member, staff member, or student without a friendly face. Thanks to the McMaster Steel Research Centre, and the High Manganese Steelmaking grant team. The opportunity to work closely with industrial partners and receive feedback has helped me grow immeasurably, and its an experience I would not trade for anything.

To my fiancé Hannah, it was only supposed to be a two-year master's degree, for that I guess I should apologize. But here we stand, on the cusp of our future. Everything I have achieved in the past 6 years has been better because of you, and I look forward to making these accomplishments a fraction of what we will experience together.

Finally, thanks to my family for their support and encouragement. To my mom, a port in the storm, a rock that never breaks; what you have faced in life cannot be adequately described, and so I will simply say *thank you*. In memory of my father; it has been a long time since I needed your help with my trigonometry homework, but if you could, just look where that has led.

Table of Contents

List of Figures and Tables.....	x
Abbreviations and Symbols	xvi
Declaration of Academic Achievement	xvii
Contributions to the Enclosed Literature	xviii
Chapter 1	
1. Introduction	1
1.1. Motivation for this Study	1
1.2. Objectives of this Study	2
1.3. Organization of this Thesis.....	3
1.3.1. Overlap within Scholarly Articles	4
Chapter 2	
2. Literature Review	5
2.1. Silicothermic Reduction Studies	5
2.1.1. Pidgeon Process	6
2.1.2. Silicothermic Reduction of Manganese Oxide	9
2.2. Carbothermic Reduction Studies.....	13
2.2.1. Carbothermic Reduction of Manganese Oxide.....	13
2.3. Slag Basicity & Viscosity.....	22
2.4. Surface Tension & Dynamic Interfacial Phenomena	26
2.4.1. Surface Active Elements.....	28
2.4.2. Dynamic Interfacial Phenomena.....	31
2.5. Bloated Droplets.....	40
2.6. Summary & Gaps in the Literature	42
2.6.1. Summary & Gaps in Silicothermic Reduction Literature.....	42
2.6.2. Summary & Gaps of Carbothermic Research.....	44
2.6.3. Summary & Gaps in Other Highlighted Topics	46
Chapter 3	
3. Kinetics of Silicothermic Reduction of Manganese Oxide for Advanced High Strength Steel Processing	47
Copywrite & Bibliographic Information	47
Contributions & Context.....	47
Abstract	49
3.1. Introduction	49
3.2. Experimental Procedure	56
3.2.1. Materials Usage	56
3.2.2. Sample Preparation	56
3.2.3. Procedure	57
3.3. Results	61
3.4. Discussion	77
3.5. Conclusions	82
3.6. Acknowledgements	83

3.7.	References	83
------	------------------	----

Chapter 4

4.	Kinetic Modelling of the Silicothermic Reduction of Manganese Oxide from Slag.....	86
	Copywrite & Bibliographic Information	86
	Contributions & Context.....	86
	Abstract	88
4.1.	Introduction	89
4.2.	Experimental Procedure	91
4.3.	Numerical Modelling	92
4.3.1.	Past Findings & Influences	92
4.3.2.	Outline of the Model	93
4.3.3.	Solution Method.....	98
4.3.4.	Fit Optimization	98
4.4.	Results	100
4.4.1.	Dynamic Area Change	100
4.4.2.	Modelling Results	105
4.5.	Discussion & Sensitivity Analysis	112
4.5.1.	Metal vs. Slag Control	113
4.5.2.	Individual Species Control.....	115
4.5.3.	Bubble Layer Transition Time.....	117
4.5.4.	Impact of the Rate Constant for SiO Formation, k_{fwd}	119
4.5.5.	Findings on SER & Gas Stability	119
4.6.	Conclusions	121
4.7.	Acknowledgements	123
4.8.	References	123

Chapter 5

5.	Kinetics of the Carbothermic Reduction of Manganese Oxide from Slag.	127
	Copywrite & Bibliographic Information	127
	Contributions & Context.....	127
	Abstract	129
5.1.	Introduction	130
5.2.	Experimental Procedure	131
5.2.1.	Material & Preparation	131
5.2.2.	Equipment	132
5.2.3.	Procedure	134
5.3.	Results	136
5.3.1.	Observations of CO Evolution.....	136
5.3.2.	Formation of Metal in the Slag	151
5.3.3.	Evidence of Slag Transport Control from Failed Experiments.....	154
5.4.	Discussion	155
5.4.1.	First Contact of Slag and Metal	159

5.4.2.	Internal Nucleation and Droplet Bloating.....	159
5.4.3.	External CO Nucleation Post Bloating	160
5.5.	Conclusions	164
5.6.	Acknowledgements	165
5.7.	References	165

Chapter 6

6.	Mixed Mass Transport Control and Viscosity during Reduction of FeO and MnO from Slag	168
	Copywrite & Bibliographic Information	168
	Contributions & Context.....	168
	Abstract	170
6.1.	Introduction	170
6.1.1.	Mass Transport Relationships.....	173
6.1.2.	Viscosity Relationships.....	174
6.2.	Literature Review	176
6.2.1.	Review of MnO Reduction Literature with Transport Limitations	176
6.2.2.	Review of MnO Reduction Literature with Chemical Reaction Limitations	183
6.2.3.	Review of Non-MnO Reduction Literature with Transport Limitations	186
6.2.4.	Review of Non-MnO Reduction Literature with Chemical Reaction Limitations	188
6.2.5.	Other Reviewed Literature with Comparative Findings	191
6.3.	Trend Analysis	192
6.3.1.	Mass Transfer Coefficients vs. Optical Basicity.....	192
6.3.2.	Viscosity vs. Slag Mass Transfer Coefficients	194
6.3.3.	Cationic Conductivity vs. Slag Mass Transfer Coefficients	196
6.3.4.	Manganese Partition Coefficient vs. Slag Mass Transfer Coefficient	199
6.4.	Discussion	202
6.4.1.	Reaction Control Mechanisms	203
6.5.	Conclusions	207
6.6.	Acknowledgements	209
6.7.	References	209
6.8.	Appendix 1 – Mass Transfer Coefficients & Calculated Data.....	214
6.9.	Appendix 2 – Mass Data from Past Workers.....	217

Chapter 7

7.	Conclusions	221
7.1.	Summary & Conclusions.....	221
7.2.	Future Work	225

Chapter 8

8.	References	227
----	------------------	-----

Chapter 9

9.	Appendix A – Energy Dispersive Spectroscopy Data.....	234
9.1.	Sample A – 2 Minutes into Reaction.....	234
9.2.	Sample B – 3 Minutes into Reaction.....	236
9.2.1.	Optical Microscope Region of Interest	236
9.2.2.	Site 1 – Linescan	236
9.2.3.	Site 2 – Linescan	237

List of Figures and Tables

Figures

Chapter 2

Figure 2.1: Effect of temperature on wt%Si loss for fixed reaction times; reprinted with permission from Canadian Science Publishing: Can. J. Chem. [12] (1961)...	8
Figure 2.2: Calculated distribution equilibria for the metal system Mn-Si-0.5%C in coexistence with MnO-SiO ₂ -CaO slag; reprinted with permission from Fagbokforlaget [9]	12
Figure 2.3: Effect of ambient pressure on MnO and FeO contents in slag: 35g metal, 10g 45% SiO ₂ slag, 19mm diameter graphite crucible; reprinted with permission from Ironmaking & Steelmaking (http://www.tandfonline.com) [22] (1973).....	16
Figure 2.4: Plot of $\ln(\%MnO) - \ln(\%Mn)$ vs. time; reprinted with permission from Ironmaking & Steelmaking (http://www.tandfonline.com) [22] (1973).....	17
Figure 2.5: Proposed mechanism for manganese oxide reduction process; reprinted with permission from Ironmaking & Steelmaking (http://www.tandfonline.com) [22] (1973)	17
Figure 2.6: The reduction ratio of (MnO) and the behaviour of (FeO) vs. time; reprinted with permission from ISIJ International [32] (1993).....	19
Figure 2.7: Effect of slag basicity on the MnO reduction at 1450°C (calculated results); reprinted with permission from Canadian Metallurgical Quarterly [24] (2002)	21
Figure 2.8: Micrograph image of cross sectional view of slag-carbon interface and metal drop; reprinted with permission from ISIJ International [37] (2010)	22
Figure 2.9: Schematic illustration of the charge-balancing and structural relationships of the cation (M^{x+}), bridged oxygen (O^0), and non-bridged oxygen (O^-) in silicate melts; reprinted with permission from Steel Research International (John Wiley & Sons Publishing) [39] (2012)	23
Figure 2.10: A partially polymerized silicate slag structure; black – silicon, white – oxygen, grey – basic oxides; reprinted with permission from AIST [25] (1998).	25
Figure 2.11: Ion distributions of alkali and alkali-earth cations and of aluminate anions within the silicate polymer structure; reprinted with permission from Steel Research International (John Wiley & Sons Publishing) [39] (2012)	26
Figure 2.12: Schematic of a liquid metal placed on an oxide substrate; reprinted with permission from M.A. Rhamdhani [45] (2005)	27
Figure 2.13: Surface tension of the iron-oxygen system; reprinted with permission from ISIJ International [58] (1984).....	30
Figure 2.14: Effect of oxygen content in molten iron on the interfacial tension and the surface tension at 1580°C; reprinted with permission from ISIJ International [58] (1984).....	31
Figure 2.15: Surface turbulence on liquid tin; spot of oxide moving radially outwards from the center; reprinted by permission from Springer Nature: Met. Trans. [63] (1972)	32

Figure 2.16: Successive X-ray pictures of the profile of a metal droplet immersed in a slag (x4): (a) 7min; (b) 18min; (c) 40min; reprinted with permission from Canadian Metallurgical Quarterly [66] (1981)	34
Figure 2.17: Interfacial tension as a function of time: metal initial composition 4.45%Al-bal.Fe; slag CaO-Al ₂ O ₃ -SiO ₂ ; reprinted with permission from Canadian Metallurgical Quarterly [66] (1981)	34
Figure 2.18: (a) through (f) feature of initiation of emulsification at the slag-alloy interface; reprinted by permission from Springer Nature: Met. Trans. B [70] (2000)	36
Figure 2.19: (a) through (d) formation of perturbation and emulsification by Kelvin-Helmholtz instability; reprinted by permission from Springer Nature: Met. Trans. B [70] (2000).....	37
Figure 2.20: Emulsification enhanced by Marangoni flow; reprinted by permission from Springer Nature: Met. Trans. B [70] (2000)	38
Figure 2.21: Evolution of metal droplet geometry immersed in slag as a function of time at 1873K (1600°C); adapted by permission from Springer Nature: Met. Trans. B [75] (2015).....	40
Figure 2.22: Schematic diagram of the behaviour observed by X-Ray fluoroscopy of a Fe-C drop in a slag containing 20wt%FeO; reprinted by permission from Springer Nature: Met. Trans. B [80] (2002)	41

Chapter 3

Figure 3.1: Schematic Diagram of the Vertical Tube Furnace, Not to Scale	58
Figure 3.2: Diagram of Droplet Location at Various Times within the Furnace Setup, Not to Scale.....	60
Figure 3.3: Concentration vs. Time Plot for the 15wt%MnO, 5wt%Si, 1.5g Droplet, and 1873K (1600°C).....	61
Figure 3.4: Concentration vs. Time Plot for the 15wt%MnO, 10wt%Si, 1.5g Droplet, and 1873K (1600°C).....	62
Figure 3.5: Concentration vs. Time Plot for the 10wt%MnO, 15wt%Si, 1.5g Droplet, and 1923K (1650°C).....	62
Figure 3.6: Concentration vs. Time Plot for the 15wt%MnO, 15wt%Si, 0.5g Droplet, and 1873K (1600°C).....	63
Figure 3.7: Concentration vs. Time Plot for the 15wt%MnO, 15wt%Si, 1.0g Droplet, and 1873K (1600°C).....	63
Figure 3.8: Concentration vs. Time Plot for the 15wt%MnO, 15wt%Si, 1.5g Droplet, and 1823K (1550°C).....	64
Figure 3.9: Concentration vs. Time Plot for the 15wt%MnO, 15wt%Si, 1.5g Droplet, and 1873K (1600°C).....	64
Figure 3.10: Concentration vs. Time Plot for the 15wt%MnO, 15wt%Si, 1.5g Droplet, and 1923K (1650°C).....	65
Figure 3.11: Concentration vs. Time Plot for the 20wt%MnO, 15wt%Si, 1.5g Droplet, and 1923K (1650°C).....	65

Figure 3.12: Colour Gradients Surrounding the Droplet (Lower Middle of the Image) and Gas at 185 Seconds of Reaction; The Lightest Area is to the Left and Darkest to the Bottom Right	66
Figure 3.13: Negligible Color Gradients Found Surrounding the Droplet at 20 Seconds of Reaction; Note the Distinct Outline of Spherical Gas Bubbles Surrounding the Large Central Droplet	67
Figure 3.14: Small Light to Dark Gradient from Left to Right across the Image at 20 Minutes of Reaction; Note the Destabilization of Bubbles Seen at Long Times Resulting in Elongated Shapes.....	67
Figure 3.15: [Mn] Concentration Data Plotted as a Function of Droplet Size and Time, Using Equation 3.4 for Mass Transport of MnO in the Slag; Initial Conditions 15wt%Si, 15wt%MnO, 1873K (1600°C), Variable Mass	71
Figure 3.16: [Mn] Concentration Data Plotted as a Function of Droplet Size and Time, Using Equation 3.6 for Mass Transport on Mn in the Metal; Initial Conditions 15wt%Si, 15wt%MnO, 1873K (1600°C), Variable Mass	71
Figure 3.17: [Mn] Concentration Data Plotted as a Function of Initial (MnO) and Time, Using Equation 3.4 Control by Mass Transport of MnO in the Slag; Initial Conditions 15wt%Si, Variable MnO, 1923K (1650°C), 1.5g Droplet	72
Figure 3.18: [Mn] Concentration Data Plotted as a Function of Initial [Si] and Time, Using Equation 3.4 for Control by Mass Transport of MnO in the Slag; Initial Conditions Variable Si, 15wt%MnO, 1873K (1600°C), 1.5g Droplet	73
Figure 3.19: [Mn] Concentration Data Plotted as a Function of Temperature and Time, Using Equation 3.4 for Control by Mass Transport of MnO in the Slag; Initial Conditions 15wt%Si, 15wt%MnO, Variable Temperature, 1.5g Droplet	74
Figure 3.20: Localized Flattening on a Droplet Interface at 4 Minutes of Reaction	75
Figure 3.21: Cleared Metal Surface Surrounded by Slag Deposits in a Web-Like Pattern at 2 Minutes of Reaction.....	76
Figure 3.22: Diagram Illustrating how Gas Generation may Affect the Diffusion Pathway and Change both Volume and Area Terms in the Rate Equation	81
Figure 3.23: Zoomed Version of Figure 3.15 where the Initial Y-Axis Jump is Displayed	82

Chapter 4

Figure 4.1: Color gradients surrounding the droplet (lower middle of the image) and gas at 185 seconds of reaction; the lightest area is to the left and darkest to the bottom right. Reprinted from Ref. [7]......	92
Figure 4.2: Proposed concentration gradients at the interface of the slag-metal couple.....	94
Figure 4.3: Diagram of Close-Packed Spherical Bubbles Obstructing 1 Unit Area of the Interface Representing a 91% Decrease in Effective Mass Transfer Area	101
Figure 4.4: Observance of closely sized and spherical bubbles across the metal surface for a sample quenched at 20 seconds. Reprinted from Ref. [7].	102

Figure 4.5: Rate Plot Demonstrating the Fitted Data Crossing the y-Axis below Zero Time (Derived Assuming that Manganese Oxide Mass Transport Control was Rate Controlling)	103
Figure 4.6: Model vs. Dataset 1 for 5wt%Si, 15wt%MnO, 1.5g Droplet, at 1873K (1600°C).....	108
Figure 4.7: Model vs. Dataset 2 for 10wt%Si, 15wt%MnO, 1.5g Droplet, at 1873K (1600°C).....	108
Figure 4.8: Model vs. Dataset 3 for 15wt%Si, 10wt%MnO, 1.5g Droplet, at 1923K (1650°C).....	109
Figure 4.9: Model vs. Dataset 4 for 15wt%Si, 15wt%MnO, 0.5g Droplet, at 1873K (1600°C).....	109
Figure 4.10: Model vs. Dataset 5 for 15wt%Si, 15wt%MnO, 1.0g Droplet, at 1873K (1600°C).....	109
Figure 4.11: Model vs. Dataset 6 for 15wt%Si, 15wt%MnO, 1.5g Droplet, at 1823K (1550°C).....	110
Figure 4.12: Model vs. Dataset 7 for 15wt%Si, 15wt%MnO, 1.5g Droplet, at 1873K (1600°C).....	110
Figure 4.13: Model vs. Dataset 8 for 15wt%Si, 15wt%MnO, 1.5g Droplet, at 1923K (1650°C).....	110
Figure 4.14: Model vs. Dataset 9 for 15wt%Si, 20wt%MnO, 1.5g Droplet, at 1923K (1650°C).....	111
Figure 4.15: Change in RMS Error with Respect to Change in Multiplier Comparing k_{Slag} & k_{Metal}	114
Figure 4.16: Change in RMS Error with Respect to Change in Multiplier Comparing k_{Mn} & k_{Si}	115
Figure 4.17: Change in RMS Error with Respect to Change in Multiplier Comparing k_{MnO} & k_{SiO_2}	116
Figure 4.18: Impact of Bubble Blocking Effect on Arithmetic Difference of Average RMS Error	118
Figure 4.19: Example Model without Including the Change in Area Associated with Bubble Formation	119

Chapter 5

Figure 5.1: Schematic diagram of vertical tube furnace, not to scale.....	133
Figure 5.2: Change in moles of [Mn], [Si], and CO gathered through individual quenching experiments for a series of reactions with identical starting conditions (2.5 wt pct C, 15 wt pct MnO, 1823K (1550°C), and 1.5g droplet)	136
Figure 5.3: X-Ray photos of a metal droplet from dataset 1 (initial conditions 2.5wt pct C, 15 wt pct MnO, 1.5g droplet, 1873K [1600°C]). In order: (0s) reaction start, (1s) external nucleation of CO, (1.5s) partial internal nucleation, (3-7s) majority internal nucleation and small slag foam, (7s) CO production slowing [collection of metal at base of droplet], (15s) droplet buoyancy lost, (30s) periodic CO release from droplet, (60s) observable reaction essentially complete.	138
Figure 5.4: CO evolution versus time for variations in the initial carbon content of the metal droplet (normalized for manganese and silicon gains).....	141

Figure 5.5: Plot of initial carbon content vs. rate of reaction.	141
Figure 5.6: Comparison of 3 different initial carbon concentration droplets. Droplets with higher carbon content take longer to bloat and stay bloated longer. The left image column shows the time where internal nucleation first become visible, the center where the droplet is maximally bloated, and the right column when droplet buoyancy is lost.....	144
Figure 5.7: CO evolution versus time for variations in the initial manganese oxide content in slag (normalized for manganese and silicon gains).	147
Figure 5.8: Comparison of bloated droplets vs. initial MnO content; 5 wt pct MnO slags do not lead to complete bloating of the metal droplets.	147
Figure 5.9: CO evolution versus time for variations in reaction temperature (normalized for manganese and silicon gains).....	148
Figure 5.10: Comparison of 1823K (1550°C) and 1923K (1650°C) maximally bloated droplets; in all cases droplets at the lower temperature had a metal pool at their base indicating slower reactions rates.	149
Figure 5.11: CO evolution versus time for variations in metal droplet mass (normalized for manganese and silicon gains).....	149
Figure 5.12: Relationship between rate of CO generation and metal volume	150
Figure 5.13: Transition from primarily external to primarily internal CO nucleation in a droplet from dataset 8 (initial conditions 2.5wt pct C, 15 wt pct MnO, 1.0g droplet, 1873K [1600°C]) showing clear evidence that the external CO nucleation slows dramatically and that there is an incubation period for internal nucleation.	151
Figure 5.14: Appearance of metal fragment in a high carbon sample.	152
Figure 5.15: Growth of metal in the slag corresponding with largely external CO evolution.	153
Figure 5.16: Plot of CO evolution measured from the CVPT when a crucible failed after 23 minutes; at 1400s a sharp pressure increase can be seen in the plot.....	155
Figure 5.17: Quenched slag (near 22min) and droplet from dataset 1 (initial conditions 2.5wt pct C, 15 wt pct MnO, 1.5g droplet, 1873K [1600°C]); initial conditions 2.5 wt pct C in 1.5g metal, 15 wt pct MnO, and 1873K [1600°C] ...	161
Figure 5.18: Quenched slag (approximately 4min) surrounding metal droplet from dataset 6 (initial conditions 2.5 wt pct C in 1.5g metal, 15 wt pct MnO, and 1823K [1550°C]). Significant faceting is present on the metal surface, CO bubbles are leaving the metal surface to the top of the slag, left and right edges show homogeneous bulk slag.	162

Chapter 6

Figure 6.1: All slag mass transfer coefficients plotted against the corrected optical basicity.	193
Figure 6.2: All slag mass transfer coefficients (without the droplet experiments).	193
Figure 6.3: Viscosity modelled from the data of Mills & Sridhar [20]	196
Figure 6.4: Viscosity data modelled from the data of Ray & Pal [22]	196

Figure 6.5: Slag mass transfer coefficients vs. cationic conductivity of the slags.	198
Figure 6.6: Partition vs. overall mass transfer coefficient.	201
Figure 6.7: Partition vs. overall mass transfer coefficient with trendline.	202

Chapter 9

Figure 9.1: Point scan left to right moving away from the metal droplet; the metal droplet is the dark region in the bottom left corner.....	234
Figure 9.2: Weight percent data associated with the points scanned in Figure 9.1.	235
Figure 9.3: Line scan data for a similar region of the slag near the metal interface; manganese data trends upwards (Y-axis units unknown).	235
Figure 9.4: Image of the prepared sample (x1) and zoomed image of the specific site of interest (x5).	236
Figure 9.5: BSE image of linescan site and chemical data for the linescan; the slag is the grey region on the left and the black is the epoxy cavity.	237
Figure 9.6: BSE image of linescan site and chemical data for the linescan; the slag is the grey region on the left and the black is the epoxy cavity.	238

Tables

Chapter 2

Table 2.1: Reactions for which drastic decrease of effective interfacial tension has been observed; adapted with permission from Canadian Metallurgical Quarterly [66] (1981).....	35
--	----

Chapter 3

Table 3.1: Chemical Composition of Six Melt Species	56
Table 3.2: Definition of Z , Y_m , and Y_s Used to Plot Rate Equations	70
Table 3.3: Silicon Efficiency Ratio for Different Starting Concentrations and Over Time	79

Chapter 4

Table 4.1: Residual Error Summary of the Modelled Laboratory Data.....	111
--	-----

Chapter 5

Table 5.1: Chemical Composition of Slag Components.....	132
Table 5.2: Summary of Mechanisms and Rate Constants from Literature.....	156

Chapter 6

Table 6.1a: Summary of Select Conditions from Kawai <i>et al.</i> [12] for Mixed Mass Transport Control.....	179
Table 6.2: Estimate of Rate Coefficients from Wu <i>et al.</i> [16].....	180
Table 6.3: Summary of data from Shibata <i>et al.</i> [5] for lowest, average, and highest mass transfer coefficients.....	181
Table 6.4: Data from Ashizuka <i>et al.</i> [26] for the Carbothermic Reduction of MnO	185
Table 6.5: Chemical Reaction Control Studies with Low Temperature	204

Abbreviations and Symbols

Concentration Parameters

$wt\%[i]$	Weight percent of species i in the metal
$wt\%(i)$	Weight percent of species i in the slag
p_i	Partial pressure of species i in the gas phase

X_i	Mole fraction of species i
C_i^j	Concentration of species j at the interface i
C_b^j	Concentration of species j in the bulk b

Kinetic Parameters

k_m^i	Mass transfer coefficient of species i in the metal [m/s]
k_s^i	Mass transfer coefficient of species i in the slag [m/s]
k_{Fwd}^i	Forward reaction constant of species i at the interface [m/s]
D_i	Diffusion coefficient of species i [m^2/s]
δ_i	Conceptual boundary layer thickness [m]

Optical Basicity Parameters

Λ	Optical basicity calculated from slag components
Λ^{corr}	Corrected optical basicity; calculated after charge balance considerations
Λ_i	Optical basicity parameter of slag species i
n_i	Number of oxygen atoms associated with slag component i

Thermodynamics

K_i	Equilibrium constant of the reaction
-------	--------------------------------------

Miscellaneous

T	Temperature [K]
k	Boltzmann Constant [1.381E-23 J/K]
η	Viscosity [Pa·s]
λ	Mean interatomic distance [m]
γ	Surface tension [J/m ²]

Declaration of Academic Achievement

The enclosed work is an effort to better understand the fundamentals of manganese reductive alloying processes. Past studies are almost entirely focused on flat-bath style experiments, leaving space in the field for the study of metal droplets reacting with slag found here. With respect to both silicon and carbon, there are discrepancies in the literature regarding the specific mechanism and controlling steps within these reduction systems; this work seeks to clarify these discrepancies. With respect to silicothermic reduction of manganese oxide, the volume of literature on the subject is small, thus this work presents important new additions to the field in terms of collected data and kinetic models. The identification of the impact of stagnant gas bubbles is a significant contribution to the literature. While the carbothermic reduction system is much better studied, some of the same discrepancies exist in the literature with respect to the rate controlling mechanism. A possible reason for these discrepancies has been proposed with a critical review of new data and the literature. The present work should support future research and implementation of process improvements to produce 3rd Generation Advanced High Strength steels.

Contributions to the Enclosed Literature

Contributions to the enclosed academic literature are discussed here. As the primary author and researcher, I was responsible for:

- (100%) Collecting the experimental data.
- (100%) Drafting of manuscripts and literature review.
- (99%) Coding and analyzing the silicothermic reduction model.
- (75%) Journal correspondence, incl. answering reviewer comments.
- (35%) Ongoing discussion of data.
- (25%) Setting the high-level direction of the project.

Kenneth S. Coley was responsible for:

- (65%) Setting the high-level direction of the project.
- (50%) Sourcing of funding.
- (35%) Ongoing discussion of data and their implications.
- (25%) Journal correspondence, incl. answering reviewer comments.

Mansoor Barati was responsible for:

- (50%) Sourcing of funding.
- (20%) Ongoing discussion of data and their implications.
- (10%) Setting the high-level direction of the project.

Yousef Tabatabaei was responsible for:

- (100%) Coaching and tutoring on MatLab.
- (10%) Ongoing discussion of data.
- (1%) Coding and analyzing the silicothermic reduction model.

All data, model code, and manuscripts for the published works included in this thesis were completed by me, in my capacity as a Ph.D. student and the primary author of the papers. This does not de-emphasize the work of my colleagues and co-authors (whose insight was invaluable in the creation of these documents) but is offered to justify these articles as my novel contribution to the field. The first article was worked on from 2015 through 2017; publication 2017. The second article was worked on 2017 through 2018; publication 2019. The third article was worked on 2016 through 2019; submitted to Metallurgical Transactions B (February 2019). The fourth article was worked on in 2019; submission pending.

Chapter 1

1. Introduction

1.1. Motivation for this Study

Manganese is an important alloying element in Advanced High Strength steel (AHSS) for its beneficial property contributions (improving both ductility and strength characteristics through a variety of mechanisms). Twinning Induced Plasticity steels (TWIP) are proposed to contain over 20wt% manganese [1], while values between 4-11wt% are of interest in 3rd generation AHSS [2]. Reduction of manganese oxide from the slag has been proposed as a method of adding manganese to 2nd and 3rd generation steels by eliminating some of the losses otherwise associated with the pre-refinement of manganese rich alloys [3,4].

Steel manufacturers are under increasing pressure to develop advanced high strength steels in response to client demands. Automotive applications are of greatest concern, where steel producers are called to produce materials with better strength to weight ratios; Corporate Average Fuel Economy (CAFÉ) standards are a major driver of 3G AHSS research and production [5]. Current production difficulties show the need for novel solutions to high manganese steel production and must be developed if industry is to take hold of the idea. Reductive alloying is proposed as one method of achieving these high manganese gains.

Reductive alloying, or direct alloying, is a method by which reductants in the metal can be utilized to reduce metal oxide in the slag. There are many benefits to

this process, including better heat utilization, reduced reheat energy costs, and reduction in the cost per unit of manganese [1].

1.2. Objectives of this Study

This work was supported with funding from the National Science and Research Council of Canada (NSERC, Grant: STPGP463252-14), and technical support from ArcelorMittal Dofasco, Stelco, Praxair, and Hatch Ltd. The objective of this project was to improve our current understanding of manganese reductive alloying for the production of steels with higher manganese concentrations.

Goals of this work are to observe and document the kinetics and physical phenomena that occur during the reaction of liquid iron and manganese oxide bearing liquid slag; silicon and carbon were studied as possible reducing agents due to their abundant usage in current steelmaking processes. Specific objectives of the study are summarized as follows:

- 1) Obtain reliable experimental kinetic data for a range of conditions related to the silicothermic reduction of manganese oxide.
- 2) Propose a reaction model for the silicothermic reduction to determine the rate-controlling step and discuss physical phenomena.
- 3) Obtain reliable experimental kinetic data for a range of conditions related to the carbothermic reduction of manganese oxide.
- 4) Propose a reaction model for the carbothermic reduction to determine the rate-controlling step as a function of conditions and develop an understanding of the important physical phenomena.

- 5) Rationalize the discrepancies reported in the literature and propose solutions for commercialization of direct alloying processes.

1.3. Organization of this Thesis

This thesis is divided into seven major chapters. Chapter 1 is the introductory chapter and explains the motivation, objectives, and structure of the thesis. Chapter 2 is a general literature review establishing context and providing insight into areas not included in the literature reviews of the individual articles in Chapters 3 to 6. Chapter 3 and Chapter 4 are in-print scholarly articles. Chapter 3 presents experimental data and rudimentary analysis of the “Kinetics of Silicothermic Reduction of Manganese Oxide for Advanced High Strength Steel Processing”. Chapter 4 entitled “Kinetic Modelling of the Silicothermic Reduction of Manganese Oxide from Slag” builds a detailed kinetic model using the data presented in Chapter 3. Chapter 5, a submitted article, considers another mode of reduction presenting experimental data and rudimentary analysis of the “Kinetics of the Carbothermic Reduction of Manganese Oxide from Slag”. Chapter 6, to be submitted, brings together insights and data from the previous chapters along with data from the literature and discusses “Mixed Mass Transport Control and Viscosity during Reduction of FeO and MnO from Slag”. Chapter 7 concludes the thesis, summarizing findings and stating the importance of the work, and offers suggestions for future work related to these findings. References in Chapter 3 to 6 are as included within the published or submitted articles (and are numbered accordingly); references outside of these chapters are found at the end of this thesis.

Further, an appendix is included (Chapter 9) which provides the Energy Dispersive Spectroscopy data which corroborates that colour changes in the slag are associated with concentration gradients in the slag.

1.3.1. Overlap within Scholarly Articles

This work is presented as a series of published articles. The standalone nature of these articles requires some repetition of introductory and background material as well as experimental methods.

Chapter 2

2. Literature Review

The purpose of this section is to discuss topics that are important in establishing the context of the current body of research. Section 1.1 of this thesis covers the commercial and industrial interest of this work as one of the motivators for this study. Sections 2.1 and 2.2 will offer context for some of the motivations of this work on the study of reductants; because the published articles focus so heavily on these subjects, the literature review only provides a condensed overview of what is otherwise discussed in the following chapters. Section 2.3 discusses common slag properties important in an industrial and scientific context. The other sections of this literature review are topics that may have some relevance to the topic but have not been covered in detail in subsequent chapters.

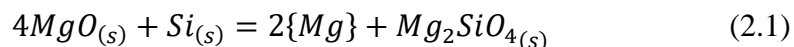
2.1. Silicothermic Reduction Studies

Using silicon as a reductant is not a new concept in steelmaking. There are two primary uses for silicon or ferrosilicon in modern steelmaking: producing semi-killed low oxygen steel and recovery of chromium from stainless steel slags. The former is a common practice in ladle metallurgical processes: silicon is added as a ferroalloy [6] and deoxidizes the steel producing silica that is stirred to the slag phase. The latter is an important stage of the Argon Oxygen Decarburization (AOD) process [7,8]. AOD processes have been proposed as a method of producing high or mid-manganese steels, thus an improved understanding of silicothermic reduction as it might apply to manganese oxide recovery is important. Further, the

production of iron alloys high in manganese is not a novel concept [1,9,10]; silicon is both a reductant and co-product of many ferromanganese production processes. The major problem associated with using ferromanganese alloys to raise the manganese concentration of the steel melt is one of economics: if relatively inexpensive grades of ferromanganese are used a dirty steel will be produced which is unacceptable for end use applications and if higher purity alloys are used the cost of the manufactured product may not be viable for end users [1].

2.1.1. Pidgeon Process

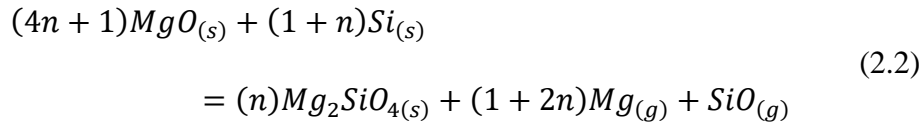
The most common application of silicothermic reduction is the Pidgeon Process [11] used in the production of high purity magnesium. This process relies on the reaction of solid reactants to form gaseous Mg, at a temperature as low as 1100°C. Equation 2.1 shows a basic representation of the reaction stoichiometry.



Toguri *et al.* [12] studied the reduction mechanism between the temperatures of 1100-1440°C. It was clear that the formation of product species choked the reaction [12]. An important finding of these authors was the identification of condensate on various components of their system after reaction. This condensate was determined to be Mg₂SiO₄, a species with a low vapour pressure. The authors concluded that SiO and Mg_(g) evolution was the cause of deposition; SiO could escape as a gas and react in the presence of carbon, sulfur, or silicon carbide ultimately producing some silicate compound with a brown tinge [12]. Compared to traditional steelmaking temperatures, the temperatures in this study were quite

low; an implication of these findings is that SiO formation and subsequently silicon loss may be higher with higher temperatures.

Further study by these authors revealed Equation 2.2 as the most likely scenario for silicon loss; this also marks the global reduction reaction for the process assuming SiO formation occurs. This explained the residue deposition process, as SiO decomposed on the baffles to SiO₂ and Si, which could react with Mg_(g) to form Mg₂SiO₄ and Si; the overall stoichiometry of these reactions is shown in Equation 2.2 [12].



These findings indicate that in order to optimize the output of magnesium twice the stoichiometric amount of silicon must be used [12], supported by industrial data from Morsi and Ali [13]. This is interesting as it appears multiple stable silicon products can form during the reduction; not only is Mg₂SiO₄ produced as a solid product but SiO gas as well.

The partial pressure of SiO_(g) in the system was 43.3Pa (or 4.3·10⁻⁴atm) at 1300°C; at this temperature SiO distillation (evaporation and condensation to other compounds) becomes significant as evidenced in Figure 2.1. Higher temperatures evolved SiO at faster rates and generated more of the distillate product [12]. This work indicates that in reactions involving silicothermic reduction there is a high likelihood of SiO formation at temperatures in excess of 1623K (1300°C). These

results indicate that more than one product species can be simultaneously evolved during a reaction process with silicon.

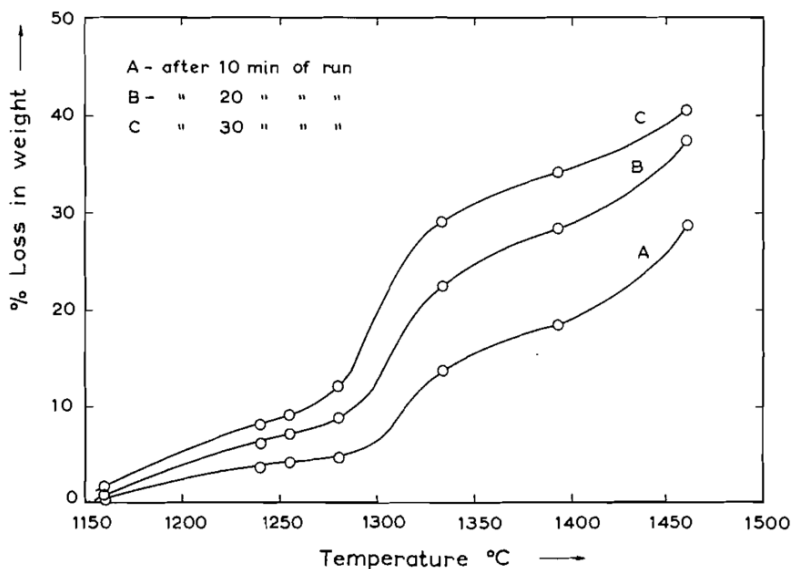


Figure 2.1: Effect of temperature on wt%Si loss for fixed reaction times; reprinted with permission from Canadian Science Publishing: *Can. J. Chem.* [12] (1961)

Brewer and Edwards [14] carried out experiments to clarify the phase stability of SiO. It was found that SiO was unstable below 1450K (1177°C) in any phase. Silica in contact with silicon will readily produce SiO gas; SiO₂ decomposition can form SiO and O₂ [14]. These observations are important as they indicate the cusp of SiO_(g) stability is relatively low compared to steelmaking/experimental temperatures, and that if silica and silicon are present together the formation of silicon monoxide gas is likely. Their work indicates that SiO is only stable as a gas. This may present issues in industrial steelmaking systems where multiple gases are injected or evolved during the reaction process: silicon monoxide could readily escape in pre-existing gas bubbles causing some

amount of silicon loss and underutilization of any form of silicon used in the reduction process.

2.1.2. Silicothermic Reduction of Manganese Oxide

Traditionally manganese has been added to steel by the addition of manganese ferroalloys; steelmaking alone consumes 90% of all manganese produced [6,9]. In-situ silicothermic reduction of manganese oxide during the steelmaking process carries the benefit of tight stoichiometric control and what is assumed to be a more economical production method of high manganese steels [3,4]; general process losses would be reduced and energy expenditures associated with material reheating would be decreased. Ferrosilicon or even ferromanganese can be added via a bin after the decarburization stage in the basic oxygen furnace or during secondary steelmaking; these ferroalloys can be pre-pelletized with manganese ore to further increase the manganese yield in steel.

2.1.2.1. Reductive Alloying Equivalents

There are two thermodynamically viable pathways for metallic silicon to reduce manganese oxide. These pathways are shown in Equations 2.3 and 2.4, taken from FactSage™ and the FTDemo database [15], which takes data from the NIST JANAF Tables [16]:



The kinetics of the silicothermic reduction of manganese oxide are not a well researched topic with respect to fundamental research: almost all studied systems

involved either carbon in the metal or a graphite crucible when silicon was used as a reductant within liquid iron; a review of literature has revealed essentially two fundamentally ‘pure’ studies [17,18]. Daines and Pehlke studied what was typically 4g of Si in 300g Fe (1.3wt%Si) and 10g MnO per 190g slag (5.3wt%MnO). Their work showed that manganese mass transport in the metal was the rate-limiting step, where k_m^{Mn} was equal to $7 \cdot 10^{-6}$ m/s. The system showed significant rate enhancement with stirring, confirming mass transport control.

Heo *et al.* [18] performed experiments using metal with 29.9wt%Si and 56.5%Mn, with a slag containing 40wt%MnO; these conditions are closer to ferroalloy processing than steelmaking. Slags were varied with and without CaF₂. In the CaF₂ slag a stoichiometrically balanced amount of SiO₂ and Mn was produced, whereas in its absence a greater than stoichiometric quantity of silicon was consumed. These authors proposed SiO generation as the alternate manganese reduction pathway. This is unsurprising given the well documented effects of small amounts of CaF₂ on reducing slag viscosity [19,20]. The authors concluded that silica mass transport in the slag was controlling the manganese reduction process. However, they acknowledged the work of Sohn *et al.* [21] who suggested for high viscosity slags mass transport of MnO would be the rate controlling step. The reasons for concluding that mass transport of silica was controlling (as opposed to MnO) were not well justified, though this may be from the common understanding that silicates are slower moving than metal cations in slag. With a very similar outcome to the findings of carbothermic reduction researchers, slag basicity appears

to very strongly influence the apparent rate controlling step. MnO activity coefficients are highly dependent on slag basicity [22] and must be carefully incorporated into any rate model. The overall controlling step may shift with decreasing basicity for two reasons: a decrease in activity of MnO and an increase in slag viscosity, both of which may decrease the rate of reaction.

Shibata *et al.* [23] performed a series of experiments involving multiple simultaneous reactions. Experiments were performed with either 20% or 40% MnO, silicon contents were approximately 0.2%, and carbon contents were around 3.8%. The concentration of CaF₂ was manipulated to decrease slag viscosity. MnO was reduced by silicon and carbon simultaneously; the authors concluded that MnO reduction was more likely to be controlled by manganese mass transport in the metal than the slag. They further noted that desiliconization appeared to finish within the first 300 seconds of reaction. These findings are important in the context of reductants: desiliconization is fast but decarburization is slow even for the same slag; it thus makes it unlikely that the system is limited by mass transfer in the slag for carbothermic reduction.

2.1.2.2. Ferromanganese Production

Ferromanganese production is an extensively studied topic thanks to workers like Ostrovski *et al.* [24] and especially Olsen *et al.* [9], but its relevance to steelmaking is limited because the reduction processes almost always use solid ore. Silicothermic reduction is used in the production of low carbon ferromanganese alloys [9]. Lime is used to control slag basicity and enhance the MnO activity;

typical basicity values are between 1.1-1.3 (an acidic slag regime). In Figure 2.2, the data indicates that a substantial amount of silicon must remain in the metal in order to completely reduce MnO from the slag. It was further noted that large additions of iron to the melt will help drive the reaction by lowering the activity of manganese, thus driving the reaction towards manganese production.

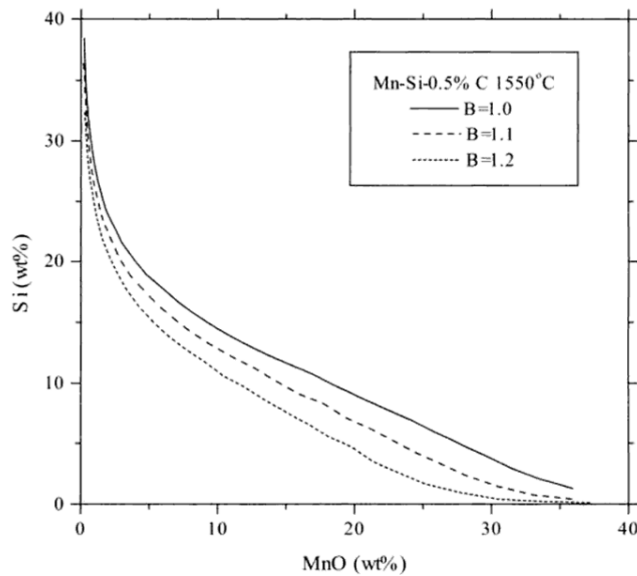


Figure 2.2: Calculated distribution equilibria for the metal system Mn-Si-0.5%C in coexistence with MnO-SiO₂-CaO slag; reprinted with permission from Fagbokforlaget [9]

These findings may yield promise for high manganese steelmaking. Given that a typical steelmaking slag can have a basicity of 3 [25], the obvious conclusion is that attaining low silicon levels with low MnO loss could be possible with high basicity steelmaking slags; admittedly there will be diminishing returns as the activity coefficient is 0.9 near a basicity of 1.2 [22]. Further, given that iron will be in abundance during direct alloying, the activity of metallic manganese should remain low until an appreciable concentration of [Mn] can be achieved.

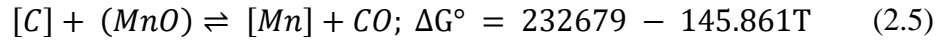
2.2. Carbothermic Reduction Studies

The most well-known application of carbothermic reduction is in the blast furnace during ironmaking. Using carbon in the form of coke and the heat of reaction generated when forming CO and CO₂ iron ore is reduced from Fe₂O₃ to Fe₃O₄ to FeO, finally yielding high carbon iron in the hearth of the blast furnace. Blast furnaces are also used to produce high carbon ferromanganese alloys although their popularity has waned in favour of electric arc furnace technology [9]. Many authors have shown the importance of carbothermic reduction in controlling the silicon content of blast furnace iron by producing silicon monoxide in the tuyere zone of the blast furnace. Pomfret and Grieverson [26] suggested that the reduction of silica by carbon is carried out through intermediates, with emphasis on silicon monoxide; these mechanistic findings are clearly supported in systems where solids are reacting but their application to gas-liquid metallurgy may not be so straightforward. Ozturk and Fruehan [27] studied the blast furnace reaction and claimed that the reaction of coke with ash is the cause for gaseous SiO generation. This gas later interacts with high carbon molten iron and silicon is reduced into the melt. The rate control was described as the gas-phase transport of SiO to the gas-metal interface.

2.2.1. Carbothermic Reduction of Manganese Oxide

At temperatures above approximately 700°C carbon monoxide becomes a more favourable reaction product than carbon dioxide. CO favourability increases from this temperature as it approaches typical steelmaking temperatures. For the carbothermic reduction of MnO, the principle reaction path can be found in

Equation 2.5. The thermodynamic data has been determined from FactSage™ and the FTDemo database [15], which draws its data from NIST JANAF tables [16].



Tarby and Philbrook [28] showed a two stage reaction involving manganese oxide and carbon saturated iron within a graphite crucible. Slag crucible interactions were deemed negligible. In the presence of iron the system showed a two stage reaction: the first stage saw significant gas generation and the latter did not. Two major slag types were tested: those with high silica levels and those without silica. Slags with high silica reacted on average seven times slower than those without [28]. The justification is twofold: silica is a network former which will slow the rate of mass transport in the slag, and silica will make the slag more acidic which will lower the activity of manganese oxide in the slag. Pomfret and Grieveson characterized the activity changes in their later work [22]. The justification for differences in the rate of reaction was that the CO generated caused a degree of stirring within the slag during stage 1, whereas in stage 2 the system was left to natural convection only. The mass transfer coefficients for stage two at 1575°C for high and low silica slags were $1.3 \cdot 10^{-6}$ m/s and $5.5 \cdot 10^{-6}$ m/s respectively. The authors were unable to quantify the mass transfer coefficient for stage 1 as CO nucleation was not consistent during this stage.

Daines and Pehlke [29] performed similar experiments in graphite crucibles, finding that a chemical reaction at the slag-metal interface was the controlling step. The rate constant was approximately $2 \cdot 10^{-8}$ m/s. The slag composition for these

experiments was similar to that reported in the study of Tarby and Philbrook [28]. Both authors appear to have described the same rate; however, the proposed mechanisms are in conflict. Daines and Pehlke ruled out mass transport control by mechanically stirring the system; their findings indicate that the agitation did not increase the rate constant, thus they concluded chemical reaction control as the rate limiting step.

Pomfret and Grieveson [22] attempted to explain this disagreement. Like Tarby and Philbrook their findings showed a fast and slow reaction period. Significant gradients of MnO were found in the slag indicative of slag mass transport control. By raising the silica content in slag the fast stage of reaction was suppressed; citing the activity coefficient data of Bodsworth and Bell [30], Pomfret and Grieveson calculated a decrease in activity coefficient for MnO from 0.9 to 0.14 moving from a 45% silica slag to a 64% silica slag [22]. This finding is important because it implies the fast rate of reaction is limited by the availability of easily reducible oxygen within the slag. FeO was generated early in the reaction but was reduced to a low value by the time the system reached equilibrium. The authors found that changing the ambient pressure of the system from 1atm to 0.25atm did not affect the manganese reduction rate, however, the amount of FeO formed increased with decreasing pressure as evidenced in Figure 2.3; this implied iron and carbon compete to reduce the MnO, when less CO is available more iron oxidation occurs. Pomfret and Grieveson concluded that the findings of Daines and Pehlke were for the second slower reaction step [22], which may explain why there was

little response to stirring as the system was already approaching equilibrium. No difference was found in reaction rates for either graphite or alumina crucibles.

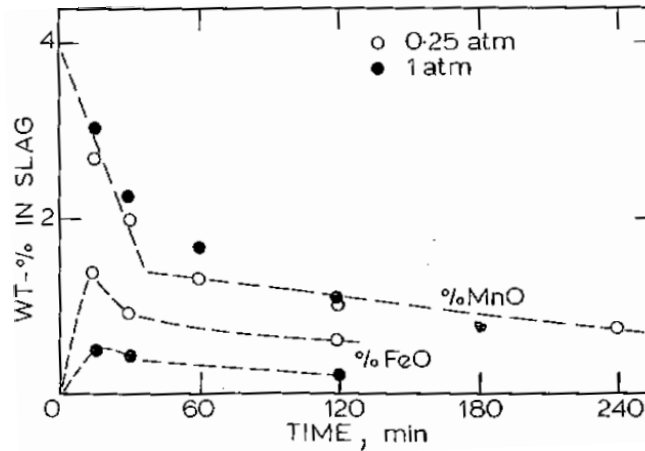


Figure 2.3: Effect of ambient pressure on MnO and FeO contents in slag: 35g metal, 10g 45% SiO₂ slag, 19mm diameter graphite crucible; reprinted with permission from Ironmaking & Steelmaking (<http://www.tandfonline.com>) [22] (1973)

In order to better explain the two-stage reaction Pomfret and Grieveson plotted the manganese partition over time and showed that a critical ratio of $(\text{wt}\% \text{MnO})/[\text{wt}\% \text{Mn}]$ characterized the transition from faster to slower rates. A fast rate of reaction occurs until the $(\text{wt}\% \text{MnO})/[\text{wt}\% \text{Mn}]$ ratio drops below 3.3; the slow rate occurs between this value and the equilibrium $(\text{wt}\% \text{MnO})/[\text{wt}\% \text{Mn}]$ ratio of 0.5. These rate distinctions are shown in Figure 2.4. It can be concluded that high manganese partitions are at least partially responsible for promoting high reaction rates. Clear evidence of surface roughening was found on quenched samples and is consistent with the presence of gas bubbles along the reaction interface. These authors partially attributed the switch to the complete consumption of O^{2-} ions in the slag leading to much slower transport in highly networked slags [22].

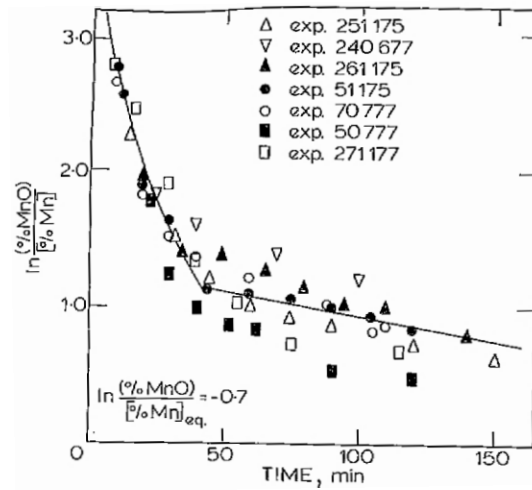


Figure 2.4: Plot of $\ln(\%MnO) - \ln(\%Mn)$ vs. time; reprinted with permission from Ironmaking & Steelmaking (<http://www.tandfonline.com>) [22] (1973)

One of the more interesting conclusions from this work was the proposed reaction mechanism for MnO reduction. These authors claimed that the fast reaction stage proceeds according to Equations 2.6 and 2.7, visualized in Figure 2.5. While the overall rate of reaction during bubble generation was greater than expected from natural convection, it did not reach the level expected for bubble stirred mass transport. This mechanism is, based on a thermodynamic calculation [15], only feasible when the product of $[Mn]$ and (FeO) activities is less than 0.01.

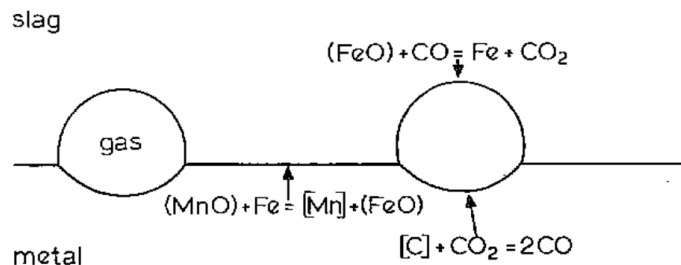
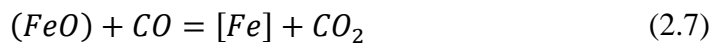
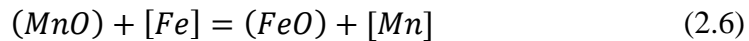


Figure 2.5: Proposed mechanism for manganese oxide reduction process; reprinted with permission from Ironmaking & Steelmaking (<http://www.tandfonline.com>) [22] (1973)

Further tests with nickel were performed to verify this theory, where a carbon-nickel alloy was used to replace the carbon saturated iron. Since nickel oxide is less stable than iron oxide, it is unlikely to form in the slag and will not participate in an exchange reaction; no fast reaction occurred in these experiments [22]. This mechanism indicates that while MnO reduction from slag using carbon or iron are both possible, nucleation of CO is slower than the iron-manganese exchange thus iron oxidation will be favoured until the driving force for the exchange reaction falls below that of CO nucleation. The authors concluded that the mean mass transfer coefficient was $5 \cdot 10^{-6} \text{m/s}$; this value is very close to that determined by Tarby and Philbrook. This finding is interesting because Tarby and Philbrook stated that the mass transfer coefficient applied to what they described as the second stage of reaction, while Pomfret and Grieveson said that their value applied to the first stage of reaction; either there is an insignificant difference between the two stages which caused the misidentification, or the real reaction path is three stages in length (where Tarby and Philbrook studied stage 1 and 2 and Pomfret and Grieveson studied stages 2 and 3). It is also plausible that, because the slag of Pomfret and Grieveson contained a large amount of silica, they documented a slower reaction comparable to that of Tarby and Philbrook.

Ashizuka *et al.* [31] were able to demonstrate similar results to Daines and Pehlke in carbon saturated iron with copper and silicon alloying elements. Their findings indicate that higher silica content slags result in higher activation energies; the data follows very closely with the activity coefficient conclusions made by

Pomfret and Grieveson [22]. Silicon contents were varied and increases in silicon resulted in an increased rate of reaction but did not influence the rate for Si contents greater than 5wt%. Below 5wt%Si they claimed that CO evolution was the rate controlling step, while above 5wt% the controlling step became manganese mass transport in the slag.

Xu *et al.* [32] used x-ray fluoroscopy techniques to observe nucleation and growth sites for carbon monoxide along the slag-metal interface in a study related to high carbon ferromanganese production. Several manganese concentrations in the metal were tested ranging from 10-100wt%Mn, and slags contained 40-50wt%MnO. Slags without any initial FeO were found to exhibit a rapid spike in FeO content at the beginning of the reaction as shown in Figure 2.6.

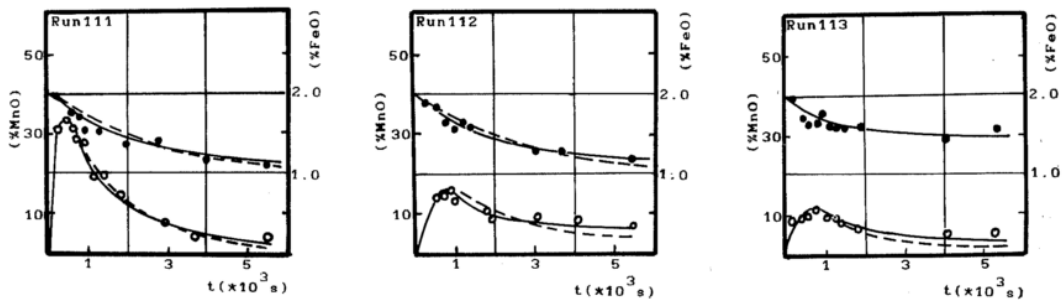


Figure 2.6: The reduction ratio of (MnO) and the behaviour of (FeO) vs. time; reprinted with permission from ISIJ International [32] (1993)

These findings agree with the reaction mechanism catalogued by Pomfret and Grieveson, and they proposed a similar exchange mechanism. In order to test the controlling step of the reaction the authors studied the poisoning effect of surface active elements by varying sulfur contents in the metal; their findings indicate that the reaction rate drops with increasing sulfur content. This response is attributed to

surface poisoning of reaction sites [32]. It was concluded that the rate of generation of CO along the interface was the rate controlling step.

Separate doctoral research of Skjervheim [33] and Tangstad [34] was reported by Ostrovski *et al.* [24]. Slag stirring did not benefit the reaction rate so slag mass transport could not be a rate controlling mechanism. High silica contents were found to reduce the rate of reduction [33]. Ostrovski *et al.* analyzed the conference work of Skjervheim and Olsen [35], documenting a series of carbothermic reductions of manganese metal and finding the two stage reaction presented by many other authors. Highly acidic slags appeared to suppress the appearance of the initial fast stage of reaction and basic slags did not; a threshold value for the fast stage of reaction was documented at a slag basicity of 2. These findings support the importance of slag properties for the overall reaction.

Ostrovski *et al.* [24] used the data of several other authors to model the reduction of MnO from liquid slag; the reactants were different forms of solid graphite. The findings indicate that the greatest contributor to reaction rate is MnO concentration and activity [24]. The models showed that slag basicity plays a major role on equilibrium MnO contents; the final extent of MnO reduction is higher in more basic slags but the reaction rate is not modified by basicity. This trend is shown in Figure 2.7.

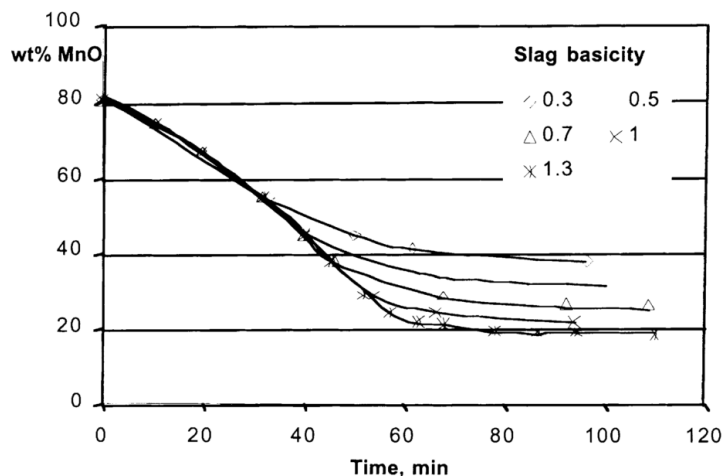


Figure 2.7: Effect of slag basicity on the MnO reduction at 1450°C (calculated results); reprinted with permission from Canadian Metallurgical Quarterly [24] (2002)

A more recent publication by Kononov *et al.* [36] demonstrated the importance of gaseous species in affecting the rate of manganese reduction. The experiments were performed using pure gases and solid particles. Different temperatures and different ratios of C/MnO were used in hydrogen, helium, and argon environments. The results indicate increasing reaction rates with increasing temperature. Further, the densest gas (argon) had the lowest CO diffusivity which was reflected by lower MnO reduction rates. Helium had a higher CO diffusivity than argon, resulting in a faster rate. Hydrogen participated in the reduction and had a high CO diffusivity thus it had the fastest rate of all.

Sun *et al.* [37] reacted a range of slags with a carbon substrate where it generated a reduced metal product. Energy Dispersive Spectroscopy (EDS) analysis revealed a manganese concentration gradient in the slag moving away from the slag-metal interface (shown in Figure 2.8); such a gradient may imply that MnO transport contributes to the reduction process. Their work did not find a detectable reduction rate at 1723K (1450°C), though this became very noticeable at 1823K

(1550°C). The final conclusion was that MnO mass transport controlled the reaction [37].

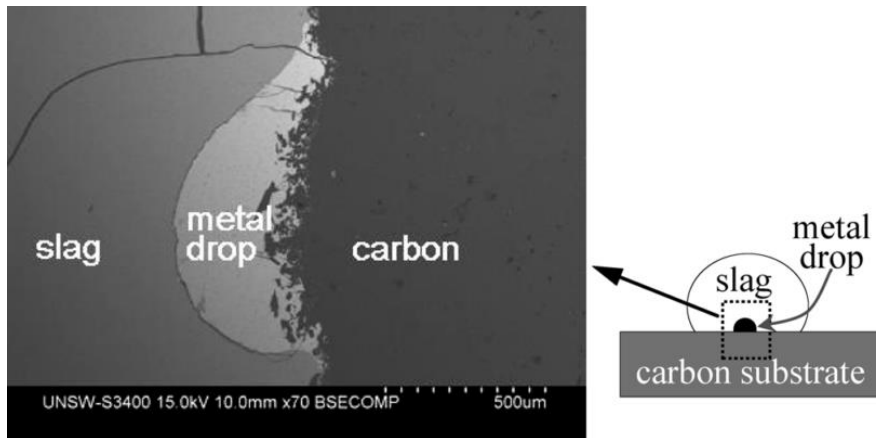


Figure 2.8: Micrograph image of cross sectional view of slag-carbon interface and metal drop; reprinted with permission from ISIJ International [37] (2010)

2.3. Slag Basicity & Viscosity

Metallurgical slags play an important role in steelmaking by controlling residuals and protecting the melt from oxygen entry. Almost all slags are based on the silicate anion, a Si^{4+} cation bound with four oxygen atoms, creating a standard SiO_4^{4-} tetrahedral unit [38]. In slags where silica is the primary oxide, the acidic conditions create a highly polymerized system. Pure silica will take on a crystalline form, where all oxygen atoms are shared between silicon cations; as a crystal this structure has a continuous 3D shape. As basic oxides are added they occupy octahedral sites in the lattice and the crystal structure is broken down. Charged oxygen ions become ionically associated with the basic cations instead of covalently bound within the silicate lattice. Glassy slags retain some degree of ordering but have much shorter chain lengths thus they move more easily through the liquid slag. An example of the tetrahedral and octahedral bonding that occurs in

silicate slags is shown in Figure 2.9; the former applies to the Si^{4+} structures and the latter to $\text{M}^{\text{x}+}$.

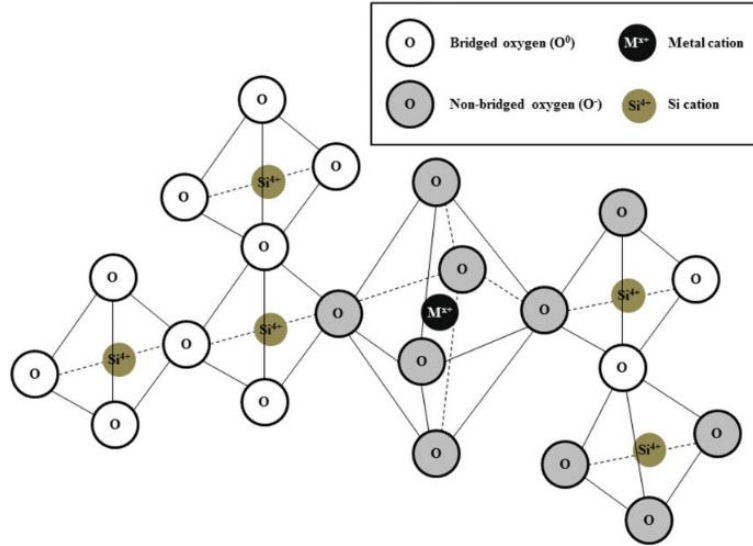


Figure 2.9: Schematic illustration of the charge-balancing and structural relationships of the cation ($\text{M}^{\text{x}+}$), bridged oxygen (O^0), and non-bridged oxygen (O^-) in silicate melts; reprinted with permission from Steel Research International (John Wiley & Sons Publishing) [39] (2012)

An understanding of the physical properties of silicate slag systems is important as mass transport in a liquid is affected by viscosity. A simple mass transport equation is demonstrated in Equation 2.8. With Higbie’s Penetration Theory shown in Equation 2.9, a proportionality to \sqrt{D} also exists.

$$J_i = k_i \cdot (C_i - C_b) \quad (2.8)$$

$$k_i = \sqrt{\frac{4D_i}{\pi t_i}} \quad (2.9)$$

The Eyring equation relates diffusivity with temperature (T), viscosity (η), and the interatomic distance (λ) according to Equation 2.10 [38]; k is the

Boltzmann constant. From these equations, it is clear that a proportionality should exist between calculated slag mass transfer coefficients and the slag viscosity.

$$D_i = \frac{kT}{\eta\lambda} \quad (2.10)$$

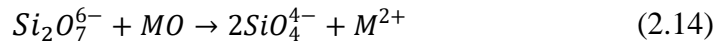
In order to create strong conditions for desulphurization and dephosphorization of steels, slags are made to be basic, having a high activity of oxide anions [38]. There are many interpretations to determine the effects of a specific oxide components on slag basicity, but below are three common interpretations. Equation 2.11 represents the ‘V’ ratio [25], Equation 2.12 represents the ‘B’ ratio [25], and Equation 2.13 is used to determine optical basicity; parameters for the latter calculations are well documented, both in general terms and specific to steelmaking [40–42].

$$\frac{\%(CaO)}{\%(SiO_2)} \quad (2.11)$$

$$\frac{\%(CaO) + 1.4 \cdot \%MgO}{\%(SiO_2) + 0.84 \cdot \%(P_2O_5)} \quad (2.12)$$

$$\Lambda = \frac{\sum(X_i n_i \Lambda_i)}{\sum(X_i n_i)} \quad (2.13)$$

As slags become more basic, the structure of the slag breaks down. Bridging oxygen between silicon (O^0) reacts with basic metal oxides, either M_2O or MO , which break apart the silicate chains; the breakdown of a silicate dimer is shown in Equation 2.14 [25]. Non-Bridging Oxygen (NBO) is formed as O^- ; a completely depolymerized silicate anion has four NBOs [39]. The point at which this occurs is when there is a 2:1 molar ratio of $CaO:SiO_2$ [25].



Transport processes improve as the silicate structure breaks down and smaller unit cells are available for transport. The breakdown of the silicate network also tends to reduce energy requirements associated with chemical reactions involving oxygen [25]. An example is shown in Figure 2.10; basic oxides break up the long polymers, reducing viscosity and transport conditions.

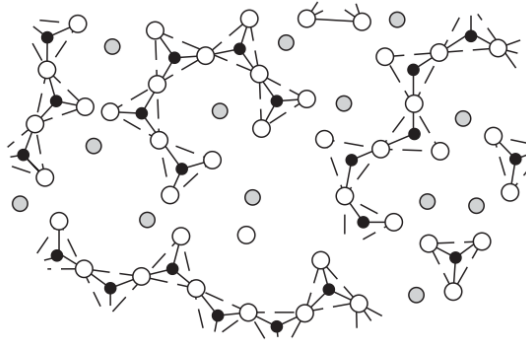


Figure 2.10: A partially polymerized silicate slag structure; black – silicon, white – oxygen, grey – basic oxides; reprinted with permission from AIST [25] (1998)

The silicate anion is tetrahedrally coordinated within the slag; alumina may join the tetrahedral structure as well when it is incorporated into the structure. Alkali metal cations are more effective than doubly charged cations as network modifying (breaking) species because of their characteristically smaller ion radius and ability to bond with only a single charged oxygen species [39]; an example is demonstrated in Figure 2.11. When alumina enters the silicate network, the 3+ charge must be accommodated by cationic species; this is an important consideration for optical basicity calculations as any species coordinating with alumina for charge balancing purposes is no longer available for network modification [42].

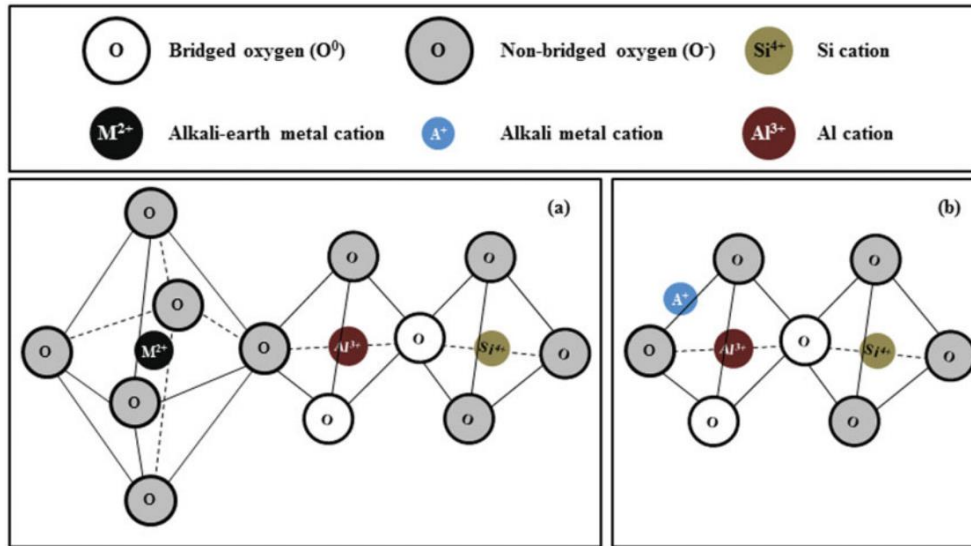


Figure 2.11: Ion distributions of alkali and alkali-earth cations and of aluminate anions within the silicate polymer structure; reprinted with permission from Steel Research International (John Wiley & Sons Publishing) [39] (2012)

2.4. Surface Tension & Dynamic Interfacial Phenomena

Free surface energy is the energy term associated with the difference between an atom surrounded by like neighbours in the bulk and the energy of an atom on the surface with an exposed face; this term is used interchangeably with interfacial energy, which typically refers to the energy of one phase coming into contact with another. Free surface energy minimization is a well-known phenomenon and, in the absence of external influences, is responsible for shaping liquids into spheres. A liquid suspension will almost always retain a spherical figure in the absence of external energy; this surface energy (J/m^2) details the energy required to expand a surface by a square meter [43].

In a three-phase system where liquid sits on a substrate there is an energy balance that interrelates the three phases. The degree to which a fluid binds with a solid is known as its wettability, as was first alluded by Young [44]. A phase that

remains tightly bound to itself in a sphere has strong internal cohesion forces, while a material that actively spreads across the surface of another has stronger adhesion forces. The degree to which three phases interact within a system is typically characterized through the contact angle, schematically represented by Figure 2.12.

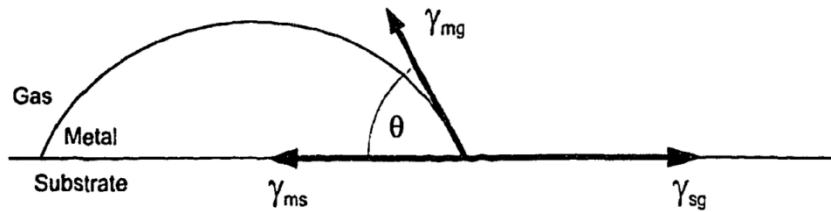


Figure 2.12: Schematic of a liquid metal placed on an oxide substrate; reprinted with permission from M.A. Rhamdhani [45] (2005)

This relationship is known as Young's equation which typically represents the relationship between γ_{sg} (the interfacial tension between substrate and gas), γ_{mg} (for metal and gas), and γ_{ms} (for metal and substrate). In three-phase steelmaking, except at reactor walls, a substrate does not exist in the typical system. Instead the system is better understood as interfacial tension at the metal-slag contact (γ_{ms}), at the slag-gas contact (γ_{sg}), and at the metal-gas contact (γ_{mg}). This is shown in Equation 2.15.

$$\gamma_{ms} - \gamma_{sg} \cos \theta - \gamma_{mg} = 0 \quad (2.15)$$

The above can be modified by further factors including gravity [46] and droplet size [47] depending upon the goal of the analysis. For this analysis, understanding the relationship between contact angle and surface tension is enough.

One issue faced by researchers in high temperature reactions is the observability of this contact angle. The nature of the containment materials in a traditional reactor and the materials under observation means it is often impossible

to observe the contact angle without the assistance of X-Rays. The alternative would be to quench the samples, which adds error associated with quench time and the ability to get a true cross-section; with X-Ray, observability can still be an issue depending on the strength of the beam and any ‘fuzzing’ that occurs around the edges of the droplet [48]. The best method of contact angle measurement comes from furnaces with optical windows. Lone *et al.* [49] determined the wettability of graphite by a $\text{SiO}_2\text{-Al}_2\text{O}_3\text{-CaO-MnO}$ synthetic slag, testing variations in MnO content using a horizontal tube furnace with quartz viewing windows. A clear depression in interfacial tension occurs over time as the graphite substrate reacts with the slag. Samples with a high MnO fraction did not exhibit the same extent of surface tension decrease [49]. Along with the work of others [50,51], these results indicate that silica tends to decrease surface tension, while MnO increases it. This may cause dynamic surface phenomena in a reacting system.

2.4.1. Surface Active Elements

Elements and compounds that preferentially segregate to the surface of a material are known as surface active elements [52]. Four of the most surface active elements in iron are oxygen, sulfur, selenium, and tellurium [53,54]; other elements can impact the surface tension but typically to a much lesser degree [55]. Of these four, oxygen and sulfur are the most important in the study of interfacial tension in high temperature ferrous systems. Sulfur has been shown to slow reactions involving CO_2 formation by blocking potential reaction sites at the surface [56]. This blockage is typically described as a fraction of the surface using the Langmuir isotherm [57]. The isotherm for sulfur is shown in Equation 2.16; as the

concentration of sulfur and equilibrium constant for sulfur adsorption (K_{Ads}) rise so does the fraction of blocked sites Θ . In Equation 2.17, Γ is the concentration of available sites for chemical adsorption to the interface and Γ_0 is the total concentration of reaction sites; as the fraction of blocked sites rises the fraction of available sites falls.

$$\Theta = \frac{K_{Ads}(\%S)}{1 + K_{Ads}(\%S)} \quad (2.16)$$

$$\Gamma = \Gamma_0(1 - \Theta) \quad (2.17)$$

For a chemical reaction to occur, the chemical species do not simply meet at the interface and react, instead they must first adsorb onto the interface. An example is provided for a chemical reaction forming CO in Equation 2.18 through Equation 2.20; \blacksquare represents one reaction site (a fraction of Γ), in this example the electrons would be collected by a cationic species joining the metal phase.



What this reaction shows is that a high concentration of carbon in the metal or oxygen in the slag are not simply enough to drive the reaction: if interfacial sites are blocked with adsorbed species, dramatic decreases in the reaction rate can occur. The industrial implications of this are obvious, but for research purposes it gives workers the option of selectively poisoning the interface in order to test whether a chemical reaction influences the reaction rate.

The rate of oxygen transfer is believed to be the cause of surface tension decrease during rapid reactions [57]. This means that the appearance of dynamic surface tension changes (or their absence) may directly correlate to rates of reaction.

Ogino *et al.* [58] produced a series of graphs comparing the change in surface tension of iron with dissolved oxygen and sulfur contents. The former is shown in Figure 2.13. In the case of oxygen, at a level of 100ppm σ_m has fallen by nearly 600 dyne per cm (equivalent to 0.6J/m^2).

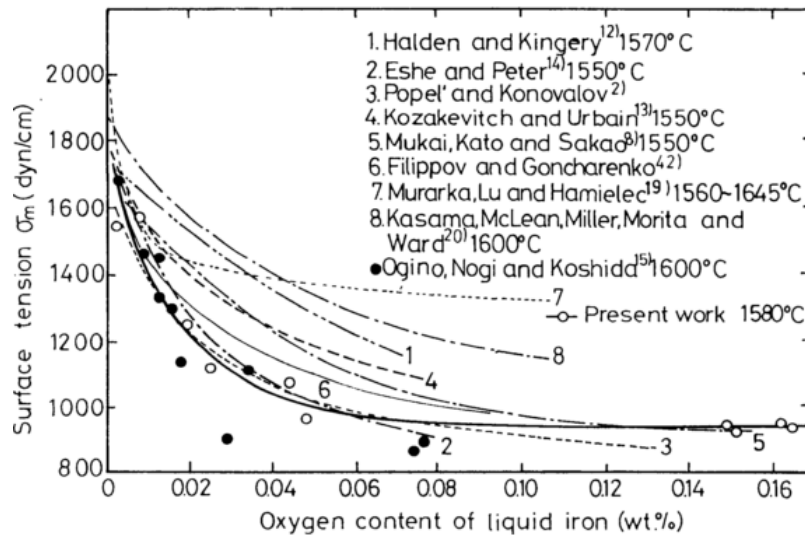


Figure 2.13: Surface tension of the iron-oxygen system; reprinted with permission from ISIJ International [58] (1984)

The effect of oxygen content on interfacial tension in a slag-iron system is shown in Figure 2.14. The drop in this case is larger than that in the case of iron only, which is attributed to the effects of slag components on interfacial tension [50]. Certain slag species like silica have also been demonstrated to be surface active [42].

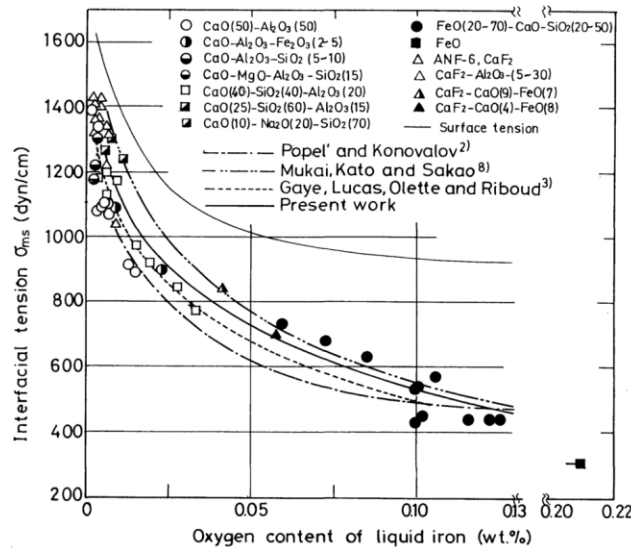


Figure 2.14: Effect of oxygen content in molten iron on the interfacial tension and the surface tension at 1580°C; reprinted with permission from ISIJ International [58] (1984)

2.4.2. Dynamic Interfacial Phenomena

Dynamic Interfacial Phenomena (DIP) are interesting physical phenomena that occur spontaneously (without external agitation) during intense periods of some reactions. The first observance and correct documentation of these phenomena was on the surface of liquors by James Thomson in 1855; the phenomenon would come to be known as Tears of Wine from the apparent streaking caused by the pull of surface tension in alcohol/water emulsions [59]. Sterling and Scriven began an extensive documentation of the phenomena, first in attempts to model the phenomena with water, ethanol, and toluene [60]. These mixtures showed spontaneous movement and area change when the latter two were brought into gentle contact with the water's surface. While a complete model was not achieved, these authors recognized the importance of spontaneous area change on reaction rates for all systems. Their findings were that the Marangoni effect (where

small changes in surface tension cause flow along an interface) may be responsible [60,61].

Ooi *et al.* [62] were able to show that liquid iron with greater than 2wt% aluminum underwent a spontaneous interfacial tension decrease (to a value less than 100dyn/cm) when reacted with silica slag. A similar reaction, using a sulfur-containing carbon-saturated iron droplet only decreased the surface tension to 500dyn/cm [62]. In the same year, Brimacombe and Weinburg [63] used a high speed camera with a low velocity jet of oxygen (blown onto the surface of molten copper and tin samples) to capture oxide undergoing interfacial phenomena during the reaction. One such image is presented in Figure 2.15. Marangoni flow causes high surface tension liquid to ‘pull’ out fluid from low surface tension regions; in Figure 2.15 the oxygen blow lowers surface tension in the middle of the bath, and stringers of this surface are pulled outwards. Similar findings appeared when Cu_2S was added to a molten copper bath [64].

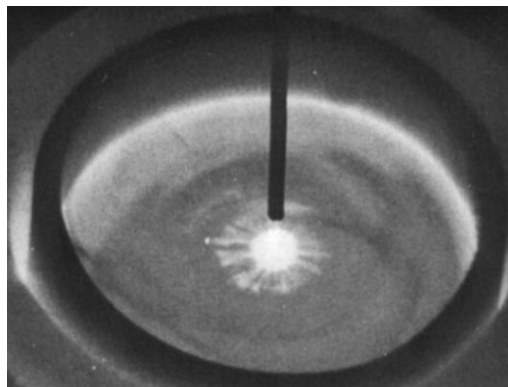


Figure 2.15: Surface turbulence on liquid tin; spot of oxide moving radially outwards from the center; reprinted by permission from Springer Nature: *Met. Trans.* [63] (1972)

Gaye and Riboud [65] performed a series of experiments between droplets of Fe-C, Fe-C-P, and Fe-C-S with an oxidizing slag and found that DIP occurred and

the system recovered in the later stages of the reaction. Emulsified Fe-C droplets recombined and recovered their original form while Fe-C-S droplets only partially recombined leaving substantial material separated from the primary droplet [65]. Since this work has been performed, the understanding of physical phenomena has improved in carbothermic reduction systems, and it is unlikely that the Fe-C droplets experienced “true” DIP effects; the formation of CO during droplet bloating is enough to break apart some droplets.

Riboud and Lucas [66] established three principals of DIP: hydrodynamic movement induced by interfacial changes, including eddies and convection cells; lowering of the interfacial tension; and spontaneous emulsification by the mechanism of ‘diffusion and stranding’ where material ejected from the interface became unable to return [66]. Using droplets of metal and an x-ray imaging system they were able to scan the reaction in situ, showing the apparent breakdown and coalescence of the interface, as seen in Figure 2.16. Aluminum in the metal droplets reduced silica from the slag and caused a breakdown of the interface during the reaction and was so severe that the apparent interfacial tension was calculated to have fallen to zero (Figure 2.17) [66]; it is important to note that this value is an approximation based on visual quantification of the decrease in surface tension.

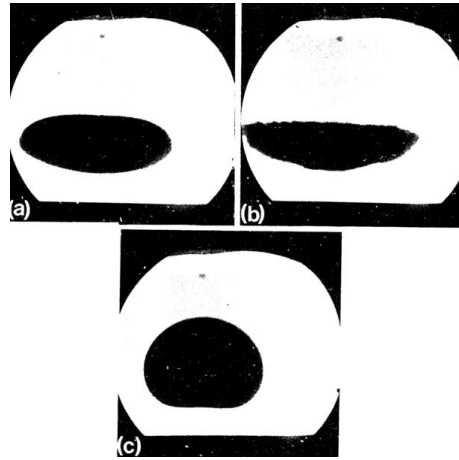


Figure 2.16: Successive X-ray pictures of the profile of a metal droplet immersed in a slag (x4): (a) 7min; (b) 18min; (c) 40min; reprinted with permission from Canadian Metallurgical Quarterly [66] (1981)

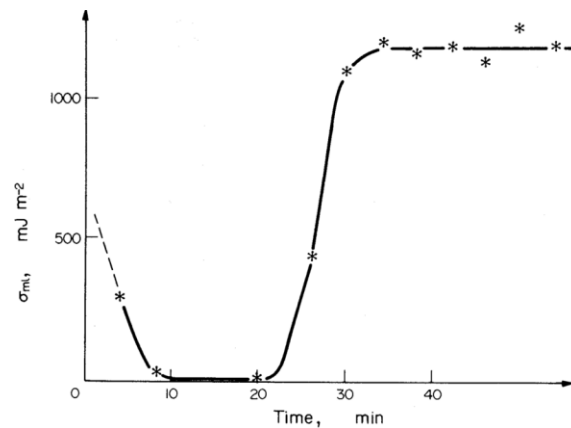


Figure 2.17: Interfacial tension as a function of time: metal initial composition 4.45%Al-bal.Fe; slag CaO-Al₂O₃-SiO₂; reprinted with permission from Canadian Metallurgical Quarterly [66] (1981)

These authors documented a series of systems in which similar phenomena had been observed, shown in Table 2.1. They concluded that a critical oxygen flux of 0.1mole/m²/s was necessary in order to cause the interfacial breakdown to occur [66]. An important conclusion was that a build-up of product near the interface was able to significantly slow the reaction and block emulsification, showing that liquid systems can be slowed by the amount of product generated. This system and others were further analyzed by Gaye *et al.* [67] where similar

results were found; the importance of oxygen transfer in these reactions was once more emphasized. It is clear from this comprehensive piece of work that dynamic phenomena are not confined to specific systems but are a function of reaction severity; many examples are shown in Table 2.1.

Table 2.1: Reactions for which drastic decrease of effective interfacial tension has been observed; adapted with permission from Canadian Metallurgical Quarterly [66] (1981)

Metal	Slag	Reaction
Fe-Al	CaO-SiO ₂	$2[Al] + 3/2(SiO_2) \rightarrow (Al_2O_3) + 3/2[Si]$
Fe-Al	CaO-SiO ₂ -Al ₂ O ₃	$2[Al] + 3/2(SiO_2) \rightarrow (Al_2O_3) + 3/2[Si]$
Fe-Al	CaO-Al ₂ O ₃ -Fe ₂ O ₃	$2[Al] + (Fe_2O_3) \rightarrow (Al_2O_3) + 2[Fe]$
Fe-C-S	CaO-SiO ₂ -Al ₂ O ₃	$[S] + (O) \rightarrow (S) + [O]$
Fe-Ti	CaO-SiO ₂ -Al ₂ O ₃	$[Ti] + (SiO_2) \rightarrow (TiO_2) + [Si]$
Fe-P	CaO-Al ₂ O ₃ -Fe ₂ O ₃	$2[P] + 5/3(Fe_2O_3) \rightarrow (P_2O_5) + 10/3[Fe]$
Fe-B	CaO-SiO ₂ -Al ₂ O ₃ -Fe ₂ O ₃	$2[B] + (Fe_2O_3) \rightarrow (B_2O_3) + 2[Fe]$
Fe-Cr	CaO-SiO ₂ -FeO	$2[Cr] + 3"FeO" \rightarrow (Cr_2O_3) + 3[Fe]$
Fe	Cu ₂ O	$[Fe] + (Cu_2O) \rightarrow 2[Cu] + "FeO"$
Fe-Si	Cu ₂ O-Al ₂ O ₃	$2[Si] + 2(Cu_2O) \rightarrow (SiO_2) + 4[Cu]$

Sharan and Cramb [68] were able to identify the phenomena in a ferronickel alloy with CaO-SiO₂-Al₂O₃ based slags; titania had a significant impact on lowering the interfacial tension, while alumina caused small increases. Jakobsson *et al.* [69] studied the effects of phosphorus in iron with a CaO-SiO₂-Fe₂O₃ slag, again documenting dynamic changes to the interfacial tension. Further work was performed in a copper system based around the transfer of arsenic and antimony from metal to Na₂CO₃; vigorous changes in the interfacial tension occurred.

Chung and Cramb [48] were able to document emulsification via both x-ray imaging during reaction and by scanning electron microscopy on quenched samples. Slag emulsion was identified within the metal phase in these quenched samples; an example from their later work [70] is shown in Figure 2.18. It was

found that iron with 0.25wt%Al underwent small changes in surface tension, but did not result in emulsification like 3.28wt% did; this agrees with earlier reports by Ooi *et al.* [62] who did not observe significant changes for less than 2wt%Al.

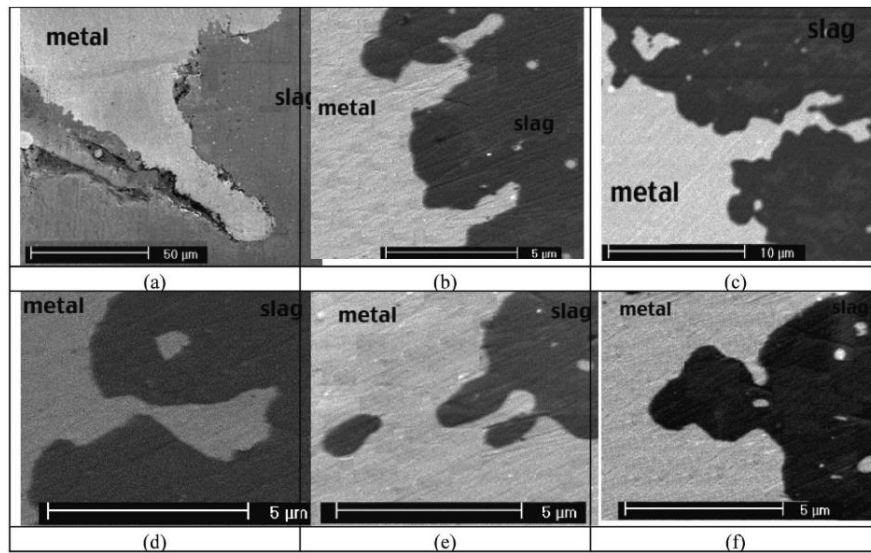


Figure 2.18: (a) through (f) feature of initiation of emulsification at the slag-alloy interface; reprinted by permission from Springer Nature: *Met. Trans. B* [70] (2000)

A later paper by Chung and Cramb [70] analyzed the effects of replacing aluminum with titanium; while emulsification was found it wasn't until almost 11wt%Ti; a minimum of 2.2wt%Ti was required to experience a very slight change in interfacial tension [70]. It is an interesting finding that triple the amount of titanium is required compared to aluminum in order to achieve the same interfacial destabilization; one would expect titanium's higher oxygen affinity to more readily promote emulsification. A more interesting conclusion from their work was the observation and analysis of waves that had formed along the slag-metal interface. The authors justified that during the interfacial exchange fluid flow along the interface lead to wave formation due to Marangoni effects. Naturally large waves

or those that grow through constructive interference could hit a critical dimension characterized by Kelvin-Helmholtz instability that results in the collapse of the wave leads to emulsification behaviour [70]; a diagram of their proposed breakdown mechanic is shown in Figure 2.19. Ultimately their calculations disproved this theory (i.e. the waves generated were not of sufficient size to cause breakdown under Kelvin-Helmholtz criterion).

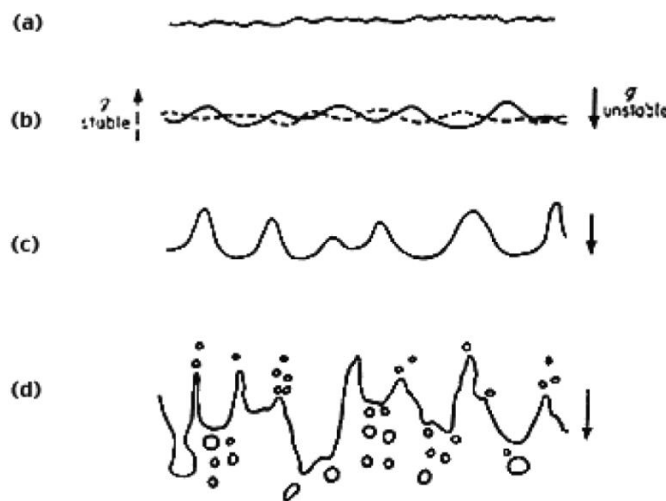


Figure 2.19: (a) through (d) formation of perturbation and emulsification by Kelvin-Helmholtz instability; reprinted by permission from Springer Nature: Met. Trans. B [70] (2000)

This mechanism is aided by another proposed breakdown mechanism: necking and stranding [70]. Stringers of metal pushed into the slag would face stronger reactions on their leading edge, resulting in a drop in forward surface tension that would pull material along the interface towards the rear of the stringer, creating a sphere. The base of the stringer would have a diameter smaller than the accumulated sphere, and the combination of an eddy in the slag and the now spherical metal having a higher surface tension than the neck would cause the

fracture of the neck stranding the metal droplet in the slag. This mechanism is shown schematically in Figure 2.20.

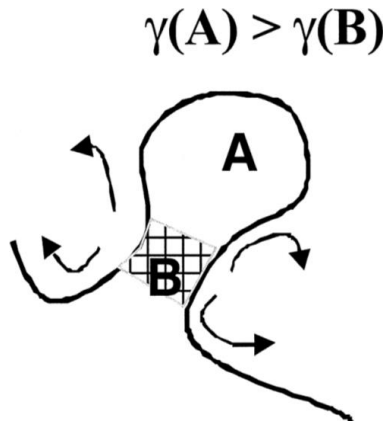


Figure 2.20: Emulsification enhanced by Marangoni flow; reprinted by permission from Springer Nature: Met. Trans. B [70] (2000)

Rhamdhani *et al.* [71] performed a series of experiments on the [Al]/(SiO₂) system. Rhamdhani found an effective method of measuring surface area of reacted droplets, using this analysis to generate a dynamic area change plot over time; it was found that emulsification can lead to an over 400% increase in surface area of the reaction. These area changes are interesting in the context of rate analysis as they require the utilization of a dynamic interfacial area term that must be integrated across the length of the reaction [72]. Rhamdhani also performed a detailed evaluation on the effects of thermocapillarity, solutocapillarity, and electrocapillarity on the system: electrocapillarity (i.e. the interfacial tension depression caused by differences of electrical charge around the interface) contributed 85% of the calculated decrease in interfacial tension; solutocapillarity (i.e. the effect of solute atom differences) contributed the remaining 15%, while thermocapillary effects were negligible [73]. However, these calculated

contributions were much smaller than the total change in the system. These findings indicate that the charge flux of oxygen near the interface is the likely cause for interfacial tension depression (not the static presence of oxygen atoms alone). The gradient range for the solutocapillary affect was estimated to be between 1-2 μm [73]. The system was found to be rate controlled by aluminum mass transport in the metal [72].

White and Sichen [74] performed a recent series of experiments where the rates of mass transfer in a stirred system of Si and CaO-SiO₂ were investigated. Rapid transfer of calcium across the interface dropped the interfacial tension to a level low enough that mechanical agitation caused emulsification; this breakdown was not experienced with a non-reacting system that underwent stirring. Such observations imply that reacting systems which do not normally exhibit spontaneous emulsification may be induced to do so with stirring.

Recently, Assis *et al.* [75] and Spooner *et al.* [76] showed examples of emulsification during reactions in confocal microscopes; it should be noted that Spooner identified some issues related to the heating regime applied during the second set of experiments. While this changed the reproducibility of the work of Assis, it did not alter the fact that the reaction led to emulsification. These authors concluded that the effect of surface tension on interfacial oxygen transfer rather than that of phosphorous is likely to be the dominant cause of emulsification. The work was performed in a confocal microscope in order to prepare samples small

enough to be used for 3D x-ray tomography; this analysis provides the best visual evidence to date of the reaction phenomena, as shown in Figure 2.21.

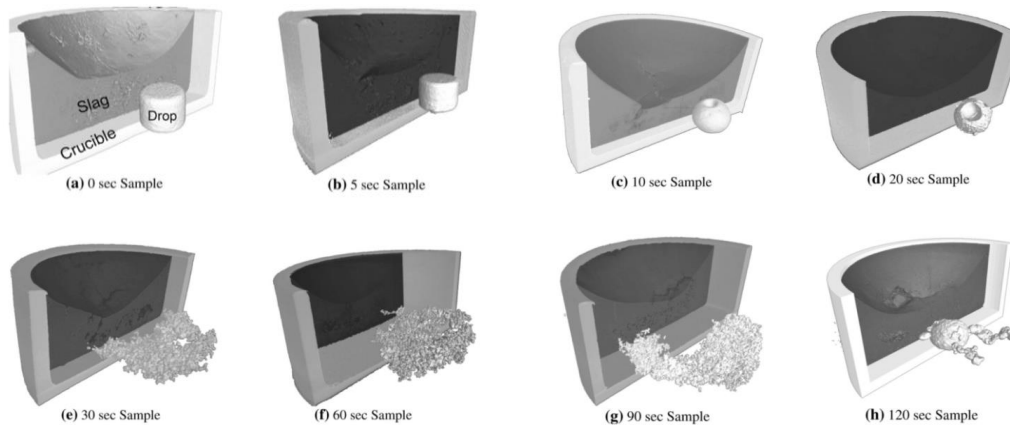


Figure 2.21: Evolution of metal droplet geometry immersed in slag as a function of time at 1873K (1600°C); adapted by permission from Springer Nature: *Met. Trans. B* [75] (2015)

The latest work of Spooner *et al.* [77,78] shows evidence that the interfacial breakdown occurs when the rate of free energy exchange exceeds the interfacial tension of the slag/metal system. Thus, as most observations indicate, when the intensity of reaction rises the emulsification and DIP effects are calculated to increase.

2.5. Bloated Droplets

The presence of slag-metal-gas foams during oxygen steelmaking is a well-known phenomenon. The kinetic energy of the oxygen jet produces metal droplets that mix violently with the slag; carbon in the metal reacts with FeO in slag to form CO that causes foaming of slag. Of interest to this study (more specifically to the study of carbothermic reduction of manganese oxide) is the possibility of droplet bloating during reaction.

During the initial contact of Fe-C with slag it is expected that the surface carbon will react with the slag to form CO; this mechanism is known as external nucleation. Once the surface carbon has depleted, oxygen from the slag must diffuse into the metal to continue the decarburization [79]. At this point, CO nucleation and growth will occur within the metal causing the droplet to swell; this phenomenon was termed bloating by Brooks *et al.* [79]. A schematic illustration of this behaviour has been created from the observations of Molloseau and Fruehan [80] and is shown in Figure 2.22. The figure details the stages of reaction: the metal falling into the slag, the metal shell expanding with CO and forming foam, and the decrease in gas generation. Internal nucleation of CO has been determined to be a very fast reaction in the systems studied and the CO readily stirs the system improving mass transport rates [81].

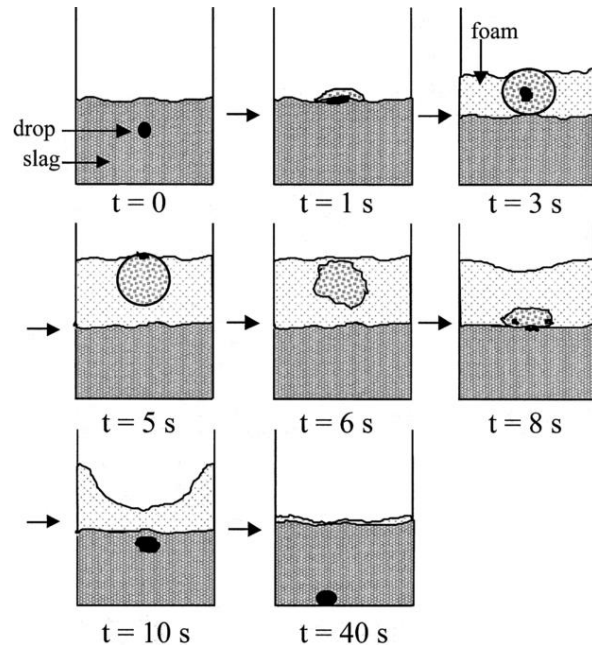


Figure 2.22: Schematic diagram of the behaviour observed by X-Ray fluoroscopy of a Fe-C drop in a slag containing 20wt%FeO; reprinted by permission from Springer Nature: *Met. Trans. B* [80] (2002)

Like emulsification, this phenomenon results in a dynamic interfacial area and rapid mass transport within the droplet, both of which may dramatically change the rate of reaction. Unlike emulsification, metal that breaks off from the bloated droplet likely left as a film on bubbles of CO instead of as spontaneously emulsified material. While bubble films and spontaneous nucleation are very different, undoubtedly the reaction causes disruptions in the surface tension of the bloated droplet, so some of these arguments and distinctions may largely be semantic.

2.6. Summary & Gaps in the Literature

2.6.1. Summary & Gaps in Silicothermic Reduction Literature

With respect to liquid phase reaction kinetics for the silicothermic reduction of MnO, there is very little fundamental research data available that is not subject to interference by other chemical species. If the search is widened to ferroalloys, solid state reduction processes, or gas phase interactions the field is better studied. Of the research that does exist for Fe-Si alloys and MnO reduction from slag, the rate-limiting step has not been clarified and may be related to transport processes in either the metal or slag. The work of Daines and Pehlke [17] and Shibata *et al.* [23] both point towards rate control by manganese mass transport in the metal. Ashizuka *et al.* [31] claimed that silicon contents above 5wt% would result in control by MnO mass transport in the slag. Sohn *et al.* [21] claimed that, in low silicon systems, rate control was dependent on the viscosity of the slag. High manganese partition ratios (L_{Mn}) and high viscosity were responsible for slag being the rate limiting phase, while a low partition and low viscosity shifted the control to the metal phase. Heo *et al.* [18] came to the conclusion of slag mass transport

control by silica was responsible for the rate control. Sohn *et al.* and Heo *et al.* both noted a similar influence of CaF_2 on the systems; additions of CaF_2 fluidized the slag and shifted control from the slag to the metal [18,21]. Ferromanganese production literature is also very clear on the effects of slag basicity on the equilibrium partitions within the silicothermic reduction [9]. This information implies that the actual control for the silicothermic reduction (and carbothermic reduction) is very complex and readily switches between metal and slag control; SiO formation during the reactions could also mean chemical reaction rate control at the interface becomes rate-controlling. Further research needs to be done to study the reduction of liquid MnO from slags with liquid silicon dissolved in iron.

Two important findings come from the Pidgeon Process literature with regards to manganese reductive alloying. The first is the stoichiometry of products introduced by Toguri *et al.* [12], where multiple silicon bearing products are produced simultaneously. The second finding from this literature is the relative ease at which silicon monoxide is produced at temperatures in excess of 1200°C [14]. The present study seeks to assess the viability of silicothermic reduction processes in a reductive alloying setting, thus it is important to learn whether SiO is a major product species in the reaction. If true, the application of silicon as a reductant will be less efficient because it does not completely react in the 2:1 molar ratio demonstrated by Equation 2.3.

There is also room for metal droplet and slag reactions within the literature, as the majority of past researchers studied systems where the metal volume was much greater than the slag volume.

2.6.2. Summary & Gaps of Carbothermic Research

The carbothermic reduction process has been extensively researched. Matters of rate control and equilibrium conditions have been studied. A well-documented two-stage reaction occurs during the carbothermic reduction of liquid MnO from slag, composed of a fast first stage [22,28] and slow second stage [29]. The first stage was best described by Pomfret and Grieveson [22] as an exchange reaction of (MnO) with [Fe] aided by rapid CO evolution [28]. Daines and Pehlke are believed to have only documented a single slow stage [29], and claimed chemical reaction control was responsible because stirring did not result in rate increases. Pomfret and Grieveson changed the iron-carbon system to a nickel-carbon system; where nickel oxide, being less stable than iron oxide, could not participate in the exchange reaction; this system showed no initial fast stage of reaction [22]. Xu *et al.* [32] demonstrated the same mechanism in their work on high carbon ferromanganese research; slags containing no initial FeO rapidly generated a small amount of FeO in the slag which then decreased over time (as seen in Figure 2.6) [32]. Many authors [22,24,33–35] have documented the strong effects that slag basicity has on the effectiveness of the reaction; a change in silica content from 64wt% to 45wt% results in a γ_{MnO} increase from 0.14 to 0.9 [22,30]. This may impact the reaction in one of two ways: if the reaction is chemical reaction controlled then the activity increase of MnO will increase the rate of reaction, if the system is under slag mass

transport control lowering the viscosity by decreasing the silica content will decrease the resistance to mass transport in the slag. Sun *et al.* [37] documented the reaction between an MnO containing slag and a graphite substrate, finding that MnO gradients in the slag were a sign of slag mass transport control. There may be some disagreement between whether the reaction rate is controlled by mass transport in the slag or chemical reaction, however, what seems likely is that both conditions are true in different reaction regimes; these regimes can exist serially within the same reaction.

The first stage of reaction appears to be related to MnO activity in the slag (which is a function of concentration and basicity); the rate may be improved through slag stirring caused by CO nucleation. The second stage of reaction appears to be solely related to a slow chemical reaction after the bulk of the reaction has already occurred. What is lacking from the literature is a comprehensive evaluation of the controlling steps for the carbothermic reduction of manganese oxide. Future work should aim to amalgamate past data and observations, taking into consideration the effects of slag basicity and MnO content across a range of metal and slag concentrations. Further, most observations are focused on low concentrations of carbon or manganese oxide or on high concentrations of these species, and these studies are conducted with low slag/metal volume ratios; studying concentrations in the middle of these values and studying high slag/metal ratios will be a useful contribution to the literature. It seems probable that different conditions control these systems based on the specific regime of study so studying

intermediary values may help elucidate the points of transition from one rate controlling mechanism to another.

2.6.3. Summary & Gaps in Other Highlighted Topics

The kinetics of carbothermic and silicothermic reduction are the primary purpose of this research. While the enclosed studies looked for DIP effects none could be identified and so no gaps were filled. Despite a hypothesis that the silicothermic reduction could cause DIP effects, none were found.

Droplet bloating is related to the activity of oxygen and carbon in the metal, in most instances the oxygen must also be transported from the slag into the metal. Most of the studies on bloated droplets have been limited to FeO in the slags [81] which shows very high reaction rates. If MnO is used instead, the availability of oxygen will fall because of the oxide's stability. Presumably this will decrease the formation and growth of internal CO nucleation; the present study can identify if reactions rates and the bloating phenomenon are less favourable.

Chapter 3

3. Kinetics of Silicothermic Reduction of Manganese Oxide for Advanced High Strength Steel Processing

Copywrite & Bibliographic Information

This chapter contains the pre-publication version of “Kinetics of Silicothermic Reduction of Manganese Oxide for Advanced High-Strength Steel Production”. Final version Copyright © 2017 by The Minerals, Metals & Materials Society and ASM International. Used with permission. Complete bibliographic information is shown below.

Authors: Jamieson, B.J.; Coley, K.S.

Journal: Metallurgical and Materials Transactions B

Year: 2017

Volume: 48

Issue: 3

Pages: 1613-1624

DOI: 10.1007/s11663-017-0967-z

Contributions & Context

The attached article was the first publication of the primary author and served to communicate a collection of experimental data gathered entirely by the author. All data analysis and manuscript drafting was completed by the primary author. Discussions were shared between the primary author and Dr. K.S. Coley.

This work sought to add a significant amount of experimental data to the literature on the silicothermic reduction of manganese oxide process. Very little

work existed in the literature specifically targeted towards fundamental research; as far as a critical literature review was able to reveal there have only been two past researchers, Daines & Pehlke [17] and Heo *et al.* [18] who studied the silicothermic reduction of manganese oxide *without carbon in the metal or a graphite crucible*. Considering simultaneous carbon and silicon reaction allows the inclusion of the work of Ashizuka *et al.* [31], Shibata *et al.* [23], and Sohn *et al.* [21]. Across these five groups of authors, despite relatively similar reaction conditions, three potential rate limiting steps were identified: transport of manganese in the metal, transport of manganese oxide in the slag, and transport of silica in the slag. Further research is needed to clarify the rate determining step.

This work supported the conclusion of mass transport control by MnO in the slag, however, the analysis was complicated by the effects of initial silicon content which appeared to break the assumed transport model that worked for all other conditions; a mass transfer coefficient k_{MnO} was proposed at 1600°C ($4.0 \cdot 10^{-5}$ m/s). SiO gas formed and had a blocking effect on the interface. The data in this article is the subject of the kinetic modelling efforts presented in the subsequent chapter. Within an industrial context, it appears quite clear that silicon is a viable reductant for manganese oxide reduction, however, slag volumes may pose a concern in real reactors. Rates of reaction are fast and proceed to a high extent; within 5 minutes the final [Mn] contents can exceed 25wt% of the metal droplets. The effect of gas bubbles is an obstruction to the process and needs further assessment. Later work (Chapter 4) indicates that SiO₂ is linked to the rate limiting step as well.

Kinetics of Silicothermic Reduction of Manganese Oxide for Advanced High Strength Steel Processing

B.J. Jamieson & K.S. Coley (coleyk@mcmaster.ca)
McMaster University, Hamilton, Canada L8S 4L8

Abstract

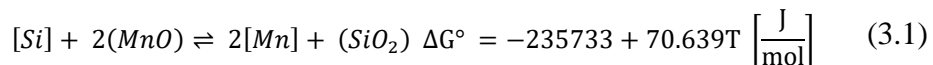
The kinetics of silicothermic reduction of manganese oxide from MnO-SiO₂-CaO-Al₂O₃ slags reacting with Fe-Si droplets were studied in the temperature range of 1823-1923K (1550-1650°C). The effects of initial droplet mass, initial droplet silicon content, and initial slag manganese oxide content were studied. Data obtained for 15% silicon showed agreement with control by mass transport of MnO in the slag with a mass transfer coefficient (k_s) of 4.0×10^{-5} m/s at 1873K (1600°C). However, when this rate determining step was tested at different initial silicon contents the agreement was lost, suggesting mixed control between silicon transport in the metal and manganese oxide transport in the slag. Increasing temperature resulted in a decrease in the rate of reaction because of an increase in the favorability of SiO as a product. Significant gas generation was found during all experiments, as a result of silicon monoxide production. The ratio of silicon monoxide to silica formation was increased by factors favoring silicon transport over that of manganese, further supporting the conclusion that the reaction is under mixed control by transport of both silicon and manganese oxide.

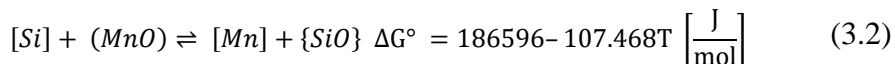
3.1. Introduction

Manganese has become an important alloying element in advanced high strength steels (AHSS) with over 20wt% being proposed for certain grades of twinning induced plasticity (TWIP) steel, and values between 4-11% being of

interest in third generation AHSS [1]. Reduction of manganese oxide dissolved in the slag has been proposed as a possible method of adding manganese to 2nd and 3rd generation steels in order to improve the economics of alloy addition [2] [3]. The present work seeks to advance the fundamental understanding of the kinetics and mechanism of silicothermic reduction of manganese oxide from slags.

The thermic reduction process promotes solute elements with high oxygen affinities to reduce slag components into the metal. There are two thermodynamically attainable pathways for metallic silicon to reduce manganese oxide. The reduction of manganese in the slag requires the supply of electrons from silicon, either by the formation of tetravalent silicon or, if the supply of Mn^{2+} is inadequate, divalent silicon; the former results in silicon being incorporated into the slag as silicate while the latter requires the net transfer of one O^{2-} ion from the slag to form SiO gas with the divalent silicon. Whilst the authors do not make any claims to the detailed mechanism, conceptually and stoichiometrically these reactions can be written as Equations 3.1 and 3.2. Bracket notation of [metal], (slag), and {gas} is used in this work. The free energies for these reactions were taken from FactSage Reaction Module and the FTDemo database [4], which take the following data from the NIST JANAF Tables [5]. At 1873K (1600°C) Equation 3.1 yields -103kJ/mol while Equation 3.2 yields -14.7kJ/mol; under standard conditions it is clear that while SiO_2 may be more favorable SiO can still form.





Some of the earliest quantitative work regarding the reduction of MnO using Si in non-graphite crucibles comes from Daines and Pehlke [6]. Their work showed that manganese mass transport in the metal was the rate-limiting step, where the mass transfer coefficient (k_m) was equal to $7 \times 10^{-6} \text{m/s}$. The system showed significant rate enhancement with stirring, confirming mass transport control. The system underwent a two-stage reaction, the first stage faster than the second.

Shibata *et al.* [7] performed a series of experiments involving multiple simultaneous reactions. MnO was reduced by silicon and carbon simultaneously; the authors concluded that MnO reduction was more likely to be controlled by mass transport in the metal than the slag. They further noted that desiliconization appeared to finish within the first 300 seconds of reaction.

The work of Heo *et al.* [8] shows interesting correlations with CaF_2 addition to the slag; a ferromanganese slag reduced with metallic silicon was shown to produce a stoichiometrically balanced amount of SiO_2 and Mn in the presence of CaF_2 , whereas in its absence a greater than stoichiometric quantity of silicon was consumed. These authors proposed SiO generation as the alternate manganese reduction pathway. Such a result would appear to indicate that mass transport in the slag may play a role in rate control of the system. The authors concluded that silica mass transport in the slag was controlling. However, they acknowledged the work of Sohn *et al.* [9] who suggested for high viscosity slags mass transport of MnO would be the rate controlling step.

Similar work can be found in the ferromanganese production literature; however, most of this work is directed towards understanding carbothermic reduction of manganese oxide. Early authors like Tarby and Philbrook [10] were the first to show a two-stage reaction of MnO with C, the first stage exhibiting significant gas generation and the second producing nearly no gas. The initial fast stage of reaction was proposed to be controlled by manganese transport in the slag. Daines and Pehlke [11] claimed that the reaction was under chemical reaction control at the slag-metal interface.

Pomfret and Grieveson [12] claimed that the observations of Daines and Pehlke were for the slower second stage of the reaction. Pomfret and Grieveson plotted the manganese partition over time, defined in their case as the activity of MnO in the slag (a_{MnO}) divided by the activity of Mn (a_{Mn}) in the metal, and showed that a critical ratio of $a_{\text{MnO}}/a_{\text{Mn}}$ characterized the transition from faster to slower rates. Ashizuka *et al.* [13] were able to demonstrate similar results to Daines and Pehlke. Xu *et al.* [14] used X-ray fluoroscopic techniques to observe nucleation sites for carbon monoxide along the slag-metal interface. Here it was concluded that the rate of generation of CO along the interface was the rate controlling step.

A more recent publication by Kononov *et al.* [15] demonstrates the importance of gaseous species in affecting the rate of manganese reduction. Different temperatures and different ratios of C/MnO were used in hydrogen, helium, and argon environments. The results indicate increasing reaction rates with increasing temperature. Further, the densest gas (argon) had the lowest CO

diffusivity which was reflected in MnO reduction rates. Helium did not reduce MnO but has a higher CO diffusivity than argon, resulting in a faster rate. Hydrogen participated in the reduction and had a high CO diffusivity and so had the fastest rate of all.

Sun *et al.* [16] reacted slag with a carbon substrate where it generated a reduced metal product. Energy dispersive spectroscopy (EDS) revealed a manganese concentration gradient in the slag near the slag-metal boundary; such a gradient may imply that MnO transport contributes to reduction control. The rate of reduction was said to increase with increasing MnO content in the slag. Their final conclusion was that chemical or mixed-mode control may exist in the system.

From an analysis of the above literature, it would appear that there are two control steps in the carbothermic reduction of manganese oxide. The initial, fast step is controlled by MnO transport through the slag and the slower step appears to be controlled by CO production at the interface. These conclusions, and specifically the effect of gas formation at the interface may also be relevant to silicothermic reduction should Equation 3.2 play a significant role.

Many reacting systems have been found to exhibit dynamic interfacial phenomena influenced by the transfer of elements across the interface [17–21] where spontaneous increases in surface area can be observed; surface area recovers as the reaction slows and nears equilibrium. Many explanations for these observations have been provided, though none have fully explained the phenomena. Most explanations incorporate an apparent decrease in surface tension [18,21]

caused by one or more capillary effects: solutocapillarity based on surface active elements, electrocapillarity from charge differences, and thermocapillarity from localized temperature gradients. Surface tension decreases can manifest as dimpling, flattening, and in the most extreme case emulsification.

Previous authors have documented reaction rates associated with a wide range of reaction couples [22–24], of particular interest is the work of Rhamdhani and the aluminothermic reduction of silica. This reaction (Al/SiO_2) has a similar Gibbs energy of reaction to the current system per mole of metal solute but can only generate liquid products. Rhamdhani's work was shown to generate a metal-slag emulsion that improved the reaction kinetics through interfacial area increase.

Possibly even more relevant to the current work, is the recent work of White and Sichen [25] where the rates of mass transfer in a stirred system of Si and CaO- SiO_2 were investigated. During the course of the reaction rapid transfer of calcium across the interface dropped the interfacial tension to a level low enough that mechanical agitation caused emulsification. Such observations imply that systems which do not normally express spontaneous emulsification may be induced to do so with stirring.

Recently, Assis *et al.* [26] and Spooner *et al.* [27] showed examples of emulsification during reactions in confocal microscopes; it should be noted that Spooner identified some issues related to the heating regimen applied during the second set of experiments. While this changed the replicability of the work of Assis, it still lead to emulsification. These authors concluded that the effect on surface

tension of interfacial oxygen transfer rather than that of phosphorous is likely to be the dominant cause of emulsification. Given that reductive alloying will result in a large transfer of oxygen across the interface it is reasonable to expect that emulsification or similar surface phenomena will occur.

There is considerable disagreement in the literature regarding silicothermic reduction of manganese oxide from slag; there have been a number of different conclusions about the rate control and reaction mechanism. As it stands, no model exists to piece together the various findings. The current work is part of an ongoing study to further the collective understanding of silicothermic reduction kinetics of MnO from slag and to rationalize the apparently disparate findings in the published literature. This will be addressed firstly by collecting experimental data in the untested mid-range of silicon and manganese oxide concentrations, and secondly by analyzing not only this experimental data but that of other authors. By doing so the mechanism can be detailed and a model developed to describe changes in the rate controlling steps with changing reaction conditions. The current publication presents the first step towards this goal. Experimental data is presented and analysed for the mid-range concentrations and a tentative mechanism proposed. A subsequent publication, currently in preparation, will offer a more detailed analysis of this data on the basis of mixed control involving mass transport of silicon in the metal and manganese in the slag.

3.2. Experimental Procedure

3.2.1. Materials Usage

All ceramic components used were 99.8% alumina refractory material. Table 3.1 below shows the composition of all raw materials used in the experiments.

Table 3.1: Chemical Composition of Six Melt Species

Component	Primary wt.%	Carbon wt.%	Sulfur wt.%	Phosphorus wt.%
Silicon	99.9999	--	--	--
Electrolytic Iron	99.9	<0.0067	<0.00143	--
Silica Sand	99.8	0.00605	0.00560	0.0023
Alumina Powder	99.5	0.00322	0.00025	--
Calcium Oxide Powder	>96	0.1862	0.00671	0.0063
Manganese Oxide Powder	99	0.00371	0.00153	--

3.2.2. Sample Preparation

Slag samples were first prepared by pressing a 2:2:1 weight ratio of $\text{SiO}_2:\text{CaO}:\text{Al}_2\text{O}_3$ into pellets, and melting them in a platinum crucible using a resistance heated muffle furnace at 1873K (1600°C). Melts were quenched by pouring onto a steel I-beam. The shattered pieces of quenched slag were crushed and remixed; the melting/quenching/crushing procedure was repeated twice. MnO homogeneity with the pre-mixed slag was ensured in three ways: vigorous shaking of the powdered slag and MnO mixture prior to adding to the crucible, X-ray observation of the molten slag once in the furnace, and allowing for a minimum of 30 minutes homogenizing time in a liquid state once in the furnace. Owing to the X-ray opacity differences between the MnO and other slag components, it was quite clear when a slag was not homogenized; a lighter band of slag was observed on top of a darker band of MnO rich slag. ICP analysis of a blank slag, where all steps in

the experimental procedure were followed except for the addition of a droplet, indicates a maximum variation in composition of $\pm 0.5\text{wt}\%$ MnO across the entire slag. The total mass for all slag samples was fixed at 25g; no variations in slag mass were tested during these experiments.

Metal droplets were produced by mixing appropriate quantities of silicon and iron and melting in a vacuum arc melter. The melting atmosphere contained less than 4×10^{-10} atmospheres of O_2 ; droplets were melted 2-3 times for homogeneity; a total oxygen content of less than 50ppm [28] is expected.

3.2.3. Procedure

All reduction experiments were conducted using a vertical tube furnace heated using molybdenum disilicide elements. Reaction temperatures up to 1923K (1650°C) measured using a type-B platinum-rhodium thermocouple could be held constant within $\pm 8\text{K}$ (8°C). The 8.9cm diameter alumina furnace tube was sealed using water cooled stainless steel caps at either end, fitted to allow either inert gas to flow through the furnace or to evacuate the furnace using a vacuum pump. The furnace was equipped for X-ray imaging of the slag and metal inside the crucible to allow observation of interfacial phenomena and gas bubble formation during the experiment. A diagram of the furnace setup is provided in Figure 3.1.

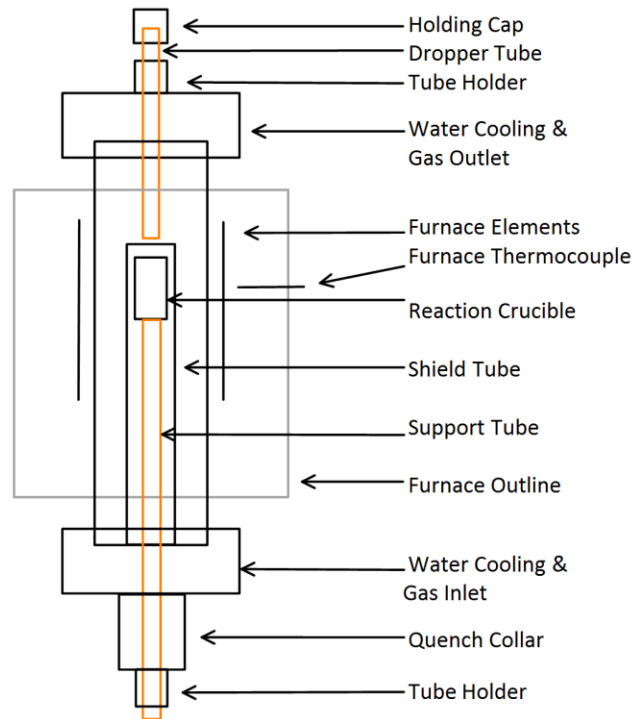


Figure 3.1: Schematic Diagram of the Vertical Tube Furnace, Not to Scale

The following paragraph uses names taken from Figure 3.1 to better explain the stepwise procedure. An alumina crucible containing slag was placed in the cold zone of the furnace, located inside the quench collar at the base of the furnace and supported by an alumina support rod; the O-ring connections at the base were sealed. The holding cap above the furnace was removed, and a metal droplet was placed inside supported by an external neodymium magnet. The cap was attached and sealed to the dropper tube such that the droplet can fall when the magnet is removed (without unsealing the furnace). With all seals closed the system was evacuated and backfilled with argon. Thereafter, the system was continuously flushed with argon for the duration of the experiment. The crucible was raised from the bottom of the furnace into the hot zone over the course of approximately one hour to prevent thermal shock to the crucible. The hot zone temperature was

uniform to approximately $\pm 1\text{K}$ (1°C) for 4cm, or $\pm 10\text{K}$ (10°C) for 10cm. The experiment was started by removing the magnet from the exterior of the holding cap, thus allowing the metal droplet to fall to the base of the dropper tube which was situated near the mouth of the crucible. This tube had a small hole drilled in the end, too small for a solid metal droplet to fall through but large enough for liquid metal to pass. This ensured that the metal was fully liquid prior to the start of the reaction; the length of melting was dependent on the size of the droplet. The X-ray equipment was used to determine the precise time when the metal droplet melted, moved through the hole, and entered the slag which established precise zero times for each reaction. The location of the droplet at various times is demonstrated in Figure 3.2. The crucible that contained both slag and metal could be quenched in less than one second by removing the support tube, which allowed for accurate end times to be established. In order to generate a concentration versus time profile for a specific set of initial conditions several of these experiments were conducted; the collection of many discrete data points allowed for the fitting of the data to a continuous curve for each initial reaction condition.

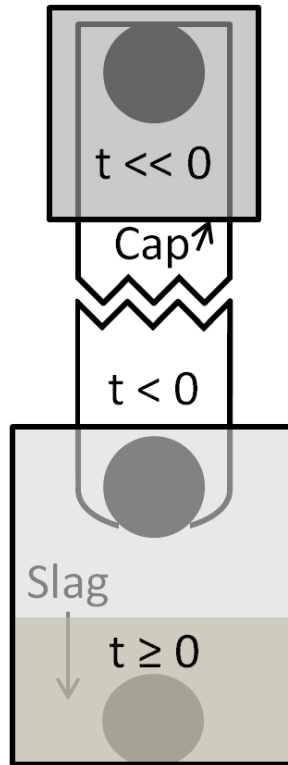


Figure 3.2: Diagram of Droplet Location at Various Times within the Furnace Setup, Not to Scale

Inductively Coupled Plasma – Optical Emission Spectroscopy (ICP-OES) was used to analyse the quenched metal droplets for manganese and silicon. Approximately 0.1g samples of metal were dissolved using a microwave digester and a solution of 3mL HCl, 2mL HNO₃, and 2mL HBF₄. Samples from the digester were then diluted to 100mL twice to get them into a measurable concentration range for the elements of interest (0-40ppm). Experimental slags were not analyzed with ICP as concentration gradients formed within the slag rendered bulk concentration measurements meaningless.

3.3. Results

Figure 3.3 through Figure 3.11 show the change in metallic silicon and manganese contents as a function of time for the various reaction conditions. The solid lines in these figures have been “drawn” through the data using exponential functions by the author. The dashed line shows the predicted manganese value by converting the change in wt%Si to wt%Mn using Equation 3.1, while the dotted line shows the same conversion using Equation 3.2. During the initial seconds of reaction the measured data appears to be almost entirely described by Equation 3.1. Beyond this time deviation can be found, where the amount of manganese reduced to the metal is less than calculated from the stoichiometry from Equation 3.1, implying contribution from Equation 3.2. A depletion of Mn^{2+} ions would improve the favorability of the SiO reaction, which may explain this behaviour. The time to achieve equilibrium for these reactions was between 240 and 360 seconds. This value is in agreement with the desiliconization data of Shibata *et al.* [7].

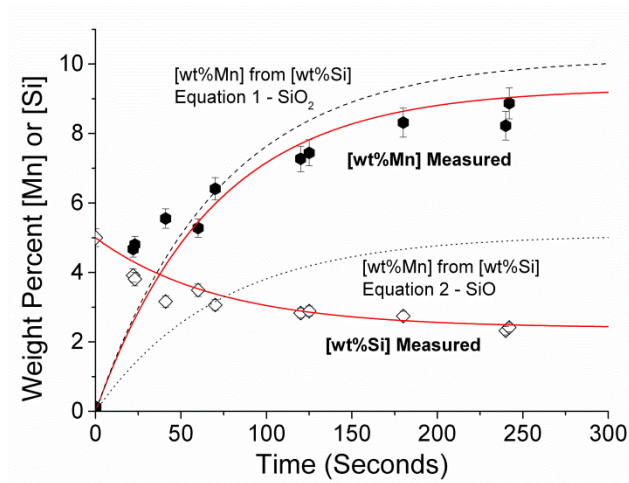


Figure 3.3: Concentration vs. Time Plot for the 15wt%MnO, 5wt%Si, 1.5g Droplet, and 1873K (1600°C)

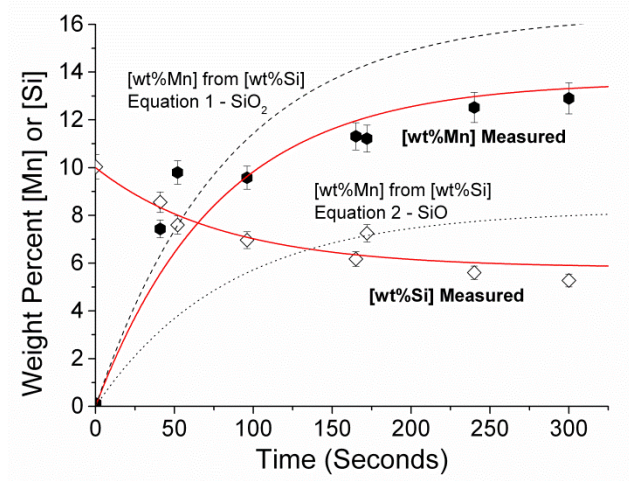


Figure 3.4: Concentration vs. Time Plot for the 15wt%MnO, 10wt%Si, 1.5g Droplet, and 1873K (1600°C)

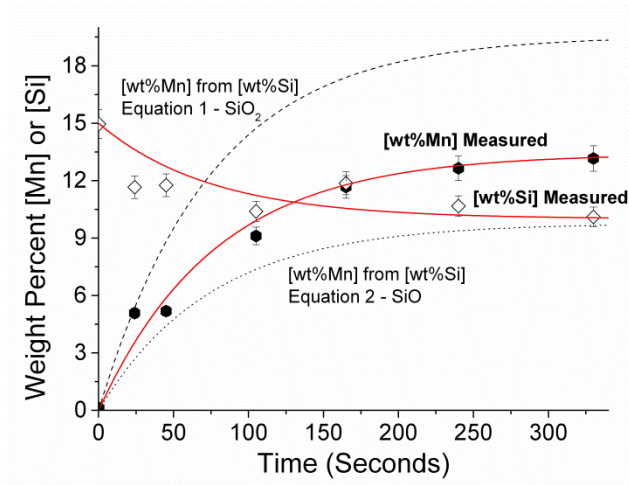


Figure 3.5: Concentration vs. Time Plot for the 10wt%MnO, 15wt%Si, 1.5g Droplet, and 1923K (1650°C)

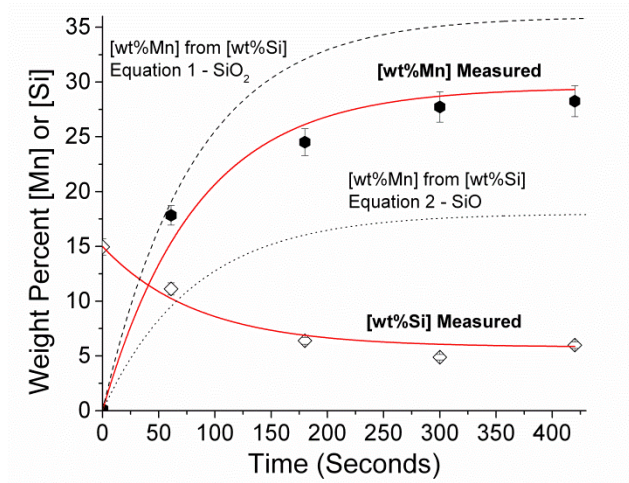


Figure 3.6: Concentration vs. Time Plot for the 15wt%MnO, 15wt%Si, 0.5g Droplet, and 1873K (1600°C)

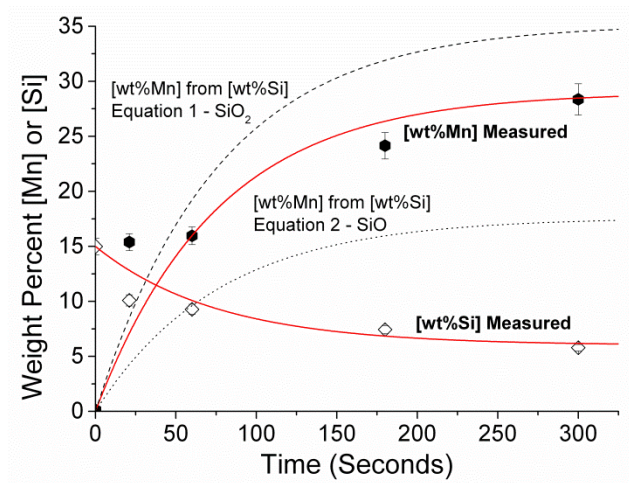


Figure 3.7: Concentration vs. Time Plot for the 15wt%MnO, 15wt%Si, 1.0g Droplet, and 1873K (1600°C)

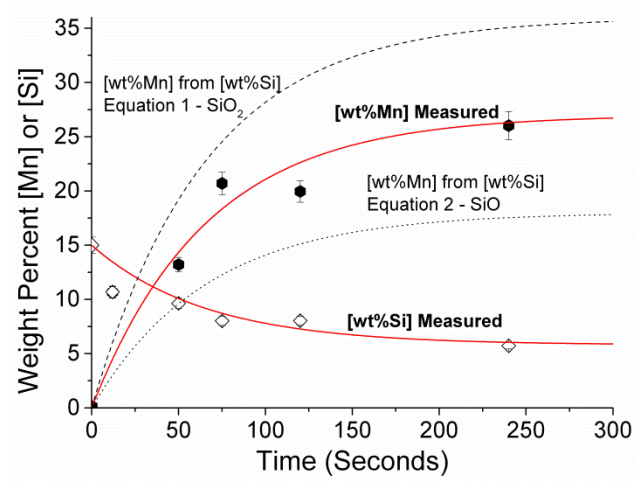


Figure 3.8: Concentration vs. Time Plot for the 15wt%MnO, 15wt%Si, 1.5g Droplet, and 1823K (1550°C)

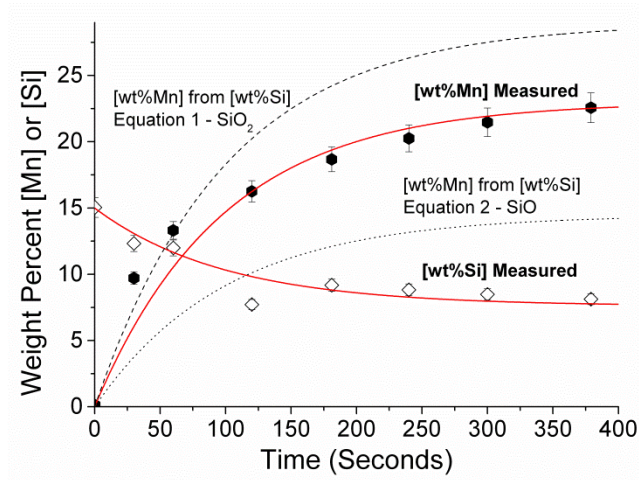


Figure 3.9: Concentration vs. Time Plot for the 15wt%MnO, 15wt%Si, 1.5g Droplet, and 1873K (1600°C)

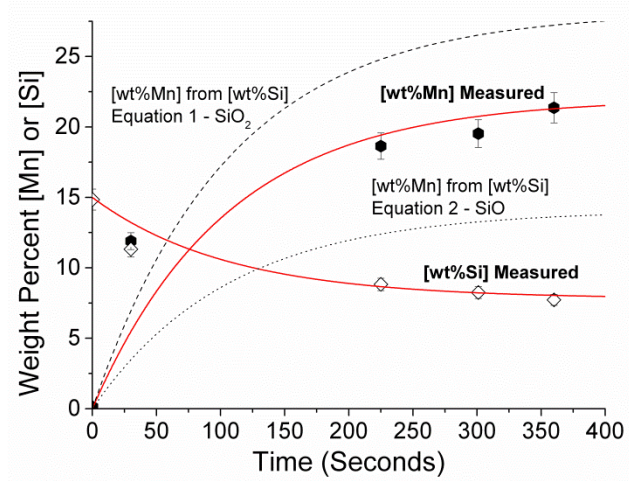


Figure 3.10: Concentration vs. Time Plot for the 15wt%MnO, 15wt%Si, 1.5g Droplet, and 1923K (1650°C)

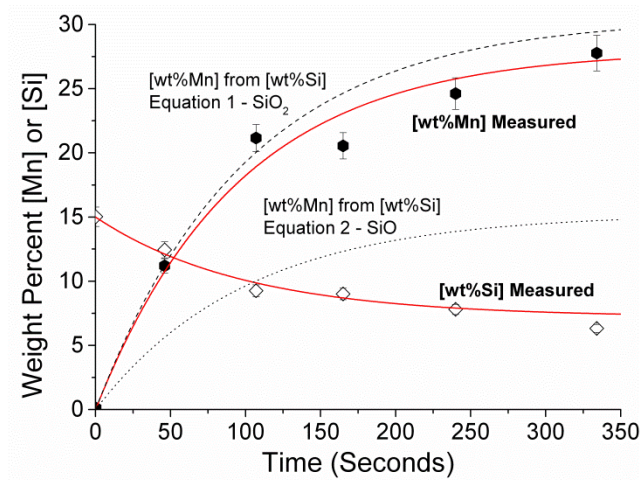


Figure 3.11: Concentration vs. Time Plot for the 20wt%MnO, 15wt%Si, 1.5g Droplet, and 1923K (1650°C)

Visual observation of quenched slags, such as Figure 3.12, shows a distinct color gradient exists within the sample taken at around three minutes. Given that MnO is the only species to cause significant pigmentation of the slag, this gradient appears to be related to manganese depletion of the slag and is not found in slags near time zero or slags that are at equilibrium. Hence it is reasonable to assume that transport of manganese oxide in the slag contributes to control of the reaction for a

large portion of the reaction time. Figure 3.13, taken after twenty seconds of reaction, is consistently dark in both the interface and bulk slag, implying that no significant gradient exists. Figure 3.14 taken at twenty minutes of reaction is consistently lighter in color. In all cases gas bubbles can be observed forming along the slag-metal boundary, though each image has a different bubble shape associated with it. This is believed to be associated with how the gas bubbles evolve over time.

Note that these images have had small adjustments made to their color and contrast in order to make the changes in the slag more apparent for readers. This action has not changed the position of the MnO depleted zone. An overlay has further been added to point out key areas of interest. While only three images have been presented, similar observations by the author were found for nearly all samples.

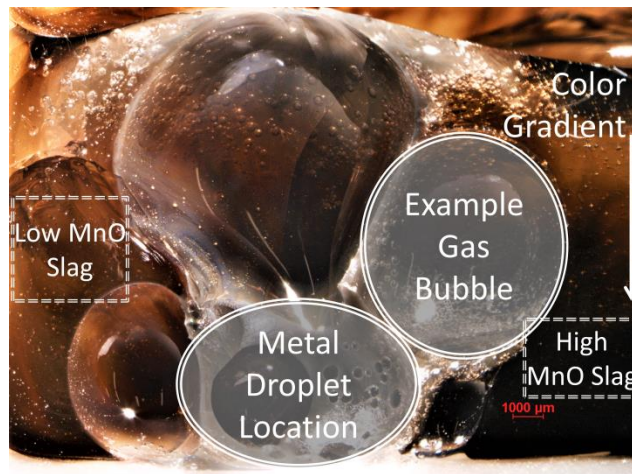


Figure 3.12: Colour Gradients Surrounding the Droplet (Lower Middle of the Image) and Gas at 185 Seconds of Reaction; The Lightest Area is to the Left and Darkest to the Bottom Right

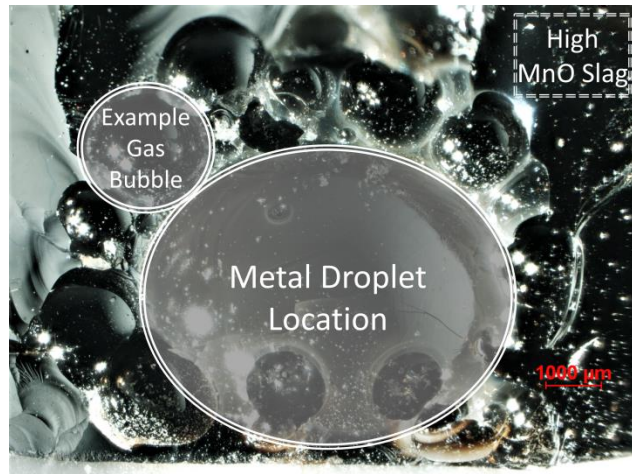


Figure 3.13: Negligible Color Gradients Found Surrounding the Droplet at 20 Seconds of Reaction; Note the Distinct Outline of Spherical Gas Bubbles Surrounding the Large Central Droplet

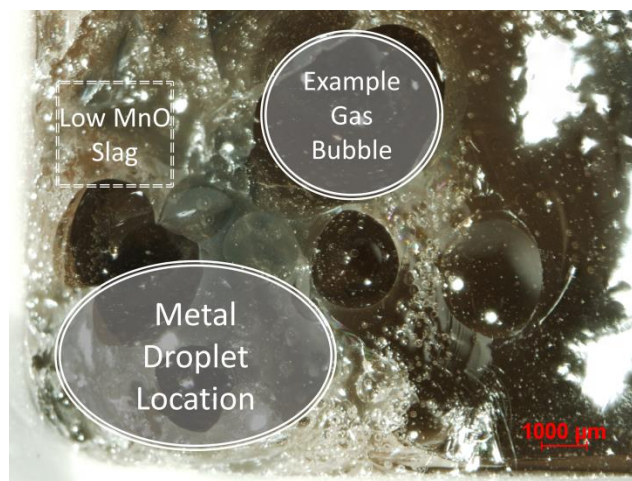


Figure 3.14: Small Light to Dark Gradient from Left to Right across the Image at 20 Minutes of Reaction; Note the Destabilization of Bubbles Seen at Long Times Resulting in Elongated Shapes

In order to quantify the correlation between color and (MnO) concentration, EDS was performed at different distances from the slag/metal interface. The data shows concentration increasing from approximately 4wt%Mn to 6wt%Mn over a 0.7mm distance in the direction perpendicular to the interface. Without a standard to reference in the SEM these values cannot be taken at face value, however their

trend can, where the manganese content increases by 50%. This further reinforces the idea that manganese transport in the slag controls the reaction rate.

Based on the above qualitative evidence for mass transport control in the slag, Equation 3.3 was used to plot the experimental data. The mass transfer coefficients are represented as k_s and k_m for slag and metal respectively in units of m/s; similarly volume is given as V_s or V_m in m^3 . Time is represented as ‘t’ in seconds and A the interfacial area in m^2 . The number of moles of a particular species in either the slag or metal are given as n_s or n_m respectively (and can have the desired species substituted); the superscripts denote whether the value is taken at equilibrium ‘e’ or at the initial composition ‘o’, and the superscript free variable is for any arbitrary time. Masses of slag or metal are represented as m_s or m_m . Molar mass is given as capital M. Equation 3.3 was developed assuming control by mass transport in the slag employing a molar balance such that the equation could be written in terms of number of moles of the relevant species in the metal. Equation 3.4 is Equation 3.3 where an appropriate conversion of moles to mass has been applied. Further, this derivation includes the initial moles of manganese in the metal as part of the expression; this is a negligible non-zero value that could be assumed away, but was tracked in this expression regardless.

$$-k_s t = \frac{V_s}{A} \left(\frac{n_m^e}{n_m^0 + n_s^0} \right) \ln \left(\frac{n_m - n_m^e}{n_m^0 + n_s^0} \right) \quad (3.3)$$

$$-k_s t = \frac{V_s}{A} \left(\frac{\left(\frac{[\text{wt}\% \text{Mn}^e] * m_m^e}{M_{\text{Mn}}} \right)}{\left(\frac{[\text{wt}\% \text{Mn}^o] * m_m^o}{M_{\text{Mn}}} + \frac{[\text{wt}\% \text{MnO}^o] * m_s}{M_{\text{MnO}}} \right)} \right). \quad (3.4)$$

$$\ln \frac{([\text{wt}\% \text{Mn}] * m_m - [\text{wt}\% \text{Mn}^e] * m_m^e)}{([\text{wt}\% \text{Mn}^o] * m_m^o - [\text{wt}\% \text{Mn}^e] * m_m^e)}$$

Further, in order to verify that metal transport is not the rate control, Equation 3.5 for metal control is shown below. Note that the significant differences are the use metal versus slag volume and the pre-logarithmic term. The molar terms in Equation 3.5 have been converted to mass terms in Equation 3.6.

$$-k_m t = \frac{V_m}{A} \left(\frac{n_m^o + n_s^o - n_m^e}{n_m^o + n_s^o} \right) \ln \left(\frac{n_m - n_m^e}{n_m^o - n_m^e} \right) \quad (3.5)$$

$$-k_m t = \frac{V_m}{A} \left(\frac{\frac{[\text{wt}\% \text{Mn}^o] * m_m^o}{M_{\text{Mn}}} + \frac{[\text{wt}\% \text{MnO}^o] * m_s}{M_{\text{MnO}}} - \frac{[\text{wt}\% \text{Mn}^e] * m_m^e}{M_{\text{Mn}}}}{\frac{[\text{wt}\% \text{Mn}^o] * m_m^o}{M_{\text{Mn}}} + \frac{[\text{wt}\% \text{MnO}^o] * m_s}{M_{\text{MnO}}}} \right) \quad (3.6)$$

$$\ln \left(\frac{([\text{wt}\% \text{Mn}] * m_m - [\text{wt}\% \text{Mn}^e] * m_m^e)}{([\text{wt}\% \text{Mn}^o] * m_m^o - [\text{wt}\% \text{Mn}^e] * m_m^e)} \right)$$

If mass transport of manganese oxide in the slag is assumed to control the reaction rate, the change in the manganese concentration in the metal with time is given by Equation 3.4, whereas if mass transport in the metal controls Equation 3.6 would apply. This information is displayed in Table 3.2 for clarity.

Table 3.2: Definition of Z, Y_m, and Y_s Used to Plot Rate Equations

Z – Figures 3.15 to 3.19	$\frac{([\text{wt}\% \text{Mn}] * m_m - [\text{wt}\% \text{Mn}^e] * m_m^e)}{([\text{wt}\% \text{Mn}^o] * m_m^o - [\text{wt}\% \text{Mn}^e] * m_m^e)}$
Y – Figure 3.16 (mass transfer in metal)	$\frac{V_m \left(\frac{[\text{wt}\% \text{Mn}^o] * m_m^o}{M_{\text{Mn}}} + \frac{[\text{wt}\% \text{MnO}^o] * m_s}{M_{\text{MnO}}} - \frac{[\text{wt}\% \text{Mn}^e] * m_m^e}{M_{\text{Mn}}} \right)}{A \left(\frac{[\text{wt}\% \text{Mn}^o] * m_m^o}{M_{\text{Mn}}} + \frac{[\text{wt}\% \text{MnO}^o] * m_s}{M_{\text{MnO}}} \right)}$
Y – Figures 3.15 and 3.17 to 3.19 (Slag Control)	$\frac{V_s \left(\frac{[\text{wt}\% \text{Mn}^e] * m_m^e}{M_{\text{Mn}}} \right)}{A \left(\frac{[\text{wt}\% \text{Mn}^o] * m_m^o}{M_{\text{Mn}}} + \frac{[\text{wt}\% \text{MnO}^o] * m_s}{M_{\text{MnO}}} \right)}$

In the current work different droplet sizes, different starting [Si], and different starting (MnO) contents have been used to alter the value of Y. The effect of temperature has also been studied. Figure 3.15 and Figure 3.16 are plotted for different droplet sizes below according to Equation 3.4 and Equation 3.6 respectively. The data plotted according to control by MnO mass transport in the slag can be fitted well to a single straight line whereas the data plotted according to metal control does not fit as well. This suggests that manganese oxide reduction is controlled by mass transport in the slag. Figure 3.15 shows an excellent fit of the data to a single straight line, with significant deviation only occurring following the 300 second mark. Meanwhile Figure 3.16 shows that the equivalent plot for mass transport in the metal appears to diverge at a much earlier time. The mass transfer coefficient k_s is approximately 4.0×10^{-5} m/s.

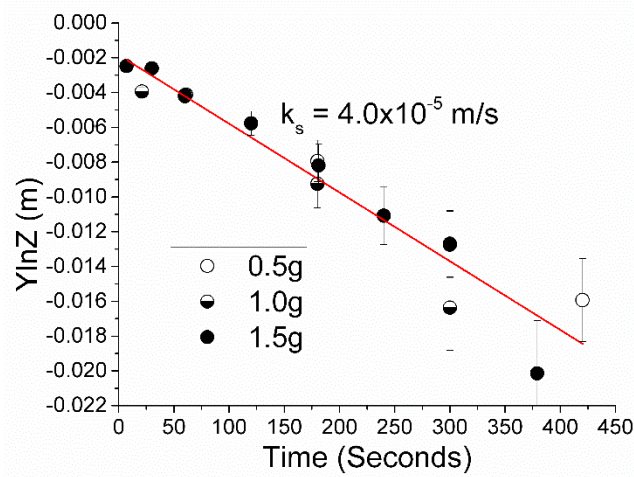


Figure 3.15: [Mn] Concentration Data Plotted as a Function of Droplet Size and Time, Using Equation 3.4 for Mass Transport of MnO in the Slag; Initial Conditions 15wt%Si, 15wt%MnO, 1873K (1600°C), Variable Mass

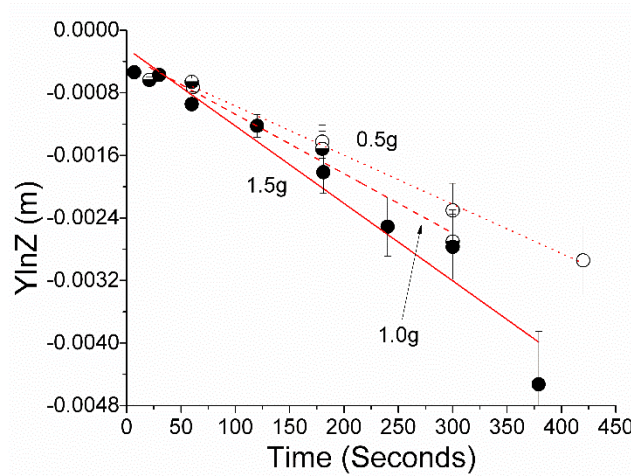


Figure 3.16: [Mn] Concentration Data Plotted as a Function of Droplet Size and Time, Using Equation 3.6 for Mass Transport on Mn in the Metal; Initial Conditions 15wt%Si, 15wt%MnO, 1873K (1600°C), Variable Mass

This result does not agree with the work of Daines and Pehlke who stated that mass transport of manganese in the metal was the rate controlling step [6]. Daines and Pehlke used much lower amounts of [Si] and (MnO) in their system, and made the bulk of their observations at times greater than the five to seven minute mark; this could explain the discrepancy. The more recent work of Heo *et al.* is in

agreement with slag control findings, even though their claim is a silica control pathway and not manganese oxide [8].

Carrying forward the conclusion that the system is under slag mass transport control, the following figures show the results of changing initial (MnO) concentrations and initial [Si] concentrations. Figure 3.17 shows that changing the initial concentration of (MnO) in the system does not change the rate constant of reaction. This provides further evidence towards the idea of control by transport of manganese oxide slag. Note that as expected the k_s value here is near that established in Figure 3.15 (approximately a ten percent difference).

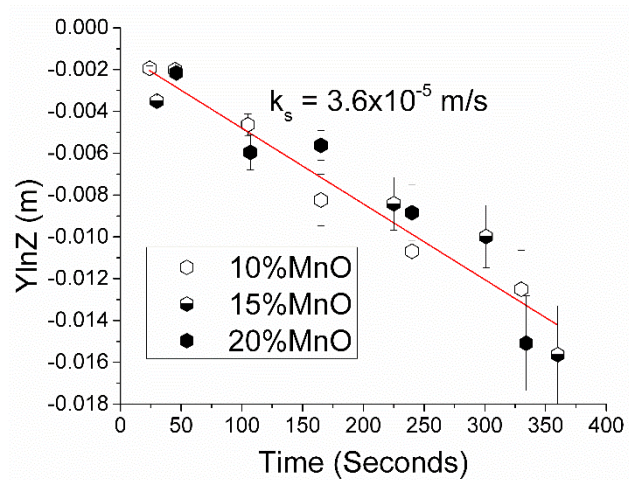


Figure 3.17: [Mn] Concentration Data Plotted as a Function of Initial (MnO) and Time, Using Equation 3.4 Control by Mass Transport of MnO in the Slag; Initial Conditions 15wt%Si, Variable MnO, 1923K (1650°C), 1.5g Droplet

Figure 3.18 shows that by increasing the initial concentration of silicon in the metal an increase in the slope of the rate plot can be observed. This observation appears to be in contradiction to the previous evidence of mass transport control by manganese oxide in the slag, as the pre-logarithmic term is not successfully

normalizing the data with changes in silicon. This finding is contradictory to the previous findings, and may imply mixed control is controlling this system.

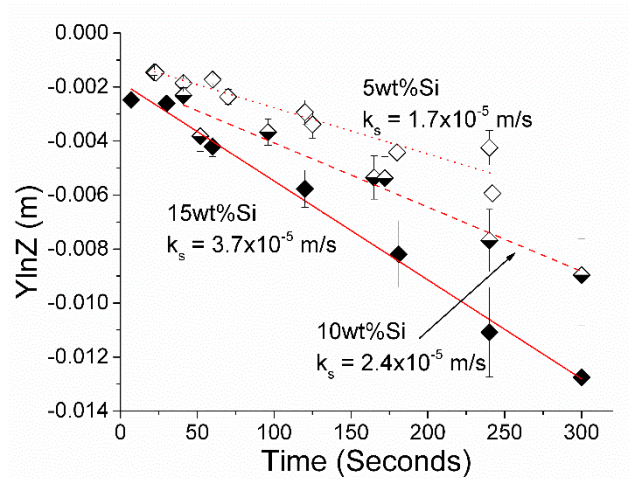


Figure 3.18: [Mn] Concentration Data Plotted as a Function of Initial [Si] and Time, Using Equation 3.4 for Control by Mass Transport of MnO in the Slag; Initial Conditions Variable Si, 15wt%MnO, 1873K (1600°C), 1.5g Droplet

Figure 3.19 compares changes in temperature among reactions. Strangely, it appears as if increasing temperature may result in a decline in the rate constant. This is atypical of most systems under mass transport control, as an increase in temperature typically corresponds to an increase in the mass transfer coefficient. This anomalous change in the apparent mass transfer coefficient could be because of a shift in balance between two rate determining steps in a mixed control system or because of different levels of bubble formation on the metal surface. Further, near time zero it appears as if the higher temperature starts from a lower $Y \ln Z$ than that of the lower temperatures. This may imply that a reaction occurs near time zero, without the presence of gas, corresponding well to bulk mass transfer and the increased rate constant that temperature typically brings.

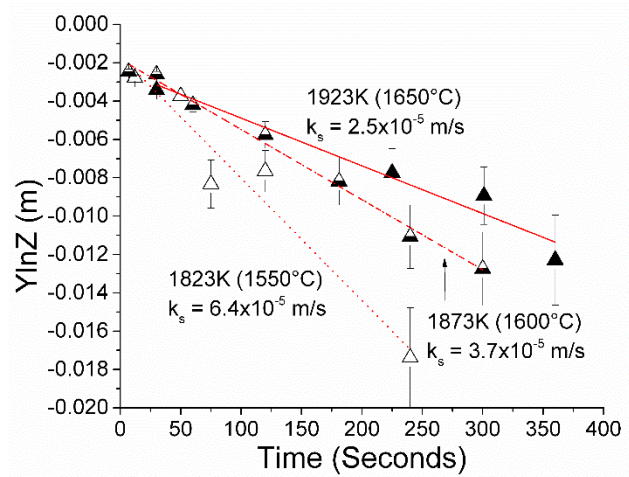


Figure 3.19: [Mn] Concentration Data Plotted as a Function of Temperature and Time, Using Equation 3.4 for Control by Mass Transport of MnO in the Slag; Initial Conditions 15wt%Si, 15wt%MnO, Variable Temperature, 1.5g Droplet

One final observation from this work is the marks left by bubbles on the metal surface. Figure 3.20 shows a metal droplet that has been extracted from slag with large flattened areas. These appear to be gas nucleation and growth sites, where the pressure exerted by {SiO} manages to flatten the interface. From thermodynamic calculations silicon monoxide is the most likely gas present. This flattening is likely to happen when gas generation is at a maximum and would exert the greatest pressure on the interface. In some cases the X-ray equipment allowed for the in-situ observation of large gas bubbles in the slag, apparently breaking away from the metal. It is believed that these larger bubbles are the result of coalescence of many small bubbles into a single large bubble that can break away from the surface of the metal droplet. Unfortunately the image quality is not sufficient to measure the volume of the bubble film around the metal surface.

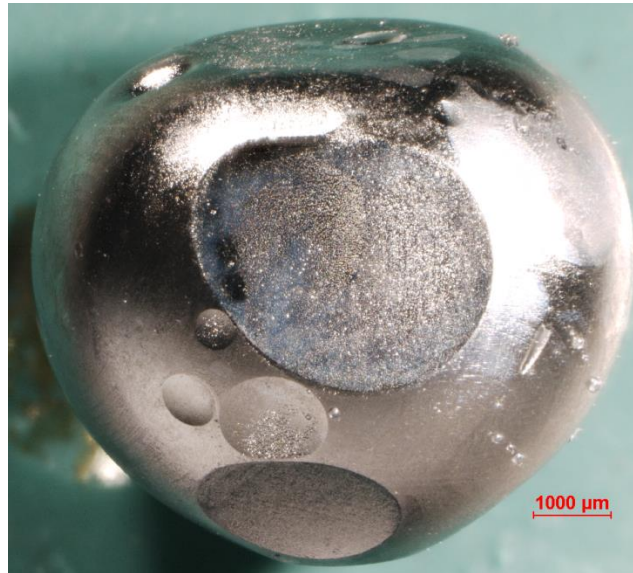


Figure 3.20: Localized Flattening on a Droplet Interface at 4 Minutes of Reaction

Meanwhile Figure 3.21 shows marks left by bubbles attached to the metal interface with a network of slag surrounding the sites. These circular areas of apparently clean metal show how the gas sticks directly to the metal and displaces slag around the nucleation and growth sites. This observation provides credible evidence to the theory that a dynamic volume/area term may exist over the course of the reaction relating the ability of (MnO) to diffuse past the bubble layer and react with the metal in the slag regions; this is discussed in more detail below.

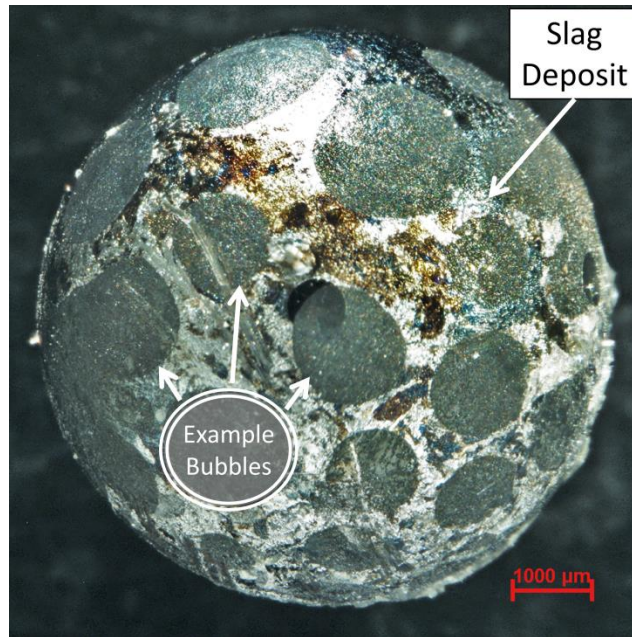


Figure 3.21: Cleared Metal Surface Surrounded by Slag Deposits in a Web-Like Pattern at 2 Minutes of Reaction

It is worth noting that none of the dynamic interfacial phenomena (flattening, roughening, or emulsification) as identified by previous workers [20,22,26] were found during the experiments. The localized flattening shown in Figure 3.20 is likely attributed to bubble nucleation and not surface tension breakdown. Despite exceeding the $0.1 \text{ mol/m}^2/\text{s}$ interfacial oxygen transfer rate criterion proposed by Riboud and Lucas [20], the system did not exhibit interfacial breakdown; the formation of a stable bubble film around the droplet may inhibit spontaneous emulsification. This hypothesis is purely speculative, although other workers in the authors' laboratory studying iron carbon droplets have found that when bubbles are present the interface remains remarkably stable even at high oxygen flux [29].

3.4. Discussion

The results presented above offer strong evidence for control by mass transport of manganese oxide in the slag. A gradient in slag pigmentation (indicative of depletion of manganese oxide close to the slag/metal interface) can be observed by visual observation. Rate plots assuming control by mass transport of MnO show remarkable consistency for a variety of droplet sizes and initial MnO concentration. Contrary to these findings changing the starting metallic silicon content of the metal disagrees with mass transport control by MnO; silicon transport in the metal may also impact the rate and control step for the reaction. The curves from Figure 3.3 through Figure 3.11 show that the concentration change of metallic manganese follows neither Equation 3.1 nor 3.2, falling somewhere in between, but that conditions likely to cause a greater deficit in the transport of Mn^{2+} to the interface relative to that of silicon will more closely follow the theoretical SiO curve.

Taken in their entirety the above observations imply some element of mixed control between silicon in the metal and manganese oxide in the slag which may explain the apparent discrepancies between different researchers [6–8]. Initial concentrations are likely to impact the dominant reaction pathway.

These findings are best summarized in Table 3.3 below; all MnO changes are matched with 15wt%Si droplets and all Si changes matched with 15wt%MnO slags. From Figure 3.3 through Figure 3.11 it is possible to compare the measured changes in manganese concentration to the theoretical values that would be obtained through

the SiO₂ or SiO pathways. At a minimum, one mole of silicon will reduce one mole of manganese oxide according to Equation 3.2, and at a maximum one mole of silicon will reduce two moles of manganese oxide according to Equation 3.1. One can calculate the ‘silicon efficiency ratio’ (SER) using Equation 3.7, where *wt%Mn* represents the measured concentration of manganese, *wt%Mn_{SiO}* represents the concentration of manganese assuming all silicon is converted to manganese via Equation 3.2, and *wt%Mn_{SiO₂}* represents the concentration of manganese assuming all silicon becomes silica according to Equation 3.1; all concentrations are taken from the metal.

$$SER = 1 + \left(\frac{wt\%Mn - wt\%Mn_{SiO}}{wt\%Mn_{SiO_2} - wt\%Mn_{SiO}} \right) \quad (3.7)$$

Values of SER calculated using Equation 3.7 are shown in Table 3.3 and follow the trend one would expect given the stated mechanism. High initial MnO content results in a higher initial ratio indicating that Mn²⁺ flux is high and more able to oxidize the available silicon. Low initial silicon similarly results in a slower demand for Mn²⁺. With the noted exception of 10wt%MnO there appears to be a slight downward trend in the efficiency with time, indicating as expected that depletion of Mn²⁺ near the interfaces results in more production of SiO. The other data sets do not show observable trends. From this analysis it appears that the early stages of reaction are dominated by kinetic factors which eventually become somewhat stable and approach a ratio close to the equilibrium of the system; despite differences in the ratio near 300 seconds, eight of the nine systems (with the exception of 10wt%MnO) closely approach their expected equilibrium. The

analysis shows that in order to meet the demands of the mass balance within the system the ratio of [Mn] to [Si] reacted over time must change.

Table 3.3: Silicon Efficiency Ratio for Different Starting Concentrations and Over Time

Initial wt% Slag/Metal	Time (s)					
	5	60	120	180	240	300
10%MnO	1.32	1.34	1.35	1.36	1.36	1.37
15%MnO	1.58	1.57	1.57	1.57	1.57	1.56
20%MnO	1.93	1.90	1.88	1.87	1.86	1.85
5wt%Si	1.94	1.90	1.87	1.85	1.84	1.84
10wt%Si	1.79	1.76	1.74	1.73	1.72	1.71
15wt%Si	1.62	1.61	1.61	1.60	1.60	1.59

A gas layer has been found in almost every experiment carried out. This has not been incorporated into the rate assumptions presented above and is likely also to have complicated the picture, particularly in regard to the effect of temperature on reaction rate. This result implies that mass transport of manganese oxide in the slag might not be the lone rate controlling step in this reaction. Given that all of the data for MnO differences came from droplets with 15wt% starting silicon, it is possible that at lower values of silicon the control shifts away from manganese to silicon instead. Such a result may help explain the issues authors have had explaining the reaction mechanism in the system, ranging from manganese in the metal to manganese or silicon in the slag. Given the apparent gas generation in the system, and the favourability of SiO with temperature, it is possible that higher temperatures result in more gas generation around the interface leading to blocking of the reaction pathways; this is complicated by diffusivity increases in slag with increasing temperature.

One area of concern surrounding the gas is how it affects the volume and area terms employed in any rate equation. For example, assuming that the interfacial area is the slag-metal interface is unlikely to be true if it is partially covered by gas bubbles. Figure 3.22 provides an illustration of how bubbles may impact the area of the reaction interface and thereby rate of reaction. The extent of the bubble layer and the volume of slag between the bubbles may change over time depending on a number of factors, such as temperature and the balance between silicon and manganese oxide transport. A gas layer would be expected to impact the interfacial area in two possible ways: first by taking up space along the interface and preventing the reaction of slag and metal in those areas, as well as forcing all transported material to funnel between the bubbles. Given the spherical geometry, the point where the neck between bubbles is at its narrowest should impact the transport more greatly than coverage of the slag-metal interface. If one considers an imaginary sphere around the metal droplet, separated by one bubble radius from the slag-metal interface this sphere would have a defined area 'A', occupied entirely by slag. Upon the formation of a bubble layer the area occupied by slag would drop reducing the cross-sectional area of the transport path. Assuming the spherical bubbles pack tightly in a hexagonally close packed monolayer would reduce the available transport path by 89%.

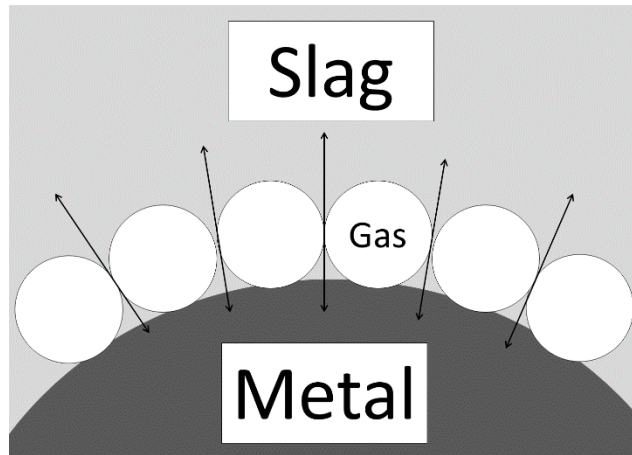


Figure 3.22: Diagram Illustrating how Gas Generation may Affect the Diffusion Pathway and Change both Volume and Area Terms in the Rate Equation

Such an assumption may help to explain what appears to be a dramatic decrease in reaction rate after the first six seconds. Close examination of the plots in Figure 3.3 through Figure 3.11 shows that the y-axis intercept at time equal to zero is always less than zero. This observation implies an early rate much faster than that evident for times greater than 6 seconds may be present. Based on the data available, it is not possible to determine the exact point at which the rate changes but if for the sake of discussion one assumes six seconds we can estimate a slope and therefore a mass transfer coefficient for this very early time period. This process is illustrated in Figure 3.23 as ' $k_{s,0}$ ' plotted alongside the calculated k_s value from Figure 3.15. The mass transfer coefficient calculated based on times greater than six seconds is approximately 11% of the estimated initial slope. The authors are not claiming that the predicted initial mass transfer coefficient can be determined quantitatively but merely propose that it is of the correct order of magnitude to support the idea of blockage of transport paths by a relatively stable bubble film. The slope plotted for time less than six seconds is a very reasonable estimate; these

first few seconds of reaction can account for up to 10% of the total reaction (as is the case with Figure 3.11).

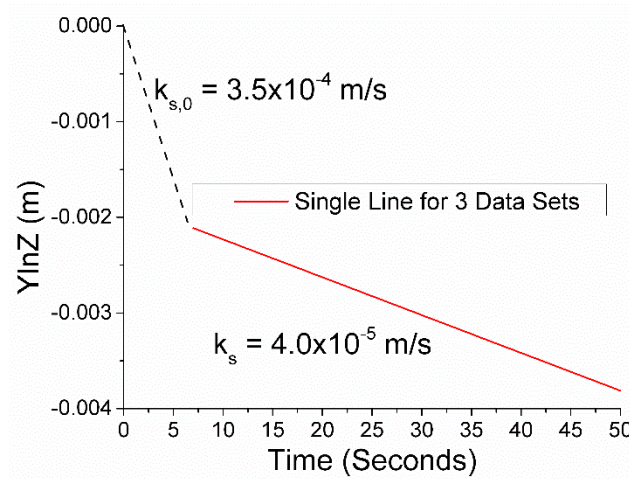


Figure 3.23: Zoomed Version of Figure 3.15 where the Initial Y-Axis Jump is Displayed

The above findings indicate that there are two major areas for future work: derivation of a rate equation involving both manganese oxide transport from the slag and silicon transport from the metal, as well as the incorporation of the change in interfacial area with time. The interfacial area appears to change over a relatively short period of time as the result of a relatively stable bubble film, and once formed does not change much over the course of the reaction.

3.5. Conclusions

1. MnO mass transfer in the slag is the rate controlling step for experiments with 15wt% silicon, the mass transfer coefficient is $4.0 \times 10^{-5} \text{ m/s}$.
2. Decreasing the initial silicon content changes the rate control to mixed control by mass transport of silicon in the metal and mass transport of MnO in the slag.

3. Lowering the temperature appears to increase the reaction rate because of the decreasing favorability of SiO formation at lower temperatures.

3.6. Acknowledgements

The authors thank the National Science and Research Council of Canada for funding support. Special thanks to Arcelor Mittal Dofasco, US Steel Canada, Praxair, and Hatch Ltd. for their in-kind support, technical expertise, and their many helpful discussions.

3.7. References

- [1] Z. H. Cai, H. Ding, X. Xue, and Q. B. Xin: *Mater. Sci. Eng. A*, 2013, vol. 560, pp. 388–95.
- [2] O. S. Bobkova and V. V. Barsegyan: *Metallurgist*, 2006, vol. 50, pp. 463–68.
- [3] L.N. Kologrivova, A.Ya. Nakonechnyi, Z.G. Trofimova, O.V. Nosochenko, and N.N. Kulik: *Metallurg*, 1987, vol. 5, pp. 28–29.
- [4] C.W. Bale, A.D. Pelton, and W.T. Thompson: 2015.
- [5] Jr. M.W. Chase, C.A. Davies, Jr. J.R. Downey, D.J. Frurip, R.A. McDonald, and A.N. Syverud: 1985.
- [6] W.L. Daines and R.D. Pehlke: *Trans. Met. Soc. AIME*, 1968, vol. 242, pp. 565–75.
- [7] Etsuro Shibata, Haiping Sun, and Katsumi Mori: *Metall. Mater. Trans. B*, 1999, vol. 30B, pp. 279–86.

- [8] Jung Ho Heo, Yongsug Chung, and Joo Hyun Park: *Metall. Mater. Trans. B Process Metall. Mater. Process. Sci.*, 2015, vol. 46B, pp. 1154–61.
- [9] H Sohn, Z Chen, and W Jung: *Steel Res.*, 2000, vol. 71, pp. 145–52.
- [10] S.K. Tarby and W.O. Philbrook: *Trans. Metall. Soc. AIME*, 1967, vol. 239, pp. 1005–17.
- [11] W.L. Daines and R.D. Pehlke: *Trans. Met. Soc. AIME*, 1971, vol. 2, pp. 1203–11.
- [12] R J Pomfret and P Grieveson: *Ironmak. Steelmak.*, 1978, vol. 5, pp. 191–97.
- [13] Masahiro Ashizuka, Atushi Moribe, and Kiyoshi Sawamura: *Tetsu-to-Hagane*, 1975, vol. 61, pp. 36–45.
- [14] Kuangdi Xu, Guochang Jiang, Weizhong Ding, Liping Gu, Shuqiang Guo, and Baixiong Zhao: *ISIJ Int.*, 1993, vol. 33, pp. 104–8.
- [15] Ring Kononov, Oleg Ostrovski, and Samir Ganguly: *Metall. Mater. Trans. B Process Metall. Mater. Process. Sci.*, 2008, vol. 39B, pp. 662–68.
- [16] Haiping Sun, M Yaser Lone, Samir Ganguly, and Oleg Ostrovski: *ISIJ Int.*, 2010, vol. 50, pp. 639–46.
- [17] A. Sharan and A. W. Cramb: *Metall. Mater. Trans. B*, 1995, vol. 26B, pp. 87–94.
- [18] H. Gaye, L. D. Lucas, M. Olette, and P. V. Riboud: *Can. Metall. Q.*, 1984, vol. 23, pp. 179–91.
- [19] A. Jakobsson, Du Sichen, S. Seetharaman, and N. N. Viswanathan: *Philos. Trans. R. Soc. Lond. A*, 1998, vol. 356, pp. 995–1001.

- [20] P.V. V. Riboud and L.D. D. Lucas: *Can. Metall. Q.*, 1981, vol. 20, pp. 199–208.
- [21] Y. Chung and A.W. Cramb: *Metall. Mater. Trans. B*, 2000, vol. 31B, pp. 957–71.
- [22] M.A. Rhamdhani, K.S. Coley, and G.A. Brooks: *Metall. Mater. Trans. B*, 2005, vol. 36B, pp. 219–27.
- [23] R J Pomfret and P Grieveson: *Can. Metall. Q.*, 1983, vol. 22, pp. 287–99.
- [24] Y. Chung and A.W. Cramb: *Philos. Trans. R. Soc. A Math. Phys. Eng. Sci.*, 1998, vol. 356, pp. 981–93.
- [25] Jesse F. White and Du Sichen: *Metall. Mater. Trans. B Process Metall. Mater. Process. Sci.*, 2014, vol. 45B, pp. 96–105.
- [26] Andre N. Assis, Jason Warnett, Stephen Spooner, Richard J. Fruehan, Mark A. Williams, and Seetharaman Sridhar: *Metall. Mater. Trans. B*, 2015, vol. 46B, pp. 568–76.
- [27] Stephen Spooner, Andre N. Assis, Jason Warnett, Richard Fruehan, Mark A. Williams, and Seetharaman Sridhar: *Metall. Mater. Trans. B*, 2016, vol. 47B, pp. 2123–32.
- [28] M.A. Rhamdhani: *PhD Thesis - McMaster Univ.*, 2005.
- [29] E. Chen and K. S. Coley: *Ironmak. Steelmak.*, 2010, vol. 37, pp. 541–45.

Chapter 4

4. Kinetic Modelling of the Silicothermic Reduction of Manganese Oxide from Slag

Copywrite & Bibliographic Information

This chapter contains the pre-publication version of “Kinetic Modeling of the Silicothermic Reduction of Manganese Oxide from Slag”. Final version Copyright © 2019 by The Minerals, Metals & Materials Society and ASM International. Used with permission. Complete bibliographic information is shown below.

Authors: Jamieson, B.J.; Tabatabaei, Y.; Barati, M.; Coley, K.S.

Journal: Metallurgical and Materials Transactions B

Year: 2019

Volume: 50

Issue: February

Pages: 192-203

DOI: 10.1007/s11663-018-1437-y

Contributions & Context

This article is a follow up to Chapter 3. The experimental data in the work comes from the previous publication [82]. Nearly 100% of the MatLab coding and data analysis was performed by the primary author. Yousef Tabatabaei was instrumental in the MatLab learning process; if there was a major hurdle Yousef Tabatabaei helped expedite the solution. Discussion of modelling parameters was shared between the primary author and Yousef Tabatabaei. Analysis of the data was

shared between Dr. Coley, Dr. Barati, and the primary author. The manuscript was completed entirely by the primary author.

Where the paper discussed in Chapter 3 shows the experimental data, including observations and a crude analysis, this article is a more fine-tuned analysis of the system. It was obvious from the previous work that gas bubbles played a role obstructing the interface, and the rate determining step of the reaction was not satisfactorily identified. The model studied four transport conditions (silicon and manganese, in either phase) and allowed the possibility that the chemical reaction forming SiO was a potential rate limit. The model further incorporated an instantaneous area change associated with the formation of a gas halo into the calculation.

The model returned a result suggesting that all transporting species were closely linked, and their mass transfer coefficients were nearly identical. A single mass transfer coefficient was justified for slag, k_{Slag} equal to $6.7 \cdot 10^{-4}$ m/s, and a single mass transfer coefficient in the metal, k_{Metal} equal to $2.3 \cdot 10^{-4}$ m/s. These findings were one order of magnitude greater than the value reported in the previous chapter. However, the area modifying parameter was not included in the previous value, thus when this is considered the values in both studies are quite close. A mechanism for the formation and stabilization of SiO gas along the interface was proposed that is supported by qualitative observations from the experimental data. Where previous conclusions suggested MnO mass transport as the rate limiting step, this work suggests counter-current mass transport of all species is necessary.

Kinetic Modelling of the Silicothermic Reduction of Manganese Oxide from Slag

B.J. Jamieson^[1], Y. Tabatabaei^[1], M. Barati^[2], and K.S. Coley^[1]

^[1]McMaster Steel Research Center, McMaster University, Hamilton, L8S 4L8, Canada. Contact coleyk@mcmaster.ca

^[2] University of Toronto, Toronto, M5S 3H7, Canada.

Abstract

A model was developed to describe the mixed rate control kinetics in systems with MnO-SiO₂-CaO-Al₂O₃ slags and Fe-Si metal droplets. During the reaction of Fe-Si droplets and slag, Mn²⁺ transport was found to be part controlling the system but could not sufficiently describe all initial conditions (chiefly, changes to initial silicon content). The current model describes the kinetics of the stated system and offers answers to the question of rate control; the model has been fitted to nine datasets of varying initial conditions including initial [Si], initial (MnO), initial droplet size, and reaction temperature. The fitted mass transfer coefficients for metal and slag were $2.3 \cdot 10^{-4}$ m/s and $6.7 \cdot 10^{-4}$ m/s respectively; these values are constant across nine datasets. Previous claims about the efficiency of silicon usage in reducing manganese have been modified; it appears that the formation of silica is favored throughout the reaction, but that the formation of a silicon monoxide gas layer on the metal surface dramatically impacts the rate of reaction. As a measure of overall fit of the model, the average of the root mean square errors for all datasets is 14%. Mass transport in slag is twice as influential to rate control as the metal phase. The simultaneous transport of both Mn²⁺ and silicate dimers controls mass transport in the slag. Both [Si] and [Mn] can control from the metal side but are dependent on the initial conditions.

4.1. Introduction

The drive to reduce vehicle fuel emissions has created a new era of materials design, requiring stronger and lighter alloys. Light metals like aluminum and magnesium have been investigated and commercialized for some vehicle components, but the steel industry remains competitive with three generations of advanced high strength steels (AHSS). The 1st generation of AHSS offers good strength but relatively poor elongation properties, characteristic of low manganese contents. 2nd generation AHSS has great strength and ductility but has not seen mainstream success because achieving the alloying requirements ($>17\text{wt\%Mn}$) is expensive and causes difficulties with formability. The current focus is 3rd generation (3G) AHSS, which has been defined to contain approximately 3-10wt%Mn [1]. This alloy content is more commercially viable while still offering desirable mechanical properties.

Process improvements beyond traditional ferroalloying are required to improve the economic viability of 3G AHSS; currently only POSCO has managed to commercially produce steel with appreciable quantities of [Mn] [2]. One proposed method of manganese addition is through direct or reductive alloying; manganese ore can be added to slag in-situ and reduced with a reductant such as silicon or coke instead of being added as a ferroalloy [3–6]. The current work seeks to improve the fundamental understanding of the silicothermic reduction process of manganese oxide in a synthetic slag, with anticipated applications to direct alloying. Silicothermic reduction is widely used as the final stage of Argon-Oxygen

Decarburization (AOD) to reclaim chromium that has been oxidized from the slag. As AOD is also a potential route for high manganese steels, the current work may be of interest in that application.

Previous work by two of the current authors [7] showed evidence that the reduction of (MnO) by [Si] was controlled by mass transport in the slag; however this alone did not fully explain the rate control for the system. Hence, it was proposed that [Si] also had an impact on the reduction rate; the assumption that the system was under mixed control will be explored in more detail in this paper.

The body of literature for carbon free silicothermic reduction of (MnO) is small and the findings are somewhat disparate. Daines and Pehlke [8] found the system to be controlled by diffusion of [Mn]. In a study of simultaneous reactions, Shibata *et al.* [9] found that desiliconization and MnO reduction were controlled by mass transport in the metal. Sohn *et al.* [10], with some carbon present in the system, showed the system can be controlled by slag or metal mass transport depending on the partition ratio and slag fluidity. Heo *et al.* [11] extensively reviewed [Si] oxidation and (MnO) reduction and showed that a diverse array of rate controlling steps had been proposed. These workers also included studies for (FeO) containing slags. Their conclusion for [Si] and (MnO) was that mass transport of (SiO₂) was the rate controlling step. Further research exists using carbon as the principal reductant, and similarly the verdict on rate control is mixed though leaned towards chemical reaction control (from CO nucleation) and MnO mass transport [12–16].

The present authors' work [7] suggested that the reaction rate was controlled by a mix of [Si] transport in the metal and (Mn^{2+}) transport in the slag. These conclusions are in line with past findings but are not definitive. Thus, the present work seeks to model the system in a way that would adequately describe the impact of all transport steps on the overall reaction rate.

4.2. Experimental Procedure

The data analyzed in this paper were reported in a previous publication [7] which also included a detailed description of the experimental procedure. For the convenience of the reader, a brief description of the experimental procedure is presented here. A powdered $\text{MnO-SiO}_2\text{-CaO-Al}_2\text{O}_3$ slag of the desired composition was placed in an alumina crucible and raised into the hot zone of a vertical tube furnace. The slag was held for 30 minutes to allow it to melt and homogenize. A Fe-Si metal droplet was held in place above the crucible by a magnet at the top of the furnace, within the argon atmosphere of the furnace but outside the hot zone. To start the experiment the droplet was released by removing the magnet. The metal droplet was delivered to the slag containing crucible through an alumina tube with a small hole in the end which protruded into the hot zone. The hole was sized to ensure the droplet was fully molten prior to dropping into the slag. The zero time for each experiment, considered to be the time when the droplet entered the slag, was determined by viewing the crucible through X-Ray fluoroscopy.

The datasets obtained examined the effect of varying the initial silicon content (5-15wt%), initial MnO content (10-20wt%), initial droplet size (0.5-1.5g), and reaction temperature from 1823-1923K (1550-1650°C).

4.3. Numerical Modelling

4.3.1. Past Findings & Influences

Visual observation of quenched slags, such as presented in Figure 4.1, shows samples taken near three minutes of reaction exhibit a distinct color gradient in the bulk slag surrounding the droplet. Note that the image has been contrast adjusted for the benefit of the reader; these changes do not change the location of the depleted zones. This figure is duplicated from the authors' previous work [7].

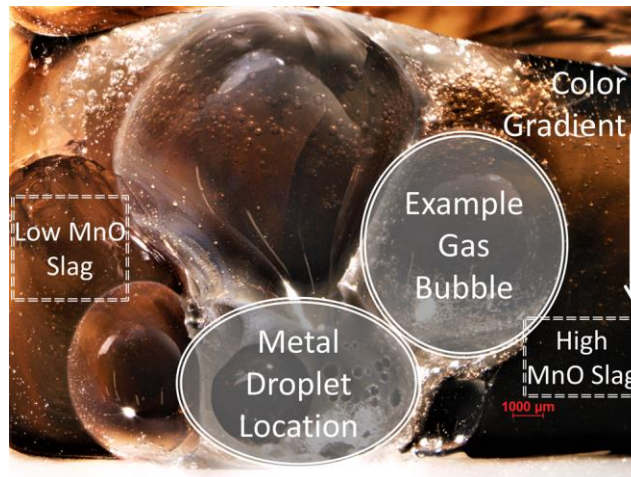


Figure 4.1: Color gradients surrounding the droplet (lower middle of the image) and gas at 185 seconds of reaction; the lightest area is to the left and darkest to the bottom right.
Reprinted from Ref. [7].

Given that MnO is the only species to cause significant pigmentation of the slag, this gradient appears to be related to manganese depletion of the slag adjacent to the droplet and is not found in slags near time zero or slags for which the reaction is close to completion. This was the premise of the qualitative conclusion that the rate was controlled by transport of (Mn^{2+}) in the slag. Exploratory use of Energy

Dispersive Spectroscopy (EDS) in a SEM confirmed that there were manganese gradients near the interface in the slag; small silicon gradients were detected as well. There are reports that silica transport is responsible for rate control [11] thus the mass transport of silica was also analyzed.

The previous analysis [7] of the impact of initial silicon content suggested some contribution of [Si] transport in controlling the rate; past research [8] also suggested [Mn] has a source of rate control. Hence the current work includes all possible transport steps in developing a mixed control model. The current model will also attempt to determine the extent to which each step contributes to the overall rate.

4.3.2. Outline of the Model

The goal of this model is to create an analysis tool to identify the mixed rate control mechanism in the system. The model works independently of these authors' collected data, only using this data to optimize the fitted parameters. Data for the model comes from literature or reasonable assumptions about the system. As part of the investigation, the transport of both metallic manganese and slag silica can impact the system. Figure 4.2 demonstrates the anticipated gradients in the system.

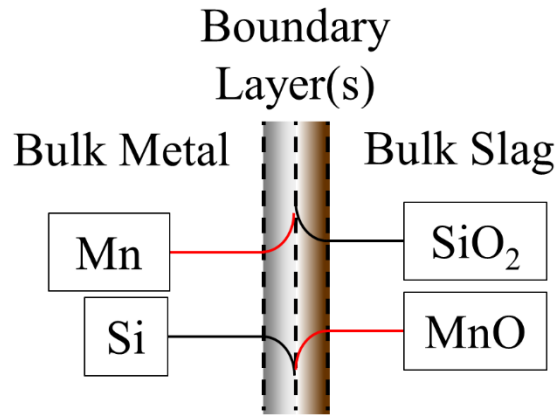


Figure 4.2: Proposed concentration gradients at the interface of the slag-metal couple

In addition to mass transport considerations, the rate of SiO formation must be considered. This brings the total number of fluxes/reaction rate steps to five, documented in Equations 4.1-4.5. These equations represent the change in number of moles with respect to time for Mn, MnO, Si, and SiO₂ as well as SiO. Equation 4.1 considers the mass transport of manganese in the metal. Equation 4.2 considers the mass transport of MnO in the slag. Equation 4.3 considers the mass transport of silicon in the metal. Equation 4.4 considers the mass transport of silica in the slag. Finally, Equation 4.5 characterizes the forward and backward rate of reaction for the formation of silicon monoxide.

For the following equations $\frac{dn^j}{dt}$ is the change in number of moles of species j with respect to the time, k_j is the mass transfer coefficient of species j , A is the interfacial area of the reacting species, C_i^j is the interfacial concentration of species j , and C_b^j is the bulk concentration of species j .

$$\frac{dn^{Mn}}{dt} = k_{Mn} \cdot A \cdot (C_i^{Mn} - C_b^{Mn}) \quad (4.1)$$

$$\frac{dn^{MnO}}{dt} = k_{MnO} \cdot A \cdot (C_i^{MnO} - C_b^{MnO}) \quad (4.2)$$

$$\frac{dn^{Si}}{dt} = k_{Si} \cdot A \cdot (C_i^{Si} - C_b^{Si}) \quad (4.3)$$

$$\frac{dn^{SiO_2}}{dt} = k_{SiO_2} \cdot A \cdot (C_i^{SiO_2} - C_b^{SiO_2}) \quad (4.4)$$

R_{SiO} is the rate of SiO formation (mol/s), k_{fwd} is the rate constant for the forward reaction, and k_{bck} is the rate constant for the backwards reaction; a_i^j is the interfacial activity of species j and the partial pressures of the species are p_j .

$$R_{SiO} = k_{fwd} \cdot a_i^{Si} \cdot p_{O_2}^{0.5} - k_{bck} \cdot p_{SiO} \quad (4.5)$$

To simplify Equation 4.5, k_{bck} can be rewritten equal to the following, where K_{SiO} is the equilibrium constant for the formation of SiO according to the following stoichiometry (Equation 4.6). K_{SiO} is calculated from NIST JANAF tables [17].



The rewritten k_{bck} looks as follows.

$$k_{bck} = \frac{k_{fwd}}{K_{SiO}} \quad (4.7)$$

The five potential points of rate control must be related to one another via a mass balance at any given time step. There are three principle relationships: the manganese balance, silicon balance, and oxygen balance; these are shown in Equations 4.8, 4.9, and 4.10 respectively.

$$0 = \frac{dn^{Mn}}{dt} + \frac{dn^{MnO}}{dt} \quad (4.8)$$

$$0 = \frac{dn^{Si}}{dt} + \frac{dn^{SiO_2}}{dt} + R_{SiO} \quad (4.9)$$

$$0 = \frac{dn^{MnO}}{dt} + \frac{2dn^{SiO_2}}{dt} + R_{SiO} \quad (4.10)$$

By the introduction of an appropriate activity coefficient the activity of silicon in Equation 4.5 can be expressed in terms of mole fraction. Bulk concentration can be rewritten as the bulk moles divided by slag volume at a given time. The interfacial concentration can be rewritten as Equation 4.11, where X_i^j is the mole fraction of species j at the interface and V_i^{phase} is the molar volume of the phase housing species j (which is a weighted average of the partial molar volumes of each species in the phase) calculated at the interface.

$$C_i^j = \frac{X_i^j}{V_i^{phase}} \quad (4.11)$$

Equations 4.8, 4.9, and 4.10 present three independent equations with five unknowns (four interfacial mole fractions and p_{O_2}). Assuming local equilibrium at the interface allows for Equations 4.12 and 4.13 to be included. The data for Equation 4.12 was taken from the FactSage™ [18] database. The data for Equation 4.13 was taken from the NIST JANAF database [17].

$$K_{MnO} = \frac{a_i^{MnO}}{a_i^{Mn} \cdot p_{O_2}^{0.5}} \quad (4.12)$$

$$K_{SiO_2} = \frac{a_i^{SiO_2}}{a_i^{Si} \cdot p_{O_2}} \quad (4.13)$$

With the two equilibrium equations, X_i^{MnO} and $X_i^{SiO_2}$ can be rearranged for and substituted into the system of Equations 4.8 through 4.10 with unknowns X_i^{Mn} , X_i^{Si} , and p_{O_2} . All other variables in the equations can be directly calculated or reasonably assumed between timesteps.

To rewrite all species in terms of manganese or silicon, it is necessary to include the fraction of silicon that reacts to form SiO and the fraction that forms SiO₂. This is done using the Silicon Efficiency Ratio (SER) [7] proposed in the authors' previous work. For 100% silica formation the SER equals 2 and for 100% SiO the SER equals 1. The method used in the current work uses the instantaneous rate of change in manganese and silicon to calculate SER. The relationship between SER and the fluxes of silicon and manganese is presented below as Equation 4.14.

J_j is the flux of species j equal to $\frac{dn^j}{dt \cdot A}$. Given that for both silicon and manganese, the flux J_j is calculated with the same timestep and area, Equation 4.14 can be rewritten as Equation 4.15. The SER is less significant than previously thought.

$$0 = SER \cdot J_{Si} + J_{Mn} \quad (4.14)$$

$$SER = -\frac{dn^{Mn}}{dn^{Si}} \quad (4.15)$$

The activity coefficients for this model have been taken from the work of Lee & Downing [19], who created equations to describe the activity coefficients in quaternary metals composed of Mn-Si-C-Fe and slags of MnO-SiO₂-CaO-Al₂O₃. As will later be shown, these values agree well with the equilibrium values predicted by FactSage™ (using FToxid, FactPS, and FStel databases).

4.3.3. Solution Method

The system thus consists of three equations and three unknowns, which require a simultaneous solution. An implementation of the Newton-Raphson method [20] was used to solve for the mole fractions of each species and p_{O_2} at every timestep. Using the conditions from the previous time step and the solved unknowns, all values at the latter timestep could be updated.

Knowing the change in the number of moles of each species at each timestep, the starting condition of the subsequent timestep can be predicted by adding the change to the previous value. The new molar composition is used to recalculate the total volume of each phase at every timestep.

For the metal droplet, knowing the mass yields the volume of the droplet, which is assumed to be spherical. This assumption allows the calculation of the changing droplet radius and subsequently the droplet surface area. Area modifiers are multiplied into the interfacial area.

4.3.4. Fit Optimization

To select the appropriate mass transfer coefficients for the system a best fit method was applied. The experimental data from previous work [7] was employed. Residuals comparing the experimental data with the model predictions were determined for each data point and the optimum combination of mass transfer coefficients was chosen based on minimizing the residuals for the entire dataset. The residuals were calculated as the difference between the measured weight fraction and modelled weight fraction. Since a best fit for all datasets was sought simultaneously across all 9 datasets, each with their own range of concentrations,

relative residuals (RR) were employed as represented by Equation 4.16 where y_{Meas} denotes the measured weight fraction of a species and y_{Mod} is the simulated weight fraction for the same time of reaction.

$$RR = \frac{y_{Meas} - y_{Mod}}{y_{Mod}} \quad (4.16)$$

With the relative residuals determined, there were two primary error checking modes for minimizing the residuals. The first is the Root Mean Square (RMS) error. The RMS for this model is calculated according to Equation 4.17 and is a standard for checking model predictions against collected data. N is the total number of datapoints in the analyzed set. The sum of squares of each RR is taken from 1 to N . The downside of this parameter is that the importance of outlying data is overestimated which is particularly bothersome in high temperature experiments where N is small.

$$RMS = \sqrt{\frac{\sum_{n=1}^N (RR_n)^2}{N}} \quad (4.17)$$

The Mean Absolute Error (MAE) was also employed. This was calculated using Equation 4.18, which accomplishes the same goal as the RMS but places less value on residuals from outlying data.

$$MAE = \frac{\sum_{n=1}^N |RR_n|}{N} \quad (4.18)$$

The calculated values for RMS and MAE are presented in the top left corner of each of the datasets.

To further compare fit, the standard deviation of the sample (s) is used to calculate the standard error (SE) of the sample mean. These equations are shown in

Equations 4.19 and 4.20 respectively. Once determined the standard error is multiplied by the appropriate t-statistic, the two-tailed 95% confidence interval [21], to compensate for the experimental count.

$$s = \sqrt{\frac{\sum_{n=1}^N (RR_n)^2}{N - 1}} \quad (4.19)$$

$$SE = \frac{s}{\sqrt{N}} \quad (4.20)$$

4.4. Results

4.4.1. Dynamic Area Change

Past work by the authors [7] discussed the impact of gas bubble formation along the reaction interface as a possible obstruction to the overall reaction rate. The bubbles form from the production of SiO gas rather than SiO₂ because of oxygen starvation in the interfacial region. The formation of SiO is well documented in the literature for similar systems [11,22].

The current work indicates that almost all the silicon reacted to form SiO₂ but in the early stages SiO bubbles must have formed. Its formation has a greater impact on the reaction rate by blocking the interface than it does on the overall stoichiometry of the reaction. This process is described in the following figures.

Initially the droplet falls into the slag and reacts across the entire surface; the area of the interface between the droplet and slag is calculated by assuming that the droplet is spherical. However, as is clear from images such as Figure 4.1, the surface does not remain unobstructed for long. The formation of bubbles, which are observed by X-Ray fluoroscopy to remain attached to the droplet, obstructs contact

between the slag and the metal. Using Figure 4.3 as a reference, the triangle represents one unit of initial reaction area of the unobstructed interface. The formation of close-packed spherical bubbles cuts this area by approximately 91%; the remaining 9% of the original unit area is the triple point at the center of the bubbles.

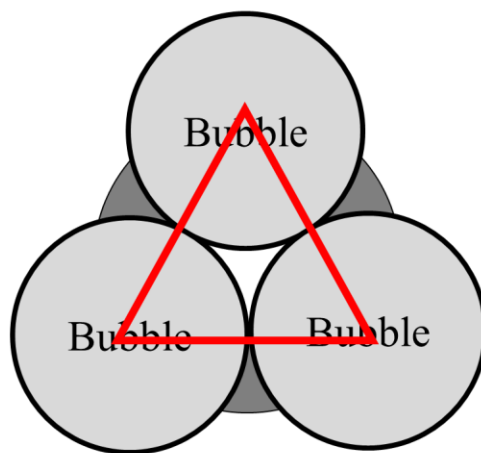


Figure 4.3: Diagram of Close-Packed Spherical Bubbles Obstructing 1 Unit Area of the Interface Representing a 91% Decrease in Effective Mass Transfer Area

The assumption of spherical bubbles comes from Figure 4.4, taken from the authors' previous work, where what appears to be a relatively constant layer of similarly sized bubbles is seen across the surface close to the beginning of the reaction. This figure is duplicated from the authors' previous work [7].

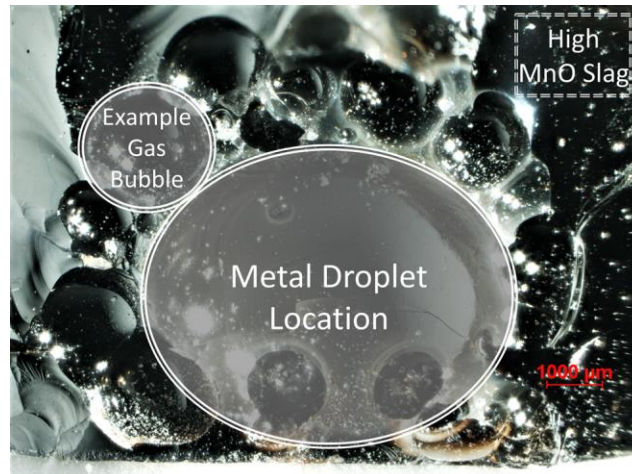


Figure 4.4: Observance of closely sized and spherical bubbles across the metal surface for a sample quenched at 20 seconds. Reprinted from Ref. [7].

This relatively simple analysis of the area reduction offers excellent agreement when viewed alongside a typical kinetic plot such as presented in Figure 4.5; which is similar to the work presented previously [7].

In such plots Z is a normalizing driving force while Y normalizes for mass balance and surface area and depends on the proposed rate determining step. As was noted in the authors' previous work the best fit line in such a kinetic plot is expected to cross through the origin or above zero time. If it crosses through zero it means that there is no reaction at zero. If it crosses above zero it means that there is an incubation time for the reaction. Figure 4.5 shows a line crossing below zero, the implication being that the reaction is much faster during the first few seconds of reaction than after.

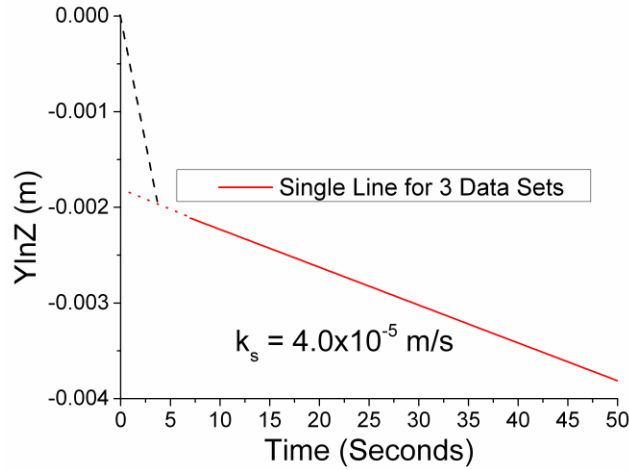


Figure 4.5: Rate Plot Demonstrating the Fitted Data Crossing the y-Axis below Zero Time (Derived Assuming that Manganese Oxide Mass Transport Control was Rate Controlling)

If a line is drawn from zero to near the beginning of the measured line (marked by the dashed line in Figure 4.5) a slope approximately one order of magnitude greater than the experimental data can be obtained. This agrees very well with the theory that the initial reaction period occurs in the absence of gas bubbles and that after a short period SiO bubbles form obstructing approximately 91% of the interface. Thus the solid line of best fit in Figure 4.5 is actually a measurement of the apparent mass transfer coefficient associated with area. The relationship between the unobstructed mass transfer coefficient and the apparent mass transfer coefficient is shown in Equation 4.21. Here the apparent mass transfer coefficient of the slag, k_{slag}^{App} , equals the initial (and real) mass transfer coefficient, k_{slag}^0 , multiplied by the effective area because of bubble blockage, A^{Eff} , divided by the initial area, A^0 .

$$k_{slag}^{App} = k_{slag}^0 \cdot \left(\frac{A^{Eff}}{A^0} \right) \quad (4.21)$$

Based on the foregoing analysis, A^{Eff} is 0.0935 of A^0 . To approximate the time it takes for the bubbles to nucleate and grow sufficiently to obstruct the interface, the intercept between the line plotted for the experimentally determined apparent mass transfer coefficient, and another line plotted from zero using k_{Slag}^0 equal to $k_{Slag}^{App}/0.0935$ (the dashed line of Figure 4.5) was determined. The transition time is approximately 4.5s. The implications of these findings are that after the transition time of 4.5 seconds is reached the model will have an area modifier applied that causes a 90.65 percent reduction in effective reaction area (i.e. $A^0 \cdot 0.0935$); the area remains fixed at this reduced value for the remainder of the reaction time. It is an important note that the k_{Slag}^0 value, representing the *real* mass transfer coefficient of the past work, is close to the values determined in the following analysis.

The stagnancy of the bubbles along the reaction interface contrasts with past workers who found that gas formed and was rapidly removed from the interface. Turkdogan *et al.* [23] studied the reaction of carbon, silicon, and manganese oxide in systems where a metal droplet fell through slag. While the experimental count was limited, they concluded that the fast reaction rates were a consequence of rapid gas mass transport kinetics. They documented that no interfacial expansion was required to achieve the stated reaction rates. Two major differences between the work of Turkdogan *et al.* and the present work are that the metal droplet is falling through slag and that carbon is present. Wu *et al.* [24] studied the transfer of silicon from slag to metal via carbothermic reduction when a metal droplet fell through a

slag column. While the system is different because of the direction of flux of silicon, it presents an interesting comparison as the CO bubbles formed do not inhibit mass transport like SiO does in the present study. The movement of metal through slag, and the high rate of gas generation (which must be much higher than in the current work) lead to enhanced stirring of the slag phase as the bubbles escape and are replenished thus ensuring continuous surface renewal. This is like sweeping SiO from the surface of the metal droplet. Further, in the case of carbon-containing droplets, CO gas may form internally which has been shown in recent work in the authors' laboratory [25,26] to cause very rapid mass transfer. This raises interesting considerations for stirred systems that can sweep the SiO away (such as stirred ladles) where a faster reaction can occur.

4.4.2. Modelling Results

The following figures (Figure 4.6 through Figure 4.14) display the chosen outputs of the modelling efforts. In effect, each plot represents two datasets as silicon and manganese data were measured independently via ICP for metal samples taken at the same time of reaction; there are nine plots and each plot contains data points for silicon and manganese.

Horizontal lines are included in each plot to represent the calculated equilibrium composition from FactSage™; the same initial conditions for the kinetic model are used. The mass transfer coefficients are fixed for all nine plots, where k_{Metal} represents the mass transfer coefficient of both [Mn] and [Si] and k_{Slag} represents (SiO₂) and (MnO) (though in reality both species exist as ions in the melt). The error calculations are shown in the top left of each figure.

All the following plots, including the analysis, were calculated with a 0.2 second timestep. Lowering the timestep further did not yield justifiable accuracy improvements for the increase in computing time.

The “best” mass transfer coefficients were chosen through iterative minimisation of residuals. The chosen values are k_{Metal} of $2.3 \cdot 10^{-4}$ m/s and k_{Slag} of $6.7 \cdot 10^{-4}$ m/s. To reiterate, once fixed, these two parameters reproduce all 18 sets of data within the relative errors presented in Table 4.1. It is interesting to find that k_{Slag} is so large relative to k_{Metal} , however, there are similar systems that have been reported to have large mass transfer coefficients in the slag (discussed below). Efforts have been made to present values in systems with similar ratios of CaO:SiO₂ and temperature.

Several authors have documented mass transfer coefficients slower than the present values. Ashizuka *et al.* [14] determined that in an Si-Fe and C saturated system the rate of reaction was limited by manganese mass transport in the slag, where k_{MnO} was $1.1 \cdot 10^{-7}$ m/s, when the amount of silicon in the metal exceeded 5 weight percent. Tarby and Philbrook [12], studying the carbothermic reduction of MnO, stated the rate control as “the [concurrent] flow of cations and anions from bulk slag to the interface” when the system was not vigorously stirred by CO nucleation, reporting a mass transfer coefficient k_{MnO} of $1.3 \cdot 10^{-6}$ m/s. Iwamasa and Fruehan [27], studying the effects of FeO and Si on desulfurization reported a mixed mass transport controlled system, where k_{Si} was $3 \cdot 10^{-5}$ m/s and k_{FeO} was $2 \cdot 10^{-5}$ m/s.

Other workers have determined mass transfer coefficients more consistent with the current work. Heo *et al.* [11] reported on the silicothermic reduction of MnO from ferromanganese slags and determined the rate controlling step to be mass transport of silica, with a mass transfer coefficient k_{SiO_2} equal to $1.4 \cdot 10^{-4}$ m/s at 1873K (1600°C). Lee *et al.* [28], while studying the aluminothermic reduction of FeO, reported the rate limiting step as mass transport of FeO in the slag with a mass transfer coefficient k_{FeO} of $4.5 \cdot 10^{-4}$ m/s at 1823K (1550°C). Narita *et al.* [29], studying silicon oxidation in hot metal claimed that depending on the amount of FeO in the slag the rate determining step changed. When the amount of FeO in the slag exceeded 40 weight percent the system was controlled by silicon transport in the metal phase; below this value the system is under mixed mass transport control by silicon in the metal and FeO in the slag until the amount of FeO falls below 10 weight percent, where control is fully limited by FeO mass transport. From their data, the mass transfer coefficient of silicon (k_{Si}) is expected to be approximately $6.5 \cdot 10^{-4}$ m/s but depends on the metal mass; no mass transfer coefficient for FeO was listed.

The above is a small sample of the available literature surrounding work like the present study. While the selected slag mass transfer coefficients are high with respect to most literature, they are not outliers.

It should be noted that in some cases the model predicts a final concentration of silicon below the value given by FactSageTM. This falls within the documented RMS error for each case. For example, in Figure 4.6 the difference between

equilibrium and model data is 0.3wt%, which from the equilibrium value is a relative difference of 12.5 percent, falling with the RMS error value of that dataset.

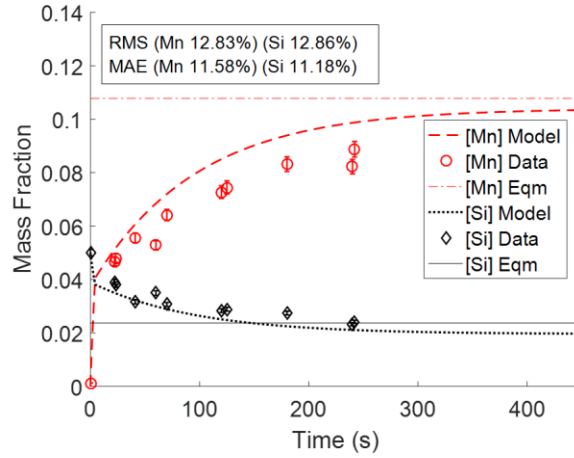


Figure 4.6: Model vs. Dataset 1 for 5wt%Si, 15wt%MnO, 1.5g Droplet, at 1873K (1600°C)

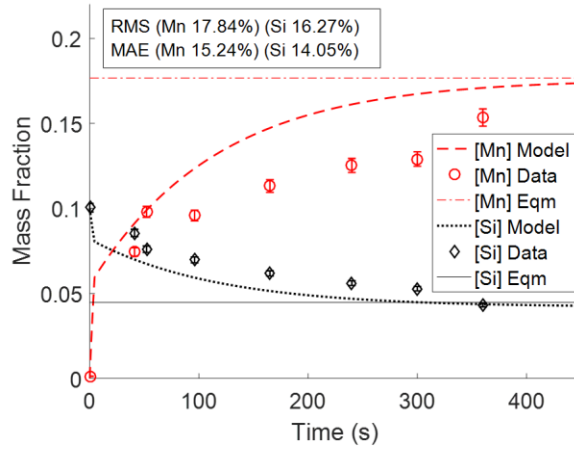


Figure 4.7: Model vs. Dataset 2 for 10wt%Si, 15wt%MnO, 1.5g Droplet, at 1873K (1600°C)

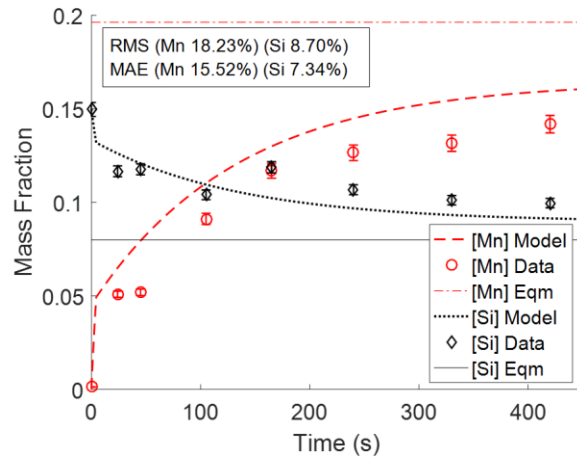


Figure 4.8: Model vs. Dataset 3 for 15wt%Si, 10wt%MnO, 1.5g Droplet, at 1923K (1650°C)

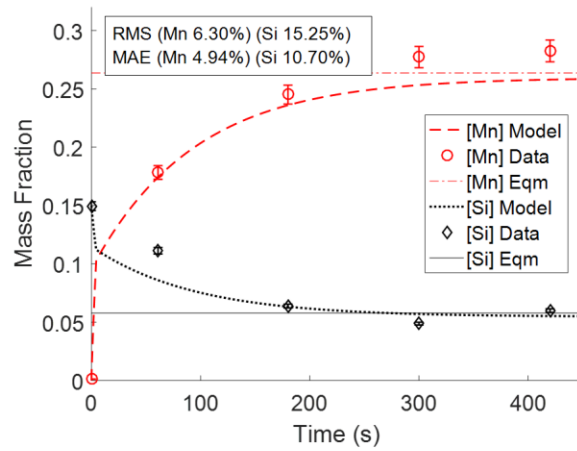


Figure 4.9: Model vs. Dataset 4 for 15wt%Si, 15wt%MnO, 0.5g Droplet, at 1873K (1600°C)

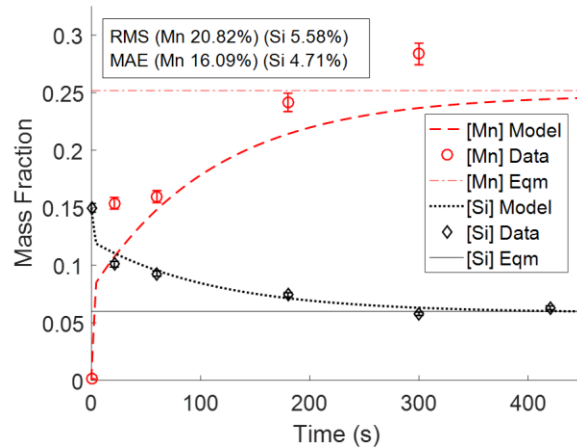


Figure 4.10: Model vs. Dataset 5 for 15wt%Si, 15wt%MnO, 1.0g Droplet, at 1873K (1600°C)

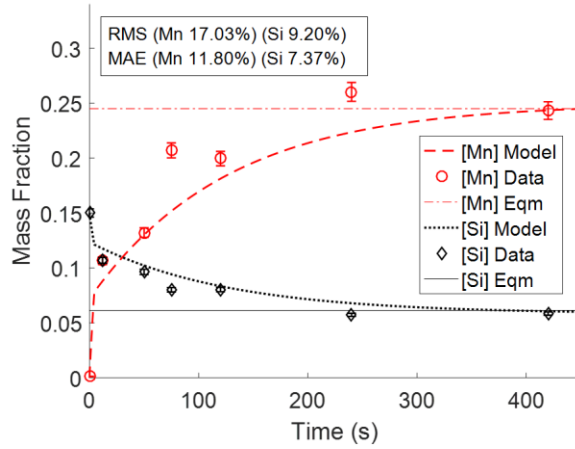


Figure 4.11: Model vs. Dataset 6 for 15wt%Si, 15wt%MnO, 1.5g Droplet, at 1823K (1550°C)

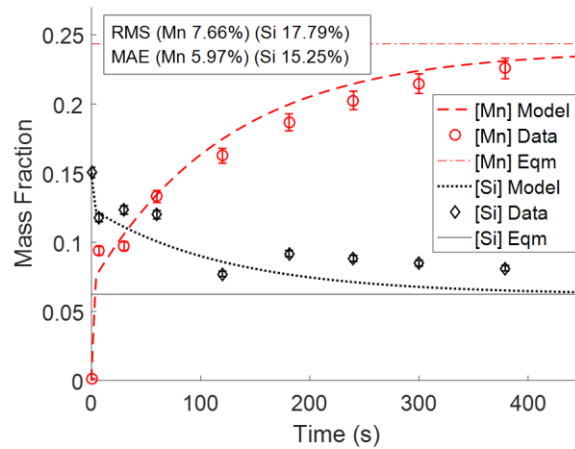


Figure 4.12: Model vs. Dataset 7 for 15wt%Si, 15wt%MnO, 1.5g Droplet, at 1873K (1600°C)

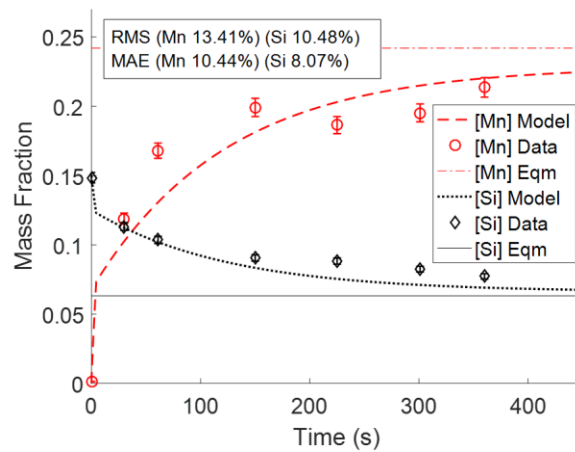


Figure 4.13: Model vs. Dataset 8 for 15wt%Si, 15wt%MnO, 1.5g Droplet, at 1923K (1650°C)

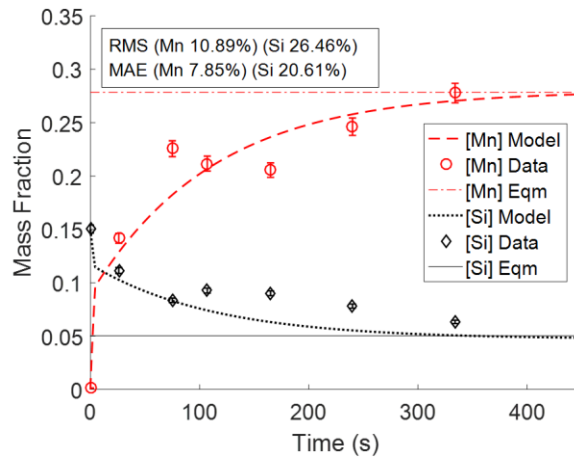


Figure 4.14: Model vs. Dataset 9 for 15wt%Si, 20wt%MnO, 1.5g Droplet, at 1923K (1650°C)

Table 4.1 summarizes the relative residuals associated with the above figures and provides the average for each calculation. As can be seen, while there are a few significant discrepancies for the residual calculation (such as the RMS of silicon in dataset 9), the average RMS is less than 14% and the MAE 11% for both elements. This level of fit is calculated from 18 different sets of data and the precision of chemical analysis is approximately 3.3% for manganese and 2.5% for silicon.

Table 4.1: Residual Error Summary of the Modelled Laboratory Data

Dataset	RMS Mn	RMS Si	MAE Mn	MAE Si
1	13%	13%	12%	11%
2	18%	16%	15%	14%
3	18%	9%	16%	7%
4	6%	15%	5%	11%
5	21%	6%	16%	5%
6	17%	9%	12%	7%
7	8%	18%	6%	15%
8	13%	10%	10%	8%
9	11%	26%	8%	21%
Avg.	14%	14%	11%	11%

Except for Figure 4.8, all the datasets and models show extremely good agreement with equilibrium near 7.5 minutes. By 300 seconds, most of the reaction has been completed which agrees with past claims of approximate desiliconization time [9].

The average standard error for the model's manganese fit is 5.8%; the average error modified for the student's t-distribution is 13.6%. Similarly, average silicon standard error is 5.3% and t-distribution error is 12.6%. Like the residuals, these values can be improved with the elimination of some of the outlying data, but otherwise shows good agreement of model and experimental data.

4.5. Discussion & Sensitivity Analysis

The system shows good agreement with only two fitted mass transfer coefficients. It is interesting to note that despite the rapid exchange of oxygen across the interface no spontaneous emulsification or breakdown of the interface was documented. According to Riboud & Lucas [30] achieving an oxygen transfer rate across the interface of $0.1 \text{ mol/m}^2/\text{s}$ is sufficient to lower the interfacial tension and trigger the spontaneous breakdown of the interface, however this system had rates calculated to be in excess of $2 \text{ moles/m}^2/\text{s}$ before the area change occurred and continued to exceed the cited value until almost 400 seconds. It is possible that the appearance of stable bubbles may obstruct the mechanism of interfacial breakdown in the system. However this could also be compared with other work in the authors' laboratory where in the case of iron carbon droplets reacting with iron oxide slags, very rapid oxygen transfer rates occurred [26,31] but no emulsification was

observed. The commonality of the work of Chen and Coley, Gu *et al.*, and the present work is bubble formation; in the work of Riboud *et al.* there were no gaseous products.

Unfortunately, achieving fit with only two mass transfer coefficients does not aid the identification of the rate controlling step. While it is possible to evaluate the flux of each component independently, the premise of mixed control on which these coefficients were determined ensures that, normalized for stoichiometry, all steps proceed at the same rate. To elucidate more information about the control step, the following sensitivity analyses were performed to test parameter changes against the overall fit change of the system. In theory, the more sensitive the system is to a given change in mass transfer coefficient, the more likely the changed parameter is responsible for controlling the system.

To best compare the sensitivity of the systems the rate of change of average RMS error with respect to change in the multiplier was used. For example, an arithmetic difference of the RMS error at a multiplier of 0.1 compared to a multiplier of 1 may be 130%, which is divided by the multiplier step (i.e. 10) to produce a y-scale value of 13% at a multiplier of 0.1.

4.5.1. Metal vs. Slag Control

To test control by mass transport in the metal versus mass transport in the slag, k_{Metal} was changed while k_{Slag} remained fixed, and then the reverse exercise was performed. Mass transfer coefficient multipliers were varied from one order of magnitude less to one order of magnitude greater than the “best” values. The effect on the rate of change of RMS error when varying each mass transfer coefficient is

shown in Figure 4.15. For a given change in the mass transfer coefficient, the error grows more rapidly when the slag mass transfer coefficient changes suggesting a stronger influence of mass transport control in the slag in controlling the overall rate. A similar analysis plotting the RMS error against the multiplier yields an identical conclusion but offers less distinction between the rate parameters under comparison, therefore we have chosen the rate of change for analysis. The dependent variable is plotted on a logarithmic scale to avoid an asymptotic plot.

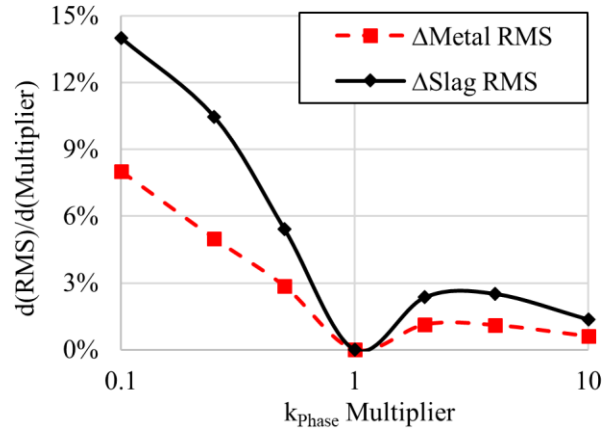


Figure 4.15: Change in RMS Error with Respect to Change in Multiplier Comparing k_{Slag} & k_{Metal}

Along with previous findings, this helps indicate that while the system is under mixed control, mass transport in the slag is relatively more important. Comparing the rate of change of error for the slag versus the metal shows that the effect of a given multiplier when applied to the slag mass transfer coefficient is twice that of the same multiplier applied to the metal mass transfer coefficient.

4.5.2. Individual Species Control

4.5.2.1. k_{Metal}

To confirm whether transport of silicon or manganese was more significant in controlling the rate, the mass transfer coefficients of either species (k_{Mn} and k_{Si}) were varied independently of one another, with a fixed k_{Slag} . Figure 4.16 shows the results of this, using the same axis as Figure 4.15.

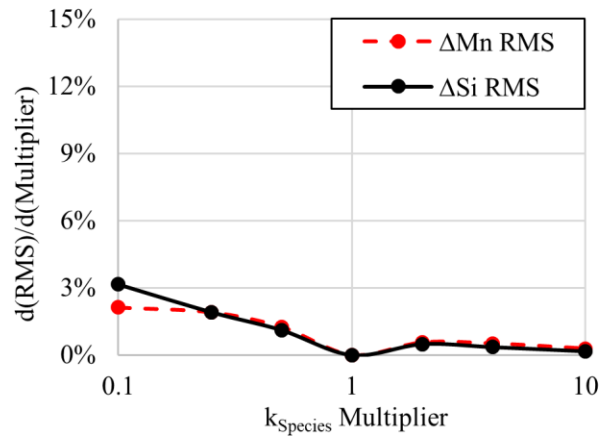


Figure 4.16: Change in RMS Error with Respect to Change in Multiplier Comparing k_{Mn} & k_{Si}

There are two findings from Figure 4.16. The first is that there is no substantial difference when modifying either k_{Mn} or k_{Si} . The second is that relative to Figure 4.15 the change in error is small.

4.5.2.2. k_{Slag}

Figure 4.17 presents the results of comparing the impact of k_{MnO} and k_{SiO_2} with a fixed metal mass transfer coefficient. Modifying the mass transfer coefficient k_{MnO} is more significant to the system than modifying k_{SiO_2} . Like previous findings, Figure 4.17 indicates mass transport control by manganese in the

slag is predominantly responsible for rate control of the system. It is also interesting that most of the change of k_{Slag} in Figure 4.15 can be attributed to modifying k_{MnO} .

There is a significant error associated with changing the mass transfer coefficient of SiO_2 . Specifically, the dotted line regions represent *arbitrary* projections of the MnO and SiO_2 lines because when the mass transfer coefficient of (SiO_2) is less (around 0.25 times) than the mass transfer coefficient of (MnO) the system does not return a solution.

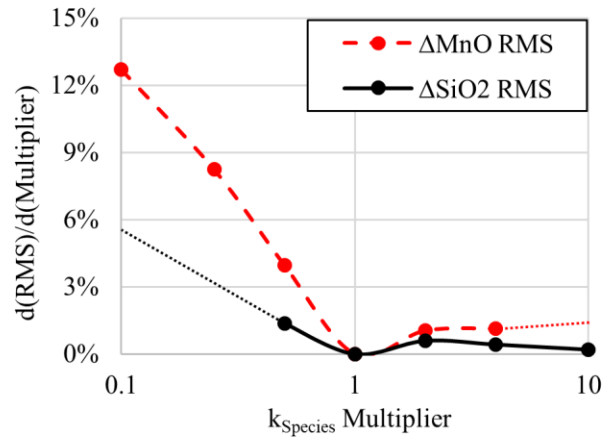


Figure 4.17: Change in RMS Error with Respect to Change in Multiplier Comparing k_{MnO} & k_{SiO_2}

In Figure 4.15 there is no issue when both slag mass transfer coefficients are modified, the lack of solutions only exists when k_{SiO_2} is less than k_{MnO} . Due to the slag's highly acidic nature, it is plausible that very few free oxide ions exist in the slag. Compared to iron oxide slags, where a balance of Fe^{2+} and Fe^{3+} exists which allows for rapid electron transport, manganese almost entirely exists as Mn^{2+} . In the absence of another charge balancing mechanism, it is likely the transport of Mn^{2+} ions will require charge balancing by rearrangement of the silicate structure. Whilst

this may be expected to be a slow process, the experimentally determined mass transfer coefficient is at the higher end of similar measurements reported in the literature. Equally, transport of complex silicate ions in the slag will require similar charge balancing.

Such an explanation helps to explain part of the historical discrepancies in the literature [8–11,14]: not only is the system mix controlled between phases but also between species within each phase.

4.5.3. Bubble Layer Transition Time

The time at which the bubble layers grows sufficiently to block the rate of reaction was tested. As a reminder, 4.5 seconds was the selected time for the model. Figure 4.18 shows the impact of changing the time for the area change associated with the bubbles presented as the arithmetic change in percent from the “best” value. Except for times near zero (which are simply wrong as they would need an overall slower mass transfer coefficient) these errors are relatively small compared to modified mass transfer coefficients.

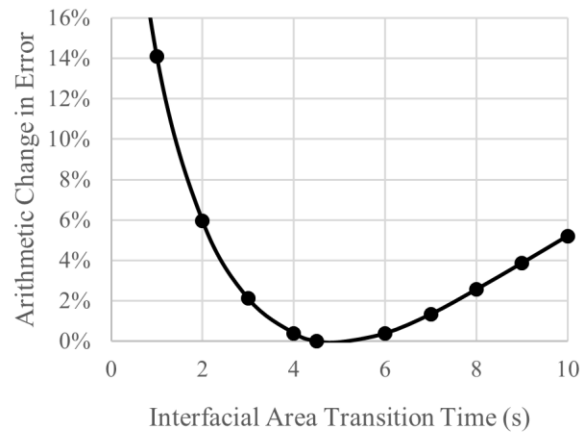


Figure 4.18: Impact of Bubble Blocking Effect on Arithmetic Difference of Average RMS Error

Figure 4.19 shows what happens when the bubbles are not allowed to generate. A reasonable fit can be achieved in the later stages of reaction but without the initial critically fast rates of reaction the initial data points cannot be fitted well. This fit was obtained assuming that the mass transfer coefficient was the best fit values multiplied by the area modifier for the entire length of reaction; the corresponding area adjusted plot is Figure 4.12. While good fit is achieved near the end of the model the initial points are poorly matched.

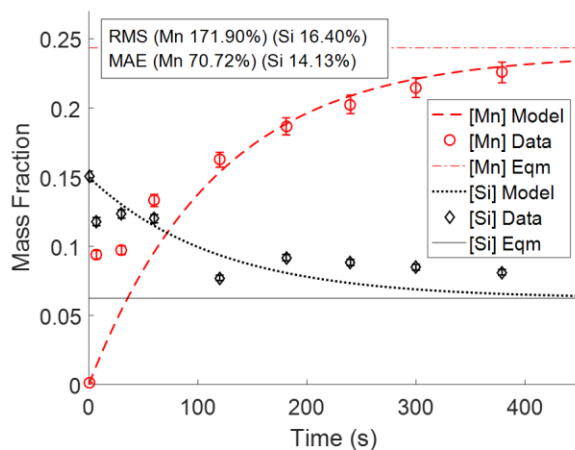


Figure 4.19: Example Model without Including the Change in Area Associated with Bubble Formation

4.5.4. Impact of the Rate Constant for SiO Formation, k_{fwd}

The above calculations were carried out with a rate constant of $5 \cdot 10^{-4}$ mol/s. Modifying this value by an order of magnitude or more appeared to have little effect on the system. Further, calculations of SER (as will be documented) did not support the idea that much SiO was present.

This value is essentially insignificant but SiO formation must be considered important because of its role in forming bubbles on the surface.

4.5.5. Findings on SER & Gas Stability

It was previously discussed how it seemed probable for the SiO to be part of the stoichiometric balance in the system. The findings of the model, as well as the findings on k_{fwd} indicate that this hypothesis may be false. Within the documented error, it is possible to fit the system without gas formation becoming a significant part of the equation. *Physically*, the formation of gas bubbles is very important, but the overall mole balance does not appear to be affected. The value can be manually

adjusted for testing purposes, but at best improves the fit of only silicon by less than one percent relative.

The stability of the gas phase along the interface may be partially attributable to a rapid change in viscosity along the interface. The polymerization of silicates is generally well understood in slag systems [32,33]. The initial values of the slag indicate an optical basicity near 0.68 and V Ratio of approximately 1. Using interfacial mole fraction data from the model to redo these calculations produces values of 0.64 and approximately 0.8. Further, comparing the moles of oxygen present with respect to silicon at these two times indicates that the slag changes from an O/Si ratio of 4 to near 2.5. This indicates that the slag transitions from a monomer/dimer structure to nearly all dimers close to the interface. The viscosity may rise by a factor of five or more because of these composition changes. Since all systems will have some variations in the initial chemistry and subsequently the chemistry during reaction, these viscosity changes may further influence mass transport in the system. Higher viscosities should result in slower mass transfer coefficients on an individual basis.

With this knowledge it is possible to formulate a qualitative argument for the reaction mechanism by considering the ionic nature of slags; Equations 4.22 to 4.24 describe the cation and anion balance for the critical species participating in the reaction. At the beginning of the experiment, there is sufficient interfacial concentration for Equations 4.22 and 4.23 to proceed in balance with each other. When two Mn^{2+} ions reach the interface they can accommodate four electrons,

which balances the decomposition of silicon into Si^{4+} . As the reaction proceeds reactants become depleted at the interface; because mass transport of Mn^{2+} is slow relative to silicon the balance cannot be maintained and is accommodated by Equation 4.24. This explains the formation of SiO , which while thermodynamically less favorable than SiO_2 forms to maintain the charge balance.



The imbalance of Mn^{2+} and silicon transport to the interface is sufficiently small that only small molar quantities of SiO form over the course of the reaction. However, the formation of SiO bubbles remains sufficient to inhibit the overall reaction by blocking the surface.

4.6. Conclusions

The silicothermic reduction of manganese oxide has been studied by developing a balanced flux model considering the mass transport of manganese and silicon in the metal, manganese oxide and silica mass transport in the slag, and the rate of silicon monoxide formation. Data from the authors' lab was tested such that changes in initial silicon concentration, initial manganese oxide concentration, metal droplet size, and reaction temperature were considered. The reaction occurred in two stages, the first one order of magnitude faster than the second which corresponded perfectly with the formation of a stable gas film on the reaction interface that slowed the reaction. Mass transfer coefficients for the metal species,

k_{Metal} , and for the slag species, k_{Slag} , were determined by minimization of residuals. Even though silicon monoxide forms it does not impact the overall stoichiometry of the reaction, as the model shows that within the established error the reduction of manganese oxide has a 2:1 ratio with silicon oxidation. A sensitivity analysis was performed to test for the rate controlling mechanism.

- 1) The mass transfer coefficient in the slag, k_{Slag} , was determined to be $6.7 \cdot 10^{-4}$ m/s. Manganese oxide mass transport is more influential on the reaction (per the sensitivity analysis) and is likely responsible for control in the slag.
- 2) The model cannot generate a solution when the mass transfer coefficient of silica, k_{SiO_2} , becomes less than $\frac{1}{4}$ the mass transfer coefficient of MnO, k_{MnO} . While there is evidence that mass transport in the slag is controlled by manganese oxide, charge neutrality requirements may mean that silica also plays a role in controlling the overall rate of reaction.
- 3) The mass transfer coefficient in the metal, k_{Metal} , was determined to be $2.3 \cdot 10^{-4}$ m/s. There does not appear to be a major difference in influence between silicon and manganese in the metal; both species are responsible for mass transport control in the metal.
- 4) Changing k_{Slag} is twice as impactful on the fit of the model as changing k_{Metal} . This indicates that findings regarding the slag being more responsible for the overall rate control of the system are correct.
- 5) The rate of reaction is initially very fast when slag and metal are in complete contact but is slowed by approximately one order of magnitude upon the

formation of a stagnant bubble layer. Simple geometric calculations show that the area blocked by the bubbles is exactly 90.35 percent corresponding with the stated decrease in rate of reaction.

- 6) Past authors who noted bubble formation in systems where the metal droplet fell through slag demonstrated that the bubbles were rapidly shed. The obvious difference between studies is agitation of the bubbles by droplet movement; in stirred or otherwise dynamic systems the interface is unlikely to be impacted by bubble blockage.

4.7. Acknowledgements

The authors thank the National Science and Research Council of Canada (NSERC, STPGP463252-14) for funding support. Special thanks to ArcelorMittal Dofasco, Stelco, Praxair, and Hatch Ltd. for their in-kind support, technical expertise, and their many helpful discussions.

4.8. References

- [1] Y.K. Lee and J. Han: *Mater. Sci. Technol.*, 2015, vol. 31, pp. 843–56.
- [2] G. Kim, S.K. Kim, S.C. Kang, and I.R. Sohn: *CAMP-ISIJ2*, 2008, vol. 21, p. 593.
- [3] O.S. Bobkova and V.V. Barsegyan: *Metallurgist*, 2006, vol. 50, pp. 463–68.
- [4] L.N. Kologrivova, A.Ya. Nakonechnyi, Z.G. Trofimova, O.V. Nosochenko, and N.N. Kulik: *Metallurg*, 1987, vol. 5, pp. 28–29.

- [5] O.I. Nokhrina, V.P. Komshukov, and V.I. Dmitrienko: *Metallurgist*, 2004, vol. 48, pp. 264–65.
- [6] M. Eissa, H. El-Faramawy, and G. Farid: *Steel Res.*, 1998, vol. 69, pp. 373–80.
- [7] B.J. Jamieson and K.S. Coley: *Metall. Mater. Trans. B*, 2017, vol. 48, pp. 1613–24.
- [8] W.L. Daines and R.D. Pehlke: *Trans. Met. Soc. AIME*, 1968, vol. 242, pp. 565–75.
- [9] E. Shibata, H. Sun, and K. Mori: *Metall. Mater. Trans. B*, 1999, vol. 30B, pp. 279–86.
- [10] H. Sohn, Z. Chen, and W. Jung: *Steel Res.*, 2000, vol. 71, pp. 145–52.
- [11] J.H. Heo, Y. Chung, and J.H. Park: *Metall. Mater. Trans. B Process Metall. Mater. Process. Sci.*, 2015, vol. 46B, pp. 1154–61.
- [12] S.K. Tarby and W.O. Philbrook: *Trans. Metall. Soc. AIME*, 1967, vol. 239, pp. 1005–17.
- [13] R.J. Pomfret and P. Grieveson: *Ironmak. Steelmak.*, 1978, vol. 5, pp. 191–97.
- [14] M. Ashizuka, A. Moribe, and K. Sawamura: *Tetsu-to-Hagane*, 1975, vol. 61, pp. 36–45.
- [15] K. Xu, G. Jiang, W. Ding, L. Gu, S. Guo, and B. Zhao: *ISIJ Int.*, 1993, vol. 33, pp. 104–8.

- [16] H. Sun, M.Y. Lone, S. Ganguly, and O. Ostrovski: *ISIJ Int.*, 2010, vol. 50, pp. 639–46.
- [17] Jr. M.W. Chase, C.A. Davies, Jr. J.R. Downey, D.J. Frurip, R.A. McDonald, and A.N. Syverud: *NIST Stand. Ref. Database 13*, 1985, vol. 1.
- [18] C.W. Bale, E. BÉlisle, P. Chartrand, S.A. Decterov, G. Eriksson, A.E. Gheribi, K. Hack, I.H. Jung, Y.B. Kang, J. Melançon, A.D. Pelton, S. Petersen, C. Robelin, J. Sangster, and M.A. Van Ende: *Calphad*, 2016, vol. 54, pp. 35–53.
- [19] Y.E. Lee and J.H. Downing: *Can. Metall. Q.*, 1980, vol. 19, pp. 315–22.
- [20] A. Gilat and V. Subramaniam: *Numerical Methods for Engineers and Scientists: An Introduction with Applications Using MatLab*, John Wiley & Sons, Inc., 2008.
- [21] NIST/SEMATECH: *E-Handb. Stat. Methods*, 2013, pp. 1–4.
- [22] W. Ding and S.E. Olsen: *ISIJ Int.*, 2000, vol. 40, pp. 850–56.
- [23] E.T. Turkdogan, G.J.W. Kor, and R.J. Fruehan: *Ironmak. Steelmak.*, 1980, vol. 7, pp. 268–80.
- [24] A. Wu, P.C. Hayes, and H.G. Lee: *ISIJ Int.*, 1998, vol. 38, pp. 213–19.
- [25] K. Gu, N. Dogan, and K.S. Coley: *Metall. Mater. Trans. B Process Metall. Mater. Process. Sci.*, 2017, vol. 48, p. 3408.
- [26] K. Gu, N. Dogan, and K.S. Coley: *Metall. Mater. Trans. B Process Metall. Mater. Process. Sci.*, 2018, vol. 49, pp. 1119–35.

- [27] P.K. Iwamasa and R.J. Fruehan: *Metall. Mater. Trans. B Process Metall. Mater. Process. Sci.*, 1997, vol. 28, pp. 47–57.
- [28] J. Lee, J.S. Oh, and J. Lee: *Jom*, 2016, vol. 68, pp. 2359–64.
- [29] K. Narita, T. Makino, H. Matsumoto, A. Hikosaka, and J. Katsuda: *ISIJ*, 1983, vol. 69, pp. 1722–29.
- [30] P.V.V. Riboud and L.D.D. Lucas: *Can. Metall. Q.*, 1981, vol. 20, pp. 199–208.
- [31] E. Chen and K.S. Coley: *Ironmak. Steelmak.*, 2010, vol. 37, pp. 541–45.
- [32] M.D. Dolan and R.F. Johnston: *Metall. Mater. Trans. B Process Metall. Mater. Process. Sci.*, 2004, vol. 35, pp. 675–84.
- [33] I. Sohn and D.J. Min: *Steel Res. Int.*, 2012, vol. 83, pp. 611–30.

Chapter 5

5. Kinetics of the Carbothermic Reduction of Manganese Oxide from Slag

Copywrite & Bibliographic Information

This chapter contains the pre-publication version of “Kinetics of the Carbothermic Reduction of Manganese Oxide from Slag”. The manuscript has been submitted to Materials & Metallurgical Transactions B; permissions will be sought like those for Chapter 3 and 4. Available bibliographic information is shown below.

Authors: Jamieson, B.J., Barati, M., Coley, K.S.

Journal: Metallurgical and Materials Transactions B

Manuscript Number: E-TP-19-153-B

Year: 2019

Contributions & Context

This article is like Chapter 2 and presents many qualitative findings found during the experimental investigation of the carbothermic reduction of manganese oxide from slag. All experimental data was collected by the primary author. All data analysis and manuscript drafting was completed by the primary author. Discussions were shared between the primary author, Dr. Barati, and Dr. Coley.

Unlike the silicothermic reduction system, a library of past literature exists studying the carbothermic reduction of manganese oxide from slag. Ultimately, despite the strong documentation, a similar problem appears to exist within the carbothermic literature as it does with silicon: despite apparently similar systems a variety of rate controlling mechanisms have been proposed. Some of the earliest

work was performed by Tarby and Philbrook [28] as well as Pomfret & Grieveson [83] who both claimed that the system was rate limited by transport of manganese oxide in the slag; despite a temperature difference of 125°C these authors reported a mass transfer coefficient k_{MnO} of approximately $5 \cdot 10^{-6}$ m/s. An alternate proposal was presented by Daines and Pehlke [29] who claimed the system was chemical reaction rate limited where k_{Rxn} was approximately $5 \cdot 10^{-8}$ m/s.

This work sought to find an explanation for these rate discrepancies. The results are largely qualitative but may explain why so many different authors have identified different reaction mechanisms as the rate controlling step. Three unique stages of reaction have been presented through a combination of rate data, X-Ray fluoroscopy, and quenched sample imaging. Each stage has no less than two potential rate controlling mechanisms. The system moves through stages and appears to change its rate limiting step throughout the process. In this light, it becomes clearer why many different authors have proposed a variety of mechanistic rate limits in these processes.

Kinetics of the Carbothermic Reduction of Manganese Oxide from Slag

B.J. Jamieson^[1], M. Barati^[2], and K.S. Coley^[1]

^[1]McMaster Steel Research Center, McMaster University, Hamilton, L8S 4L8,
Canada. Contact coleyk@mcmaster.ca

^[2] University of Toronto, Toronto, M5S 3H7, Canada.

Abstract

Experiments were performed using a range of test conditions to elucidate the rate controlling step during the reaction of liquid iron-carbon droplets and slags containing manganese oxide. Four conditions were tested in the system: initial MnO content in the slag (5, 10, and 15 wt pct), initial carbon content of the metal (1, 2.5, 4.3 wt pct), initial droplet mass (0.5, 1.0, and 1.5g), and reaction temperature (1823K [1550°C], 1873K [1600°C], and 1923K [1650°C]). Data was collected using the Constant Volume Pressure Increase (CVPI) technique which tracked the continuous pressure increase in the sealed furnace over time. Samples were quenched at the end of each experiment and chemistry was checked using LECO Carbon Analysis and ICP for manganese. The rate of reaction can be broken into a faster initial period related to internal CO formation, and a slower second reaction controlled by a complex mechanism involving transport of oxygen from slag to metal via CO₂ and decomposition of the CO₂ at the gas-metal interface.

5.1. Introduction

Past studies [1,2] by the authors on the silicothermic reduction of MnO from slag were conducted to better understand the reduction mechanism and provide data to support direct or reductive alloying as a method for manganese addition to 3rd Generation Advanced High Strength steels (3G AHSS). Should direct alloying processes prove feasible for material addition, an opportunity exists for significant economic improvements related to the production of the 3G AHSS [3].

Direct or reductive alloying is a proposed method of alloying element addition to steel; in the current case manganese ore can be added to slag in-situ and reduced with reductants such as silicon or carbon [4–7]. Such additions avoid (or offset) ferroalloy requirements saving producers the need to purchase finished product to add in the ladle.

The current work addresses the fundamental reduction process of MnO by high carbon iron. Previous work by two of the current authors [1] showed evidence that the reduction of (MnO) by [Si] was under mixed mass transport control in the regime of study; the greatest contributor to transport resistance was MnO mass transport in the slag however this alone did not fully explain the rate control for the system. It was proposed that [Si] transport in the metal also had an impact on the reduction rate.

In contrast to the authors' past work, the carbothermic reduction of MnO is a much more widely studied topic than that of silicothermic reduction. However, across a wide range of studies there is significant variation in the described

mechanism for the reaction. Some authors have concluded that chemical reaction controls the rate [8–11]. Others provided evidence of control by mass transport of manganese ions in the slag [12–14]. Another group of authors analyzed the systems assuming mixed mass transport control of manganese in the metal and manganese ions or oxygen in the slag [15–17]. All authors ultimately provided evidence for their assumed controlling step. All studies were conducted using experiments where a layer of slag rests atop a layer of metal, and with a greater metal volume than slag volume.

The goal of the present study is to document the rate of reduction of MnO by carbon dissolved in liquid iron droplets. Compared to past literature, where flat bath experiments are more representative of reactions occurring directly between the metal bath and slag layer of a reactor, the present study represents metal droplets ejected into bulk slag and slag foam. Further, findings here will be compared to past work by the authors on the silicothermic reduction of MnO from slag in order to make processing recommendations for the production of the 3G AHSS.

5.2. Experimental Procedure

5.2.1. Material & Preparation

Iron carbon droplets were prepared from high purity electrolytic iron and electrode graphite. The electrolytic iron has been measured with a LECO carbon-sulfur analyzer and contains 0.0047 ± 0.0010 wt pct carbon and 0.0032 ± 0.0025 wt pct sulfur. The iron also contains 0.016 ± 0.005 wt pct Mn and 0.072 ± 0.022 wt pct Si. The electrode graphite is 6N purity. The materials were weighed to achieve the composition targets for the specific experiment and melted using a welding arc

melter. The partial pressure of oxygen within the arc melter was less than $4 \cdot 10^{-10}$ atm and produced metal droplets with less than 50ppm oxygen [18].

Slag component purity is presented in Table 5.1. Slag samples were prepared by weighing out an appropriate mass of MnO and mixing with a 2:2:1 weight ratio of SiO₂:CaO:Al₂O₃; total slag mass was 25g for all experiments. Once combined, the oxide powders were vigorously shaken until the solids were well mixed. To validate this method, unreacted (but molten) slag samples were quenched and broken apart. Shards of the sample were analyzed using Inductively Coupled Plasma Optical Emission Spectroscopy (ICP-OES); the tested slag pieces varied by less than ± 0.5 wt pct MnO.

Table 5.1: Chemical Composition of Slag Components

Component	Primary wt pct	Carbon wt pct
Silica Sand	99.8	0.00605
Aluminum Oxide	99.5	0.00322
Calcium Oxide	>96	0.1862
Manganese Oxide	99	0.00371

5.2.2. Equipment

A standing vertical tube furnace with attached pressure transducer was used for the experiments; a schematic is provided in Figure 5.1. All ceramics used were 99.8% alumina. The system is heated with molybdenum disilicide heating elements. The base of the furnace can be detached in order to load slag filled crucibles; these crucibles must be raised up to the hot zone of the furnace over the course of one hour to ensure that the crucible does not crack. The hot zone of the furnace is between the X-Ray viewing windows and is checked regularly to ensure there is no drift; the hot zone has less than a ± 1 K (1°C) temperature difference across a 3cm

height and less than $\pm 10\text{K}$ (10°C) across 10cm. With Type-B thermocouples, at 1600°C the error associated with the temperature readout is $\pm 8\text{K}$ (8°C); the thermocouples are checked regularly with a calibrated thermocouple to account for any drift.

At the base of the furnace, below the lower water-cooling cap and gas inlet, is a cooling column wrapped in a copper coil circulating cool water. The temperature within the cooling column is approximately 363K (90°C). This region ensures that when quenching of the sample occurs a large temperature gradient is achieved from hot zone to cool region.

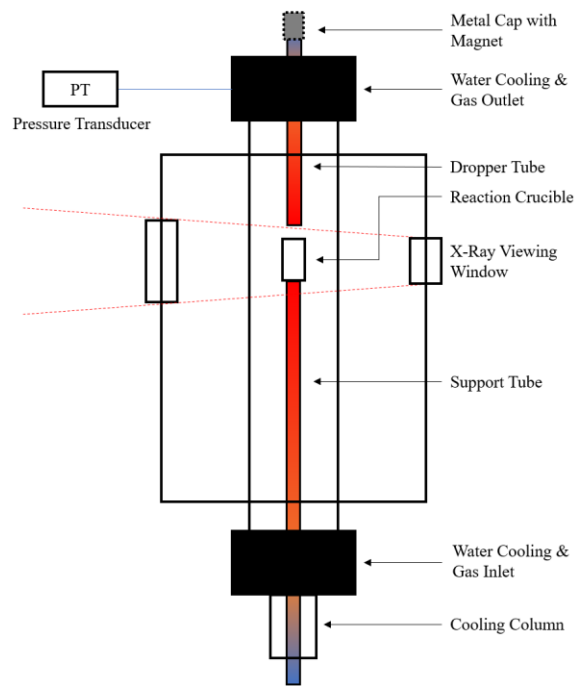


Figure 5.1: Schematic diagram of vertical tube furnace, not to scale.

At the top of the furnace is a metal cap which holds the metal droplet outside of the hot zone of the furnace until the experiment begins; the droplet shares the sealed atmosphere of the furnace. Prior to raising the crucible, the system is

vacuumed to remove most of the gas, then backfilled with high purity (5N) argon. While heating the system it is continually purged with argon to maintain a low oxygen content in the furnace.

An X-Ray fluoroscope surrounds the furnace such that a video can be taken of the experiment. X-Ray imaging shows density differences between slag, metal, and the surroundings and allows for some degree of physical characterization of the reaction over time. Further, X-Ray imaging allows for accurate determination of the reaction start time.

The pressure transducer continually tracks pressure change within the sealed furnace. Pressure change can be used to calculate the number of moles of gas produced using a calibration conducted prior to each experiment. The conversion method will be discussed in the procedure.

5.2.3. Procedure

To begin the procedure, the support tube is removed by unscrewing the fastener at the cooling column base. The slag sample (inside the reaction crucible) is loaded onto the platform and support tube and the base is fastened back on. The crucible is now within the cooling column in Figure 5.1, just below the lower water cooler). The metal cap above the furnace is unscrewed and a metal droplet is loaded in, secured with a magnet. The cap can be screwed back onto the dropper tube thus sealing the furnace. The furnace is vacuumed and then the system is backfilled with argon. Once the pressure is equalized the exhaust is opened allowing for a continual argon flush.

Over the course of approximately 1 hour the crucible is raised into the hot zone of the furnace. Once the crucible is in position a timer is started to ensure that the slag is well homogenized (approximately 30 minutes).

In final preparation for the experiment, the inlet argon and exhaust are closed so that any CO gas generated during the reaction will register on the pressure transducer. To start the experiment the magnet on the upper cap is removed and the droplet falls to the base of the dropper tube. The base of the dropper tube has a hole which is too small for the solid droplet to pass prior to melting; it takes approximately 30 seconds for the droplet to melt and fall into the crucible.

Using X-Ray imaging, the zero time of the experiment occurs when the metal droplet contacts the slag; the droplet immediately sinks to the bottom of the crucible. The reaction is observed and tracked with video and Constant Volume Pressure Increase (CVPI) for approximately 20 minutes. After this time the support tube is released from the furnace, quenching the reaction crucible and ensuring the chemistry at the time of quench is locked for LECO and ICP analysis.

Prior to vacuuming the system, while a crucible is at the base of the cooling column, the system is calibrated to obtain the conversion factor for pressure to moles. Three known volumes of room temperature air are injected into the hot furnace; the air volume can be converted to moles which do not change with temperature. This conversion is used to convert continuously recorded pressure data from each experiment into moles of gas produced. Metal droplets are extracted from the slag and used for carbon analysis with LECO or Mn/Si analysis using ICP.

5.3. Results

5.3.1. Observations of CO Evolution

Figure 5.2 shows how droplet composition changes with time, based on the chemical analysis of quenched droplets; the conditions were 2.5 wt pct carbon in a 1.5g metal droplet, 15 wt pct MnO, and at 1823K (1550°C). The figure presents data for metallic manganese measured by ICP, metallic silicon measured by ICP, CO calculated under the assumption that all Mn and Si added to the metal are a result of carbon oxidation, and CO calculated from the measured change in carbon (measured by LECO). Further, the gas evolution as monitored with the CVPT is overlaid on the plot.

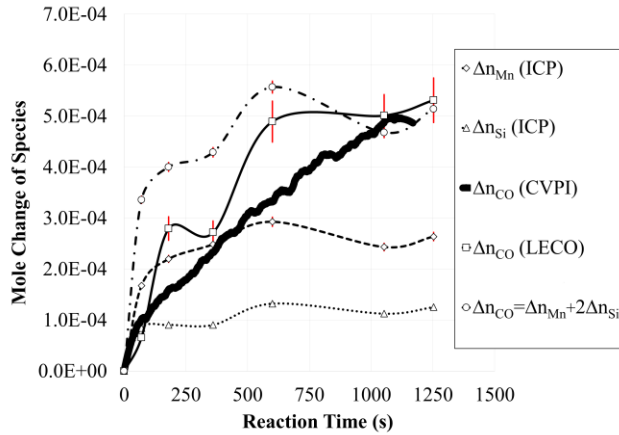
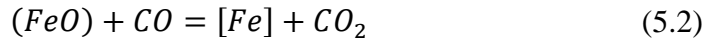
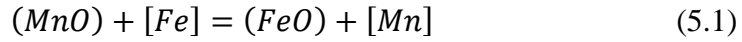


Figure 5.2: Change in moles of [Mn], [Si], and CO gathered through individual quenching experiments for a series of reactions with identical starting conditions (2.5 wt pct C, 15 wt pct MnO, 1823K (1550°C), and 1.5g droplet)

The plot shows there is a fast reaction during the first 100 seconds and then a significantly slower reaction follows; the system appears to reach complete equilibrium between 1100 and 1500 seconds. The most interesting finding in this figure is the misalignment of the two CO calculations: before 700 seconds the amount of CO required to form the measured amount of [Mn] and [Si] exceeds that

of the measured CO evolved. This supports the mechanism proposed by previous researchers that the reaction involves a complex exchange characterized by Reactions 5.1-5.3 [11,14].



The exchange of MnO and Fe is fast and explains the rapid rise in [Mn]. While not stated in the work of past researchers, it is safe to assume that silica reduction is similar; the initially low values of a_{FeO} and a_{Si} support this reaction.

This rate interpretation corresponds well with X-Ray video evidence. Figure 5.3 demonstrates the physical phenomena occurring over time as seen through X-Ray video. Nucleation of CO begins externally before rapidly transitioning over to internal bloating. This period essentially tapers off by 60 seconds, but periodic bloating can still be observed until approximately 100 seconds. This video evidence further supports the distinction between stage 1 and stage 2 rates. For all the figures showing X-Ray images, the upper leftmost image is overlaid with labels for the metal and slag phases. In Figure 5.3 a scale is provided that applies to all images.

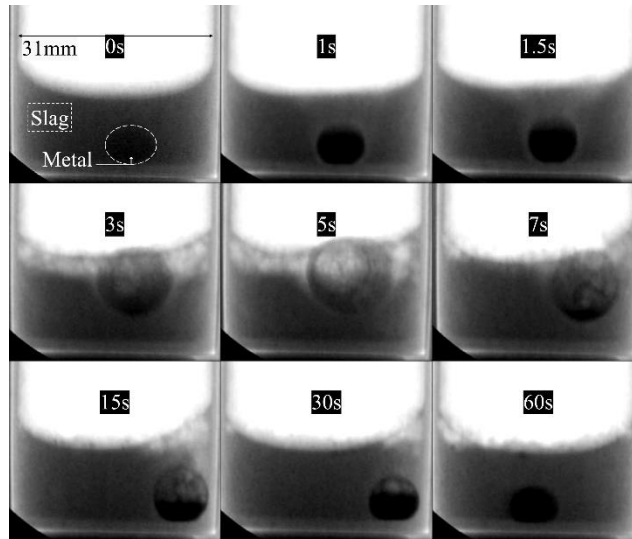
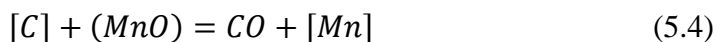


Figure 5.3: X-Ray photos of a metal droplet from dataset 1 (initial conditions 2.5wt pct C, 15 wt pct MnO, 1.5g droplet, 1873K [1600°C]). In order: (0s) reaction start, (1s) external nucleation of CO, (1.5s) partial internal nucleation, (3-7s) majority internal nucleation and small slag foam, (7s) CO production slowing [collection of metal at base of droplet], (15s) droplet buoyancy lost, (30s) periodic CO release from droplet, (60s) observable reaction essentially complete.

While the evolution of [Mn] and [Si] after 100 seconds in Figure 5.2 appears quite flat, the evolution of CO continues. This occurs because FeO transferred to the slag during the initial stage of reaction, is reduced in the second period a mechanism proposed and measured by previous workers [11,14]. During the fast reaction, FeO has been shown to rise above its final equilibrium value, reverting to metal as the reaction slowed [11,14]. By equilibrium the level of FeO in the slag will have returned to a very low value.

After 700 seconds the story is different: there is an apparent imbalance in the amount of CO generated with respect to metal reduced. The only scenario under which this can occur is if metal oxides are being reduced but not making their way to the metal being measured. This possibility will be discussed in greater detail as part of the discussion.

Most of the data was not generated using the quenching method demonstrated in Figure 5.2. Instead continuous CO evolution data was tracked using a pressure transducer and the Constant Volume Pressure Increase (CVPI) technique. The pressure transducer outputs pressure data every 0.1 seconds which can be analyzed. In order to verify the accuracy of the continuous pressure curve the data is compared to LECO and ICP data collected from the metal droplet representing each system of interest; all curves were duplicated at least once to ensure that gas evolution followed the same trend. It was determined that ICP data presented the most consistent results thus was used to normalize the CO evolution curves. A sum of Reactions 5.4 and 5.5 were used to normalize the CO plot.



Many past researchers have not considered the reduction of silica by carbon as part of their experiments. It is unknown what the cumulative impact of ignoring these values will be on their experimental data.

5.3.1.1. Effect of Initial Carbon Content

Figure 5.4 shows the CO generation curve comparing cumulative CO generation against time. It is immediately obvious that compared to past research on carbothermic reduction with droplets [19–21] these reactions were very slow by as much as two or three orders of magnitude. This difference is interesting because, using FactSageTM to estimate the equilibrium constant, the ratio of equilibrium constants in this temperature range for decarburization by FeO versus MnO is 200-

300; this change in driving force accounts for much of the difference in the rate of reaction.

It is important to draw attention to the rapid evolution of CO before 100 seconds and the slower increase following this time. This finding is in reasonable agreement with the trend found in Figure 5.2. A fast reaction occurs prior to approximately 100 seconds and cedes to a slower second reaction following this time. Assessing the systems for an exact transition time does not yield valuable information. For consistency throughout the remainder of this analysis, rate or stage 1 refers to the time before 100 seconds and rate 2 encompasses all reaction times afterwards. This split between stage one and two will be further justified with evidence from X-Ray video. In order to standardize the rate determination process, each of the curves below has been fitted with a single straight line to obtain the rate in mol/s. It is acknowledged that this simplification is not completely accurate as the systems do show signs that they are approaching equilibrium by approximately 1200 seconds (necessitating a decrease in gas generation), however the simplification holds for the majority of the CO generation plots and the fitting is reasonably good.

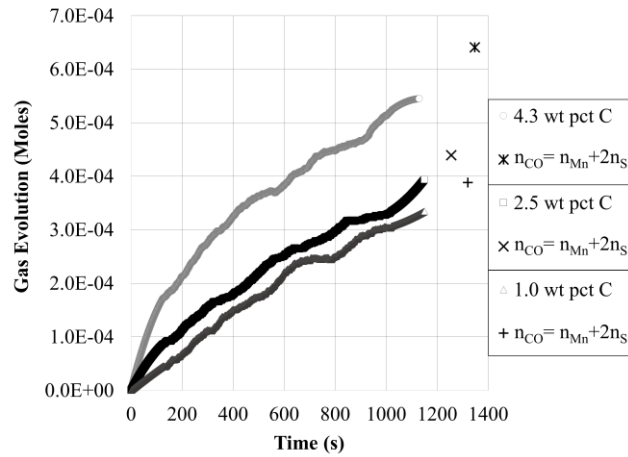


Figure 5.4: CO evolution versus time for variations in the initial carbon content of the metal droplet (normalized for manganese and silicon gains).

The rate of CO generation in the first stage of reaction increases favorably with increasing initial carbon concentration. There is little change in the rates of the second stage. The change in rate with respect to carbon is plotted in Figure 5.5. This indicates that the rate determining step is dependent on carbon concentration.

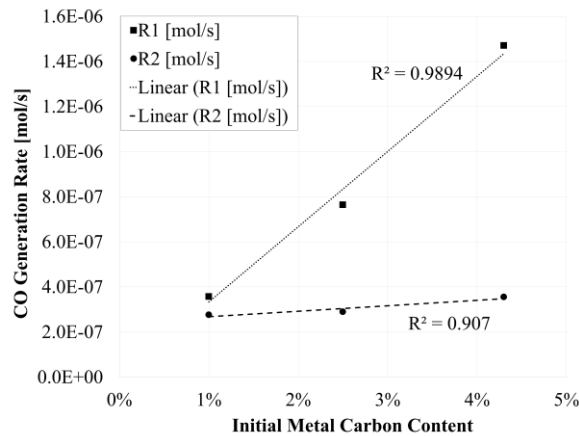


Figure 5.5: Plot of initial carbon content vs. rate of reaction.

When analyzing these plots two important equations must be considered: a rearranged flux equation (Equation 5.6) and rearranged chemical reaction rate equation (Equation 5.7). Both equations represent the change in the number of

moles of a species with respect to time $\left(\frac{dn^i}{dt}\right)$. Both rates are functions of the mass transfer coefficient or reaction rate constant (k_i or k_i^{Fwd}), and the interfacial area ($A_{Interface}$). The mass transport equation also relies on phase volume (V_{Phase}), the number of moles of reacting species in the bulk and at the reacting interface (n_{Bulk}^i and n_{Eqm}^i), and the term Y is a mass balancing term between phases that changes depending on the specific boundary conditions and rate controlling step. The reaction rate equation considers the product of activities of reactants ($a_{Interface}^i$), the product of activities of products ($a_{Interface}^j$), and the equilibrium constant of the reaction of interest (K^i).

$$\frac{dn^i}{dt} = k_i \left(\frac{A_{Interface}}{V_{Phase}} \right) (Y) (n_{Bulk}^i - n_{Eqm}^i) \quad (5.6)$$

$$\frac{dn^i}{dt} = k_i^{Fwd} (A_{Interface}) \left(\prod a_{Interface}^i - \frac{(\prod a_{Interface}^j)}{K^i} \right) \quad (5.7)$$

These equations are useful, even without data, as trends can be predicted between the rates and the parameter of study. Passing through zero is important because, as Equation 5.6 and 5.7 are defined, when the difference between current and equilibrium carbon content is the same there can be no rate. In reference to Figure 5.5 this condition is true for rate 1; the condition need not apply for rate two because this rate does not start from zero.

Past work by the present authors [2] shows the mass transfer coefficients of slag species and metal species to be rapid: k_{Slag} equal to $6.7 \cdot 10^{-4}$ m/s and k_{Metal} equal to $2.3 \cdot 10^{-4}$ m/s. Sain and Belton [22] have summarized the carbon mass

transfer coefficient k_C as $3.5 \cdot 10^{-4}$ m/s in inductively stirred melts. While the carbon mass transfer coefficient is likely to be lower (as the droplet will not be stirred until bloating occurs) these mass transfer coefficients do not correspond well with the rate of reaction (neither Figure 5.2 nor Figure 5.4 show CO evolution rates fast enough to accommodate these mass transfer coefficients). Further, when compared to similar research with metal droplets performed by Gu *et al.* [20,23] (where FeO was the primary oxygen source in the slag), there is a pronounced difference in the appearance of the bloated metal droplets. The bloated droplets presented in this study are small and appear to have a relatively difficult time bloating.

Figure 5.6 compares the time it takes for droplets of different initial carbon content to demonstrate various physical phenomena. The images displayed represent, left to right, the first signs of internal nucleation (low density region appearing at the top of the droplet), the point of maximum expansion during the bloat, and the first point at which the droplet loses buoyancy within the slag. Higher carbon contents exhibit two effects: droplets take longer to present signs of internal nucleation and stay bloated longer. Initial carbon concentration is listed for each row of images, the other conditions are fixed across rows (15 wt pct MnO, 1.5g metal, 1873K [1600°C]). The scales in the leftmost image of each row apply only to their respective row.

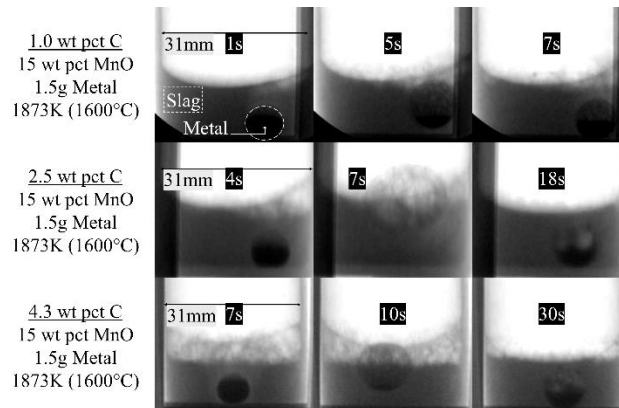


Figure 5.6: Comparison of 3 different initial carbon concentration droplets. Droplets with higher carbon content take longer to bloat and stay bloated longer. The left image column shows the time where internal nucleation first become visible, the center where the droplet is maximally bloated, and the right column when droplet buoyancy is lost.

Based on the suggested mass transfer coefficients, mass transport is not a likely controlling phenomenon within this system. The findings in Figure 5.6 explain the initial few seconds of reaction. Per Equation 5.7, if a chemical reaction is the rate limiting step there is an expectation that increasing carbon content will increase the driving force of the reaction and subsequently the rate; this is true for Figure 5.4 and Figure 5.6. The transitioning period before the onset of droplet bloating may be controlled by a chemical reaction at the interface involving carbon. If more carbon is present in the melt more oxygen is consumed at the interface; it is obvious however that some oxygen passes through the interface as a precursor condition to internal CO nucleation. This incubation period has been reported by past authors [24].

For a droplet to experience bloating, oxygen flux must exceed carbon flux to the slag-metal interface; CO bubbles cannot form inside the metal droplet unless there is an oxygen supply to the carbon. In order for CO to nucleate p_{CO} must exceed one atmosphere. Droplet buoyancy is a physical manifestation of the reaction rate:

droplet bloating is a function of the rate of internal CO generation and rate at which CO is lost through the metal droplet surface. In most cases the droplets triple their surface area upon bloating (which is consistent across most tested conditions); assuming CO loss through the interface is proportional to the surface area means that the rate of CO loss is similar in all systems. Thus, the length of time a droplet remains bloated is related to the rate of internal CO generation. Since high carbon droplets remain bloated longer, the rate limiting mechanism must be proportional to carbon in the metal; this agrees well with the changes in reaction rate presented in Figure 5.5.

The mole generation plot presented in Figure 5.4 shows that the rate of gas generation is essentially linear in the first stage of reaction. Contrast this to Figure 5.3 and Figure 5.6 where an area change in the system obviously occurs. This indicates that the rate of reaction for internal CO generation is independent of the droplet surface area and the only reaction mechanism that the authors can imagine independent of droplet surface area is internal CO nucleation.

Nucleation of new CO bubbles essentially ceases before the end of stage 1 but growth of pre-existing bubbles continues. The growth of pre-existing bubbles and nucleation of fresh bubbles are both driven by chemistry within the metal droplet. Nucleation is an energetically expensive reaction when compared to growth, so the appearance of larger CO bubbles over time is not surprising. Once these bubbles form, any oxygen remaining inside of the metal is likely relegated to the task of bubble growth.

5.3.1.2. *Effect of Initial Manganese Oxide Content*

Figure 5.7 shows the gas evolution associated with changes in initial manganese oxide content; rates of each stage are listed in the figure. Interestingly, the curves are in reverse order of what one might expect, where lower manganese oxide contents produce faster rates of CO evolution. It is important to remember that these curves are representative of CO evolution from *both* SiO₂ and MnO reduction. Previous work by the authors [2] has shown that the mass transfer coefficient for silica is essentially the same as for manganese oxide in this slag system, however the concentration of silica in the slag is much higher than MnO. Per Equation 5.6, if the system was limited by mass transport, the rate of reaction would be proportional to the mass transfer coefficient times driving force and for a fixed mass transfer coefficient, one would expect systems with lower MnO to react more quickly as more carbon is available to reduce silica. What is likely, since internal nucleation is occurring, is that there is no impediment to oxygen transport and the oxygen content of the metal droplet is determined from the equilibrium of manganese and manganese oxide at the interface. This is further complicated by the apparent simultaneous reduction of silica and the associated equilibrium associated with silicon and silica at the interface. Ultimately the confounding effect of oxygen sources makes isolating the effects of initial manganese oxide content difficult to interpret.

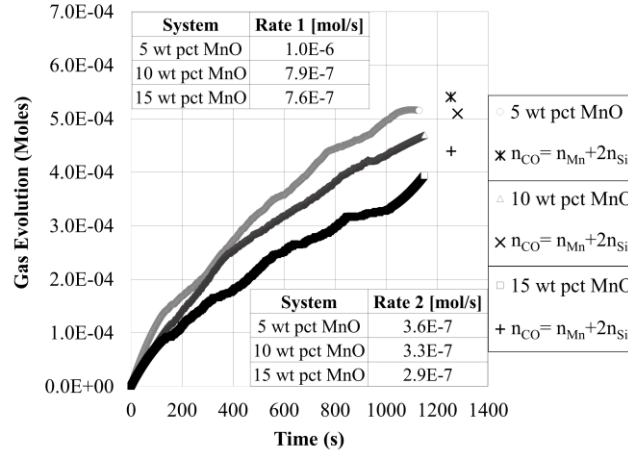


Figure 5.7: CO evolution versus time for variations in the initial manganese oxide content in slag (normalized for manganese and silicon gains).

Figure 5.8 compares bloated droplets in slags ranging from 5 to 15 wt pct MnO. There is apparently very little difference in reaction rates between reference (15 wt pct) and the 10 wt pct MnO samples, per Figure 5.8, but the 5 wt pct trials show interesting evidence for the influence of oxygen on the system. Despite the fact that the quantified rate of decarburization is faster in the 5 wt pct MnO system the rate of internal decarburization must be slower as evidenced by the degree of bloating. This suggests that the rate of external decarburization is faster than internal decarburization.

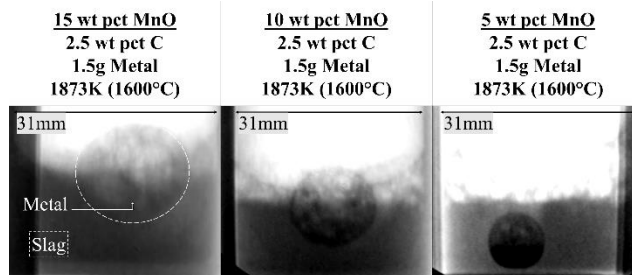


Figure 5.8: Comparison of bloated droplets vs. initial MnO content; 5 wt pct MnO slags do not lead to complete bloating of the metal droplets.

5.3.1.3. Effect of Reaction Temperature

Figure 5.9 shows the CO evolution as it relates to temperature increases. The rate data is quantified in the figure; there is an apparent discrepancy in the initial rate data, but the data for the second stage of reaction shows that the two lower temperatures have the same rate of reaction and the higher temperature is faster. Further, Figure 5.10 shows X-Ray observations from the droplets. The lower temperature system does not bloat as completely as higher temperature droplets. With respect to the initial rate of reaction, the lower temperature reaction is faster because a greater degree of decarburization is performed along the interface. The Gibbs energy exchange associated with the reaction of carbon and manganese oxide is more favorable with increasing temperature [25]; at lower temperatures this interfacial chemical reaction may have more of an influence on the system. This lower temperature reaction has similarities to the low MnO system. At higher temperatures, CO nucleation is more favorable and the reaction proceeds quickly.

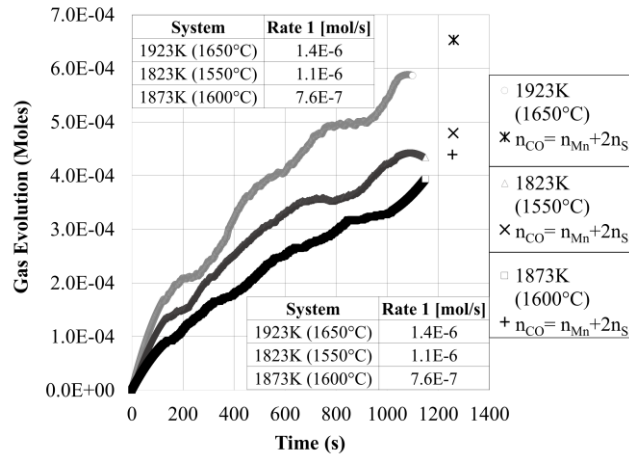


Figure 5.9: CO evolution versus time for variations in reaction temperature (normalized for manganese and silicon gains).

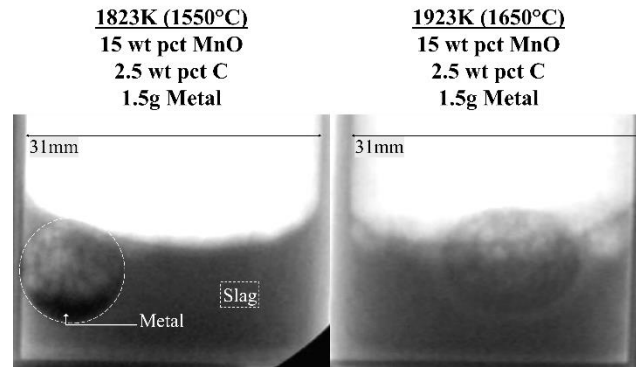


Figure 5.10: Comparison of 1823K (1550°C) and 1923K (1650°C) maximally bloated droplets; in all cases droplets at the lower temperature had a metal pool at their base indicating slower reactions rates.

5.3.1.4. Effect of Metal Droplet Mass

Figure 5.11 shows the relationship between CO evolution and droplet mass; the rate data is included within the figure. There is an increase in the absolute rate of reaction as the droplet mass rises for both the first and second stage of reaction.

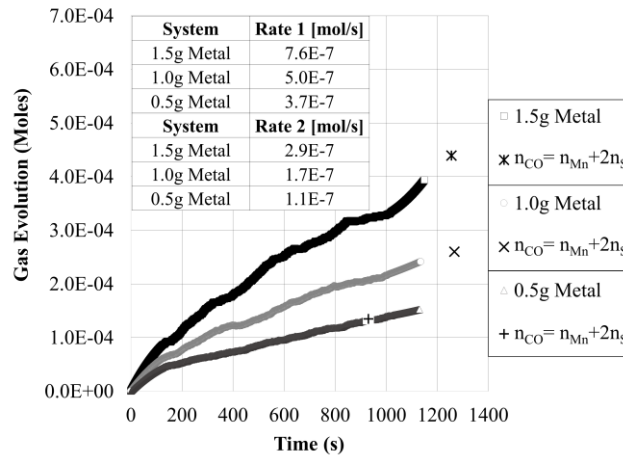


Figure 5.11: CO evolution versus time for variations in metal droplet mass (normalized for manganese and silicon gains).

It has already been established that a relationship does not exist between area and rate during the first stage of reaction. Figure 5.12 shows the relationship between the rate of reaction and metal volume. The smaller droplet is somewhat of

an outlier, but the volumes can be reasonably fit through zero. Interestingly the volume relationship for stage two has an even stronger relationship with the rate.

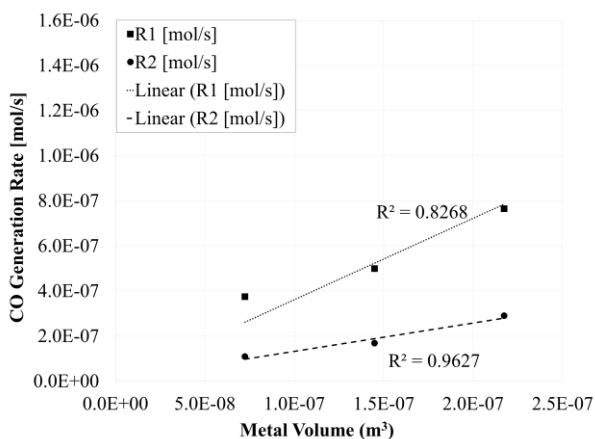


Figure 5.12: Relationship between rate of CO generation and metal volume

An analysis of X-Ray video evidence suggests that smaller droplets spend less time bloated than the larger droplets. If MnO mass transfer (and oxygen supply) were rate controlling this should not have happened because no changes were made to the oxygen supply.

There is an interesting observation regarding the switch from external to internally nucleated CO. Figure 5.13 shows the progression of a 1.0g metal droplet in the early stages of reaction. At 2s the droplet is suspended in the slag by an external cloud of CO. At 3s the droplet is seen to blur as it loses buoyancy and falls. At 3.5s the droplet has lost density on its upper surface, characteristic of internal CO formation. The droplet once again ascends by 5 seconds and is fully bloated. This suggests that early in the reaction, the supply of oxygen and carbon to the droplet surface are sufficient to sustain an external halo of CO. After some time, the external gas nucleation slows as carbon concentration at the interface falls. This

is supported by the observation of subsequent internal nucleation of CO. Once internal nucleation starts it seems likely that the droplet will be well stirred and that the reaction rate will be controlled by either supply of oxygen to the droplet or the rate of nucleation and growth of CO bubbles. The fact that the bubble loses buoyancy in the transition step from external to internal nucleation supports a conclusion that: the two decarburization stages are distinct and that there is an incubation time associated with the internal CO generation. The two reactions may occur in parallel, but if they do it is at significantly different rates such that one appears to stop when the other begins.

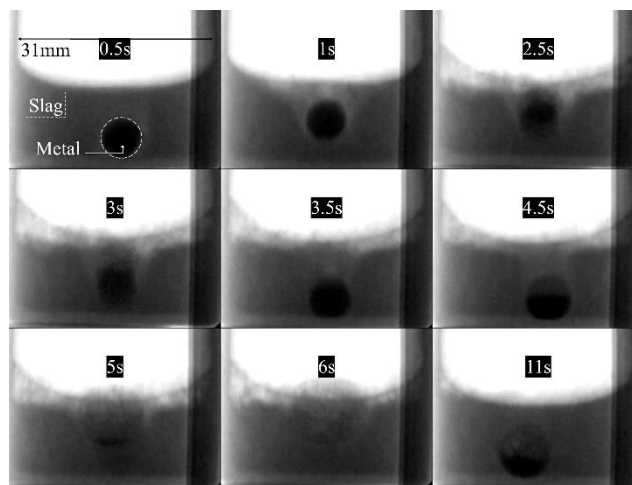


Figure 5.13: Transition from primarily external to primarily internal CO nucleation in a droplet from dataset 8 (initial conditions 2.5wt pct C, 15 wt pct MnO, 1.0g droplet, 1873K [1600°C]) showing clear evidence that the external CO nucleation slows dramatically and that there is an incubation period for internal nucleation.

5.3.2. Formation of Metal in the Slag

An interesting phenomenon is found in the systems when compared to the work of past authors who studied the carbothermic reduction of FeO using iron carbon alloys. Sommerville *et al.* [9] discovered iron globules on the surface of their quenched *slag* samples. Two alternatives were proposed: they were a product

of the reduction reaction of FeO from slag or that they originated in the bulk material and were carried to the top of the slag. The same phenomenon was discovered when they analyzed nickel oxide reduction, where nickel was found on the slag surface, leading them to believe that the reduction reaction was the primary source of this material.

In the present work, there is evidence supporting both droplet dispersion and oxide reduction as a possible mechanism. Figure 5.14 comes from a sample where the metal droplet had 4.3 wt pct carbon. There is no obvious evidence that any metal has broken away from the main droplet up to 10 seconds. Little happens until 60s where a fragment of metal is detected in the bottom right of the crucible. The next four images are important and demonstrate how fragmentation of the bulk is at least partially responsible for the metal scattered about the slag. At 61s the fragment bloats internally and begins to rise into 61.5s. At 62s the bloated droplet pops and the metal begins to fall reaching the bottom by 62.5s. If these fragments were composed of reduced metal oxide there should not be any carbon in the metal, thus they could not bloat.

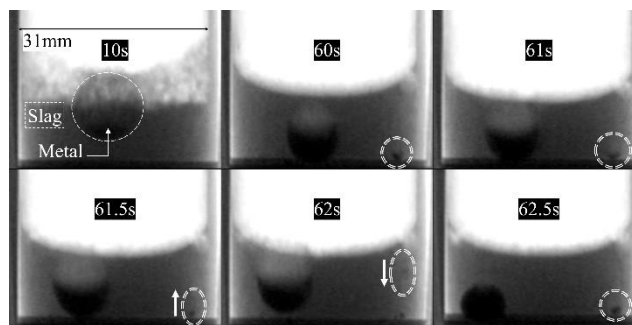


Figure 5.14: Appearance of metal fragment in a high carbon sample.

Comparatively, Figure 5.15 shows a sample where the slag contained 5 wt pct MnO; this system produces much more CO externally than the high carbon sample. The release of externally generated CO bubbles is much less violent than the release of internal CO from the metal, reducing the degree to which dispersion would be a viable mechanism. At 30s a small droplet of metal can be detected along the slag foam's surface. This metal moves and grows over time, seen from 50 to 150s. A second piece of metal is detected at 180s as well, immediately above the main droplet. This sample may support the conclusion of Sommerville *et al.* as the secondary droplet appears to be growing with CO evolution and CO bubbles are not large enough to “burst” and scatter the main droplet. There is still the possibility that the CO is forming in or along the metal side of the interface causing a metal film to be pulled away with each CO bubble.

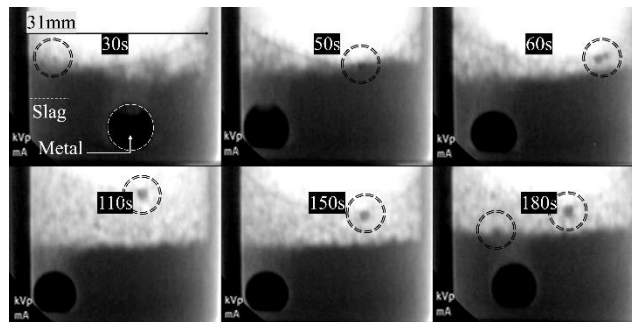


Figure 5.15: Growth of metal in the slag corresponding with largely external CO evolution.

Amongst the other presented information, this supports the conclusions about a transition in the rate limiting step of the reaction. When the decarburization is primarily internal there is an explicit requirement that oxygen (and charge balancing metal ions) are reaching the interface of the metal and entering the metal droplet, thus the only fragments of metal found in the slag away from the bulk

droplet during the initial period are those caused by the ejection of a metal film. When the reaction is primarily external, and the metal interface is essentially blocked by gas, there is a high likelihood that gas shuttling across the bubbles occurs and thus metal oxides are reduced at the slag-gas interface, becoming trapped inside the slag. These findings coincide with the findings in Figure 5.2, and it seems possible that some degree of metal oxide reduction can occur in the slag.

5.3.3. Evidence of Slag Transport Control from Failed Experiments

With the experimental design and crucibles used in this work, it is possible for the alumina crucible to crack as it is being elevated in the furnace. Upon liquification of the slag the leak becomes obvious and the experiment must be aborted. In a few outlying cases, the crucibles may fail during the experiment as well. These few experiments produced very interesting results as shown in Figure 5.16 below. Up until 1400s the experiment proceeds as normal, the rate curve can be divided into an initial fast period and a slower second period where pressure rise decays over time. At 1400s the crucible fails, slag begins to leak, and a large rise in moles of CO generation occurs. At 1600s the rise stops and holds (as the crucible runs out of slag) until the system is quenched (breaking the seal on the furnace caused the pressure drop).

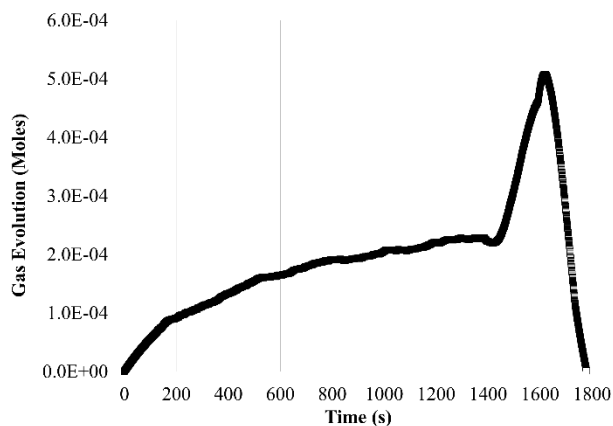


Figure 5.16: Plot of CO evolution measured from the CVPT when a crucible failed after 23 minutes; at 1400s a sharp pressure increase can be seen in the plot.

The above trend is repeated in several failed experiments where the same pressure rise can be documented. When a crucible fails, slag begins to flow from the crucible (but the metal remains largely stagnant). Unintentionally flowing slag mimics some of the properties of stirred slag, thus, if the system were under transport control in the slag one would expect an increase in the rate of reaction *if* the transport limitation were altered via slag stirring.

An alternate hypothesis for this sharp rise in pressure can be explained by the wiping of gas bubbles from the metal surface by agitated slag. There is strong evidence to support this claim in the absence of slag mass transport limitations.

5.4. Discussion

Several rate controlling mechanisms have been supported with the preceding data, and others have been dismissed. The first stage of reaction appears to involve internal nucleation of CO: the reaction rate remains higher for longer with increasing the carbon content, droplets reacting with low MnO slags do not bloat

as fully as those with higher MnO concentration, and a relationship may exist between the reaction rate and metal volume. For the second stage of reaction the only identifier presented so far is that the system returns to a reaction occurring on the surface of the metal droplet: there is a low likelihood that a reaction within the metal controls this stage of reaction. In order to better understand the system, the work of past authors will be analyzed in more detail.

The following section offers a summary of some of the past reported rate limiting steps and rate constants. Table 5.2 summarizes these values. A brief commentary on comparisons between the literature is provided afterwards.

Table 5.2: Summary of Mechanisms and Rate Constants from Literature

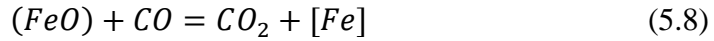
Authors	Temperature	Mechanism	Rate Constant (m/s)
Tarby & Philbrook [12]	1848K (1575°C)	MnO Transport	1.3×10^{-6}
Tarby & Philbrook [12]	1773K (1500°C)	MnO Transport	3.3×10^{-7}
Yagi & Ono [13]	1773-1873K (1500-1600°C)	Mn ²⁺ Transport	4×10^{-6}
Daines & Pehlke [8]	1823K (1550°C)	Chemical Reaction	5×10^{-8}
Pomfret & Grieverson [14]	1723K (1450°C)	MnO Transport	5×10^{-6}
Kawai <i>et al.</i> [15]	1873K (1600°C)	Mixed Mass; k_{Mn}	7.4×10^{-5}
Kawai <i>et al.</i> [15]	1873K (1600°C)	Mixed Mass; $k_{O^{2-}}$	1×10^{-5}
Shinozaki <i>et al.</i> [16]	1873K (1600°C)	Mixed Mass; k_{Slag}	1.2×10^{-5}
Xu <i>et al.</i> [11]	1823K (1550°C)	Chemical Reaction	4.7×10^{-7}
Sohn <i>et al.</i> [17]	1873K (1600°C)	Mixed Mass; k_{Mn}	1.1×10^{-4}
Sohn <i>et al.</i> [17]	1873K (1600°C)	Mixed Mass; k_{MnO}	2.0×10^{-5}

Comparing the values of Tarby and Philbrook and Pomfret and Grieveson is interesting because despite large differences in temperature the reaction rates of the latter authors are greater than the former. Slag viscosity does not account for these differences. Similarly, Shinozaki *et al.* and Sohn *et al.* report similar mass transfer coefficients in the slag, but the ratio of CaO/SiO₂ for the former authors is 0.8 and the latter authors is 3-4.

There are two groups of authors who deserve special attention in this study and are detailed here. Wei *et al.* [26] originally studied desiliconization from iron containing carbon and with a slag containing FeO. The system was described to be mixed transport control, where k_{Si} was 5×10^{-4} and k_{FeO} was 3×10^{-5} .

These authors also studied decarburization from the same system [10]. Their analysis is similar to work done by Sommerville *et al.* [9] so their work is discussed together here. Sommerville *et al.* [9] laid the foundation for the chemical reactions occurring within the carbothermic reduction system, where Wei *et al.* [10] emphasized the significance of gas phase transport. Experiments and modelling showed three likely mechanisms become or share the rate-limiting step of the reaction. A primary assumption of this theory is that any contact between slag and metal is obstructed by gas, thus the gas acts as an oxygen transport intermediary.

At the slag-gas interface Equation 5.8 occurs, subdivided into Equation 5.8a and Equation 5.8b for a better physical understanding of the interface; \blacksquare and \blacksquare^O represent a vacant site and oxygen filled site on the interface, subscripts $_{GS}$ and $_{GM}$ represent the gas-slag and gas-metal interfaces.



Iron oxide dissociates to iron and oxygen along the interface; for this condition to be true iron must be found in the slag as it is assumed it has no way of travelling to the metal, the work of Sommerville *et al.* [9] substantiates this claim. Wei *et al.* [10] have reported that the reaction has a relative independence on p_{CO} , thus reaction 5.8 is assumed limited by iron oxide dissociation. The oxygen is retrieved by CO in the bubble and transported to the gas-metal interface by CO_2 where the reaction described by Equation 5.9, proceeds via Equations 5.9a and 5.9b.



Wei *et al.* [10] had success when applying this mechanistic understanding of the reacting system to their experimental data. When CO bubbles at the interface are large the system shifts to CO_2 transport control across the bubbles. When the slag oxygen supply is low (less than 2.5 wt pct FeO [9]), reaction 5.9a is the rate limiting step because there is an insufficient partial pressure of CO_2 ; this is supported by studies noting a drop in reaction rate with increasing [S] content [9,22]. When the oxygen content in the slag is high, the rate limiting step is reaction 5.8a; 5.8b was eliminated because research shows that the system is relatively independent of gas pressure above 0.5atm [10]. Wei *et al.* [10] also tested

the effect of phosphorus in the slag on the reaction rate and showed that the decarburization slowed down with increasing phosphorus content, confirming that the system can experience rate limitation along the gas-slag interface. This model can be applied to the second stage of reaction of the present study. This model is very similar to findings of Min and Fruehan [24] who studied decarburization with iron droplets and FeO in the slag. This idea will be returned to when the second stage of reaction of the current study is discussed.

5.4.1. First Contact of Slag and Metal

In the moments after the metal droplet contacts the slag, externally nucleated CO is obvious and likely corresponds with a relative balance between carbon supply from the metal and oxygen supply from the slag. Mass transfer coefficients from the literature [2,22] are too fast for the documented rate of CO generation. In comparison to past literature on FeO reduction [21,24], the equilibrium constant for MnO reduction by carbon is 200-300 times less which corresponds well with the difference in reaction rate of this system. It seems likely that this brief stage of reaction is related to the chemical reaction of MnO and C at the interface.

5.4.2. Internal Nucleation and Droplet Bloating

There is sufficient evidence to suggest that the rate of CO generation is the rate-limiting step during this stage of reaction; this would be a combination of nucleation and growth phenomena. Evidence to support this claim is listed below.

- Every condition tested shows evidence of droplet bloating evidenced by X-Ray video.

- The initial rate of reaction is linear despite changes in area; thus the rate of reaction is independent of the interfacial area.
- The rate of reaction is strongly linked to initial carbon content; the rate of nucleation and growth would improve with increasing carbon activity. Further, droplets take longer to bloat and remain bloated for longer as carbon content rises; all of this suggests that the carbon supply is a rate limitation to CO generation.
- The rate of reaction is linked to droplet volume; the rate of nucleation rises with increasing nucleation sites explaining the volume relationship.
- When temperature is low or MnO content is low bloating is reduced; this indicates a chemical reaction with oxygen dependence as part of the rate-limiting step.
- A rapid exchange of manganese and silicon with iron occurs here; this reaction is believed to occur outside of the decarburization mechanism.

5.4.3. External CO Nucleation Post Bloating

Figure 5.17 helps describe the mechanism. This droplet is from the dataset 1 with 2.5wt pct C, 15 wt pct MnO, 1.5g droplet, 1873K [1600°C]. The highly faceted interface is covered in a halo of CO bubbles, *which likely block any direct contact of slag and metal*; this differs significantly from SiO formed in previous work [1] which only blocks a fraction of the interface. This faceting is not present in samples that are low in reactants (i.e. 1 wt pct C or 5 wt pct MnO) implying that

these reactions have nearly reached equilibrium by the time of quench, or that the CO bubbles are leaving before they have a chance to facet the interface.

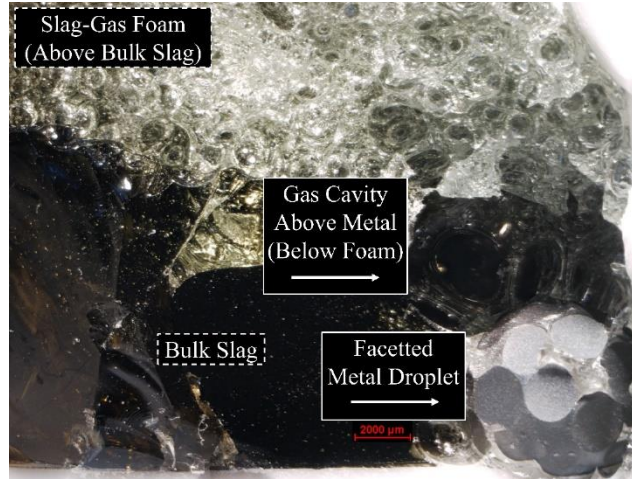
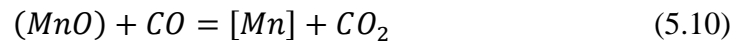


Figure 5.17: Quenched slag (near 22min) and droplet from dataset 1 (initial conditions 2.5wt pct C, 15 wt pct MnO, 1.5g droplet, 1873K [1600°C]); initial conditions 2.5 wt pct C in 1.5g metal, 15 wt pct MnO, and 1873K [1600°C]

Under the assumption that the interface between slag and metal is blocked by gas, the model and findings of Sommerville *et al.* [9] and Wei *et al.* [10] can be discussed. These authors described the stoichiometry at the gas-slag interface with Equation 5.8; for the present system Equation 5.10 or Equation 5.11 are their equivalents. Silicon transport could also occur by SiO transport in place of CO₂; metallic silicon is unlikely to remain in the slag when (MnO) is present.



For these reactions to occur there must be evidence of metal build up in the slag, away from the primary metal droplet. Figure 5.15 demonstrates how metal builds up in the slag as the system reacts, and that this metal is not the result of fragmentation of the main droplet. Figure 5.18 below shows more faceting and

shows that there is some degree of MnO reduction from the slag where CO is in direct contact with the slag. Further, it should be added that the final mass of metal droplets was less than the initial mass of the droplet: because [C] is exchanged with heavier elements the mass would be expected to rise with time. This decrease in mass can be accommodated by this mechanism.

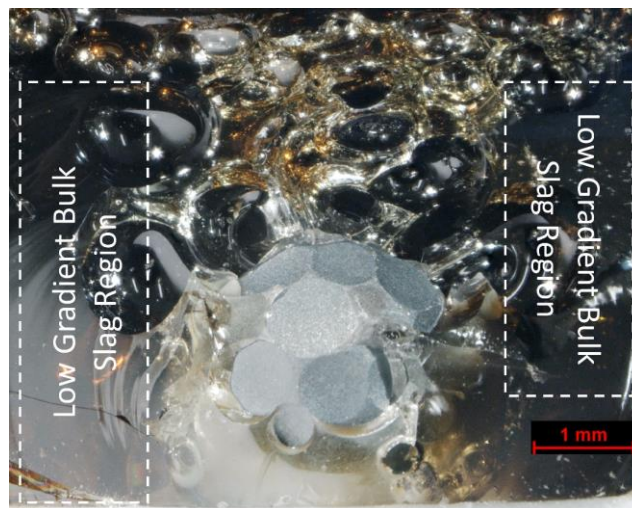


Figure 5.18: Quenched slag (approximately 4min) surrounding metal droplet from dataset 6 (initial conditions 2.5 wt pct C in 1.5g metal, 15 wt pct MnO, and 1823K [1550°C]). Significant faceting is present on the metal surface, CO bubbles are leaving the metal surface to the top of the slag, left and right edges show homogeneous bulk slag.

The CO₂ produced by these reactions ferries oxygen across the gas bubbles where it reacts with carbon at the interface to regenerate CO. Thus, the system could be controlled by metal oxide decomposition at the gas-slag interface, CO₂ transport, or CO₂ decomposition at the gas-metal interface. Wei *et al.* quantified the critical diameter at which transport in the gas bubble became negligible to be 2mm [10]. The figures presented here show bubble diameters ranging from 0.5 to 4mm, thus CO₂ transport may play a role in the rate determining step as well as a chemical reaction at either the gas-metal or slag-metal interfaces.

The findings of Sommerville *et al.* [9] can be extrapolated to the present system to determine which of the chemical reactions is more important. They stated that because the CO_2/CO ratio created by FeO decomposition was low with respect to that created by either NiO or PbO, the rate limiting chemical reaction was the gas-metal interface; reaction 5.8 produced little CO_2 creating a scarcity of CO_2 in reaction 5.9. NiO and PbO are significantly more reducible than FeO, and FeO is significantly more reducible than MnO or SiO_2 , thus the logical extrapolation is that the chemical reaction responsible for rate control in the present system is the decomposition of CO_2 at the gas-metal interface (Equation 5.9a).

This proposed mechanism may also explain the stage 2 reaction rate results from Figure 5.7 where the slag with lowest MnO content has the highest rate of CO evolution. If a stable layer of gas cannot be formed along the metal interface, then the slag and metal are not forcibly separated thus the system does not experience a rate limitation association with CO_2 .

The apparent increase in reaction rate in Figure 5.16 associated with crucible breakage can be explained because stirring of the slag agitates and detaches gas bubbles from the surface of the metal, which brings fresh slag into contact with the metal. This will allow for an exchange reaction such as in Equation 5.1 to occur or for direct carbon oxidation to occur such as in Equation 5.4 or Equation 5.5; neither reaction is limited by the transport or reaction kinetics of CO_2 .

In summary, post bloated droplet the system is rate limited by CO₂ transport across the bubble layer that forms around the metal droplet and by decomposition of CO₂ once it reaches the gas-metal interface.

5.5. Conclusions

The carbothermic reduction of manganese oxide from slag to metal droplets was studied across a range of conditions. Initial concentrations of carbon and manganese oxide were varied to 1, 2.5, and 4.3 and 5, 10, and 15 wt pct respectively. Temperatures were varied from 1823-1923K (1550-1650°C). Droplet masses were varied from 0.5-1.5g. Plots for total CO gas generation can be simplified to two reaction regimes, the first described by internal CO nucleation (demonstrated in X-Ray imaging) and the second which is limited by the formation and transport of CO₂. The reacting system is highly complex and explains why a variety of documented rate limiting mechanisms have been discussed by past authors. Compared to the reduction of MnO by silicon, the rates found in these experiments are significantly slower. Further research is required to quantify the dynamic reaction mechanisms and rate constants for the proposed controlling steps. In summary the following statements can be made.

- 1) The rate of reaction for the studied systems can be broken into an initial fast stage and slower second stage; the difference between these rates is less than a factor of four.
- 2) The initial rate is controlled by internal CO nucleation and growth, demonstrated with the X-Ray video evidence and by analyzing plots of

increasing carbon content and droplet volume against the CO evolution rate. Oxygen from the slag must transport through the interface faster than carbon reaches the interface from the metal for droplet bloating to occur.

- 3) The second rate is limited by CO₂ mass transport through stagnant or partially stagnant bubbles, from the gas-slag interface to the gas-metal interface, and the corresponding decomposition of CO₂ at the gas-metal interface. This mechanism agrees well with past authors studying the carbothermic reduction of FeO.
- 4) With respect to its use in direct alloying applications, a fast period of material exchange may occur at the beginning of reactions which could contribute some net manganese to the melt within a reasonably short period of time; this gain is less than 0.5 wt pct. The kinetics of the slower second step of reaction do not support bulk manganese additions to metal.

5.6. Acknowledgements

The authors thank the National Science and Research Council of Canada (NSERC, STPGP463252-14) for funding support. Special thanks to ArcelorMittal Dofasco, Stelco, Praxair, and Hatch Ltd. for their in-kind support, technical expertise, and their many helpful discussions.

5.7. References

- [1] B.J. Jamieson and K.S. Coley: *Metall. Mater. Trans. B*, 2017, vol. 48, pp. 1613–24.
- [2] B.J. Jamieson, Y. Tabatabaei, M. Barati, and K. S. Coley: *Metall. Mater.*

Trans. B, 2019, vol. 50, pp. 192–203.

- [3] R. Elliott, K. Coley, S. Mostaghel, and M. Barati: *Jom*, 2018, vol. 70, pp. 1–11.
- [4] O.S. Bobkova and V.V. Barsegyan: *Metallurgist*, 2006, vol. 50, pp. 463–68.
- [5] L.N. Kologrivova, A.Ya. Nakonechnyi, Z.G. Trofimova, O.V. Nosochenko, and N.N. Kulik: *Metallurg*, 1987, vol. 5, pp. 28–29.
- [6] O.I. Nokhrina, V.P. Komshukov, and V.I. Dmitrienko: *Metallurgist*, 2004, vol. 48, pp. 264–65.
- [7] M. Eissa, H. El-Faramawy, and G. Farid: *Steel Res.*, 1998, vol. 69, pp. 373–80.
- [8] W.L. Daines and R.D. Pehlke: *Metall. Trans.*, 1971, vol. 2, pp. 1203–11.
- [9] I.D. Sommerville, P. Grieveson, and J. Taylor: *Ironmak. Steelmak.*, 1980, vol. 7, pp. 25–32.
- [10] P. Wei, M. Sano, M. Hirasawa, and K. Mori: *ISIJ Int.*, 1991, vol. 31, pp. 358–65.
- [11] K. Xu, G. Jiang, W. Ding, L. Gu, S. Guo, and B. Zhao: *ISIJ Int.*, 1993, vol. 33, pp. 104–8.
- [12] S.K. Tarby and W.O. Philbrook: *Trans. Metall. Soc. AIME*, 1967, vol. 239, pp. 1005–17.
- [13] T. Yagi and Y. Ono: *Trans. Iron Steel Inst. Japan*, 1970, vol. 10, pp. 36–37.
- [14] R.J. Pomfret and P. Grieveson: *Ironmak. Steelmak.*, 1978, vol. 5, pp. 191–97.

- [15] Y. Kawai, N. Shinozaki, and K. Mori: *Can. Metall. Q.*, 1982, vol. 21, pp. 385–91.
- [16] N. Shinozaki, K. Ishido, K. Mori, and Y. Kawai: *Tetsu-to-Hagane*, 1984, vol. 70, pp. 73–80.
- [17] H. Sohn, Z. Chen, and W. Jung: *Steel Res.*, 2000, vol. 71, pp. 145–52.
- [18] M.A. Rhamdhani: *PhD Thesis - McMaster Univ.*, 2005.
- [19] C. L. Molloseau and R. J. Fruehan: *Metall. Mater. Trans. B Process Metall. Mater. Process. Sci.*, 2002, vol. 33, pp. 335–44.
- [20] K. Gu, N. Dogan, and K.S. Coley: *Metall. Mater. Trans. B Process Metall. Mater. Process. Sci.*, 2017, vol. 48, p. 3408.
- [21] E. Chen and K.S. Coley: *Ironmak. Steelmak.*, 2010, vol. 37, pp. 541–45.
- [22] D.R. Sain and G.R. Belton: *Metall. Trans. B*, 1976, vol. 7, pp. 235–44.
- [23] K. Gu, N. Dogan, and K.S. Coley: *Metall. Mater. Trans. B Process Metall. Mater. Process. Sci.*, 2018, vol. 49, pp. 1119–35.
- [24] D. J. Min and R. J. Fruehan: *Metall. Trans. B*, 1992, vol. 23, pp. 29–37.
- [25] C.W. Bale, E. Bélisle, P. Chartrand, S.A. Decterov, G. Eriksson, A.E. Gheribi, K. Hack, I.H. Jung, Y.B. Kang, J. Melançon, A.D. Pelton, S. Petersen, C. Robelin, J. Sangster, and M.A. Van Ende: *Calphad*, 2016, vol. 54, pp. 35–53.
- [26] P. Wei, M. Sano, M. Hirasawa, and K. Mori: *Trans. Iron Steel Inst. Japan*, 1988, vol. 28, pp. 637–44.

Chapter 6

6. Mixed Mass Transport Control and Viscosity during Reduction of FeO and MnO from Slag

Copyright & Bibliographic Information

This chapter contains the pre-publication version of “Mixed Mass Transport Control and Viscosity during Reduction of FeO and MnO from Slag”. Manuscript submission is pending at the time of thesis submission; this work should be submitted to Metallurgical & Materials Transactions B, subject to similar copyright and permissions for the previous chapters. Available bibliographic information is shown below.

Authors: Jamieson, B.J.; Barati, M.; Coley, K.S.

Journal: Metallurgical and Materials Transactions B

Year: 2019

Contributions & Context

This article is a critical review of literature, looking to compare why apparently similar systems have had very different mass transfer coefficients assigned even for the same rate controlling mechanism. All data analysis and manuscript drafting was completed by the primary author. Discussions were shared between the primary author, Dr. Barati, and Dr. Coley.

While performing literature review for the preceding chapters and papers, some data from the literature appeared to trend (even across systems). For oxidants like (MnO) and (FeO), or reductants like [Si] and [Al], a similar clustering of mass transfer coefficients was reported. Yet there were some systems, despite apparently

similar slag compositions and experimental procedures, that had significant deviations from the apparent trend. Most concerning were the values determined in Chapter 4 of the present work [84] which appeared to be two orders of magnitude greater than the reports of other authors in the field.

As part of the search, metal systems containing Fe-Si, Fe-C, and Fe-Si-C were examined in reactions with slags containing either FeO or MnO (or both). The work of Wu *et al.* [85] was an important finding, as they were one of the only research groups who studied droplets reacting with large slag volumes and whose data suggests similar mass transfer coefficients to those calculated here. Essentially all other researchers who were cited as part of this work performed experiments where the metal volume was much greater than the slag volume, and as a result presented slag mass transfer coefficients that were smaller than those determined as part of this thesis. Ultimately, using the assumption of mixed mass transport control between a metal species and slag species, there are both volume and chemistry trends supporting the importance of the slag/metal partition coefficient. The data trends as one would expect based on the effects of the partition coefficient on transport resistance.

Mixed Mass Transport Control and Viscosity during Reduction of FeO and MnO from Slag

B.J. Jamieson^[1], M. Barati^[2], and K.S. Coley^[1]

^[1]McMaster Steel Research Center, McMaster University, Hamilton, L8S 4L8, Canada. Contact coleyk@mcmaster.ca

^[2] University of Toronto, Toronto, M5S 3H7, Canada.

Abstract

During the study of silicothermic and carbothermic reduction of slags with manganese oxide, a range of proposed mechanisms and mass transfer coefficients have been offered by past researchers. There are major differences between reported mass transfer coefficients in metal droplet experiments compared to those where the metal volume exceeds the slag volume. Within similar experimental designs, quantified mass transfer coefficients also vary. Slag viscosity should play a major role in influencing the rate controlling step and value of the mass transfer coefficient, so these systems have been analyzed across a broad range of work. A relationship has been found between optical basicity and the mass transfer coefficients of MnO, SiO₂, and FeO in the slag, which is consistent with structural understandings of silicate slags. However, no obvious relationship was found with respect to viscosity. Differences in mass transfer coefficient of the slag have been explained by showing the effects of total resistance to transport versus initial chemical conditions and the ratio of metal volume to slag volume.

6.1. Introduction

Direct alloying is a method of alloy addition where metal melts react directly with slag, causing the reduction of a desirable species from slag to metal. These processes have potential applications to steelmaking, specifically the production of

3rd Generation Advanced High Strength steels (3G AHSS) where high manganese contents are desirable; adding manganese via reductive alloying reduces the dependence on ferroalloys [1].

The present authors have studied systems where silicon or carbon were used as reductants to reduce manganese oxide from the slag [2,3]. During the literature review process many different proposed reaction mechanisms were reported alongside a number of proposed rate determining steps for what, at first inspection, appear to be essentially the same systems. During the kinetic modelling process for the silicothermic reduction of MnO, it was concluded that the system experiences mixed control by all four components [3]; the system is so tightly balanced that changes to any component were shown to have some degree of impact on the system. More importantly the impact of the slag mass transport was found to be twice as significant as that of metal mass transport, which aligned with qualitative findings from previous work [2]. These findings disagreed with other authors who concluded different options for the rate limiting step: control by manganese transport in the metal [4,5] or control by silica transport in slag [6]. Further, when one studies the carbothermic reduction of MnO from slag, they will see a body of literature with similar problems. Past authors have demonstrated rate limiting steps including chemical reaction control [7,8], manganese mass transport in the slag [9–11], and mixed mass transport control of both manganese in the metal and manganese oxide in the slag [12–14]. Without further explanation these seemingly conflicting results are difficult to rectify.

The seed for this study came from Sohn *et al.* [14] who discussed the idea of the rate controlling step changing with slag viscosity. When slags are viscous, fluid flow is difficult and thus mass transport of a species such as Mn^{2+} will proceed slowly with the potential to become a rate limiting step. The most important claim was made by Narita *et al.* [15] who studied silicon oxidation in hot metal using an iron oxide slag. These authors stated that there were three rate controlling steps in the system: when the FeO concentration is high the rate is limited by Si transport in the metal, when the FeO concentration is low the rate is limited by FeO transport in the slag, and when the concentration of FeO is at intermediate levels mixed mass transport control of both metallic Si and FeO in the slag is responsible for rate control. This is a reasonable conclusion, and it is assumed that a similar pattern can be found during the manganese oxide reduction from slag. This offers a possible explanation for the wide range of mechanisms proposed by authors studying seemingly similar systems; these systems are documented in detail in the following sections.

The current work seeks to analyze the possible mechanism shift believed to exist in systems where FeO or MnO are reduced from the slag. The authors will combine data from their own laboratory with data reported in the literature to develop a holistic picture of the reacting systems.

Unless explicitly noted all percentages are weight percent and ratios are by weight. A further goal of this study is to compare mass transfer coefficients in systems where metal droplets were reacted in slag and compare them to

experiments designed with a metal volume greater than the slag volume; the former conditions, evidenced by the present authors [2,3] and calculated from the work of Wu *et al.* [16] (discussed in detail in the following sections) are significantly faster than those reported by other researchers.

6.1.1. Mass Transport Relationships

Typically, when dealing with high temperature systems, chemical reaction steps are fast and are assumed to be in local equilibrium. For this reason, the authors will focus on mass transfer steps in the subsequent analysis. One exception to this statement is when a reaction step requires the nucleation of gas bubbles; in this case a chemical reaction step may be rate determining. A section is dedicated to the discussion of workers who have found chemical reaction control mechanisms and why these mechanisms may have been rate limiting.

The mass transfer coefficient of a species (k_i) is inversely proportional to the viscosity of the phase in which the controlling step exists. First, assuming transport through a stagnant film or Penetration Theory yields a proportionality between the mass transfer coefficient and the diffusion coefficient of $k_i \sim D_i$ or $k_i \sim D_i^{0.5}$ respectively. The Eyring or Stokes-Einstein relations [17] relate the diffusion coefficient to viscosity; in either case the proportionality is $D \sim \eta^{-1}$. Based on these relations the expected relationship between mass transfer coefficient and viscosity will be between $k_i \sim \eta^{-0.5}$ and $k_i \sim \eta^{-1}$. Similar relationships could be derived using the Sherwood number for boundary layer transport scenarios.

Ultimately, while these relationships are mathematically correct, the ionic nature of slag requires simultaneous charge balancing to occur alongside mass transport which may complicate these proportionalities.

Not all authors have reported their findings in a similar manner. Further, few have reported slag viscosities alongside their kinetic studies. The present work seeks to unify these authors conclusions with a consistent interpretation of the data using structured data conversions. First, reaction rate constants must be changed into consistent units of meters per second ($\frac{m}{s}$). Second, viscosity must be calculated from slag chemistry. The former is a matter of converting units, while the latter requires the use of an appropriate model to convert slag composition into viscosity; the models used for these calculations are discussed below. Molar volume and slag density data have been obtained from values in the Slag Atlas [17].

6.1.2. Viscosity Relationships

In order to convert a wide range of slag composition data into a consistent format, optical basicity has been calculated based on the available chemical data. Optical basicity parameters were obtained from Mills [18] and Duffy [19]; because there are so many proposed values for optical basicity, the values proposed in the original correlation were selected. Per the recommendations of Mills and Sridhar [20] a Λ_{CaF_2} value of 1.2 should be used for CaF_2 when calculating viscosity. The corrected optical basicity parameter Λ^{Corr} is used in the calculation to account for any effective loss in CaO concentration with aluminate bearing slags [21]. For general reference, V ratio ($\frac{CaO}{SiO_2}$) values for mono-, di-, and

tricalcium silicate are compressed onto the optical basicity scale as approximately 0.66, 0.74, and 0.79.

Two models have been used to interpret viscosity data. These models were chosen because they are the most generalized to analyzing a wide range of slag compositions and can handle the widest array of input compositions. Mills and Sridhar [20] proposed the following model that produces a viscosity number from optical basicity data. Equation 6.1 and Equation 6.2 are taken directly from these authors' work; Equation 6.3 is a fitted polynomial that represents B from the work of the authors (this fit should not be used for Λ^{Corr} greater than one).

$$\ln(\eta) = \ln(A) + \frac{B}{T} \quad (6.1)$$

$$\ln(A) = -232.69(\Lambda^{Corr})^2 + 357.32(\Lambda^{Corr}) - 144.17 \quad (6.2)$$

$$\begin{aligned} \frac{B}{1000} = & 2959.6(\Lambda^{Corr})^4 - 9754.7(\Lambda^{Corr})^3 \\ & + 12075.1(\Lambda^{Corr})^2 - 6681.5(\Lambda^{Corr})^1 \\ & + 1405.8 \end{aligned} \quad (6.3)$$

Ray and Pal [22] proposed the following model. This model tends to produce viscosity values approximately one order of magnitude higher than that of Mills and Sridhar. The model is detailed in Equation 6.4, Equation 6.5, and Equation 6.6 taken directly from the authors' work.

$$\eta = A T \exp\left(\frac{1000B}{T}\right) \quad (6.4)$$

$$-\ln(A) = 0.2056(B) + 12.492 \quad (6.5)$$

$$B = 297.14(\Lambda^{Corr})^2 - 466.69\Lambda^{Corr} + 196.22 \quad (6.6)$$

6.2. Literature Review

This section contains a review of the reduction literature analyzed as part of this study. It is broken into sections for easier reading and comparison. Appendix 1 summarizes all mass transfer coefficients and calculated values for each authors' dataset. Appendix 2 presents all initial mass data for the slag and metal systems. The chemical reactions have not been summarized because they were not analyzed in this paper. Some authors whose work was not incorporated into the study, but whose work adds important discussion, is also included.

6.2.1. Review of MnO Reduction Literature with Transport Limitations

Tarby and Philbrook [9] studied the rate of reduction of FeO and MnO via carbothermic reduction in CaO-SiO₂-Al₂O₃ slags. A graphite crucible and induction furnace were used to test several reduction conditions. The reaction was documented to occur in two stages: an initial fast stage characterized by a high degree of stirring from CO evolution and a second slower stage where CO evolution was slower. Both stages were described to be rate limited by mass transport of MnO or FeO in the slag but only the latter stage was quantified. To perform these tests 400g of carbon saturated iron and 100g of slag were used. Approximately 3.5 wt pct MnO was used for the MnO tests (the amount of FeO used is not clear but is assumed to be the same). Three major conditions were tested for the lime-silica-alumina ratio: slag 1 used a 50:50 ratio of CaO:Al₂O₃, slag 2 was 50:40:10 of CaO:Al₂O₃:SiO₂, and slag 3 was 50:10:40 CaO:Al₂O₃:SiO₂. For a reaction temperature of 1848K (1575°C), the mass transfer coefficients of MnO (k_{MnO}) for

slags 1, 2, and 3 were $5.5 \cdot 10^{-6}$ m/s, $6.2 \cdot 10^{-6}$ m/s, and $1.3 \cdot 10^{-6}$ m/s respectively. For FeO, k_{FeO} was $0.5 \cdot 10^{-6}$ m/s, $5.7 \cdot 10^{-6}$ m/s, and $2.3 \cdot 10^{-6}$ m/s for these same conditions.

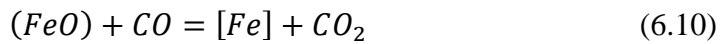
Daines and Pehlke [4] studied the silicothermic reduction of manganese oxide. A resistance furnace and zirconia crucible were used for 304g of metal (1.3 wt pct Si, balance Fe) and 210g of slag (5:43:33:10:10 ratio of MnO:CaO:SiO₂:Al₂O₃:MgO). These authors claimed that the reaction was rate limited by the mass transport of manganese in the metal, with a k_{Mn} value of $7 \cdot 10^{-6}$ m/s.

Yagi and Ono [10] studied the carbothermic reduction of MnO. A graphite crucible and induction furnace were used for reactions of 70g metal (carbon saturated iron) and 25g of slag (10:43:35:12 MnO:CaO:SiO₂:Al₂O₃). These authors analyzed the rate of reaction for two different temperatures and presented a calculation of the boundary layer thickness δ as a function of the rate of reaction (a method of quantifying the stirring effects of the rate of CO generation). At 1873K (1600°C) the mass transfer coefficient can be extracted from their data as a function of the rate of reaction in Equation 6.7; k_{MnO} is the mass transfer coefficient in the slag in $\frac{m}{s}$ and r_{Mn} is the rate of reaction in $\frac{mol}{s}$.

$$k_{MnO} = 0.0019 \cdot (r_{Mn})^{0.4579} \quad (6.7)$$

Pomfret and Grieveson [11] studied the carbothermic reduction of MnO. Typical metal samples were 100g of carbon-saturated iron while slags were a 4:45:45:6 ratio of MnO:CaO:SiO₂:MgO. They observed two reaction steps, first a high rate of CO generation and slag stirring followed by a slower stage slower with

much less CO generation occurring. They characterized the transition point from stage 1 to stage 2 to occur when the wt pct ratio (MnO)/[Mn] fell below about 3.3. Stage 2 of the reaction fit a model of manganese mass transport in the slag where k_{MnO} was $5 \cdot 10^{-6}$ m/s; the authors approximated a similar system under forced convection and estimated k_{MnO} as $8.6 \cdot 10^{-5}$ m/s. Evidence was presented demonstrating a complex three-part reaction mechanism. The individual components of the net reaction are Equation 6.8, Equation 6.9, and Equation 6.10; the overall reaction represented by Equation 6.11.



Kawai *et al.* [12] have performed what is perhaps the most comprehensive review on the exchange reaction of iron and manganese to date; no carbon or silicon was used as a reductant. A resistance furnace, at a fixed temperature of 1873K (1600°C), was used to react samples with 200g of iron and 20g of slag. The first part of their work studied the oxidation of manganese from the metal, and the second the reduction of MnO from slag. A mixed mass transport control model was used to analyze the data. Their data is displayed in Table 6.1.

Table 6.1a: Summary of Select Conditions from Kawai *et al.* [12] for Mixed Mass Transport Control

Dataset Label	Mn	Fe	MnO	CaO	SiO ₂	Al ₂ O ₃	FeO
2	0.6%	99.4%	0.0%	0.0%	25.1%	0.0%	74.6%
5	0.5%	99.5%	0.0%	25.3%	28.4%	0.0%	45.1%
6	0.5%	99.5%	0.0%	24.8%	35.4%	0.0%	37.1%
16	0.5%	99.5%	0.0%	23.5%	29.3%	10.4%	36.8%
22	0.0%	100%	17.4%	34.6%	37.0%	0.0%	9.5%
25	0.0%	100%	28.4%	26.8%	39.5%	0.0%	2.7%
31	0.0%	100%	33.1%	15.4%	32.5%	13.5%	5.5%

Table 6.1b: Summary of Select Conditions from Kawai *et al.* [12] for Mixed Mass Transport Control

Dataset Label	K_{Total}	k_{Slag}	k_{Metal}
2	0.79	5.9E-06	1.7E-04
5	0.46	1.6E-05	1.8E-04
6	0.91	2.3E-05	1.8E-04
16	0.33	6.1E-06	1.3E-04
22	0.88	1.2E-05	2.2E-04
25	0.88	2.1E-05	2.4E-04
31	0.97	1.2E-05	2.3E-04

Shinozaki *et al.* [13] studied the carbothermic rate of reduction of MnO from slag. Carbon levels were varied in iron samples of 100g and a 20g slag was used. The procedure here closely mirrors Kawai *et al.* [12]. The reaction was said to be controlled by transport of reacting species; k_{Metal} was approximately $2.0 \cdot 10^{-4}$ m/s for all conditions and k_{Slag} varied from $1.9 \cdot 10^{-6}$ m/s to $2.1 \cdot 10^{-5}$ m/s. The authors concluded that since the mass transfer coefficients determined here are similar to those without carbon in the melt [12] the impact of CO bubbling must be quite small.

Wu *et al.* [16] studied the simultaneous reduction of MnO and SiO₂ by carbon in molten iron. The experiments were designed such that the carbon-saturated iron

droplet (1.5g) fell through a slag column (170g, 15cm in depth) in approximately 1s. Slag transport control was ruled out as a rate-limiting step because the slag-metal interface was continually refreshed by fresh slag as the droplet sank. Table 6.2 is an attempt to quantify what the rate coefficients in the system might be, had they been calculated. The mass transfer coefficients were derived assuming only a single phase controlled the rate of reaction. The reaction rate coefficient assumes that the carbothermic reduction of silica is strictly a forward reaction dependent on the activities of carbon and silica. Under the assumption that k_{SiO_2} and k_{MnO} cannot be rate limiting, silicon transport in the metal is always (at least partially) rate limiting the system, sometimes alongside manganese (such as for 3B) or the silica reduction reaction (example 2B).

Table 6.2: Estimate of Rate Coefficients from Wu *et al.* [16]

Major Conditions				Reaction Constants (m/s)				
Slag	Λ^{Corr}	MnO	Si	k_{Si}	k_{SiO_2}	k_{Mn}	k_{MnO}	k_{Rxn}
1A	0.626	0.1%	0.4%	9.0E-04	3.2E-04	6.7E-03	3.4E-02	1.5E-03
1B	0.626	0.1%	1.9%	2.3E-04	1.1E-04	7.0E-03	4.5E-02	2.7E-04
2A	0.651	0.7%	0.4%	5.0E-03	1.2E-03	1.5E-02	1.2E-01	7.4E-03
2B	0.651	0.7%	1.1%	9.0E-05	2.6E-05	6.3E-04	5.6E-03	1.4E-04
2C	0.651	0.7%	1.9%	1.7E-03	5.6E-04	4.9E-04	4.9E-03	2.2E-03
3A	0.648	5.7%	0.4%	4.8E-03	1.4E-03	1.2E-02	5.1E-02	1.6E-02
3B	0.648	5.7%	1.9%	1.5E-04	6.2E-05	2.2E-04	1.0E-03	5.9E-04

Shibata *et al.* [5] studied the simultaneous oxidation of carbon, phosphorus, and silicon in slags containing MnO. An alumina crucible and resistance furnace were used to react 120g of metal alloy with 20g of slag. The authors devised a balanced flux model to study mass transfer coefficients for silicon, manganese, phosphorus, and sulfur in the system. Basicity was found to improve the partitioning of phosphorus and sulfur but had little effect on silicon and manganese.

Each species was assumed to experience a degree of transport control in both phases, thus the solutions provided were overall mass transfer coefficients. With these values they calculated the fraction of resistance experienced in each phase to overall transport and concluded that both manganese and silicon transport are limited in the metal phase. A summary of some of their data is found in Table 6.3; Λ^{Corr} is the corrected optical basicity estimate, k_{Si}^T the total mass transfer coefficient of Si species, and k_{Mn}^T the total mass transfer coefficient of Mn species.

Table 6.3: Summary of data from Shibata *et al.* [5] for lowest, average, and highest mass transfer coefficients

Slag	Temp. (K)	C	Si	Mn	Λ^{Corr}	k_{Si}^T (m/s)	k_{Mn}^T (m/s)
B1	1723	3.8%	0.17%	0.02%	0.7157	2.3E-05	1.3E-04
H1	1723	3.8%	0.20%	0.03%	0.7177	1.5E-04	2.4E-04
F1	1723	3.9%	0.24%	0.01%	0.7422	3.0E-04	4.1E-04

Sohn *et al.* [14] studied (MnO) reduction by carbon in liquid iron. 300g of iron alloy and 40g of slag were reaction with a range of compositions and temperature in a MgO crucible and resistance furnace. A mixed mass transport model of manganese was developed. General trends in the data were that for changes in temperature the overall mixed mass transfer coefficient is essentially fixed, the slag mass transfer coefficient rose, and the manganese partition fell. Changes to basicity were tested: at a value of 2 (consistent with dicalcium silicate) the largest total mass transfer coefficient was determined. As the basicity increased the partition ratio rose and the mass transfer coefficient of MnO fell. Both manganese partition and overall mass transfer coefficient rose with initial iron oxide content and k_{MnO} rose with (FeO) until 10 wt pct where no further increase was detected. Both total and slag mass transfer coefficients are at their peak in the

range of 2 to 4 wt pct carbon. Finally, an increase in the partition ratio of manganese is linked to an increase in the overall mass transfer coefficient but decrease in the slag mass transfer coefficient. All mass transfer coefficient information is provided graphically and needs interpretation, there is reasonable agreement for a value of k_{Mn} of $2.1 \cdot 10^{-5}$ m/s, k_{MnO} of $7.4 \cdot 10^{-5}$ m/s, and k_{Total} of $1.9 \cdot 10^{-5}$ m/s. Most of the transport resistance is found in the metal phase.

Vargas-Ramirez *et al.* [23] studied MnO reduction from slag by high carbon molten iron. An open induction furnace with 10kg of metal and 300g of slag was used for the experiments. They modelled their system with a balanced flux model, using mass transfer coefficients taken from the work of Ohguchi *et al.* [24]; these values were k_{slag} $4 \cdot 10^{-4}$ m/s and k_{Metal} $2 \cdot 10^{-4}$ m/s. The authors found the rate of manganese reduction increased with a higher starting carbon content in the melt. Basicity had essentially no effect on the rate.

Heo *et al.* [6] studied the silicothermic reduction of MnO from ferromanganese slag. They assumed that the silicon species controlled the reduction and that the induction furnace prevented [Si] from being the rate limiting step. A MgO crucible and induction furnace were used to study reactions between a 30:57:13 Si:Mn:Fe melt (150g) and slags (200g) with 40 wt pct MnO, 1:1 CaO:SiO₂ ratio and variable amounts of CaF₂. Two major conditions were tested: changes in temperature and changes in CaF₂ content of the slag. Equation 6.12 shows the relationship of the mass transfer coefficient k_{SiO_2} to temperature. The mass transfer

coefficient rose to approximately $1.1 \cdot 10^{-4}$ m/s with the addition of 5 wt pct CaF_2 but fell for higher concentrations (explained by the formation of solid cuspidine).

$$\ln(k_{\text{SiO}_2}) = -\left(\frac{26210}{T}\right) + 5.11 \quad (6.12)$$

Jamieson and Coley [2] studied the silicothermic reduction of MnO from slag. Alumina crucibles and a resistance furnace were used to study the reaction between metal droplets between 0.5-1.5g and with 5-15 wt pct silicon and 25g slags varied between 5-15 wt pct MnO and a 2:2:1 balance of $\text{CaO}:\text{SiO}_2:\text{Al}_2\text{O}_3$. They found the system could be reasonably fit assuming mass transport by MnO in the slag except when silicon contents were changed in the metal. Building from this, Jamieson *et al.* [3] built a balanced flux model considering mass transport of [Si], [Mn], (SiO_2) , and (MnO) , as well as the reaction to form SiO as potential rate-limiting steps. It was found that all nine tested datasets could be reasonably fit using mass transfer coefficients of k_{Metal} equal to $2.3 \cdot 10^{-4}$ m/s for both metal species and k_{Slag} of $6.7 \cdot 10^{-4}$ m/s for both slag species. SiO was found to have little chemical effect on the model, but caused a significant slowdown associated with reduction of the slag-metal interface.

6.2.2. Review of MnO Reduction Literature with Chemical Reaction Limitations

Daines and Pehlke [7] studied the carbothermic reduction of MnO. Graphite was the principle crucible type and the furnace type was not stated (it is likely to be a resistance furnace based on their past work [4]). Approximately 410g of carbon saturated iron and 210g of 5:43:33:10:10 $\text{MnO}:\text{CaO}:\text{SiO}_2:\text{Al}_2\text{O}_3:\text{MgO}$ slag were

used in the experiment. Stirring of the crucible was performed to rule out the impact of mass transport limitations (as no change in rate was documented in these tests). Chemical reaction control was claimed to be the rate limiting step, with a reaction rate constant k_1 of approximately $1.7 \cdot 10^{-8}$ m/s. A major foundation of this claim was that stirring did not impact the rate of reaction in the system. Wei *et al.* [25] (studying simultaneous desiliconization and decarburization with FeO) showed that CO could stir the system such that the effects of mechanical stirring were unnoticeable when FeO content of the slag was high. It is possible that the stirring effects of CO in the work of Daines and Pehlke masked the effects of mechanical stirring which would explain why mass transport did not appear as a viable rate limiting mechanism. Pomfret and Grieveson [11] also commented on the work of Daines and Pehlke and postulated that the reason chemical reaction control was observed was because sampling times were later in the reaction than either themselves or those of Tarby and Philbrook [9], thus chemical reaction control did apply to this later reaction mechanism. Daines and Pehlke calculated mass transfer coefficients (assuming that mechanism was correct) which were k_{Mn} of $1 \cdot 10^{-7}$ m/s and k_{MnO} of $2 \cdot 10^{-6}$ m/s; the slag mass transport term is in reasonable agreement with the findings of several of the discussed authors. The only difference between this work and their earlier work [4] is a change from silicon to carbon in the metal. Slag transport control cannot be rate limiting with the carbothermic reduction if the mechanism is different than their earlier work but the slag compositions are the same.

Ashizuka *et al.* [26] studied the carbothermic and silicothermic reductions of MnO from slag. An induction furnace and graphite crucible were used with a range of test conditions. The data from Table 6.4 applies to reactions of 100g carbon-saturated iron and 50g of slag. The carbothermic work was chemical reaction rate limited, described by k_1 . The authors claimed that for a purely carbothermic reduction reaction the rate limiting step was the anodic CO generation reaction (contrast to over 5 wt pct Si where the rate controlling mechanism switched to manganese transport control in the slag). Most literature simply says that a reaction is chemical reaction controlled, without specifying whether it is CO nucleation or growth at the interface; this is an important distinction that should be considered by future authors.

Table 6.4: Data from Ashizuka *et al.* [26] for the Carbothermic Reduction of MnO

MnO	CaO	SiO ₂	Al ₂ O ₃	T (K)	T (°C)	k_1 (m/s)
4%	40%	50%	10%	1773	1500	9.8E-08
4%	40%	50%	10%	1873	1600	2.0E-07
3.9%	50%	40%	10%	1773	1500	3.4E-07
3.9%	50%	40%	10%	1873	1600	1.2E-06
2.3%	50%	0%	50%	1773	1500	1.9E-07
2.3%	50%	0%	50%	1873	1600	3.1E-07

Xu *et al.* [8] studied the carbothermic reduction of MnO in systems that started high in metallic manganese. The reported kinetic data is from datasets with 600g of ferromanganese between 0-30 wt pct Mn. The slag contained an approximately 40:29:26:5 ratio of MnO:CaO:SiO₂:FeO. The authors tracked a rapid increase in FeO content in the first 1000 seconds of reactions which essentially fell to zero by reactions' end. This evidence is used to support the exchange mechanism proposed by Pomfret and Grieveson (Equation 6.8) [11]. Geometric data for the

system was not reported, but some assumptions about the A/V ratio of the system allow for a conversion of reaction coefficients where k_{Eqn1} was $4.6 \cdot 10^{-7}$ m/s. Sulfur was found to slow the reaction further supporting reaction rate limitations.

Ostrovski *et al.* [27], using the doctoral work of several students, modelled the rate of reduction of MnO from ore in a ferromanganese slag assuming that chemical reaction was rate limiting. The rate constant k_{Rxn} in m/s equaled $1.2 \cdot 10^{-7}$ m/s at 1673K (1400°C) and fell with decreasing temperature. Several findings were discussed: when X_{SiO_2} is greater than 33 pct the rate of the system slows significantly (this is dynamic and occurs during the reaction if the condition is met as a result of SiO₂ product), reaction extent is increased with temperature (as is rate of reduction), and MnO equilibrium concentration in the ore falls with increasing basicity (though the effect of slag basicity is less apparent past a basicity of 1).

6.2.3. Review of Non-MnO Reduction Literature with Transport Limitations

Narita *et al.* [15] studied silicon oxidation by FeO. An induction furnace was used for the experiments, but the slag was held in an MgO crucible (with a graphite sheath). Between 1.5 and 3 kg of hot metal (4.3 C, 0.5Si, and 0.5Mn) was melted and then 100g of flux (containing FeO) was added. The authors identified conditions under which different mass transport steps operated. When FeO exceeds 40 wt pct the system is controlled by mass transport of silicon in the metal (where k_{Si} was approximately $4.4 \cdot 10^{-4}$ m/s). When the FeO was less than 10 wt pct of the slag the system was controlled by iron transport in the slag. Finally, when the slag composition was in between these values mixed mass transport control limited the

rate of reaction. Mass transfer coefficients were not listed for these latter two conditions.

Wei *et al.* [25] studied the reaction of silicon and carbon in iron with FeO in the slag. A graphite crucible was heated in a resistance furnace. Slag samples contained approximately 20 wt pct Li₂O; this slag component has the same optical basicity parameter as CaO, but as an alkali cation is expected to have a greater effect on decreasing viscosity [28]. Variations in initial [Si] and (FeO) were tested: the mass transfer coefficient of silicon k_{Si} rose linearly from $1.7 \cdot 10^{-4}$ m/s to $5.5 \cdot 10^{-4}$ m/s when iron oxide content in the slag was varied from 5 to 30 wt pct; when the initial silicon content is changed no change in k_{Si} was found. Stirring was found to increase the mass transfer coefficient of silicon, however, when the FeO concentration in the slag was high the authors commented that stirring had little effect because the high rate of decarburization already stirred the system. The mass transfer coefficients k_{FeO} and k_{SiO_2} were determined to be $3 \cdot 10^{-5}$ m/s and $2 \cdot 10^{-5}$ m/s; the rate of desiliconization was controlled by mixed mass transport because of a dependence on both k_{Si} and k_{FeO} .

Iwamasa and Fruehan [29] studied the reaction of silicon and iron oxide happening concurrently with desulfurization. An MgO crucible contained the slag and metal within an induction furnace. The carbon-saturated iron was 30g and tests were performed with different silicon concentrations (around 0.3 pct); the slag was 300g with a 50:45:5:0.14 CaO:SiO₂:MgO:S basis and FeO added between 0 and 5

pct. The best fit mass transfer coefficients for a mixed transport controlled reaction were k_{Si} equal to $3 \cdot 10^{-5}$ m/s and k_{FeO} equal to $2 \cdot 10^{-5}$ m/s.

Lee *et al.* [30] studied the aluminothermic reduction of FeO from slag using an induction furnace and MgO crucible. 5g of metal alloy, 40:60 Al:Fe was reacted with slags of variable composition; the slag mass was 70g and a standard slag had a basicity of 1.1. The authors assumed and modelled mass transport of FeO as the rate limiting step. The lowest reported value of k_{FeO} was $1.85 \cdot 10^{-4}$ m/s at 1773K (1500°C) which rose approximately by a factor of 2.5 when the basicity was increase to 1.4 or the temperature was raised by 50K.

6.2.4. Review of Non-MnO Reduction Literature with Chemical Reaction Limitations

Sain and Belton [31] studied the kinetics of decarburization in liquid iron in a system designed to eliminate mass transport as a rate controlling step. The liquid iron-carbon alloy was blown with a jet of CO/CO₂. The authors summarized that carbon mass transport is approximately $3.5 \cdot 10^{-4}$ m/s at a temperature of 1823-1873K (1550-1600°C) in induction furnaces. Results indicated that the rate of decomposition of chemisorbed CO₂ is the rate limiting step, with a predictable reaction coefficient in the range of 1433 to 1873K (1160 to 1600°C) shown in Equation 6.13; the output is in units of $\left(\frac{\text{mole}}{\text{cm}^2 \cdot \text{s} \cdot \text{atm}}\right)$. At 1873K (1600°C) a reaction constant of 1.8m/s is expected; this reaction constant is extremely fast compared to other workers but may be a consequence of the controlled atmosphere of the reactions with a high CO₂ pressure. Sulfur additions to the melt lowered the reaction rate further substantiating these findings.

$$k_f = \exp\left(-\frac{11700}{T} - 0.48\right) \quad (6.13)$$

Sommerville *et al.* [32] studied the reduction of FeO from slag via carbon in molten iron. The experiment was conducted in a resistance furnace; the crucible in contact with metal was Al₂O₃ and slag was mild steel. 30g of carbon saturated iron reacted with approximately 31g of slag with a 38:41:19:2 ratio of CaO:SiO₂:Al₂O₃:FeO. The authors determined that a chemical reaction at the metal/gas interface was responsible for rate limitations (CO₂ decomposition into CO and oxygen). Further, there was essentially no interface between slag and metal because a gas layer formed and separated the two phases. Several FeO concentrations were tested, and the authors claimed that CO₂ decomposition at the gas-metal interface was rate limiting for wt pct FeO less than 2.5 pct, but above this value the limitation was on the gas/slag reaction interface. The reaction constant for FeO less than 2.5 pct was 0.45m/s. This value is only 35 pct lower than Equation 6.13 would predict.

Further work by Wei *et al.* [33] enhanced this analysis. The rate of decarburization is linearly related to the activity of FeO in the slag. Phosphorus was shown to dramatically decrease the rate of decarburization; as the small amount of phosphorus added to the slag was not believed to dramatically change the mass transport properties of the slag a different rate controlling step was investigated. Since the system showed a dependence on [P] as a surface-active element, the following reactions were proposed. Equation 6.14 represents the stoichiometric reaction (similar to the findings of the Pomfret and Grieveson [11] study), while

Equation 6.15 and Equation 6.16 represent the sub reactions of species and their interaction with vacant sites (\blacksquare) as well as sites occupied by oxygen atoms (\blacksquare^O).



Phosphorus poisons reaction sites, which means FeO transport is no longer the slowest kinetic step. When CO bubbles are large, the authors' model demonstrated that transport of CO₂ in the bubbles becomes rate limiting, while when the CO bubbles are small the poisoned interface interferes with the binding reaction in Equation 6.15. The overall rate constant for this reaction is approximately $5.8 \cdot 10^{-6}$ m/s. The authors found a slight increase in reaction rate with stirring and justified its effect on the chemical reaction by stating that CO bubbles at the interface were more readily detached (thus keeping the bubble radius smaller) when stirring occurred. These findings are interesting as they very thoroughly describe how a single system can exhibit multiple rate limiting steps. Their initial work reveals what appeared to be mixed mass transport control, as desiliconization had a dependency on both [Si] and (FeO). The decarburization reaction, for essentially identical slags, is slower than the silicothermic reaction. The system experiences a shift in mechanism from CO₂ transport to FeO decomposition at bubble interfaces, dependent on the radius of CO bubbles and amount of phosphorus poisoning the interface; lower bubble radii and higher phosphorus content of the slag pushes the system to reaction control by Equation 6.16.

6.2.5. Other Reviewed Literature with Comparative Findings

Ashizuka *et al.* [26] studied the carbothermic and silicothermic reductions of MnO from slag. An induction furnace and graphite crucible were used with a range of test conditions; systems studied used 100g carbon-saturated iron and 50g of slag. Silicothermic reduction experiments were carried out by adding silicon to the carbon-saturated iron. When silicon was added to the iron and exceeded 5 wt pct the rate controlling mechanism switched to manganese transport control in the slag. Note that the work of these authors was not incorporated into the analysis because the distinction between chemical reaction constants and mass transfer coefficients was not clear within the work. These findings are important because they demonstrate that despite the same slag composition different rate controlling steps exist within the system: when silicon reduced MnO, k_{MnO} was the most important kinetic parameter but when carbon was the reductant the system was limited by chemical reaction. This strongly indicates that while slag mass transport is the slowest step when silicon is present, nucleation control is likely to be responsible for the reaction rate limitation with carbon present.

Skjervheim and Olsen [34] offered a good review of the parameters effecting MnO reduction from ferromanganese slags. Synthetic and industrial slags 50g in mass were reacted with high carbon ferromanganese. Rate constants provided by the authors do not compare well with the work of others, however, a range of conditions were tested worth discussing. They found that stirring had no effect on the system, claiming this to mean that transport control was not present. They found

that MnO reduction was faster at the slag/graphite interfaces than the slag/metal interface. The authors blew CO and Ar at the interface during reactions, finding no significant increase in the rate of reaction when CO was blown but that there was an increase when argon was blown. These findings indicated that some form of reaction control, likely related to CO production because of the Ar experiments, was responsible for the rate controlling mechanism.

Sun [35] studied reaction rates with an iron-carbon alloy with FeO in the slag. Their study uses kinetic parameters from the work of others with their own model and offers a strong discussion on the rate limiting steps and factors influencing rate within the system. Their model had good agreement with experimental data up to 10 wt pct FeO in the slag; at this value internal oxidation of the metal droplet occurred causing surface area expansion of the melt which was not accommodated in the model. The rate of decarburization increased with FeO in the slag, carbon in the droplet, and size of the droplet but decreased with metal silicon content and ambient pressure.

6.3. Trend Analysis

6.3.1. Mass Transfer Coefficients vs. Optical Basicity

The following figures show the results of the data compilations. The mass transfer coefficients plotted in the following series of figures were assumed to have been determined from correctly identified rate determining steps in the original source. Figure 6.1 shows the slag mass transfer coefficients k_{SiO_2} , k_{MnO} , and k_{FeO} plotted against the corrected optical basicity. Initially there does not appear to be a trend, but with further consideration of the specific datasets a relationship exists.

Figure 6.2 shows the same data except the data of Wu *et al.* [16] and Jamieson *et al.* [3] has been removed; these authors are the only ones to have performed experiments with large slags and metal droplets. As will be seen, these droplet experiments appear not to trend with the rest of the data for optical basicity, viscosity, or conductivity.

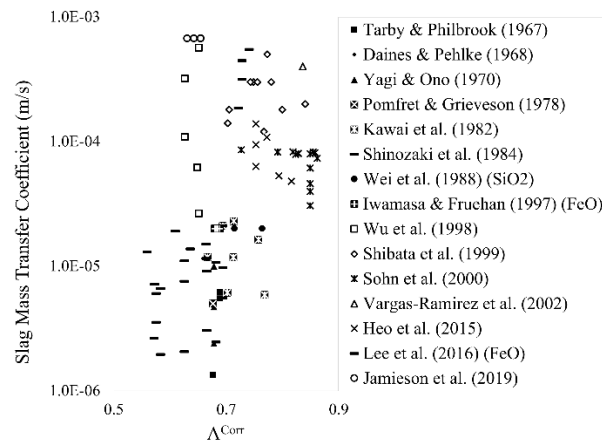


Figure 6.1: All slag mass transfer coefficients plotted against the corrected optical basicity.

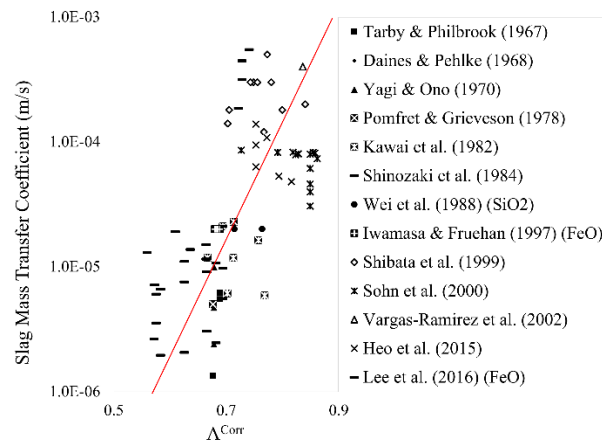


Figure 6.2: All slag mass transfer coefficients (without the droplet experiments).

In Figure 6.2 a sharp jump in mass transfer coefficients can be seen that corresponds with this structural shift in the slag from approximately 0.66 to 0.74; a line has been *drawn* to demonstrate this trend. This trend corresponds well with the

current understanding of polymeric slag: below a 2:1 molar ratio of CaO:SiO₂ the slag is polymeric with dimers in the melt. These dimers are larger and therefore harder to move through the slag than smaller ions. At a 2:1 ratio all silica is broken down to the SiO₄⁴⁻ ion, the smallest unit cell of silica. There is a gap in the data that appears to indicate that two apparent groups of data exist, but this can easily be attributed to a lack of data from the literature.

As one would expect the optical basicity has no relationship with mass transfer coefficient in the metal. Most authors report k_{Metal} equal to approximately $3 \cdot 10^{-4}$ m/s for a temperature ranging from 1673 and 1873K (1400 and 1600°C).

6.3.2. Viscosity vs. Slag Mass Transfer Coefficients

The models proposed relating viscosity to optical basicity apply to liquid slags. This poses a problem for some of the highly basic slag systems in the analyzed datasets with a high solid fraction. Solids dramatically increase the viscosity of slags in which they exist. Roscoe [36] developed Equation 6.17 to describe the impact of spheres suspended in a liquid: η_S is the viscosity of the suspension, η_L is the viscosity of the liquid slag only, and V_f is the volume fraction of solid in the slag.

$$\eta_S = \eta_L (1 - V_f)^{-2.5} \quad (6.17)$$

A study of basic slags performed by Seok *et al.* [37] revealed that the behavior of basic slags is different than most other solutions and proposed a modified form of Roscoe's equation. Equation 6.18 is similar to that of Roscoe, though a and n are incorporated to better describe non-standard systems. The latter value remains

fixed at 2.5 for spherical particles. In order to estimate a the compositional data of Seok *et al.* [37] and Liu *et al.* [38] were converted to optical basicity values, and these values plotted against the proposed a coefficient for that dataset. An approximation of the relationship is found in Equation 6.19 but, as most authors studying these coefficients readily admit, the fit is poor.

$$\eta_S = \eta_L(1 - aV_f)^{-n} \quad (6.18)$$

$$a = -4.62 \cdot \Lambda^{Corr} + 6.82 \quad (6.19)$$

FactSage™ was used to estimate the solid fraction of the slags. This poses a difficulty with some datasets because the proposed equilibrium slag is 100% solid which is obviously not a viable solution. In these circumstances, a value of V_f of 0.25 is fixed; this is essentially a stand-in for saying that the data from a specific authors work indicates viscosity is very high, it should not be quantitatively considered.

The effects of viscosity on the slag mass transfer coefficient are plotted in Figure 6.3 and Figure 6.4. As can be seen there is no apparent effect of viscosity on the slag mass transfer coefficient.

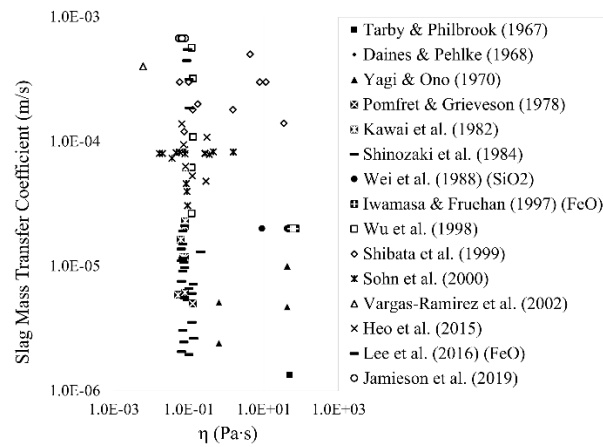


Figure 6.3: Viscosity modelled from the data of Mills & Sridhar [20]

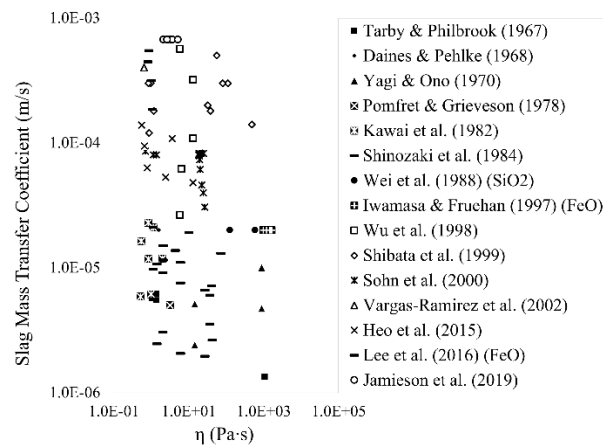


Figure 6.4: Viscosity data modelled from the data of Ray & Pal [22]

This is not an expected outcome, but as the figures above show that scatter of data is so wide that no reasonable approximation can be made.

6.3.3. Cationic Conductivity vs. Slag Mass Transfer Coefficients

The ionic nature of slags means that transport processes are not simply about mass flow but charge balancing and transport as well. This analysis looks at the cationic conductivity of the slag systems. In slags where MnO is the primary oxidant the oxygen potential of the system is expected to be quite low, thus it is assumed that charge hopping of electrons such as is common in Fe^{3+}/Fe^{2+} systems

will not occur. The extended Nernst-Einstein equation [39] is presented in Equation 6.20 where D is the diffusion coefficient ($\frac{cm^3}{s}$), C is the concentration of the conducting cation ($\frac{mol}{cm^3}$), z is the charge number of the conducting cation (i.e. 2), F is the Faraday constant ($96485 \frac{C}{mol}$), R is the gas constant ($8.314 \frac{J}{mol-K}$), and T is the temperature in Kelvin.

$$\sigma_{Total} = \sum \frac{D_i C_i (z_i F)^2}{RT} \quad (6.20)$$

For this analysis the sum of Ca^{2+} , Mn^{2+} , Fe^{2+} , and Mg^{2+} charges were used to calculate the total conductivity. Electronic conductivity associated with Mn^{3+}/Mn^{2+} at these reaction temperatures is quite low, because Mn^{2+} is very stable. For FeO rich systems, the work of Barati and Coley [39–41] was used to estimate the Fe^{3+}/Fe^{2+} ratio. The slags of Lee *et al.* [30] may have as much as 33 pct Fe^{3+} and the works of Sohn *et al.* [14] and Shibata *et al.* [5] may have around 10% Fe^{3+} . All other systems should have negligible electronic conductivity compared to cationic conductivity.

Diffusivity data for this analysis was taken from a curve fit of data from Dolan and Johnston [42] at 1773K (1500°C) because the data was plotted as a function of optical basicity; extrapolation of the data may break down at very high optical basicity values (greater than 0.75) but that is a relatively small portion of the dataset. No relationship of Mg^{2+} with optical basicity was found, so an estimate of $D^{Mg^{2+}}/D^{Ca^{2+}}$ was obtained from the work of Saito and Maruya [43] and Oishi *et*

al. [44] to be approximately 3.3. Thus, the estimated diffusion coefficient of magnesium is 3.3 times that of calcium for a given optical basicity.

Figure 6.5 shows the outcome of this analysis, where slag mass transfer coefficients are plotted against conductivity. A line has once again been *drawn* with an identical slope to Figure 6.2. Data from Wu *et al.* [16] and Jamieson *et al.* [3] has been excluded as it shows the same offset as in Figure 6.1. This plot and Figure 6.2 share the same overall shape, indicating that mass transfer coefficients rise with optical basicity and rise with cationic conductivity in the slag. This explains why there was no relationship with viscosity: mass transport of molecules is not the rate limiting step, instead transport of charged cations in the slag is more significant.

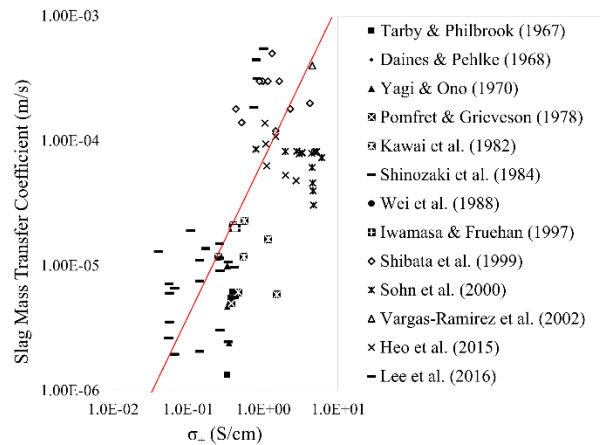


Figure 6.5: Slag mass transfer coefficients vs. cationic conductivity of the slags.

Electronic conduction was ignored but would be applied to the work of Shibata *et al.* [5], Sohn *et al.* [14], and Lee *et al.* [30]. Data from these authors are on the right side of the figure and would be expected to shift further right as the total conductivity of the system rises. In conclusion, as optical basicity rises cationic conductivity rises, and with both the slag mass transfer coefficient rises.

6.3.4. Manganese Partition Coefficient vs. Slag Mass Transfer Coefficient

A major goal of this study is to rectify the apparently large difference in mass transfer coefficients proposed by the present authors [2,3] and others [16] with many other researchers. The major difference between these sets of work seemed to be that authors who reported smaller mass transfer coefficients in the slag also performed experiments where the metal/slag volume was high (a more traditional experimental technique than droplet experiments). In order to do this all experimental data that suggested manganese transport control in either the slag or metal (or both) was analyzed under the assumption that mixed mass transport, by both manganese in the slag and metal, was rate limiting. One possible outcome of such a derivation is shown in Equation 6.21. Here J_{MnO} is the flux of MnO, k_{MnO} and k_{Mn} are the mass transfer coefficients of manganese in slag and metal respectively, C_{Mn}^b is the bulk concentration of manganese in the metal ($\frac{mol}{m^3}$), C_{MnO}^b is the bulk concentration of manganese oxide in the slag, and L_{Mn} is the partition coefficient described in Equation 6.22.

$$J_{MnO} = \frac{1}{\left(\frac{1}{k_{MnO}} + \frac{L_{Mn}}{k_{Mn}}\right)} (C_{Mn}^b L_{Mn} - C_{MnO}^b) \quad (6.21)$$

The manganese partition is described below. The local equilibrium assumption says that the ratio of interfacial concentrations of MnO (C_{MnO}^i) and Mn (C_{Mn}^i) is equal to the ratio of concentrations at equilibrium for MnO (C_{MnO}^E) and Mn (C_{Mn}^E). The final conversion yields equilibrium moles of MnO (n_{MnO}^E), equilibrium moles Mn (n_{Mn}^E), metal volume (V_M), and slag volume (V_S).

$$L_{Mn} = \frac{C_{MnO}^i}{C_{Mn}^i} = \frac{C_{MnO}^E}{C_{Mn}^E} = \left(\frac{n_{MnO}^E}{V_S} \right) \left(\frac{V_M}{n_{Mn}^E} \right) \quad (6.22)$$

The total mass transfer coefficient is the only concern in this analysis and is shown in Equation 6.23. This equation shows that the overall mass transfer coefficient is dependent on both the metal and slag mass transfer coefficients; the resistance contributed by the metal phase scales with the manganese partition. As the partition rises, the volume ratio of metal/slag rises and/or the manganese more preferentially segregates into the slag phase than the metal phase; either condition raises the relative resistance of the metal with respect to the entire system.

$$k_{Total} = \frac{1}{\left(\frac{1}{k_{MnO}} + \frac{L_{Mn}}{k_{Mn}} \right)} \quad (6.23)$$

Metal and slag volumes were calculated from initial conditions and density, and the values for n_{MnO}^E and n_{Mn}^E were estimated using the Equilib module of FactSage™ [45]. Figure 6.6 shows a plot of k_{Total} versus the partition. The outcropping of points near the center left of the plot are from the datasets of Tarby and Philbrook [9], Yagi and Ono [10], and Pomfret and Grieveson [11] all of whom analyzed the system with only a mass transfer coefficient for the slag phase. Some of the data from Shinozaki *et al.* [13] falls into this category; these leftmost points from the dataset have high amounts of alumina (40 wt pct) but this is not true for the other authors. Much of the discrepancy seems to come from reported slag mass transfer coefficients nearer to 10^{-6} m/s; it is possible that these values are too low with respect to the other systems.

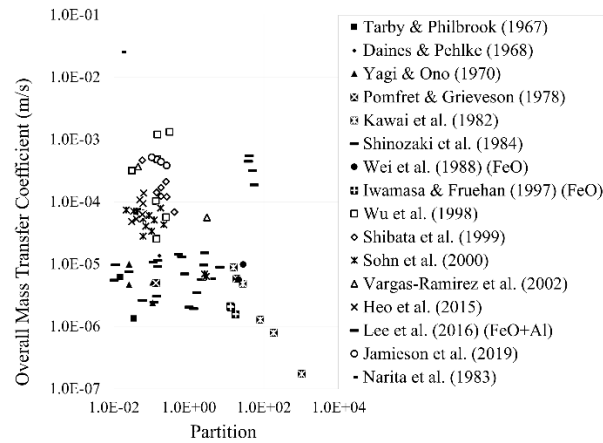


Figure 6.6: Partition vs. overall mass transfer coefficient.

Figure 6.7 removes the mentioned datasets to isolate the trendline across these systems; the system of Narita *et al.* [15] (where only k_{Si} was reported) and Lee *et al.* [30] (where the aluminothermic reduction occurred) were also removed. The red line is not fitted, but a visualization of what the trend in the data appears to be. With the noted exceptions, a very good relationship between the total transport resistance in the system and the partition is achieved for the remaining datasets, *including* the dataset Wei *et al.* [25] for mixed mass transport using k_{Si} and k_{SiO_2} and Iwamasa and Fruehan [29] for mixed mass transport using k_{Si} and k_{FeO} . The partition for these workers was calculated from the ratio of silica to silicon at equilibrium. This relationship indicates that the best method of analyzing these systems is by mixed mass transport and that the differences between calculated mass transfer coefficients can be explained by the equilibrium partition of the system. The trend is described by Equation 6.24.

$$\text{Log}_{10}(k_{Total}) = (-0.8) \cdot \text{Log}_{10}(L_{Mn}) - 4.4 \quad (6.24)$$

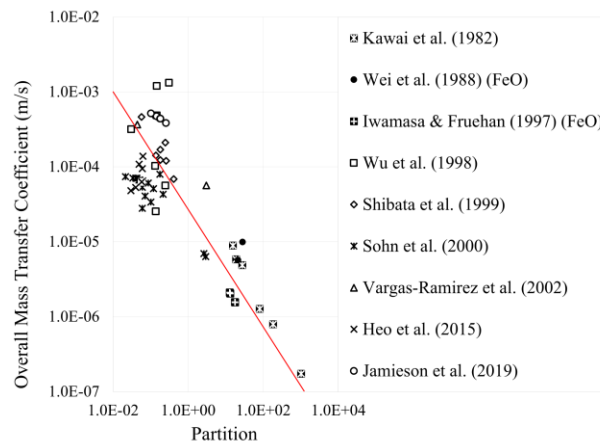


Figure 6.7: Partition vs. overall mass transfer coefficient with trendline.

Figure 6.7 is interesting because, despite different reported mass transfer coefficients and systems, factoring in the partition appears to show a good relationship between the datasets and the partition. This indicates that the best method of interpreting data from these systems is through mixed mass transport control. The work of Lee *et al.* [30] shows a clear deviation associated with the aluminothermic reduction of FeO; it would be interesting if a correlation could be developed to determine if the drawn line reliably shifts with the system of study.

6.4. Discussion

It is clear from Figure 6.7 that mixed transport control is the best method of analyzing these systems. Assuming a single phase controls the system does not properly identify the influence of the partition as an important kinetic parameter, thus the mass transfer coefficients produced from such an analysis are only able to describe similarly designed systems with similar partitions; where possible the overall mass transfer coefficient should always be investigated.

All presented figures support the conclusion that mixed mass transport control has been thoroughly documented across a wide range of systems and experimental conditions. With a few exceptions, mass transfer coefficients for silica, manganese oxide, and iron oxide can be trended on the same series of plots. These systems fit well in Figure 6.6 and show how the total overall mass transfer coefficient falls as a function of slag and metal mass transfer coefficients, but more importantly the equilibrium partition ratio of the system.

Authors studying systems with a large metal/slag ratio will see resistance contributions from the metal as a larger influence on the total resistance, thus the metal is typically found to be the rate-limiting species. When droplet experiments or experiments with a low metal/slag ratio are performed most of the transport resistance will be found in the slag, thus slag mass transport control conclusions are more obvious. The reality is that all of these findings are best considered through mixed mass transport control models.

6.4.1. Reaction Control Mechanisms

While a significant number of the studied pieces of literature support the idea that mixed mass transport control (or simpler single source mass transport control) are the rate-limiting mechanism, many others have quantified chemical reaction limitations [7,8,26,27,31–34]. It is worth spending time explaining why some systems may be chemical reaction rate limited instead of mass transport limited. Only reactions that involved a carbothermic reduction were documented to have chemical reaction rate limitations; no silicothermic reduction study reported here showed evidence of chemical reaction limitation. When silicon *and* carbon were

present, the reduction rate *could* be reaction limited. This is evidence that the formation of a new phase is likely to influence the rate limiting step of a reaction: silicon does not need to form a gas when it reduces oxides from the slag, however carbon must form CO and CO₂ during the reduction process.

Chemical reactions are known to be sensitive to temperature (much more so than transport processes) and as such it is a very common assumption that chemical reactions do not limit systems at traditional steelmaking temperatures. It should be noted that in the studied literature some authors simply assumed that chemical reactions were not responsible for the rate limiting step without numerically eliminating it (they still achieved a satisfactory fit with appropriate transport assumptions). Table 6.5 shows the temperature used for some of the noted authors' studies who reported a chemical reaction as the rate limiting step.

Table 6.5: Chemical Reaction Control Studies with Low Temperature

Sommerville <i>et al.</i> [32]	1648K (1375°C)
Wei <i>et al.</i> [33]	1573K (1300°C)
Ostrovski <i>et al.</i> [27]	1523-1673K (1250-1400°C)

Temperature alone cannot be responsible for chemical rate limitations, as Wei *et al.* [25] carried out their experiments at 1573K (1300°C) and determined that the system was transport limited; they mechanically stirred their system, but this should not affect a system that was naturally limited by the chemical reaction. These authors were the only ones who reported using Li₂O in their system. Li₂O improves fluidity by depolymerizing the silicate structure [46,47]. This was one of two studies conducted by Wei *et al.* [25], this one emphasizing the study of desiliconization. Their latter study [33] on decarburization was determined to be

chemical reaction limited. It should be assumed from these findings that the chemical reaction rate of silicon oxidation at the slag-metal interface is sufficiently fast that at comparably low temperatures it remains transport limited, unlike the carbothermic reduction. All other studies in this document that claimed mass transport limited systems were conducted above 1723K (1450°C).

For a fixed temperature, the primary difference between mass transport and chemical reaction control is that the former is first order with respect to a single species (unless mixed mass transport assumptions are applied). These examples are shown in the following sample equations; CO₂ transport is shown in Equation 6.25 and the Boudouard reaction in Equation 6.26. In the following equations, J_{CO_2} and R_{CO_2} are the flux and reaction rate of the corresponding reactions, $C_i^{CO_2}$ and $C_b^{CO_2}$ are the interfacial and bulk concentration of CO₂. The interfacial concentration can be readily converted to mole fraction $X_i^{CO_2}$ divided by the molar volume of the gas V_{Gas} ; the mole fraction is readily related to the partial pressure of CO₂ in the bubbles. For the rate equation, k_{Fwd} is the reaction constant, p_{CO_2} and p_{CO} are the partial pressures of CO₂ and CO, a_C is the activity of carbon, and K_{CO_2} is the equilibrium constant for the reaction.

$$J_{CO_2} = k_{CO_2} \cdot (C_i^{CO_2} - C_b^{CO_2}) = k_{CO_2} \cdot \left(\frac{X_i^{CO_2}}{V_{Gas}} - C_b^{CO_2} \right) \quad (6.25)$$

$$R_{CO_2} = \frac{k_{Fwd}}{V_{Gas}} \cdot \left(p_{CO_2} \cdot a_C - \frac{p_{CO}^2}{K_{CO_2}} \right) \quad (6.26)$$

What these equations show is that both the rate and flux are linearly dependent on the partial pressure of CO₂. At the temperatures under study the ratio

of CO to CO₂ is expected to be very large, which means both Equation 6.25 and Equation 6.26 would be expected to have a very slow reaction rate. The chemical reaction rate equation can be even slower if the activity of carbon is low or back pressure of CO is high. In cases where a graphite crucible is used a_C is expected to be high, but iron melts not saturated in carbon would have a lower carbon activity over the course of the reaction; all authors who reported rate control by a chemical reaction used a carbon saturated melt in a graphite crucible.

Daines and Pehlke [7] described the chemical reaction as the breakup of the oxygen ion into dissolved oxygen and two electrons. Ashizuka *et al.* [26] described the reaction as anodic CO evolution. Sain and Belton [31] determined that the rate limiting step is first order with respect to CO₂ and independent of carbon concentration; it should be noted that these authors designed the system to specifically eliminate the possibility of mass transport as the rate controlling step, which may explain why their rate data applies at high temperature. Sommerville *et al.* [32] described the rate limit, when the FeO content of slag was below 2.5 wt pct, as the decomposition of CO₂ at the gas/metal interface into CO and dissolved oxygen; above 2.5 wt pct FeO they believed that the control step was a reaction at the gas/slag interface. Wei *et al.* [33] offered what is likely the most complete explanation of the complex control mechanism: a model considering chemical reaction at the gas-slag interface, CO₂ transport across the bubble to the metal, and the chemical reaction occurring at the gas-metal interface; when the size of the CO bubbles is large transport of CO₂ controls the reaction and when the bubbles are

small chemical reactions control the system. Xu *et al.* [8] described the rate limiting reaction as the exchange of MnO with Fe at the slag-metal interface. Skjervheim and Olsen [34] described the controlling mechanism as it was related to the oxygen content in the slag: a fast reaction is associated with free oxygen in the slag and the slow reaction requires the breakdown of SiO_4^{4-} ions; Ostrovski and coworkers [27] came to the same conclusion. Using FactSageTM, in standard conditions the reduction of MnO by carbon is not favorable until just over 1573K (1300°C). Further, because few experiments are performed when a_C and a_{MnO} are equal to one, it seems highly likely that chemical reaction rate limitations occur because the driving force for the reaction is small. When comparisons are made to the carbothermic reduction of FeO, the equilibrium coefficients of the iron system are over two order of magnitude greater.

The best proposed mechanism is that by Wei *et al.* [33]. It is broad in scope and covers chemical reaction rate limitations at the gas-slag and gas-metal interface. This mechanistic explanation requires a nearly complete disruption of the slag and metal phases by gas. When this condition is true chemical reactions occur at both interfacial boundaries and CO₂ can become a transport limiting species as it ferries oxygen across the bubbles. Ultimately without a chemical reaction model to test these authors' data against, proving a specific mechanism is futile.

6.5. Conclusions

The work of many past authors has been analyzed in the context of carbothermic and silicothermic reduction of FeO, MnO, and SiO₂. An analysis of

the trends within the datasets shows that there is strong evidence supporting mixed mass transport control as the rate limiting step when the reaction temperature was above 1723K (1450°C); the only exception was the work of Sain and Belton [31] who deliberately prevented transport phenomena from being the rate limit. Where mass transport was not suggested by the original authors, descriptions of the chemical reaction are more difficult to make. Below 1673K (1400°C), where carbon is the primary reductant, the systems were always chemical reaction controlled. Where silicon is the reductant, mass transport dominates even at lower temperatures.

- 1) There is a relationship between the slag mass transfer coefficients k_{MnO} , k_{SiO_2} , and k_{FeO} and the optical basicity of the analyzed slags. The mass transfer coefficients appear to climb dramatically between 0.7 and 0.74 which corresponds to depolymerization of silicate structures to dicalcium silicate.
- 2) The mass transfer coefficient for metal species during both mixed and single species transport control is consistent among the findings between $3 \cdot 10^{-5}$ m/s and $3 \cdot 10^{-4}$ m/s across temperatures ranging from 1673 to 1873K (1400°C to 1600°C). As expected, there is no effect of slag optical basicity on the metal mass transfer coefficients.
- 3) There is a good relationship between the total transport resistance of these systems and the partition ratio. This confirms the expectation that mixed mass transport control is the best analytical method to determine the rate determining

step during the reduction of manganese oxide (where a chemical reaction is not controlling).

- 4) Chemical reaction control is typically associated with lower temperature experiments but is not limited to them. Chemical reactions appear limited to the carbothermic reduction experiments; the kinetics of desiliconization were always transport limited reactions.
- 5) For manganese reduction systems a trendline has been fitted which reasonably describes the majority of manganese reduction experiments as a function of the partition coefficient. This fit may explain why droplet experiments return faster mass transfer coefficients than those with a high metal/slag volume ratio.

6.6. Acknowledgements

The authors thank the National Science and Research Council of Canada (NSERC, STPGP463252-14) for funding support. Special thanks to ArcelorMittal Dofasco, Stelco, Praxair, and Hatch Ltd. for their in-kind support, technical expertise, and their many helpful discussions.

6.7. References

- [1] R. Elliott, K. Coley, S. Mostaghel, and M. Barati: *Jom*, 2018, vol. 70, pp. 1–11.
- [2] B.J. Jamieson and K.S. Coley: *Metall. Mater. Trans. B*, 2017, vol. 48, pp. 1613–24.
- [3] B.J. Jamieson, Y. Tabatabaei, M. Barati, and K. S. Coley: *Metall. Mater. Trans. B*, 2019, vol. 50, pp. 192–203.

- [4] W.L. Daines and R.D. Pehlke: *Trans. Met. Soc. AIME*, 1968, vol. 242, pp. 565–75.
- [5] E. Shibata, H. Sun, and K. Mori: *Metall. Mater. Trans. B*, 1999, vol. 30B, pp. 279–86.
- [6] J.H. Heo, Y. Chung, and J.H. Park: *Metall. Mater. Trans. B Process Metall. Mater. Process. Sci.*, 2015, vol. 46B, pp. 1154–61.
- [7] W.L. Daines and R.D. Pehlke: *Metall. Trans.*, 1971, vol. 2, pp. 1203–11.
- [8] K. Xu, G. Jiang, W. Ding, L. Gu, S. Guo, and B. Zhao: *ISIJ Int.*, 1993, vol. 33, pp. 104–8.
- [9] S.K. Tarby and W.O. Philbrook: *Trans. Metall. Soc. AIME*, 1967, vol. 239, pp. 1005–17.
- [10] T. Yagi and Y. Ono: *Trans. Iron Steel Inst. Japan*, 1970, vol. 10, pp. 36–37.
- [11] R.J. Pomfret and P. Grieveson: *Ironmak. Steelmak.*, 1978, vol. 5, pp. 191–97.
- [12] Y. Kawai, N. Shinozaki, and K. Mori: *Can. Metall. Q.*, 1982, vol. 21, pp. 385–91.
- [13] N. Shinozaki, K. Ishido, K. Mori, and Y. Kawai: *Tetsu-to-Hagane*, 1984, vol. 70, pp. 73–80.
- [14] H. Sohn, Z. Chen, and W. Jung: *Steel Res.*, 2000, vol. 71, pp. 145–52.
- [15] K. Narita, T. Makino, H. Matsumoto, A. Hikosaka, and J. Katsuda: *ISIJ*, 1983, vol. 69, pp. 1722–29.
- [16] A. Wu, P.C. Hayes, and H.G. Lee: *ISIJ Int.*, 1998, vol. 38, pp. 213–19.

- [17] M Allibert, H Gaye, J Geisler, D Janke, B J Keene, D Kirner, M Kowalski, J Lehmann, K C Mills, D Neuschutz, R Parra, C Saint Jours, P J Spencer, M Susa, M Tmar, and E Woermann: Slag Atlas, 2nd ed., 1995.
- [18] K.C. Mills: South. African Pyrometallurgy 2011, 2011, pp. 1–52.
- [19] J.A. Duffy: J. Chem. Educ., 1996, vol. 73, p. 1138.
- [20] K.C. Mills and S. Sridhar: Ironmak. Steelmak., 1999, vol. 26, pp. 262–68.
- [21] K.C. Mills: ISIJ Int., 1993, vol. 33, pp. 148–55.
- [22] H.S. Ray and S. Pal: Ironmak. Steelmak., 2004, vol. 31, pp. 125–30.
- [23] M. Vargas-Ramirez, A. Romero-Serrano, F. Chavez-Alcala, B. Zeifert, and M. Hallen-Lopez: Steel Res., 2002, vol. 73, pp. 378–84.
- [24] D.G.C. Robertson, B. Deo, and S. Ohguchi: Ironmak. Steelmak., 1984, vol. 11, pp. 41–55.
- [25] P. Wei, M. Sano, M. Hirasawa, and K. Mori: Trans. Iron Steel Inst. Japan, 1988, vol. 28, pp. 637–44.
- [26] M. Ashizuka, A. Moribe, and K. Sawamura: Tetsu-to-Hagane, 1975, vol. 61, pp. 36–45.
- [27] O. Ostrovski, S.E. Olsen, M. Tangstad, and M. Yastreboff: Can. Metall. Q., 2002, vol. 41, pp. 309–18.
- [28] I. Sohn and D.J. Min: Steel Res. Int., 2012, vol. 83, pp. 611–30.
- [29] P.K. Iwamasa and R.J. Fruehan: Metall. Mater. Trans. B Process Metall. Mater. Process. Sci., 1997, vol. 28, pp. 47–57.
- [30] J. Lee, J.S. Oh, and J. Lee: Jom, 2016, vol. 68, pp. 2359–64.

- Ph.D. Thesis – B. Jamieson – McMaster Univ. – Materials Science & Engineering
- [31] D.R. Sain and G.R. Belton: *Metall. Trans. B*, 1976, vol. 7, pp. 235–44.
- [32] I.D. Sommerville, P. Grieveson, and J. Taylor: *Ironmak. Steelmak.*, 1980, vol. 7, pp. 25–32.
- [33] P. Wei, M. Sano, M. Hirasawa, and K. Mori: *ISIJ Int.*, 1991, vol. 31, pp. 358–65.
- [34] T.A. Skjervheim and S.E. Olsen: *Infacon 7*, 1995, pp. 631–40.
- [35] H. Sun: *ISIJ Int.*, 2006, vol. 46, pp. 1560–69.
- [36] R. Roscoe: *Br. J. Appl. Phys.*, 1952, vol. 3, pp. 267–69.
- [37] S.H. Seok, S.M. Jung, Y.S. Lee, and D.J. Min: *ISIJ Int.*, 2007, vol. 47, pp. 1090–96.
- [38] Z. Liu, B. Blanpain, and M. Guo: in *7th Int. Symp. High-Temperature Metall. Process.*, 2016, pp. 263–69.
- [39] M. Barati and K.S. Coley: *Met. Mater. Trans. B*, 2006, vol. 37, pp. 51–60.
- [40] M. Barati and K.S. Coley: *Metall. Mater. Trans. B*, 2006, vol. 37, pp. 41–49.
- [41] M. Barati and K.S. Coley: *Metall. Mater. Trans. B*, 2006, vol. 37, pp. 61–69.
- [42] M.D. Dolan and R.F. Johnston: *Metall. Mater. Trans. B Process Metall. Mater. Process. Sci.*, 2004, vol. 35, pp. 675–84.
- [43] T. Saito and K. Maruya: *Sci. Reports Res. Institutes*, 1958, vol. 10, pp. 306–14.
- [44] Y. Oishi, N. Namba, and J.A. Pask: *J. Am. Ceram. Soc.*, 1982, vol. 65, pp. 247–53.
- [45] C.W. Bale, E. Bélisle, P. Chartrand, S.A. Decterov, G. Eriksson, A.E.

Gheribi, K. Hack, I.H. Jung, Y.B. Kang, J. Melançon, A.D. Pelton, S. Petersen, C. Robelin, J. Sangster, and M.A. Van Ende: *Calphad*, 2016, vol. 54, pp. 35–53.

[46] S. Sukenaga, N. Saito, K. Kawakami, and K. Nakashima: *ISIJ Int.*, 2006, vol. 46, pp. 352–58.

[47] H. Kim and I. Sohn: *Trans. Iron Steel Inst. Japan*, 2011, vol. 51, pp. 1–8.

6.8. Appendix 1 – Mass Transfer Coefficients & Calculated Data

Author	Year		Crucible	Furnace Type	k_{Slag}	k_{Metal}	k_{FeO}	T (K)	Λ^{Corr}	η (Pa·s) [20]	η (Pa·s) [22]	ρ_{Metal} (g/cm ³)	ρ_{Slag} (g/cm ³)	V_{Met} (cm ³ /mol)	V_{Slag} (cm ³ /mol)
Tarby & Philbrook	1967	[9]	Graphite	Induction	5.50E-06	No Value	5.00E-07	1848	0.69	8.3E-02	1.4E+00	6.27	2.82	7.54	23.95
Tarby & Philbrook	1967		Graphite	Induction	6.17E-06	No Value	5.67E-06	1848	0.69	8.3E-02	1.4E+00	6.27	2.86	7.54	22.97
Tarby & Philbrook	1967		Graphite	Induction	1.33E-06	No Value	2.33E-06	1848	0.68	4.8E+01	1.1E+03	6.27	2.77	7.54	21.55
Daines & Pehlke	1968	[4]	Zirconia	Resistance	2.00E-05	7.00E-06	No Value	1823	0.69	8.9E-02	1.6E+00	6.85	2.80	8.03	20.40
Yagi & Ono	1970	[10]	Graphite	Induction	2.40E-06	No Value	No Value	1773	0.68	6.3E-01	1.4E+01	6.25	2.89	7.45	21.17
Yagi & Ono	1970		Graphite	Induction	4.70E-06	No Value	No Value	1873	0.68	4.2E+01	8.8E+02	6.16	2.89	7.50	21.17
Yagi & Ono	1970		Graphite	Induction	5.10E-06	No Value	No Value	1773	0.68	6.3E-01	1.4E+01	6.25	2.89	7.45	21.17
Yagi & Ono	1970		Graphite	Induction	1.00E-05	No Value	No Value	1873	0.68	4.2E+01	8.8E+02	6.16	2.89	7.50	21.17
Pomfret & Grieveson	1978	[11]	Graphite	Resistance	5.00E-06	No Value	No Value	1723	0.68	1.3E-01	3.2E+00	6.41	2.70	7.48	20.85
Kawai <i>et al.</i>	1982	[12]	MgO	Resistance	5.87E-06	1.68E-04	No Value	1873	0.77	5.2E-02	5.1E-01	6.96	3.92	8.02	17.16
Kawai <i>et al.</i>	1982		MgO	Resistance	1.63E-05	1.78E-04	No Value	1873	0.76	6.1E-02	5.4E-01	6.96	3.37	8.02	18.69
Kawai <i>et al.</i>	1982		MgO	Resistance	2.30E-05	1.78E-04	No Value	1873	0.71	8.0E-02	8.3E-01	6.96	3.27	8.02	19.31
Kawai <i>et al.</i>	1982		MgO	Resistance	6.13E-06	1.29E-04	No Value	1873	0.70	7.9E-02	9.8E-01	6.96	3.26	8.02	19.48
Kawai <i>et al.</i>	1982		MgO	Resistance	1.17E-05	2.19E-04	No Value	1873	0.71	8.0E-02	8.4E-01	6.97	3.07	8.01	19.84
Kawai <i>et al.</i>	1982		MgO	Resistance	2.10E-05	2.39E-04	No Value	1873	0.69	7.8E-02	1.1E+00	6.97	3.15	8.01	19.70
Kawai <i>et al.</i>	1982		MgO	Resistance	1.19E-05	2.29E-04	No Value	1873	0.67	7.0E-02	2.0E+00	6.97	3.29	8.01	19.51
Narita <i>et al.</i>	1983	[15]	MgO	Induction	No Value	4.40E-04	No Value	1723	1.00	4.1E-08	1.4E+01	6.33	4.26	7.50	16.28
Shinozaki <i>et al.</i>	1984	[13]	Al ₂ O ₃	Induction	1.30E-05	1.91E-04	No Value	1873	0.56	2.1E-01	7.2E+01	6.82	2.69	7.91	23.33
Shinozaki <i>et al.</i>	1984		Al ₂ O ₃	Induction	6.61E-06	1.91E-04	No Value	1873	0.58	1.0E-01	2.7E+01	6.81	2.87	7.91	22.84
Shinozaki <i>et al.</i>	1984		Al ₂ O ₃	Induction	1.10E-05	1.91E-04	No Value	1873	0.63	6.4E-02	6.1E+00	6.81	2.91	7.91	22.11
Shinozaki <i>et al.</i>	1984		Al ₂ O ₃	Induction	1.90E-05	1.91E-04	No Value	1873	0.61	6.9E-02	1.0E+01	6.81	2.89	7.91	22.50
Shinozaki <i>et al.</i>	1984		Al ₂ O ₃	Induction	1.50E-05	1.91E-04	No Value	1873	0.66	6.9E-02	2.1E+00	6.82	2.87	7.91	23.00
Shinozaki <i>et al.</i>	1984		Al ₂ O ₃	Induction	6.02E-06	1.94E-04	No Value	1873	0.58	1.2E-01	3.6E+01	6.70	2.82	7.83	22.98
Shinozaki <i>et al.</i>	1984		Al ₂ O ₃	Induction	3.54E-06	1.95E-04	No Value	1873	0.58	1.2E-01	3.6E+01	6.65	2.82	7.80	22.98
Shinozaki <i>et al.</i>	1984		Al ₂ O ₃	Induction	7.13E-06	1.95E-04	No Value	1873	0.57	1.3E-01	4.1E+01	6.65	2.80	7.80	23.53
Shinozaki <i>et al.</i>	1984		Al ₂ O ₃	Induction	1.37E-05	1.96E-04	No Value	1873	0.64	6.3E-02	4.4E+00	6.65	2.84	7.80	22.01
Shinozaki <i>et al.</i>	1984		Al ₂ O ₃	Induction	9.11E-06	1.95E-04	No Value	1873	0.67	6.9E-02	2.0E+00	6.66	2.96	7.80	22.96
Shinozaki <i>et al.</i>	1984		Al ₂ O ₃	Induction	1.15E-05	1.95E-04	No Value	1873	0.66	6.9E-02	2.1E+00	6.66	2.87	7.80	23.00
Shinozaki <i>et al.</i>	1984		Al ₂ O ₃	Induction	1.07E-05	1.96E-04	No Value	1873	0.68	7.4E-02	1.4E+00	6.65	2.89	7.81	23.07
Shinozaki <i>et al.</i>	1984		Al ₂ O ₃	Induction	2.62E-06	2.07E-04	No Value	1873	0.57	1.4E-01	4.2E+01	6.29	2.79	7.58	23.56
Shinozaki <i>et al.</i>	1984		Al ₂ O ₃	Induction	7.55E-06	2.12E-04	No Value	1873	0.63	6.4E-02	6.1E+00	6.12	2.91	7.48	22.11
Shinozaki <i>et al.</i>	1984		Al ₂ O ₃	Induction	2.11E-05	2.12E-04	No Value	1873	0.69	7.8E-02	1.1E+00	6.12	2.89	7.48	22.84

Ph.D. Thesis – B. Jamieson – McMaster Univ. – Materials Science & Engineering

Author	Year	Cite	Crucible	Furnace Type	k_{slag}	k_{Metal}	k_{FeO}	T (K)	Λ^{Corr}	η (Pa·s) [20]	η (Pa·s) [22]	ρ_{Metal} (g/cm ³)	ρ_{Slag} (g/cm ³)	V, Met (cm ³ /mol)	V, Slag (cm ³ /mol)
Shinozaki <i>et al.</i>	1984		Al ₂ O ₃	Induction	1.95E-06	1.95E-04	No Value	1873	0.58	1.0E-01	2.7E+01	6.66	2.87	7.80	22.84
Shinozaki <i>et al.</i>	1984		Al ₂ O ₃	Induction	3.04E-06	1.96E-04	No Value	1873	0.67	6.9E-02	2.0E+00	6.65	2.96	7.79	22.96
Shinozaki <i>et al.</i>	1984		Al ₂ O ₃	Induction	9.70E-06	2.09E-04	No Value	1873	0.69	7.8E-02	1.1E+00	6.23	2.89	7.54	22.84
Shinozaki <i>et al.</i>	1984		Al ₂ O ₃	Induction	2.06E-06	1.94E-04	No Value	1873	0.63	6.4E-02	6.1E+00	6.69	2.91	7.82	22.11
Shinozaki <i>et al.</i>	1984		Al ₂ O ₃	Induction	2.46E-06	1.95E-04	No Value	1873	0.68	7.4E-02	1.4E+00	6.67	2.89	7.80	23.07
Shinozaki <i>et al.</i>	1984		Al ₂ O ₃	Induction	5.54E-06	2.09E-04	No Value	1873	0.69	7.8E-02	1.1E+00	6.22	2.89	7.53	22.84
Wei <i>et al.</i>	1988	[25]	Graphite	Resistance	2.00E-05	1.70E-04	3.00E-05	1573	0.71	4.2E+01	5.9E+02	6.44	2.75	7.36	21.09
Wei <i>et al.</i>	1988		Graphite	Resistance	2.00E-05	5.50E-04	3.00E-05	1573	0.76	9.0E+00	1.2E+02	6.44	3.10	7.36	19.47
Iwamasa & Fruehan	1997	[29]	MgO	Induction	No Value	3.00E-05	2.00E-05	1723	0.68	7.0E+01	1.6E+03	40.65	2.66	6.10	21.15
Iwamasa & Fruehan	1997		MgO	Induction	No Value	3.00E-05	2.00E-05	1723	0.69	5.2E+01	9.7E+02	40.66	2.72	6.10	20.82
Iwamasa & Fruehan	1997		MgO	Induction	No Value	3.00E-05	2.00E-05	1723	0.68	5.8E+01	1.2E+03	40.66	2.70	6.10	20.95
Iwamasa & Fruehan	1997		MgO	Induction	No Value	3.00E-05	2.00E-05	1723	0.68	6.6E+01	1.5E+03	40.66	2.67	6.10	21.08
Iwamasa & Fruehan	1997		MgO	Induction	No Value	3.00E-05	2.00E-05	1723	0.68	7.0E+01	1.6E+03	39.53	2.66	6.17	21.15
Iwamasa & Fruehan	1997		MgO	Induction	No Value	3.00E-05	2.00E-05	1723	0.69	5.2E+01	9.7E+02	39.45	2.72	6.18	20.82
Iwamasa & Fruehan	1997		MgO	Induction	No Value	3.00E-05	2.00E-05	1723	0.68	5.8E+01	1.2E+03	39.31	2.70	6.19	20.95
Iwamasa & Fruehan	1997		MgO	Induction	No Value	3.00E-05	2.00E-05	1723	0.68	6.6E+01	1.5E+03	39.42	2.67	6.18	21.08
Wu <i>et al.</i>	1998	[16]	Graphite	Induction	3.19E-04	8.97E-04	No Value	1733	0.63	1.3E-01	1.3E+01	5.23	2.78	6.97	22.45
Wu <i>et al.</i>	1998		Graphite	Induction	1.09E-04	2.34E-04	No Value	1733	0.63	1.3E-01	1.3E+01	6.06	2.78	7.48	22.45
Wu <i>et al.</i>	1998		Graphite	Induction	1.24E-03	5.00E-03	No Value	1733	0.65	1.2E-01	5.8E+00	6.27	2.74	7.45	22.10
Wu <i>et al.</i>	1998		Graphite	Induction	2.64E-05	9.02E-05	No Value	1733	0.65	1.2E-01	5.8E+00	6.26	2.74	7.52	22.10
Wu <i>et al.</i>	1998		Graphite	Induction	5.63E-04	4.89E-04	No Value	1733	0.65	1.2E-01	5.8E+00	6.12	2.74	7.51	22.10
Wu <i>et al.</i>	1998		Graphite	Induction	1.44E-03	4.78E-03	No Value	1733	0.65	1.2E-01	6.4E+00	6.30	2.86	7.47	21.78
Wu <i>et al.</i>	1998		Graphite	Induction	6.16E-05	1.54E-04	No Value	1733	0.65	1.2E-01	6.4E+00	6.18	2.86	7.55	21.78
Shibata <i>et al.</i>	1999	[5]	Alumina	Resistance	3.00E-04	No Value	3.00E-04	1723	0.75	9.9E-02	9.7E-01	6.46	3.39	7.53	18.66
Shibata <i>et al.</i>	1999		Alumina	Resistance	3.00E-04	3.75E-05	3.00E-04	1723	0.74	1.1E+01	1.1E+02	6.44	3.37	7.52	18.70
Shibata <i>et al.</i>	1999		Alumina	Resistance	1.80E-04	5.24E-04	1.80E-04	1723	0.80	1.5E+00	3.8E+01	6.44	3.74	7.52	17.46
Shibata <i>et al.</i>	1999		Alumina	Resistance	1.40E-04	2.18E-04	1.40E-04	1723	0.70	3.4E+01	4.8E+02	6.44	2.98	7.52	20.02
Shibata <i>et al.</i>	1999		Alumina	Resistance	5.00E-04	3.65E-04	5.00E-04	1723	0.77	4.3E+00	5.5E+01	6.43	3.73	7.52	17.65

Ph.D. Thesis – B. Jamieson – McMaster Univ. – Materials Science & Engineering

Author	Year	Cite	Crucible	Furnace Type	k_{Slag}	k_{Metal}	k_{FeO}	T (K)	Λ^{Corr}	η (Pa·s) [20]	η (Pa·s) [22]	ρ_{Metal} (g/cm ³)	ρ_{Slag} (g/cm ³)	V _{Met} (cm ³ /mol)	V _{Slag} (cm ³ /mol)
Shibata <i>et al.</i>	1999		Alumina	Resistance	1.20E-04	6.62E-05	1.20E-04	1723	0.77	7.5E-02	8.7E-01	6.45	3.40	7.52	18.34
Shibata <i>et al.</i>	1999		Alumina	Resistance	3.00E-04	1.74E-04	3.00E-04	1723	0.76	7.8E+00	8.0E+01	6.44	3.39	7.52	18.46
Shibata <i>et al.</i>	1999		Alumina	Resistance	2.00E-04	5.80E-05	2.00E-04	1723	0.84	1.7E-01	3.2E+01	6.45	4.26	7.52	16.34
Shibata <i>et al.</i>	1999		Alumina	Resistance	1.80E-04	No Value	1.80E-04	1723	0.71	1.3E-01	1.2E+00	6.47	3.18	7.53	19.76
Shibata <i>et al.</i>	1999		Alumina	Resistance	3.00E-04	1.62E-04	3.00E-04	1723	0.78	5.7E-02	8.4E-01	6.45	3.54	7.52	18.02
Sohn <i>et al.</i>	2000	[14]	MgO	Resistance	8.56E-05	2.00E-05	No Value	1873	0.73	7.8E-02	7.0E-01	6.65	3.04	7.80	18.84
Sohn <i>et al.</i>	2000		MgO	Resistance	8.23E-05	2.00E-05	No Value	1873	0.79	1.5E+00	2.5E+01	6.65	3.16	7.80	18.99
Sohn <i>et al.</i>	2000		MgO	Resistance	8.02E-05	2.00E-05	No Value	1873	0.83	2.7E-01	1.9E+01	6.65	3.24	7.80	18.97
Sohn <i>et al.</i>	2000		MgO	Resistance	8.14E-05	2.00E-05	No Value	1873	0.86	4.6E-02	1.9E+01	6.65	3.19	7.80	19.05
Sohn <i>et al.</i>	2000		MgO	Resistance	3.06E-05	1.99E-05	No Value	1773	0.85	9.3E-02	2.7E+01	6.72	3.43	7.72	18.31
Sohn <i>et al.</i>	2000		MgO	Resistance	3.97E-05	2.33E-05	No Value	1798	0.85	8.9E-02	2.4E+01	6.71	3.43	7.74	18.31
Sohn <i>et al.</i>	2000		MgO	Resistance	4.59E-05	2.59E-05	No Value	1823	0.85	8.5E-02	2.2E+01	6.69	3.43	7.76	18.31
Sohn <i>et al.</i>	2000		MgO	Resistance	6.11E-05	2.46E-05	No Value	1848	0.85	8.2E-02	2.0E+01	6.67	3.43	7.78	18.31
Sohn <i>et al.</i>	2000		MgO	Resistance	7.95E-05	2.00E-05	No Value	1873	0.85	7.9E-02	1.8E+01	6.65	3.43	7.80	18.31
Sohn <i>et al.</i>	2000		MgO	Resistance	8.27E-05	2.00E-05	No Value	1873	0.82	4.5E-01	1.9E+01	6.65	3.14	7.80	19.30
Sohn <i>et al.</i>	2000		MgO	Resistance	8.23E-05	2.00E-05	No Value	1873	0.85	5.7E-02	1.9E+01	6.65	3.16	7.80	18.29
Sohn <i>et al.</i>	2000		MgO	Resistance	7.35E-05	2.00E-05	No Value	1873	0.86	3.5E-02	1.9E+01	6.65	3.54	7.80	17.84
Sohn <i>et al.</i>	2000		MgO	Resistance	7.88E-05	2.00E-05	No Value	1873	0.82	3.5E-01	1.9E+01	6.65	3.30	7.80	19.15
Sohn <i>et al.</i>	2000		MgO	Resistance	8.02E-05	2.01E-05	No Value	1873	0.83	2.0E-02	1.4E+00	6.95	3.24	8.01	18.97
Sohn <i>et al.</i>	2000		MgO	Resistance	8.02E-05	2.00E-05	No Value	1873	0.83	2.7E-01	1.9E+01	6.79	3.24	7.90	18.97
Sohn <i>et al.</i>	2000		MgO	Resistance	8.02E-05	1.99E-05	No Value	1873	0.83	2.7E-01	1.9E+01	6.32	3.24	7.60	18.97
Sohn <i>et al.</i>	2000		MgO	Resistance	8.02E-05	1.98E-05	No Value	1873	0.83	2.7E-01	1.9E+01	6.14	3.24	7.49	18.97
Sohn <i>et al.</i>	2000		MgO	Resistance	8.02E-05	2.00E-05	No Value	1873	0.83	2.7E-01	1.9E+01	6.62	3.24	7.81	18.97
Sohn <i>et al.</i>	2000		MgO	Resistance	8.02E-05	2.00E-05	No Value	1873	0.83	2.7E-01	1.9E+01	6.59	3.24	7.83	18.97
Sohn <i>et al.</i>	2000		MgO	Resistance	8.02E-05	2.00E-05	No Value	1873	0.83	2.7E-01	1.9E+01	6.66	3.24	7.80	18.97
Sohn <i>et al.</i>	2000		MgO	Resistance	8.02E-05	2.01E-05	No Value	1873	0.83	1.6E-02	1.1E+00	6.97	3.24	8.01	18.97
Vargas-Ramirez <i>et al.</i>	2002	[23]	Al ₂ O ₃	Induction	4.00E-04	2.00E-04	No Value	1873	0.84	6.0E-03	6.4E-01	6.85	3.79	7.97	16.87
Vargas-Ramirez <i>et al.</i>	2002		Al ₂ O ₃	Induction	4.00E-04	2.00E-04	No Value	1873	0.84	6.0E-03	6.4E-01	6.61	3.79	7.81	16.87
Heo <i>et al.</i>	2015	[6]	MgO	Induction	6.30E-05	No Value	No Value	1773	0.75	8.2E-02	7.8E-01	4.18	3.24	10.11	18.88
Heo <i>et al.</i>	2015		MgO	Induction	1.08E-04	No Value	No Value	1773	0.77	3.0E-01	3.6E+00	4.18	3.44	10.11	18.28
Heo <i>et al.</i>	2015		MgO	Induction	5.30E-05	No Value	No Value	1773	0.79	1.2E-01	2.4E+00	4.18	3.67	10.11	17.65
Heo <i>et al.</i>	2015		MgO	Induction	4.80E-05	No Value	No Value	1773	0.82	2.9E-01	1.3E+01	4.18	3.94	10.11	16.99
Heo <i>et al.</i>	2015		MgO	Induction	9.45E-05	No Value	No Value	1823	0.75	7.3E-02	6.5E-01	4.12	3.24	10.27	18.88

Author	Year	Cite	Crucible	Furnace Type	k_{slag}	k_{Metal}	k_{FeO}	T (K)	Λ^{Corr}	η (Pa·s) [20]	η (Pa·s) [22]	ρ_{Metal} (g/cm ³)	ρ_{Slag} (g/cm ³)	V _{Met} (cm ³ /mol)	V _{Slag} (cm ³ /mol)
Heo <i>et al.</i>	2015		MgO	Induction	1.39E-04	No Value	No Value	1873	0.75	6.5E-02	5.5E-01	4.06	3.24	10.44	18.88
Lee <i>et al.</i>	2016	[30]	MgO	Induction	No Value	No Value	1.85E-04	1773	0.72	1.0E-01	1.1E+00	4.07	3.22	9.54	18.93
Lee <i>et al.</i>	2016		MgO	Induction	No Value	No Value	4.45E-04	1823	0.73	8.9E-02	8.2E-01	4.05	3.22	9.59	18.91
Lee <i>et al.</i>	2016		MgO	Induction	No Value	No Value	3.14E-04	1773	0.73	1.0E-01	9.9E-01	4.07	3.22	9.54	18.91
Lee <i>et al.</i>	2016		MgO	Induction	No Value	No Value	5.47E-04	1773	0.74	9.3E-02	8.6E-01	4.07	3.22	9.54	18.87
Jamieson <i>et al.</i>	2019	[2]	Al ₂ O ₃	Resistance	6.70E-04	2.30E-04	No Value	1873	0.65	6.6E-02	2.6E+00	5.47	2.96	8.69	21.14
Jamieson <i>et al.</i>	2019		Al ₂ O ₃	Resistance	6.70E-04	2.30E-04	No Value	1923	0.65	5.5E-02	2.1E+00	5.43	2.96	8.74	21.14
Jamieson <i>et al.</i>	2019		Al ₂ O ₃	Resistance	6.70E-04	2.30E-04	No Value	1823	0.65	8.1E-02	3.3E+00	5.50	2.96	8.63	21.14
Jamieson <i>et al.</i>	2019		Al ₂ O ₃	Resistance	6.70E-04	2.30E-04	No Value	1873	0.65	6.6E-02	2.6E+00	5.10	2.96	8.89	21.14
Jamieson <i>et al.</i>	2019		Al ₂ O ₃	Resistance	6.70E-04	2.30E-04	No Value	1873	0.65	6.6E-02	2.6E+00	5.89	2.96	8.47	21.14
Jamieson <i>et al.</i>	2019		Al ₂ O ₃	Resistance	6.70E-04	2.30E-04	No Value	1873	0.64	6.4E-02	3.7E+00	5.47	2.89	8.69	21.60
Jamieson <i>et al.</i>	2019		Al ₂ O ₃	Resistance	6.70E-04	2.30E-04	No Value	1873	0.63	6.3E-02	5.1E+00	5.47	2.82	8.69	22.09
Jamieson <i>et al.</i>	2019		Al ₂ O ₃	Resistance	6.70E-04	2.30E-04	No Value	1873	0.65	6.6E-02	2.6E+00	5.47	2.96	8.69	21.14
Jamieson <i>et al.</i>	2019		Al ₂ O ₃	Resistance	6.70E-04	2.30E-04	No Value	1873	0.65	6.6E-02	2.6E+00	5.47	2.96	8.69	21.14

6.9. Appendix 2 – Mass Data from Past Workers

Author	Year	Cite	[C] (g)	[Si] (g)	[Mn] (g)	[S] (g)	[Fe] (g)	m_{Metal} (g)	(MnO) (g)	(CaO) (g)	(SiO ₂) (g)	(Al ₂ O ₃) (g)	(MgO) (g)	(FeO) (g)	(CaF ₂) (g)	m_{slag} (g)
Tarby & Philbrook	1967	[9]	18.40	0.20	0.00	0.00	381.40	400.00	3.5	47.3	0.0	49.2	0.0	0.0	0.0	100.0
Tarby & Philbrook	1967		18.40	0.20	0.00	0.00	381.40	400.00	3.5	48.3	7.7	40.5	0.0	0.0	0.0	100.0
Tarby & Philbrook	1967		18.40	0.20	0.00	0.00	381.40	400.00	3.5	49.2	38.8	8.5	0.0	0.0	0.0	100.0
Daines & Pehlke	1968	[4]	0.00	4.00	0.00	0.00	300.00	304.00	10.0	90.0	70.0	20.0	20.0	0.0	0.0	210.0
Yagi & Ono	1970	[10]	3.54	0.00	0.00	0.00	66.47	70.00	2.5	10.8	8.6	3.0	0.0	0.0	0.0	25.0
Yagi & Ono	1970		3.71	0.00	0.00	0.00	66.29	70.00	2.5	10.8	8.6	3.0	0.0	0.0	0.0	25.0
Yagi & Ono	1970		3.54	0.00	0.00	0.00	66.47	70.00	2.5	10.8	8.6	3.0	0.0	0.0	0.0	25.0
Yagi & Ono	1970		3.71	0.00	0.00	0.00	66.29	70.00	2.5	10.8	8.6	3.0	0.0	0.0	0.0	25.0
Pomfret & Grieverson	1978	[11]	4.20	0.00	0.00	0.00	95.80	100.00	1.2	13.5	13.5	0.0	1.8	0.0	0.0	30.0
Kawai <i>et al.</i>	1982	[12]	0.00	0.00	1.13	0.00	198.87	200.00	0.0	0.0	5.0	0.0	0.0	14.9	0.0	20.0
Kawai <i>et al.</i>	1982		0.00	0.00	0.60	0.00	109.40	110.00	0.0	7.6	8.5	0.0	0.0	13.5	0.0	30.0
Kawai <i>et al.</i>	1982		0.00	0.00	1.05	0.00	198.95	200.00	0.0	5.0	7.1	0.0	0.0	7.4	0.0	20.0
Kawai <i>et al.</i>	1982		0.00	0.00	0.91	0.00	199.09	200.00	0.0	4.7	5.9	2.1	0.0	7.4	0.0	20.0
Kawai <i>et al.</i>	1982		0.00	0.00	0.00	0.00	200.00	200.00	3.5	6.9	7.4	0.0	0.0	1.9	0.0	20.0
Kawai <i>et al.</i>	1982		0.00	0.00	0.00	0.00	200.00	200.00	5.7	5.4	7.9	0.0	0.0	0.5	0.0	20.0
Kawai <i>et al.</i>	1982		0.00	0.00	0.00	0.00	200.00	200.00	6.6	3.1	6.5	2.7	0.0	1.1	0.0	20.0
Narita <i>et al.</i>	1983	[15]	96.75	11.25	11.25	0.14	2131	2250	0.0	10.0	0.0	0.0	0.0	90.0	0.0	100.0

Author	Year	Cite	[C] (g)	[Si] (g)	[Mn] (g)	[S] (g)	[Fe] (g)	m _{Metal} (g)	(MnO) (g)	(CaO) (g)	(SiO ₂) (g)	(Al ₂ O ₃) (g)	(MgO) (g)	(FeO) (g)	(CaF ₂) (g)	m _{Slag} (g)
Shinozaki <i>et al.</i>	1984	[13]	0.85	0.03	0.00	0.00	99.12	100.00	0.9	4.6	10.2	4.7	0.0	0.0	0.0	20.0
Shinozaki <i>et al.</i>	1984		0.88	0.08	0.00	0.00	99.04	100.00	1.1	5.3	8.0	5.2	0.0	0.0	0.0	20.0
Shinozaki <i>et al.</i>	1984		0.92	0.05	0.00	0.00	99.03	100.00	1.0	7.1	7.8	3.4	0.0	0.0	0.0	20.0
Shinozaki <i>et al.</i>	1984		0.89	0.07	0.00	0.00	99.04	100.00	0.9	6.3	6.3	5.9	0.0	0.5	0.0	20.0
Shinozaki <i>et al.</i>	1984		0.90	0.00	0.00	0.00	99.10	100.00	1.0	8.5	2.1	8.4	0.0	0.1	0.0	20.0
Shinozaki <i>et al.</i>	1984		1.62	0.00	0.00	0.00	98.38	100.00	1.0	5.1	8.8	4.8	0.0	0.1	0.0	20.0
Shinozaki <i>et al.</i>	1984		1.88	0.05	0.00	0.00	98.07	100.00	1.0	5.1	8.8	4.8	0.0	0.1	0.0	20.0
Shinozaki <i>et al.</i>	1984		1.90	0.03	0.00	0.00	98.07	100.00	0.9	5.3	6.2	7.9	0.0	0.0	0.0	20.0
Shinozaki <i>et al.</i>	1984		1.90	0.06	0.00	0.00	98.04	100.00	0.9	7.8	7.5	3.6	0.0	0.1	0.0	20.0
Shinozaki <i>et al.</i>	1984		1.90	0.00	0.00	0.00	98.10	100.00	1.0	8.3	2.1	8.0	0.0	0.0	0.0	20.0
Shinozaki <i>et al.</i>	1984		1.88	0.00	0.00	0.00	98.12	100.00	1.0	8.5	2.1	8.4	0.0	0.1	0.0	20.0
Shinozaki <i>et al.</i>	1984		1.89	0.00	0.44	0.00	97.67	100.00	0.9	9.1	1.4	8.4	0.0	0.0	0.0	20.0
Shinozaki <i>et al.</i>	1984		4.27	0.07	0.00	0.00	95.66	100.00	0.9	5.3	6.2	8.0	0.0	0.0	0.0	20.0
Shinozaki <i>et al.</i>	1984		5.56	0.00	0.00	0.00	94.44	100.00	1.0	7.1	7.8	3.4	0.0	0.0	0.0	20.0
Shinozaki <i>et al.</i>	1984		5.56	0.00	0.00	0.00	94.44	100.00	1.0	9.5	1.4	8.0	0.0	0.0	0.0	20.0
Shinozaki <i>et al.</i>	1984		1.88	0.00	0.00	0.00	98.12	100.00	1.1	5.3	8.0	5.2	0.0	0.0	0.0	20.0
Shinozaki <i>et al.</i>	1984		1.96	0.00	0.00	0.00	98.04	100.00	1.0	8.3	2.1	8.0	0.0	0.0	0.0	20.0
Shinozaki <i>et al.</i>	1984		4.75	0.00	0.00	0.00	95.25	100.00	1.0	9.5	1.4	8.0	0.0	0.0	0.0	20.0
Shinozaki <i>et al.</i>	1984		1.69	0.00	0.00	0.00	98.31	100.00	1.0	7.1	7.8	3.4	0.0	0.0	0.0	20.0
Shinozaki <i>et al.</i>	1984		1.83	0.00	0.00	0.00	98.17	100.00	0.9	9.1	1.4	8.4	0.0	0.0	0.0	20.0
Shinozaki <i>et al.</i>	1984		4.86	0.00	0.00	0.00	95.14	100.00	1.0	9.5	1.4	8.0	0.0	0.0	0.0	20.0
Wei <i>et al.</i>	1988	[25]	14.47	0.36	0.00	0.42	0.00	300.00	0.0	15.0	13.5	0.0	1.5	0.0	0.0	30.0
Wei <i>et al.</i>	1988		14.47	0.36	0.00	0.43	0.00	300.00	0.0	14.3	12.8	0.0	1.4	1.5	0.0	30.0
Iwamasa & Fruehan	1997	[29]	14.47	0.36	0.00	0.43	0.00	300.00	0.0	14.6	13.1	0.0	1.5	0.9	0.0	30.0
Iwamasa & Fruehan	1997		14.47	0.36	0.00	0.43	0.00	300.00	0.0	14.9	13.4	0.0	1.5	0.3	0.0	30.0
Iwamasa & Fruehan	1997		14.20	1.23	0.00	0.44	0.00	300.00	0.0	15.0	13.5	0.0	1.5	0.0	0.0	30.0
Iwamasa & Fruehan	1997		14.18	1.29	0.00	0.43	0.00	300.00	0.0	14.3	12.8	0.0	1.4	1.5	0.0	30.0
Iwamasa & Fruehan	1997		14.14	1.41	0.00	0.44	0.00	300.00	0.0	14.6	13.1	0.0	1.5	0.9	0.0	30.0
Iwamasa & Fruehan	1997		14.17	1.32	0.00	0.44	0.00	300.00	0.0	14.9	13.4	0.0	1.5	0.3	0.0	30.0
Iwamasa & Fruehan	1997		13.65	0.30	0.00	0.00	286.05	300.00	0.0	16.8	11.7	0.0	0.0	1.5	0.0	30.0
Iwamasa & Fruehan	1997		13.65	0.30	0.00	0.00	286.05	300.00	0.0	12.4	8.6	0.0	0.0	9.0	0.0	30.0
Wu <i>et al.</i>	1998	[16]	0.20	0.01	0.00	0.00	1.29	1.50	0.2	69.7	69.7	28.2	0.0	0.0	0.0	170.0
Wu <i>et al.</i>	1998		0.08	0.03	0.00	0.00	1.39	1.50	0.2	69.7	69.7	28.2	0.0	0.0	0.0	170.0
Wu <i>et al.</i>	1998		0.07	0.01	0.00	0.00	1.42	1.50	1.2	79.6	63.9	27.5	0.0	0.0	0.0	170.0
Wu <i>et al.</i>	1998		0.07	0.02	0.00	0.00	1.42	1.50	1.2	79.6	63.9	27.5	0.0	0.0	0.0	170.0
Wu <i>et al.</i>	1998		0.07	0.03	0.00	0.00	1.40	1.50	1.2	79.6	63.9	27.5	0.0	0.0	0.0	170.0

Ph.D. Thesis – B. Jamieson – McMaster Univ. – Materials Science & Engineering

Author	Year	Cite	[C] (g)	[Si] (g)	[Mn] (g)	[S] (g)	[Fe] (g)	m _{Metal} (g)	(MnO) (g)	(CaO) (g)	(SiO ₂) (g)	(Al ₂ O ₃) (g)	(MgO) (g)	(FeO) (g)	(CaF ₂) (g)	m _{Slag} (g)
Wu <i>et al.</i>	1998		0.07	0.01	0.00	0.00	1.42	1.50	9.7	69.2	62.9	26.5	0.0	0.0	0.0	170.0
Wu <i>et al.</i>	1998		0.07	0.03	0.00	0.00	1.40	1.50	9.7	69.2	62.9	26.5	0.0	0.0	0.0	170.0
Shibata <i>et al.</i>	1999	[5]	4.50	0.20	0.00	0.13	115.18	120.00	0.0	5.9	6.4	0.0	0.0	5.9	1.8	20.0
Shibata <i>et al.</i>	1999		4.60	0.21	0.02	0.00	115.18	120.00	4.5	6.1	6.7	0.0	0.0	0.9	1.9	20.0
Shibata <i>et al.</i>	1999		4.55	0.26	0.01	0.00	115.18	120.00	7.9	4.4	4.8	0.0	0.0	1.1	1.8	20.0
Shibata <i>et al.</i>	1999		4.56	0.27	0.04	0.00	115.14	120.00	4.2	7.1	7.9	0.0	0.0	0.8	0.0	20.0
Shibata <i>et al.</i>	1999		4.62	0.29	0.02	0.00	115.07	120.00	4.1	5.4	5.9	0.0	0.0	0.8	3.7	20.0
Shibata <i>et al.</i>	1999		4.55	0.22	0.02	0.00	115.21	120.00	7.9	4.7	5.4	0.0	0.0	1.9	0.0	20.0
Shibata <i>et al.</i>	1999		4.60	0.24	0.04	0.00	115.13	120.00	7.3	5.3	6.0	0.0	0.0	0.5	0.9	20.0
Shibata <i>et al.</i>	1999		4.49	0.24	0.02	0.00	115.25	120.00	8.4	3.6	3.9	0.0	0.0	0.4	3.5	20.0
Shibata <i>et al.</i>	1999		4.38	0.23	0.00	0.00	115.39	120.00	0.0	7.8	8.6	0.0	0.0	0.0	3.6	20.0
Shibata <i>et al.</i>	1999		4.52	0.24	0.03	0.00	115.21	120.00	7.3	5.5	5.4	0.0	0.0	0.0	1.8	20.0
Sohn <i>et al.</i>	2000	[14]	5.70	0.00	0.90	0.00	293.40	300.00	5.8	12.1	12.5	0.0	5.1	3.7	0.0	40.0
Sohn <i>et al.</i>	2000		5.70	0.00	0.90	0.00	293.40	300.00	5.9	17.0	8.8	0.0	2.7	3.9	0.0	40.0
Sohn <i>et al.</i>	2000		5.70	0.00	0.90	0.00	293.40	300.00	5.7	18.8	6.8	0.0	2.3	4.0	0.0	40.0
Sohn <i>et al.</i>	2000		5.70	0.00	0.90	0.00	293.40	300.00	5.6	21.2	5.4	0.0	2.0	3.6	0.0	40.0
Sohn <i>et al.</i>	2000		5.70	0.00	0.90	0.00	293.40	300.00	6.3	17.1	5.9	0.0	2.5	4.0	1.9	40.0
Sohn <i>et al.</i>	2000		5.70	0.00	0.90	0.00	293.40	300.00	6.3	17.1	5.9	0.0	2.5	4.0	1.9	40.0
Sohn <i>et al.</i>	2000		5.70	0.00	0.90	0.00	293.40	300.00	6.3	17.1	5.9	0.0	2.5	4.0	1.9	40.0
Sohn <i>et al.</i>	2000		5.70	0.00	0.90	0.00	293.40	300.00	6.3	17.1	5.9	0.0	2.5	4.0	1.9	40.0
Sohn <i>et al.</i>	2000		5.70	0.00	0.90	0.00	293.40	300.00	5.5	20.6	7.5	0.0	2.1	2.1	0.0	40.0
Sohn <i>et al.</i>	2000		5.70	0.00	0.90	0.00	293.40	300.00	5.8	16.6	5.7	0.0	2.5	10.3	0.0	40.0
Sohn <i>et al.</i>	2000		5.70	0.00	0.90	0.00	293.40	300.00	6.2	12.7	4.4	0.0	3.7	10.3	0.0	40.0
Sohn <i>et al.</i>	2000		5.70	0.00	0.90	0.00	293.40	300.00	5.7	19.2	6.8	0.0	2.4	2.1	0.0	40.0
Sohn <i>et al.</i>	2000		0.30	0.00	0.90	0.00	298.80	300.00	5.7	18.8	6.8	0.0	2.3	4.0	0.0	40.0
Sohn <i>et al.</i>	2000		3.00	0.00	0.90	0.00	296.10	300.00	5.7	18.8	6.8	0.0	2.3	4.0	0.0	40.0
Sohn <i>et al.</i>	2000		12.30	0.00	0.90	0.00	286.80	300.00	5.7	18.8	6.8	0.0	2.3	4.0	0.0	40.0
Sohn <i>et al.</i>	2000		16.15	0.00	0.90	0.00	282.95	300.00	5.7	18.8	6.8	0.0	2.3	4.0	0.0	40.0
Sohn <i>et al.</i>	2000		5.70	0.75	0.90	0.00	292.65	300.00	5.7	18.8	6.8	0.0	2.3	4.0	0.0	40.0
Sohn <i>et al.</i>	2000		5.70	1.65	0.90	0.00	291.75	300.00	5.7	18.8	6.8	0.0	2.3	4.0	0.0	40.0
Sohn <i>et al.</i>	2000		5.70	0.00	0.00	0.00	294.30	300.00	5.7	18.8	6.8	0.0	2.3	4.0	0.0	40.0
Sohn <i>et al.</i>	2000		0.00	0.00	0.00	0.00	300.00	300.00	5.7	18.8	6.8	0.0	2.3	4.0	0.0	40.0
Vargas-Ramirez <i>et al.</i>	2002	[23]	50.00	16.00	75.00	0.00	9859	10000	168.0	31.0	45.9	0.0	16.2	38.4	0.0	300.0
Vargas-Ramirez <i>et al.</i>	2002		200.00	16.00	75.00	0.00	9709	10000	168.0	31.0	45.9	0.0	16.2	38.4	0.0	300.0
Heo <i>et al.</i>	2015	[6]	0.00	44.85	84.75	0.00	20.40	150.00	80.0	60.0	60.0	0.0	0.0	0.0	0.0	200.0

Ph.D. Thesis – B. Jamieson – McMaster Univ. – Materials Science & Engineering

Author	Year	Cite	[C] (g)	[Si] (g)	[Mn] (g)	[S] (g)	[Fe] (g)	m _{Metal} (g)	(MnO) (g)	(CaO) (g)	(SiO ₂) (g)	(Al ₂ O ₃) (g)	(MgO) (g)	(FeO) (g)	(CaF ₂) (g)	m _{Slag} (g)
Heo <i>et al.</i>	2015		0.00	44.85	84.75	0.00	20.40	150.00	80.0	55.0	55.0	0.0	0.0	0.0	10.0	200.0
Heo <i>et al.</i>	2015		0.00	44.85	84.75	0.00	20.40	150.00	80.0	50.0	50.0	0.0	0.0	0.0	20.0	200.0
Heo <i>et al.</i>	2015		0.00	44.85	84.75	0.00	20.40	150.00	80.0	45.0	45.0	0.0	0.0	0.0	30.0	200.0
Heo <i>et al.</i>	2015		0.00	44.85	84.75	0.00	20.40	150.00	80.0	60.0	60.0	0.0	0.0	0.0	0.0	200.0
Heo <i>et al.</i>	2015		0.00	44.85	84.75	0.00	20.40	150.00	80.0	60.0	60.0	0.0	0.0	0.0	0.0	200.0
Lee <i>et al.</i>	2016	[30]	0.00	2.00	0.00	0.00	3.00	5.00	5.6	16.8	15.4	9.1	5.6	17.5	0.0	70.0
Lee <i>et al.</i>	2016		0.00	2.00	0.00	0.00	3.00	5.00	5.6	17.5	14.7	9.1	5.6	17.5	0.0	70.0
Lee <i>et al.</i>	2016		0.00	2.00	0.00	0.00	3.00	5.00	5.6	17.5	14.7	9.1	5.6	17.5	0.0	70.0
Lee <i>et al.</i>	2016		0.00	2.00	0.00	0.00	3.00	5.00	5.6	18.9	13.3	9.1	5.6	17.5	0.0	70.0
Jamieson <i>et al.</i>	2019	[2]	0.00	0.23	0.00	0.00	1.27	1.50	3.8	8.5	8.5	4.3	0.0	0.0	0.0	25.0
Jamieson <i>et al.</i>	2019		0.00	0.23	0.00	0.00	1.27	1.50	3.8	8.5	8.5	4.3	0.0	0.0	0.0	25.0
Jamieson <i>et al.</i>	2019		0.00	0.23	0.00	0.00	1.27	1.50	3.8	8.5	8.5	4.3	0.0	0.0	0.0	25.0
Jamieson <i>et al.</i>	2019		0.00	0.30	0.00	0.00	1.20	1.50	3.8	8.5	8.5	4.3	0.0	0.0	0.0	25.0
Jamieson <i>et al.</i>	2019		0.00	0.15	0.00	0.00	1.35	1.50	3.8	8.5	8.5	4.3	0.0	0.0	0.0	25.0
Jamieson <i>et al.</i>	2019		0.00	0.23	0.00	0.00	1.27	1.50	2.5	9.0	9.0	4.5	0.0	0.0	0.0	25.0
Jamieson <i>et al.</i>	2019		0.00	0.23	0.00	0.00	1.27	1.50	1.3	9.5	9.5	4.8	0.0	0.0	0.0	25.0
Jamieson <i>et al.</i>	2019		0.00	0.15	0.00	0.00	0.85	1.00	3.8	8.5	8.5	4.3	0.0	0.0	0.0	25.0
Jamieson <i>et al.</i>	2019		0.00	0.08	0.00	0.00	0.42	0.50	3.8	8.5	8.5	4.3	0.0	0.0	0.0	25.0

***For Wei *et al.* [25], the first row of mass data must also consider 5.84g of Li₂O. The second row of mass data has 4.31g Li

Chapter 7

7. Conclusions

The conclusions are broken down into two parts: the first, a summary of what has been found in the previous chapters and its implications on the state of the art; the second, a review of findings that were not satisfactorily answered or where the author sees room for future work.

7.1. Summary & Conclusions

Chapter 3 achieves the first objective of this thesis. Experiments were performed and showed that a rapid reaction occurs which approaches equilibrium within five minutes. Specific findings include:

- A slag mass transfer coefficient, k_{MnO} , was calculated to be $4 \cdot 10^{-5}$ m/s; this mass transfer coefficient was determined assuming a bubble free surface.
- The system was well described by mass transport control of (MnO) but did not fit changes in initial [Si] content; mixed mass transport control was proposed.
- SiO bubbles form along the reaction interface and block 90.35% of the available reaction area.
- Gas formation occurs because of an imbalance of (Mn²⁺) to [Si] at the interface; when a 2:1 ratio is not upheld SiO can form.
- The effect of bubble obstructions on the rate of reaction should not be a concern for steelmakers because stirring of the reactor will agitate the bubbles and separate them from the surface.

Chapter 4 demonstrates achievement of the second objective. A model considering mixed mass transfer and chemical reaction was proposed. By tracking both silicon and manganese in both phases the model is the first to consider counter-current diffusion of product species as a potential rate-controlling step. Despite the complex reaction mechanisms associated with cation and anion transport, simplifications to their molecular species and the use of phenomenological mass transport equations proved effective in predicting the progress of the reaction. Specific findings are listed below:

- The fitted mass transfer coefficients k_{Slag} and k_{Metal} were determined to be $6.7 \cdot 10^{-4} \text{m/s}$ and $2.3 \cdot 10^{-4} \text{m/s}$ respectively; modifying these values on a per species basis was not justifiable based on the overall RMS fit. This supports the conclusion that counter-current diffusion of species is rate controlling; this modifies the conclusion from Chapter 3, both SiO_2 and MnO are important transporting species in the slag.
- The mass transfer coefficients were calculated using a geometric consideration of a monolayer of close-packed SiO bubbles.
- When the area change is considered, the slag mass transfer coefficient proposed in Chapter 3 is essentially the same as that determined by this model.
- Sensitivity analysis shows that the RMS error values in the system are twice as sensitive to changes in k_{Slag} than k_{Metal} ; slag mass transport is more significant than metal mass transport, but both must be considered.

- The relative importance of the slag compared to the metal explains findings from Chapter 3 and of some past researchers; the dominant rate controlling step can switch phases depending on the properties of the system.
- Silicon efficiency was calculated to be essentially 100% despite the claims published in Chapter 3. A small amount of SiO can form but only serves to obstruct the interface; chemically, the formation of SiO is insignificant.

Chapter 3 and Chapter 4 explain why there are discrepancies in the reported literature with respect to the rate-controlling step: the system experiences mixed mass transport control and while simplification to a single transporting species may produce reasonable results, it is an incomplete answer. Further, only one other researcher has documented the presence of SiO within the system; ignoring it may have impacted past results.

Chapter 5 coincides with objective 3. The carbothermic reduction of MnO was explored and evidence of a very complex reaction mechanism was presented. Qualitative evidence was collected and analyzed to support a mechanism like that reported on by previous authors for the carbothermic reduction of FeO.

- The rate of reaction for this system is very slow; because the slag composition was identical to that of Chapter 3 the system cannot be controlled by slag transport.
- A two-stage reaction was documented. In the first stage droplet bloating occurred and in the second stage a stagnant layer of CO forms along the metal surface. The bloating is weak when compared to FeO as the oxygen source.

- The rate of reaction increases linearly with carbon content in the droplet. During stage 1 the rate of reaction is also linearly related to volume. This is characteristic of rate control by nucleation and growth of internal CO bubbles.
- At the beginning of the reaction, more [Mn] and [Si] are reduced than [C] oxidized in the same time period; [Mn] and [Si] must exchange with [Fe] to close the mass balance. Within 12 minutes the total moles of [C] oxidized and [Mn] and [Si] reduced realign.
- Metal forms in the slag towards the end of the reaction indicating that metal oxide is reduced at the gas-slag interface and *not* the gas-metal interface.
- The slow second stage of reaction and accumulation of metal in the slag indicates that transport of CO₂ from gas-slag to gas-metal interfaces occurs; at either of these interfaces a slow chemical reaction must occur. The reaction is slow because MnO is a poor oxygen source for carbon.

Chapter 6 concludes the work in the interest of objective 5. An explanation for differences between the findings of past and present researchers during metal oxide reductions by silicon or carbon was proposed. Trends between slag mass transfer coefficients and slag properties were analyzed.

- A comprehensive literature review of the carbothermic and silicothermic reduction of manganese oxide from slag was written; supplementary authors were cited where iron oxide was reduced. Mass transfer coefficients in these systems are comparable.

- A strong relationship exists between increases in optical basicity and increases in the reported slag mass transfer coefficients.
- A trend was found between the overall mass transfer coefficient and the calculated partition. Despite differences in slag composition, metal composition, temperature, and volume ratios the systems studied are similar and can likely all be described as mixed mass transport control.

The preceding conclusions show how four of the five study objectives from Chapter 1.2 have been completed. The fourth objective, modelling the carbothermic reduction of MnO from slag, remains under study and will require an ongoing investigation.

7.2. Future Work

The conclusions highlight the most obvious step for future work: Chapter 5 must be supplemented with a complex carbothermic reduction model that considers the three possible reaction stages in the work. The first stage, external CO generation, may be rate-limited by carbon transport. For bloated droplets, CO nucleation and growth must be considered. In the final stage, blockage of slag/metal contact by the gas intermediary must be considered. The system can be tested with sulfur additions to the metal to identify where the slowest chemical reaction is taking place.

The silicothermic reduction work should be validated for bath style experiments. There are two important findings to identify: whether the calculated mass transfer coefficient fits the partition trend as Chapter 6 expects, and whether

a stable film layer of SiO forms as it does with droplets. From a kinetics perspective, an experimental design that could selectively slow either the transport of SiO₂ or MnO would be valuable; one method may be to use a higher slag basicity that could improve the reaction rates and availability of charge balancing species in the slag.

A topic of further interest would be to section and chemically analyze the bulk slag concentration of quenched samples taken during the silicothermic reduction of manganese oxide. A fundamental principle of the mass transfer analyses performed in this thesis is that bulk transport of material is not a major source of resistance to overall mass transport compared to material transfer at the interface. However, it is clear from quenched samples that some degree of heterogeneity of the slag occurs during the reaction. Despite the apparent inconsistency within the slag, the developed silicothermic reduction model accurately describes what occurs within the tested systems, thus the visual and EDS findings appear to be at odds with the developed model.

Finally, some industrial experiments should be carried out to identify the best method of adding manganese to the steelmaking process. One suggestion could be Fe-Si-Mn pellets mixed with MnO ore; the ore/slag should have a basicity of no less than 1.3 but 2 is preferable. Si and MnO should be in proximity; the iron in the alloy will absorb the manganese produced. If these pellets were added at the end of the BOF or during ladle refining the heat of the melt will provide most of the heat required for the process, with the balance from silicothermic reduction.

Chapter 8

8. References

- [1] R. Elliott, K. Coley, S. Mostaghel, and M. Barati: *JOM*, 2018, vol. 70, pp. 1–11.
- [2] Z. H. Cai, H. Ding, X. Xue, and Q. B. Xin: *Mater. Sci. Eng. A*, 2013, vol. 560, pp. 388–95.
- [3] O.S. Bobkova and V.V. Barsegyan: *Metallurgist*, 2006, vol. 50, pp. 463–68.
- [4] L.N. Kologrivova, A.Ya. Nakonechnyi, Z.G. Trofimova, O.V. Nosochenko, and N.N. Kulik: *Metallurgist*, 1987, vol. 5, pp. 28–29.
- [5] Environmental Protection Agency and National Highway Traffic Safety Administration: *Corporate Average Fuel Economy Standards*, 2012, pp. 62624–200.
- [6] M. Gasik: *Handbook of Ferrous Alloys: Theory and Technology*, Butterworth-Heinemann, 2013.
- [7] J.R. Davis: *ASM Specialty Handbook® Stainless Steels*, 1994.
- [8] Outokumpu: *Handbook of Stainless Steel*, Sandvikens Tryckeri AB, Riihitontuntie, Finland, 2013.
- [9] S.E. Olsen, M. Tangstad, and T. Lindstad: *Production of Manganese Ferrous Alloys*, Tapir Academic Press, Trondheim, 2007.
- [10] R. Elliott, K. Coley, S. Mostaghel, and M. Barati: *JOM*, 2018, vol. 70, pp. 691–99.
- [11] L.M. Pidgeon and W.A. Alexander: *Trans. AIME*, 1944.

- [12] J.M. Toguri and L.M. Pidgeon: *Can. J. Chem.*, 1961, vol. 30, pp. 540–47.
- [13] I. M. Morsi and H. H. Ali: *Int. J. Miner. Process.*, 2014, vol. 127, pp. 37–43.
- [14] L. Brewer and R.K. Edwards: *J. Phys. Chem.*, 1954, vol. 58, pp. 351–58.
- [15] C.W. Bale, E. Bélisle, P. Chartrand, S.A. Deckerov, G. Eriksson, A.E. Gheribi, K. Hack, I.H. Jung, Y.B. Kang, J. Melançon, A.D. Pelton, S. Petersen, C. Robelin, J. Sangster, and M.A. Van Ende: *Calphad*, 2016, vol. 54, pp. 35–53.
- [16] M.W. Jr. Chase, C.A. Davies, J.R. Jr. Downey, D.J. Frurip, R.A. McDonald, and A.N. Syverud: *NIST Stand. Ref. Database 13*, 1985, vol. 1.
- [17] W.L. Daines and R.D. Pehlke: *Trans. Met. Soc. AIME*, 1968, vol. 242, pp. 565–75.
- [18] J.H. Heo, Y. Chung, and J.H. Park: *Metall. Mater. Trans. B*, 2015, vol. 46B, pp. 1154–61.
- [19] L. Wu, J. Gran, and D. Sichen: *Metall. Mater. Trans. B*, 2011, vol. 42, pp. 928–31.
- [20] K.Y. Ko and J.H. Park: *ISIJ Int.*, 2013, vol. 53, pp. 958–65.
- [21] H. Sohn, Z. Chen, and W. Jung: *Steel Res.*, 2000, vol. 71, pp. 145–52.
- [22] R.J. Pomfret and P. Grieveson: *Ironmak. Steelmak.*, 1978, vol. 5, pp. 191–97.
- [23] E. Shibata, H. Sun, and K. Mori: *Metall. Mater. Trans. B*, 1999, vol. 30B, pp. 279–86.

- [24] O. Ostrovski, S.E. Olsen, M. Tangstad, and M. Yastreboff: *Can. Metall. Q.*, 2002, vol. 41, pp. 309–18.
- [25] E.T. Turkdogan and R.J. Fruehan: in *Making, Shap. Treat. Steel.*, 1998, pp. 13–157.
- [26] R.J. Pomfret and P. Grieveson: *Can. Metall. Q.*, 1983, vol. 22, pp. 287–99.
- [27] B. Ozturk and R. J. Fruehan: *Metall. Mater. Trans. B*, 1985, vol. 16, pp. 121–27.
- [28] S.K. Tarby and W.O. Philbrook: *Trans. Metall. Soc. AIME*, 1967, vol. 239, pp. 1005–17.
- [29] W.L. Daines and R.D. Pehlke: *Metall. Trans.*, 1971, vol. 2, pp. 1203–11.
- [30] C. Bodsworth and H.B. Bell: *Physical Chemistry of Iron and Steelmaking*, Longmans, London, 1972.
- [31] M. Ashizuka, A. Moribe, and K. Sawamura: *Tetsu-to-Hagane*, 1975, vol. 61, pp. 36–45.
- [32] K. Xu, G. Jiang, W. Ding, L. Gu, S. Guo, and B. Zhao: *ISIJ Int.*, 1993, vol. 33, pp. 104–8.
- [33] T. Skjervheim: Norwegian Institute of Technology, Trondheim, 1994.
- [34] M. Tangstad: Norwegian Institute of Technology, Trondheim, 1996.
- [35] T.A. Skjervheim and S.E. Olsen: *Infacon 7*, 1995, pp. 631–40.
- [36] R. Kononov, O. Ostrovski, and S. Ganguly: *Metall. Mater. Trans. B Process Metall. Mater. Process. Sci.*, 2008, vol. 39B, pp. 662–68.

- Ph.D. Thesis – B. Jamieson – McMaster Univ. – Materials Science & Engineering
- [37] H. Sun, M.Y. Lone, S. Ganguly, and O. Ostrovski: *ISIJ Int.*, 2010, vol. 50, pp. 639–46.
- [38] M. Allibert, H. Gaye, J. Geisler, D. Janke, B.J. Keene, D. Kirner, M. Kowalski, J. Lehmann, K.C. Mills, D. Neuschutz, R. Parra, C.S. Jours, P.J. Spencer, M. Susa, M. Tmar, and E. Woermann: *Slag Atlas*, 2nd ed., 1995.
- [39] I. Sohn and D.J. Min: *Steel Res. Int.*, 2012, vol. 83, pp. 611–30.
- [40] J.A. Duffy: *J. Chem. Educ.*, 1996, vol. 73, p. 1138.
- [41] K.C. Mills and S. Sridhar: *Ironmak. Steelmak.*, 1999, vol. 26, pp. 262–68.
- [42] K.C. Mills: *South. African Pyrometallurgy 2011*, 2011, pp. 1–52.
- [43] R.H. Parker: *An Introduction to Chemical Metallurgy*, Pergamon Press, Oxford [England]; New York, 1978.
- [44] T. Young: *Philos. Trans. R. Soc. London*, 1805, vol. 95, pp. 65–87.
- [45] M.A. Rhamdhani: *Reaction Kinetics and Dynamic Interfacial Phenomena in Liquid Metal-Slag Systems*, McMaster University, 2005.
- [46] F. Bashforth and J.C. Adams: *An Attempt to Test the Theories of Capillary Action*, London, United Kingdom, 1883.
- [47] S. Ueda, A.W. Cramb, H. Shi, X. Jiang, and H. Shibata: *Metall. Mater. Trans. B*, 2003, vol. 34, pp. 503–8.
- [48] Y. Chung and A.W. Cramb: *Philos. Trans. R. Soc. A Math. Phys. Eng. Sci.*, 1998, vol. 356, pp. 981–93.
- [49] M.Y. Lone, H. Sun, S. Ganguly, and O. Ostrovski: in *Infacon XI*, 2007, pp. 594–602.

- [50] T.M. Kekelidze, S.M. Mikiashvili, T.I. Dzhincharadze, and R.V. Khomeriki: *Izv. Akad. Nauk Gruz. SSR, Seriya Khimicheskaya*, 1978, vol. 4, pp. 240–44.
- [51] Y. Waseda and J.M. Toguri: *The Structure and Properties of Oxide Melts: Application of Basic Science to Metallurgical Processing*, World Scientific Publishing Co., Singapore, 1998.
- [52] P. Kozakevitch: *Surface Activity in Liquid Metal Solutions*, 1968.
- [53] D.H. Bradhurst and A.S. Buchanan: *Aust. J. Chem.*, 1961, vol. 14, pp. 417–19.
- [54] K. Monma and H. Suto: *Trans JIM*, 1961, vol. 2, pp. 148–53.
- [55] G.R. Belton: *Metall. Trans.*, 1972, vol. 3, pp. 1465–69.
- [56] D.R. Sain and G.R. Belton: *Metall. Mater. Trans. B*, 1976, vol. 7, pp. 235–44.
- [57] G. R. Belton: *Can. Met. Q.*, 1982, vol. 21, pp. 137–43.
- [58] K. Ogino, S. Hara, T. Miwa, and S. Kimoto: *Trans. Iron Steel Inst. Japan*, 1984, vol. 24, pp. 522–31.
- [59] J. Thomson: *Philos. Mag. Ser. 4*, 1855, vol. 10, pp. 330–33.
- [60] C.V. Sternling and L.E. Scriven: *AIChE J.*, 1959, vol. 5, pp. 514–23.
- [61] L.E. Scriven and C.V. Sternling: *Nature*, 1960, vol. 187, pp. 186–88.
- [62] H. Ooi, T. Nozaki, and Y. Yoshii: *Tetsu-to-Hagané*, 1972, vol. 58, p. 830.
- [63] J.K. Brimacombe and F. Weinberg: *Metall. Trans.*, 1972, vol. 3, pp. 2298–99.

- [64] R.G. Barton and J.K. Brimacombe: *Metall. Mater. Trans. B*, 1976, vol. 7, pp. 144–45.
- [65] H. Gaye and P. V. Riboud: *Metall. Mater. Trans. B*, 1977, vol. 8, pp. 409–15.
- [66] P.V.V. Riboud and L.D.D. Lucas: *Can. Metall. Q.*, 1981, vol. 20, pp. 199–208.
- [67] H. Gaye, L.D. Lucas, M. Olette, and P.V. Riboud: *Can. Metall. Q.*, 1984, vol. 23, pp. 179–91.
- [68] A. Sharan and A.W. Cramb: *Metall. Mater. Trans. B*, 1995, vol. 26B, pp. 87–94.
- [69] A. Jakobsson, D. Sichen, S. Seetharaman, and N.N. Viswanathan: *Philos. Trans. R. Soc. Lond. A*, 1998, vol. 356, pp. 995–1001.
- [70] Y. Chung and A.W. Cramb: *Metall. Mater. Trans. B*, 2000, vol. 31B, pp. 957–71.
- [71] M.A. Rhamdhani, G.A. Brooks, and K.S. Coley: *Metall. Mater. Trans. B Process Metall. Mater. Process. Sci.*, 2006, vol. 37, pp. 1087–91.
- [72] M.A. Rhamdhani, K.S. Coley, and G.A. Brooks: *Metall. Mater. Trans. B*, 2005, vol. 36B, pp. 219–27.
- [73] M.A. Rhamdhani, K.S. Coley, and G.A. Brooks: *Metall. Mater. Trans. B*, 2005, vol. 36, pp. 591–604.
- [74] J.F. White and D. Sichen: *Metall. Mater. Trans. B Process Metall. Mater. Process. Sci.*, 2014, vol. 45B, pp. 96–105.

- [75] A.N. Assis, J. Warnett, S. Spooner, R.J. Fruehan, M.A. Williams, and S. Sridhar: *Metall. Mater. Trans. B*, 2015, vol. 46B, pp. 568–76.
- [76] S. Spooner, A.N. Assis, J. Warnett, R. Fruehan, M.A. Williams, and S. Sridhar: *Metall. Mater. Trans. B*, 2016, vol. 47B, pp. 2123–32.
- [77] S. Spooner, A. Rahnama, J.M. Warnett, M.A. Williams, Z. Li, and S. Seetharaman: *Nat. Sci. Reports*, 2017, vol. 7, pp. 1–16.
- [78] S. Spooner, Z. Li, and S. Sridhar: *Sci. Rep.*, 2017, vol. 7, pp. 1–12.
- [79] G. Brooks, Y. Pan, Subagyo, and K.C. Coley: *Metall. Mater. Trans. B*, 2005, vol. 36, pp. 525–35.
- [80] C.L. Molloseau and R.J. Fruehan: *Metall. Mater. Trans. B*, 2002, vol. 33, pp. 335–44.
- [81] K. Gu, N. Dogan, and K.S. Coley: *Metall. Mater. Trans. B*, 2017, vol. 48, p. 3408.
- [82] B.J. Jamieson and K.S. Coley: *Metall. Mater. Trans. B*, 2017, vol. 48, pp. 1613–24.
- [83] I.D. Sommerville, P. Grieveson, and J. Taylor: *Ironmak. Steelmak.*, 1980, vol. 7, pp. 25–32.
- [84] B.J. Jamieson, Y. Tabatabaei, M. Barati, and K.S. Coley: *Metall. Mater. Trans. B*, 2019, vol. 50, pp. 192–203.
- [85] A. Wu, P.C. Hayes, and H.G. Lee: *ISIJ Int.*, 1998, vol. 38, pp. 213–19.

Chapter 9

9. Appendix A – Energy Dispersive Spectroscopy Data

Energy Dispersive Spectroscopy (EDS) data was collected but not published and supports the conclusion that slag colour was associated with a chemical gradient. Two sets of data were collected. Manganese and silicon gradients are shown in the samples supporting earlier conclusions in this thesis.

9.1. Sample A – 2 Minutes into Reaction

In Figure 9.1 the scanned site of interest is shown with a backscatter electron (BSE) image. Several points were analyzed in Figure 9.1, labelled spectrum, and these points are shown sequentially in Figure 9.2. These points demonstrate that left to right (moving into the slag, away from the interface) the manganese concentration rises and the silicon concentration falls. This supports the conclusion of reactant and product transport limitations respectively.

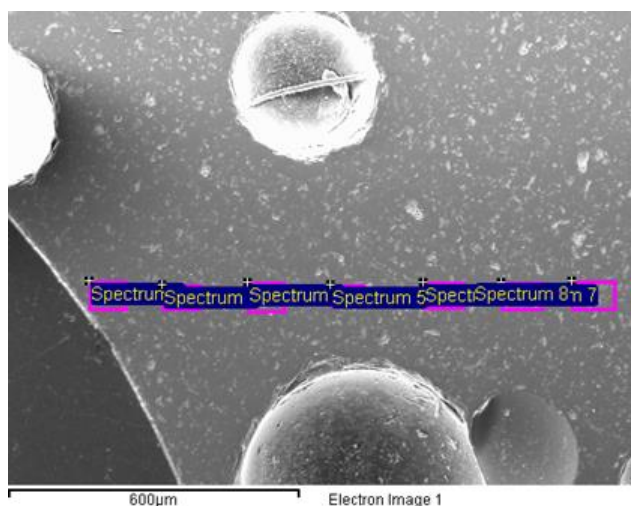


Figure 9.1: Point scan left to right moving away from the metal droplet; the metal droplet is the dark region in the bottom left corner.

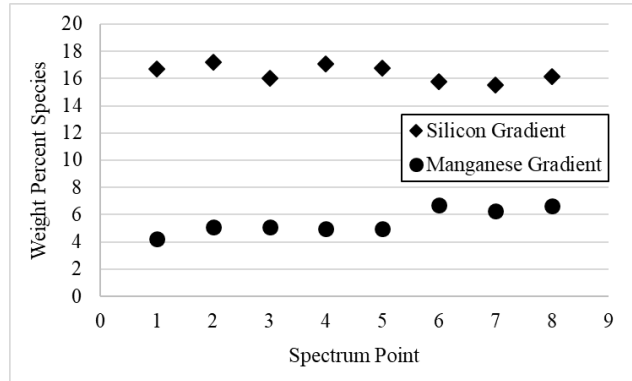


Figure 9.2: Weight percent data associated with the points scanned in Figure 9.1.

Figure 9.3 shows a linescan for the same region of slag but offers a continuous profile of the chemistry. The Y-axis units are unknown but show the trend in manganese and silicon data regardless.

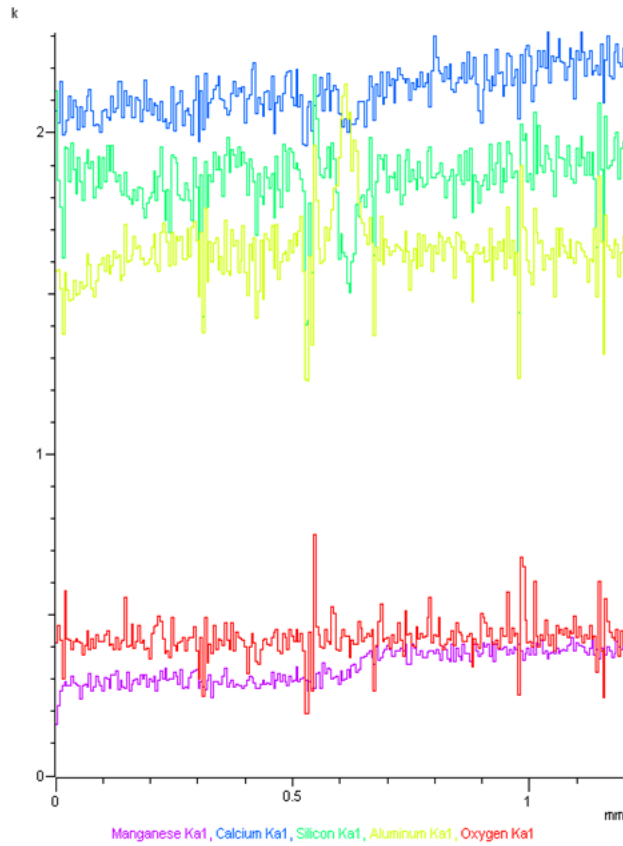


Figure 9.3: Line scan data for a similar region of the slag near the metal interface; manganese data trends upwards (Y-axis units unknown).

9.2. Sample B – 3 Minutes into Reaction

Another sample was analyzed at a later data. This analysis was more thorough than the initial analysis. A series of datapoints were collected from the bulk slag to establish a baseline concentration of Si and Mn. These values were 16.04wt% and 14.92wt% respectively and represent concentrations that should not have been affected by transport at the interface.

9.2.1. Optical Microscope Region of Interest

Figure 9.4 shows the site studied. This site was chosen because it shows a colour change and exists between gas cavities (left and right of the red rectangle) and the metal droplet (below the red rectangle).

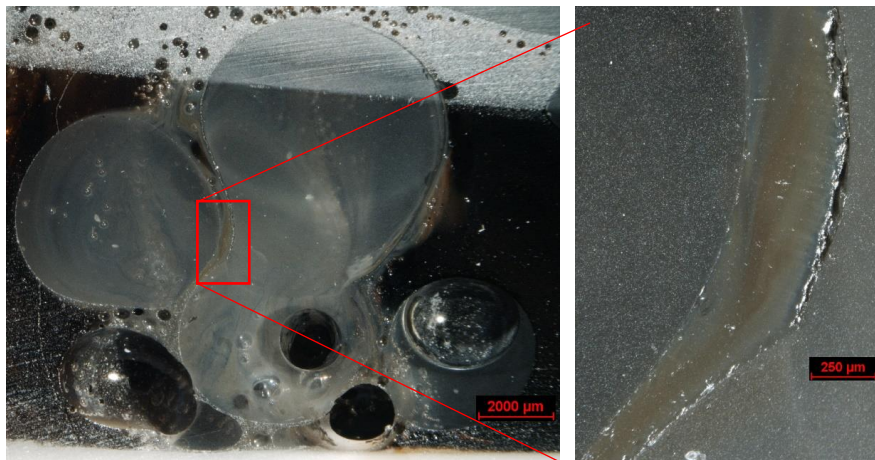


Figure 9.4: Image of the prepared sample (x1) and zoomed image of the specific site of interest (x5).

9.2.2. Site 1 – Linescan

Figure 9.5 shows where the linescan was performed and the corresponding concentrations across the horizontal yellow line. The slag is the grey region on the left and the epoxy (filling the hole where the metal droplet was located) is on the right. The vertical yellow line represents the point at which data may lose accuracy

because the interaction volume of the electron beam begins interacting with the epoxy; this is clear when viewing the oxygen data at 85 μm .

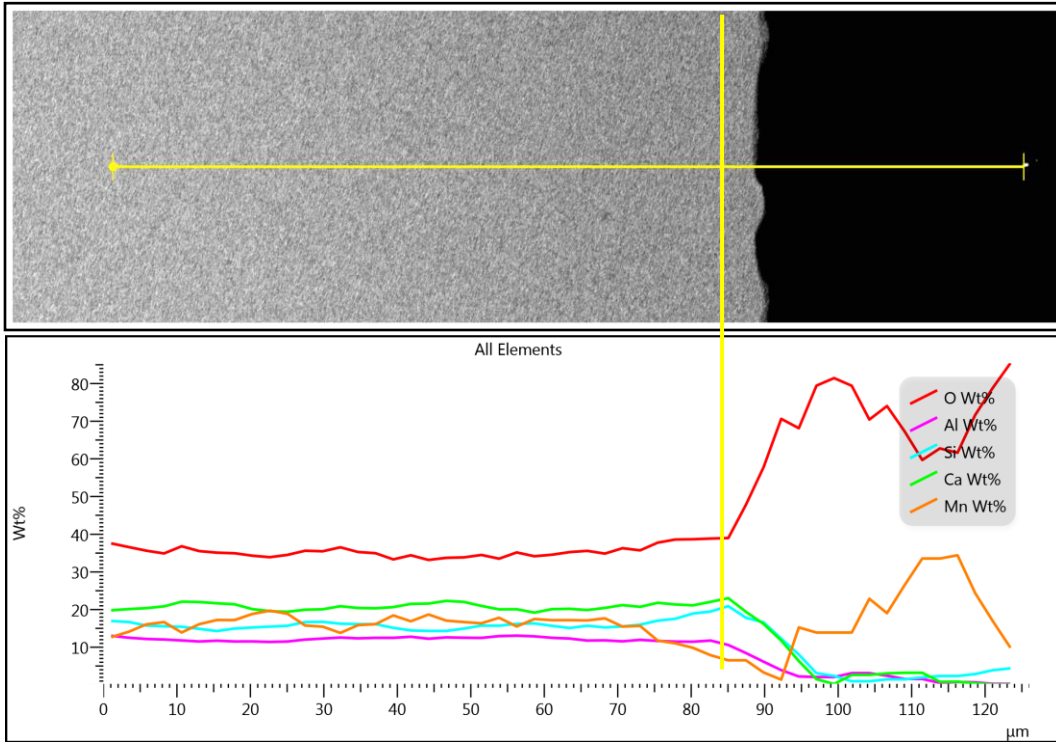


Figure 9.5: BSE image of linescan site and chemical data for the linescan; the slag is the grey region on the left and the black is the epoxy cavity.

9.2.3. Site 2 – Linescan

A second linescan was performed in the same general region as Figure 9.4 but at a different site. This data is presented in Figure 9.6. The orientation of the system is the same; slag left and epoxy right. While the output appears smoother, a manganese and silicon gradient are visible. The data should be considered unreliable for distances greater than 82 μm .

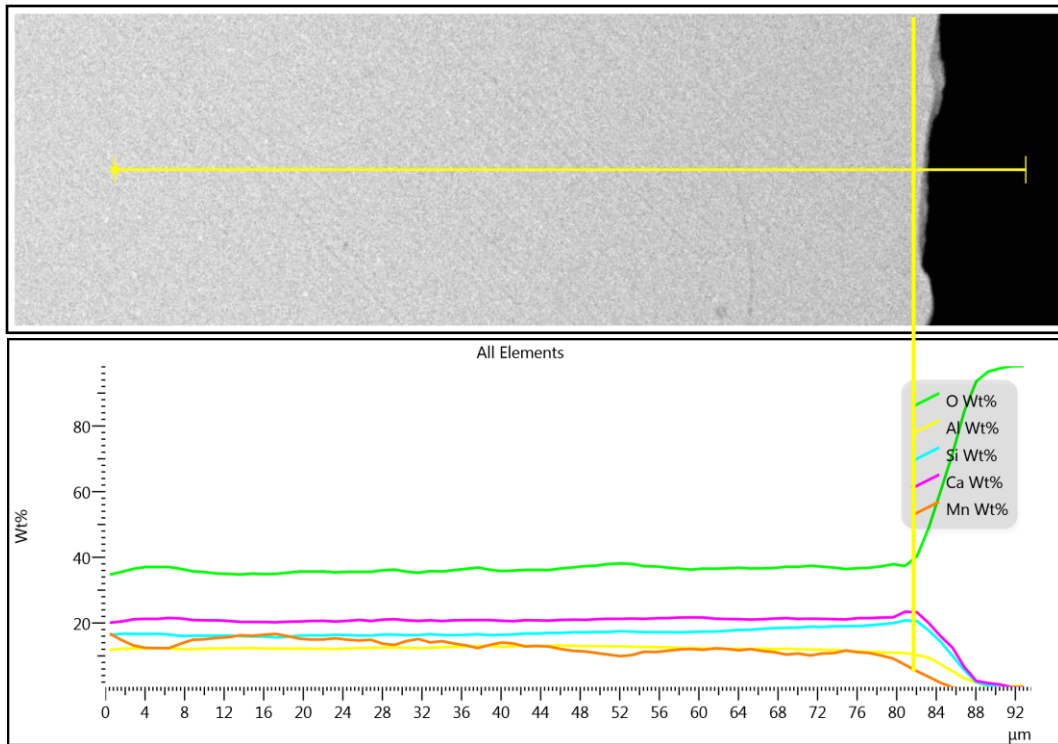


Figure 9.6: BSE image of linescan site and chemical data for the linescan; the slag is the grey region on the left and the black is the epoxy cavity.